DISSERTATION

VORTEX RECTIFICATION AND PHASE SLIPS IN SUPERCONDUCTING GRANULAR ALUMINUM

Submitted by

Weston F. Maughan II

Department of Physics

In partial fulfillment of the requirements

For the Degree of Doctor of Philosophy

Colorado State University

Fort Collins, Colorado

Fall 2020

Doctoral Committee:

Advisor: Stuart B. Field

Martin Gelfand
Kristen Buchanan
James R. Neilson

ABSTRACT

VORTEX RECTIFICATION AND PHASE SLIPS IN SUPERCONDUCTING GRANULAR ALUMINUM

Superconductivity is a unique and interesting phenomenon that manifests as a new phase of matter in a wide variety of materials. The most well-known property of superconductors is that they exhibit perfect conductivity when cooled below a critical temperature T_c. In addition to their perfect conductivity, superconductors exhibit the equally fundamental *Meissner effect* that expels magnetic fields from the interior of the material. While applications of a material that exhibits perfect conductivity, such as generating large magnetic fields via electromagnets or transmitting a large current with zero dissipation, are highly desired, the subtle details of flux penetration into mesoscopic samples may also be exploited to realize useful devices, or as a testbed to understand one-dimensional superconductivity. In this work, the nature of superconductivity in granular aluminum was explored in two mesoscopic sample classes: first, by studying Abrikosov vortices in films, and then by studying dissipation from phase slips in one-dimensional nanowires.

The penetration of an applied field is possible in film sample geometries, even though the Meissner effect generally expels flux. This penetration occurs in type-II superconductors via quantized flux bundles through normal regions or domains of the superconductor called *vortices*. The behavior and dynamics of these vortices are of significant interest as they can be exploited to realize fluxonic devices that perform circuit operations analogous to the operations performed with electrons in electronics. One method to influence the motion of vortices within a superconductor in order to realize a fluxonic device is to introduce a periodic potential landscape that causes an easy and a hard direction for vortex motion. In other words, the vortex motion is *rectified*. By realizing a so-called *vortex ratchet* with such a potential landscape,

vortices may easily be introduced or removed from the superconductor by driving them in the easy or hard directions respectively.

We begin by studying the rectification properties of both symmetrically and asymmetrically thickness-modulated superconducting films. These thickness modulations were fabricated with an elegant method of angle-sputter deposition of granular aluminum onto a glass substrate that has a sinusoidal modulation in its thickness. We then explored the rectification of these symmetric and asymmetric films by studying the motion of vortices using cryogenic transport measurements. In these measurements, vortices are driven in both directions across a modulated sample and the resulting voltages are measured. Differences in the voltages corresponding to motion in opposite directions imply that the vortices move more readily in one direction, that is, that there is an overall rectification in their motion. While these measurements performed with the symmetric washboard film seemed to exhibit reversibility in the transport properties, the asymmetric washboard exhibited a mild asymmetry that was much smaller than expected. This result indicates that the potential landscape is influenced by another source in addition to the asymmetric thickness modulation.

To better understand these effects, we tested the influence of the sample edges on the nucleation of vortices with two multi-segment films. These multi-segment films were fabricated in either an 8- or 14-probe geometry where each segment shares a vertical reference edge, while the opposing edges between pairs of voltage leads contain tapers of varying lengths which were fabricated lithographically. Clear rectification effects are observed with cryogenic transport measurements of these samples, with enhanced rectification for longer taper lengths showing the importance of the sample edge geometry on vortex motion.

Following these studies in superconducting films, we explored the nature of dissipation in one-dimensional superconducting nanowires. Recent advancements in laboratory fabrication techniques have reduced the accessible size scale of superconducting samples into the nanometer regime. As a result, superconductors can be fabricated that exhibit one-dimensional superconductivity, in which the complex superconducting order parameter ψ is restricted

to fluctuations along the length of the nanowire because its cross-sectional dimensions are smaller than ξ. Experiments performed with these nanowires exhibit a non-zero resistance even when the samples were cooled below T_c. This dissipation is understood as due to thermal fluctuations that cause $|\psi|$ to vanish in a small segment of the wire of length $\sim \xi$, allowing the superconducting phase to "slip" by $\pm 2\pi$, resulting in a voltage pulse. However, several experimental studies have observed excess nanowire resistance at low temperatures that cannot be described with this thermal fluctuation model alone. Some researchers have proposed that macroscopic quantum tunneling events lead to the excess resistance, while other studies claim that nanowire inhomogeneities influence the thermally activated phase slip rate.

In order to provide insight into the origin of the excess nanowire resistance, we performed cryogenic scanning experiments to map the local phase-slip rate along a superconducting nanowire. This was achieved by scanning either a dielectric or a magnetic tip with a home-built cryogenic atomic force microscope (cryo-AFM) to *locally* perturb superconductivity along a granular aluminum nanowire, while simultaneously measuring the nanowire resistance. This required the construction and characterization of the cryo-AFM along with a method of locating nanowire samples at cryogenic temperatures. We then fabricated one-dimensional granular aluminum nanowires with electron beam lithographic (EBL) techniques. We scanned these nanowires with the cryo-AFM and found that a dielectric tip does not locally perturb superconductivity enough to cause a measurable change in the wire resistance. However, repeating this experiment with either a magnetic tip or another material may plausibly elucidate the origins of the low-temperature nanowire dissipation.

ACKNOWLEDGEMENTS

I would like to express my deepest appreciation for the invaluable guidance, friendship, and support that was freely given by those around me during my doctoral studies.

First, I would like to thank my advisor, Stuart Field. Your guidance has shaped me as a scientist and as a person and I cannot express my gratitude enough. Thank you for your willingness to discuss or answer any questions about anything at any time and your Golden Rules will continue to influence me as I continue in life.

I would also like to thank everyone who has been in the Field research group who has helped me in graduate school. I appreciate all the work that everyone has done.

I am grateful for the support from life-long friendships that I have been blessed with. To the friends that I made at Northern Arizona University and in Arizona: You guys helped me come out of my shell for which I am eternally grateful. Even through the distance, we stayed true friends and I couldn't ask for a better squad and raid team (despite the physics of hot air and the existence exotic ghosts). To the friends (buddies!) that I made at Colorado State University: You all made graduate school an absolute blast! Thank you for all the times we spent playing magic, at weekly pizza casbah outings, on ski-cations, rock climbing, hiking, playing laser tag, watching movies (with mountains of popcorn), playing board games, booping each other off virtual ledges, and at pool parties. Thank you all for your friendship and I look forward to making even more memories.

To my parents: Your love and support means the world to me. Your cultivation of my curiosity is directly responsible for the choices that I have made and eventually gave me the intellectual tools and drive to understand the world around me. It is a precious gift that I will continue to cherish and nurture for the rest of my life. Mom, you always strive to ensure that I can pursue my passions by any means necessary and you have been a vital source of support. Dad, I would not be the man that I am today without your example and your constant curiosity has inspired me to never stop learning. Thank you both for always being proud of and believing in me.

To Aaron, Sam, and Jenna: Each of you has taught me an important lesson, which has made me a better person. Aaron–Thank you for being my true and first friend with whom I share a love of math and learning. Sam–I truly admire your outlook on the world and thank you for all of our (virtual) cosmic adventures. And Jenna–Thank you for your thoughtfulness and I know that I can always count on you. I am proud of each of you.

I would also like to thank my extended and chosen families for the constant love, encouragement, and support that I have received.

Finally, to my wonderful wife Annalise: Words cannot even begin to express my gratitude and love for you. You make me better in every way just by being you and I would not be where I am without you. Thank you for intellectually challenging and supporting me, our numerous inside jokes and adventures, and just being a constant source of happiness for me. I feel so blessed to be your partner in everything and I can't wait for what comes next. I will love you forever and ever.... Amen.

TABLE OF CONTENTS

LIST OF FIGURES

Chapter 1

Introduction to Superconducting Films

Superconductivity has been a highly active area of theoretical and experimental research since its discovery in 1911 by Heike Kamerlingh Onnes after his laboratory successfully liquified helium.[1] The allure of a material that could be described as a perfect conductor significantly motived scientists to extensively explore the newly discovered phenomenon. Researchers rapidly discovered superconductivity in a wide range of materials while also developing theoretical treatments such as the London theory, the Ginzburg-Landau (GL) theory, and the Bardeen–Cooper–Schrieffer (BCS) theory.

It became apparent that the phenomenon of superconductivity is much deeper and more significant than simply a perfect conductor. Indeed, the earliest observations of superconductors revealed that these materials have zero electrical resistance.[1] Figure 1.1a shows the transition of a granular aluminum film into the superconducting phase as the temperature of the sample is cooled below the critical temperature, T_c. Below this critical temperature, the sample becomes a *perfect conductor* with zero electrical resistance and thus seemingly behaves as an ohmic conductor with infinite conductivity. However, this model implies an infinite multiplicity of states that correspond to a single set of external conditions.[2] To see this, we note that a simple perfect conductor that is cooled below T_c in the presence of an applied magnetic field would form supercurrents on the surface of the material that would *trap* the applied field within the superconductor. If, however, the sample were to be cooled below T_c in zero field and then an applied field was introduced, then the perfect conductor theory states that supercurrents would form to preserve the zero field within the material. These scenarios would result in two distinct superconducting states that belong to identical external conditions which, according to London,[2] "offended the tastes of physicists."

In 1935, Meissner discovered another trait of superconductivity that resolved the paradox implied by the perfect conductor model. Meissner observed that superconductors *expel* an

applied magnetic field as the material is cooled below T_c.[3] This *Meissner effect*, depicted in Figure 1.1b, states that supercurrents form on the surface of a superconductor that prevent an applied field from existing within the interior of the superconductor. The addition of the Meissner effect to the superconducting model implies only a single state with $B = 0$ inside the superconductor belonging to a set of external conditions. Therefore, the Meissner effect is another fundamental property that is required for a complete representation of superconductivity.

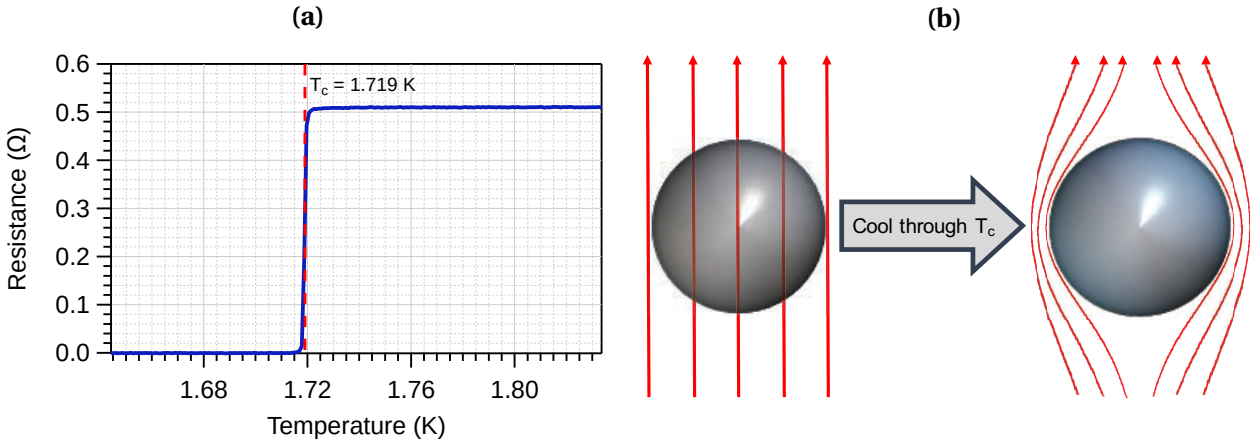

Figure 1.1: Properties of superconductivity: **(a)** Perfect conductivity of a granular aluminum film as the sample resistance is reduced to zero below the transition temperature. **(b)** The Meissner effect portrayed by the expulsion of an applied magnetic field.

An applied magnetic field may penetrate superconductors despite the existence of the Meissner screening currents, and the behavior and mechanisms of this penetration can be categorized into two distinct classes of superconductivity termed type-I and type-II. The inherent difference between type-I and type-II superconductivity is caused by a subtle interplay between the two material-dependent superconducting characteristic lengths. The first characteristic parameter is the coherence length, ξ, which is defined as the length scale over which changes in the density of superconducting charge carriers can occur. The second parameter is the penetration depth, λ, and is the length scale over which the magnetic field is screened from the surface of the superconductor, and over which the currents in a superconductor fall off. The ratio of the penetration depth to the coherence length is the *Ginzburg-Landau parameter* $\kappa = \lambda/\xi$

and is used to delineate type-I and -II superconductivity. Type-I superconductors are materials with $0 < \kappa < 1/\sqrt{2}$ and have positive surface energies associated with the interface between the normal and superconducting regions, or domains, that may exist within the material.[4] Alternatively, type-II superconductors are materials with $\kappa > 1/\sqrt{2}$ and have negative surface energies associated with the normal and superconducting domain boundaries.[4]

Flux penetrates type-I and -II superconductors via normal domain regions that possess differing characteristics between the two classes of superconductivity. Both types of superconductors exhibit the full Meissner effect for sufficiently small applied fields. As the field is increased, however, magnetic flux penetrates these superconductors via these normal domain regions and the differences between type-I and -II superconductivity becomes apparent. The positive surface energy associated with domain boundaries in type-I superconductors will cause a macroscopic subdivision of these domains resulting in the *intermediate state*.[4] In contrast, the negative surface energy of the domain interfaces belonging to type-II superconductors will cause the *mixed state* because, to maximize domain surface areas, the normal domains will microscopically subdivide until each normal region is penetrated by a single quantum of magnetic flux.[4,5] These microscopic, normal domains that are penetrated by quantized flux filaments are called *vortices* and begin to enter a superconductor when the applied field H_a reaches the first critical field H_{c1}.[5] The superconductor will then remain in the mixed state until the applied field reaches the second critical field H_{c2} where superconductivity is completely suppressed. These vortices that are present in the mixed state in type-II superconductors display a wide range of interesting physics and are the focus of the first half of this work.

The aim of the first three chapters of this dissertation is to motivate and understand the properties and dynamics of flux vortices in low-pinning type-II superconducting films. Chapter 1 will introduce several key concepts that are routinely employed to understand superconductivity in type-II films. Chapter 2 will present research performed to understand the effects of a thickness modulation on the superconducting properties of the film. Chapter 3 will then explore the effects of the edges on vortex nucleation in thin-film superconductors.

1.1 Vortices in Type-II Superconductors

As was previously discussed, magnetic flux penetrates a type-II superconductor for applied fields between $H_{c1} < H_a < H_{c2}$ in the form of microscopic flux filaments called Abrikosov vortices, named for Alexei Abrikosov for his discovery of this phenomenon.[5] Each vortex, schematically shown in Figure 1.2, carries a magnetic flux quantum of magnitude $\Phi_0 = hc/2e = 2.07 \times 10^{-7}$ G·cm^2 through a normal core;[4] the flux is sustained by circulating supercurrents that exist in the superconducting region of the material. We are interested in studying these vortices since a lattice composed of multiple vortices can be influenced in various manners such as by creating artificial pinning sites or by driving these objects into a dynamic phase with an applied current. Additionally, the details surrounding the nucleation of vortices into a type-II superconductor are of considerable interest since the onset of vortex nucleation can influence the vortex lattice and transport properties. Understanding vortex nucleation and the various interactions of these vortices within the superconductor is desired since the details of type-II superconductivity inherently depends on vortex properties and dynamics.

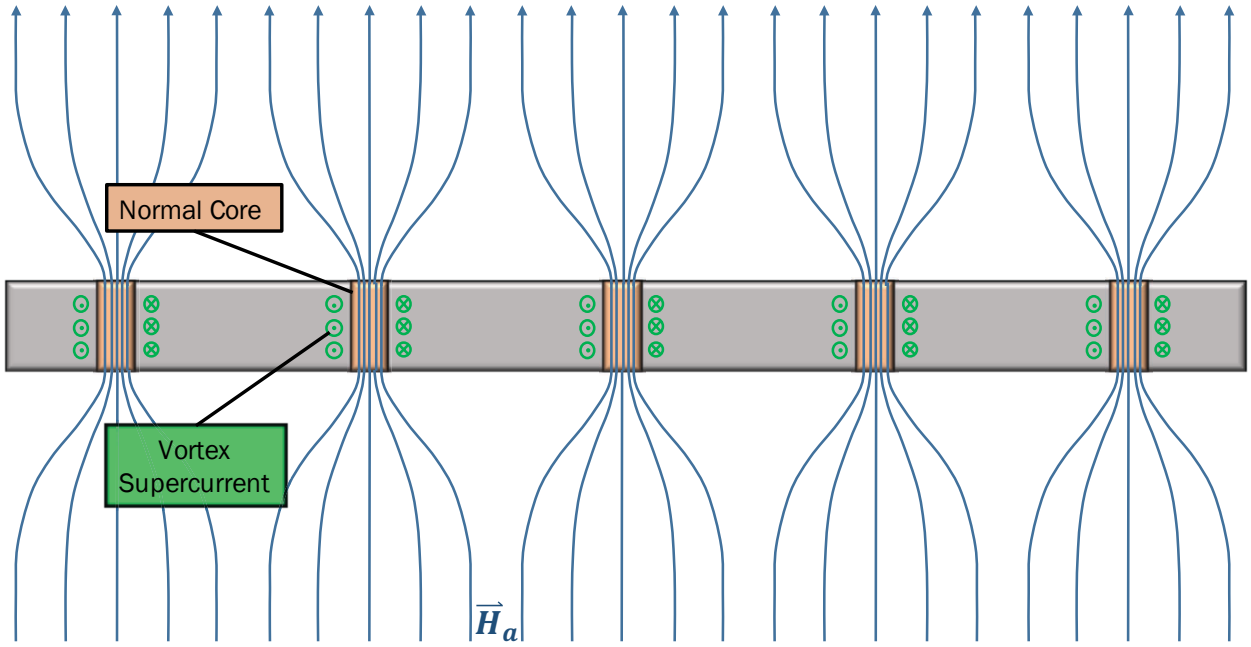

Figure 1.2: A cartoon of a type-II superconductor (grey) in the mixed state. The vortical supercurrents (green) sustain flux (blue) penetrating the normal core of the vortex (orange).

1.1.1 The Structure of a Vortex

The normal vortex core is a thin microscopic region of suppressed superconductivity with a structure that is dependent on the superconducting properties of the material. According to the Ginzburg-Landau theory, the superconducting electrons in a superconductor belong to a macroscopic many-body state that is characterized by a pseudo-wavefunction ψ, also called the *superconducting order parameter*. $|\psi|^2$ is proportional to the *local* density of superconducting charge carriers. Therefore, ψ must spatially change in magnitude from $|\psi| = 1$ to $|\psi| = 0$ (in a normalized representation) from the bulk superconducting material to the normal core of the vortex. By definition, this change in ψ occurs over a length scale that is similar to the coherence length, so the diameter of the vortex can be approximated as $\sim 2\xi$. Tinkham shows that the magnitude of the order parameter varies as $|\psi| \sim \tanh(r/\xi)$ for a vortex in a large κ, bulk superconductor[4] and is shown in Figure 1.3. Superconductivity is only totally suppressed at the exact center of the vortex where the order parameter magnitude completely vanishes. However, superconductivity is locally suppressed over a region of $\sim 2\xi$ as evidenced by the non-unity of ψ in this region.

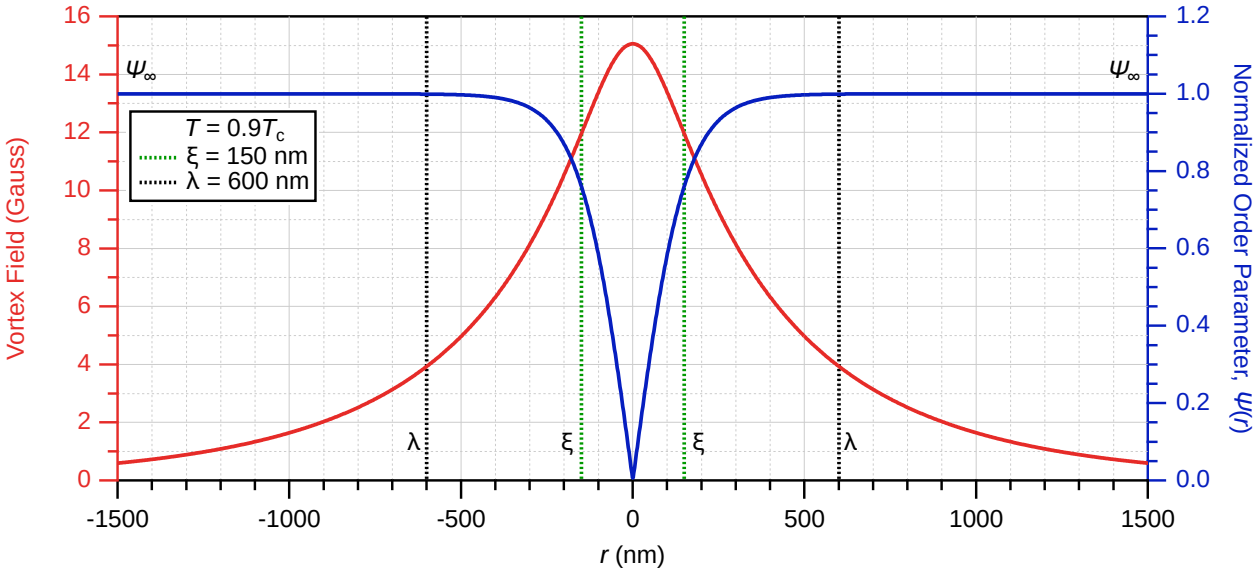

Figure 1.3: Calculations of the magnetic field (red) and of the normalized order parameter (blue) for a typical vortex. These calculations were performed at $T = 0.9T_c$, $\xi = 150\,\text{nm}$, and $\lambda = 600\,\text{nm}$ which are typical superconducting properties for granular aluminum studied in this work.

The magnetic field and current from a vortex additionally depends on the superconducting characteristic properties of the material. Clem calculated the dependence of the magnetic flux density b_z and the form of the current j_ϕ from a vortex in a bulk superconductor as[6]

$$b_z = \frac{\Phi_0}{2\pi\lambda\xi}\frac{K_0\left(\frac{R}{\lambda}\right)}{K_1\left(\frac{\xi}{\lambda}\right)} \tag{1.1}$$

$$j_\phi = \frac{c\Phi_0}{8\pi^2\lambda^2\xi}\frac{r}{R}\frac{K_1\left(\frac{R}{\lambda}\right)}{K_1\left(\frac{\xi}{\lambda}\right)} \tag{1.2}$$

where K_0 and K_1 are modified Bessel functions, the parameter R is defined as $R = \sqrt{r^2+\xi^2}$, and r is the radial location from the center of the vortex. A qualitative analysis of K_0 and K_1 that describe the magnetic field and current in Equations 1.1 and 1.2 reveals that the vortex field and current scale as $\sim e^{-r/\lambda}$ at large r and as $\sim \ln(\lambda/r)$ near the vortex core ($\xi \ll r \ll \lambda$) with the logarithmic divergence cut off below $r \sim \xi$.[4,6] The vortex field described by Equation 1.1 is also shown in Figure 1.3.

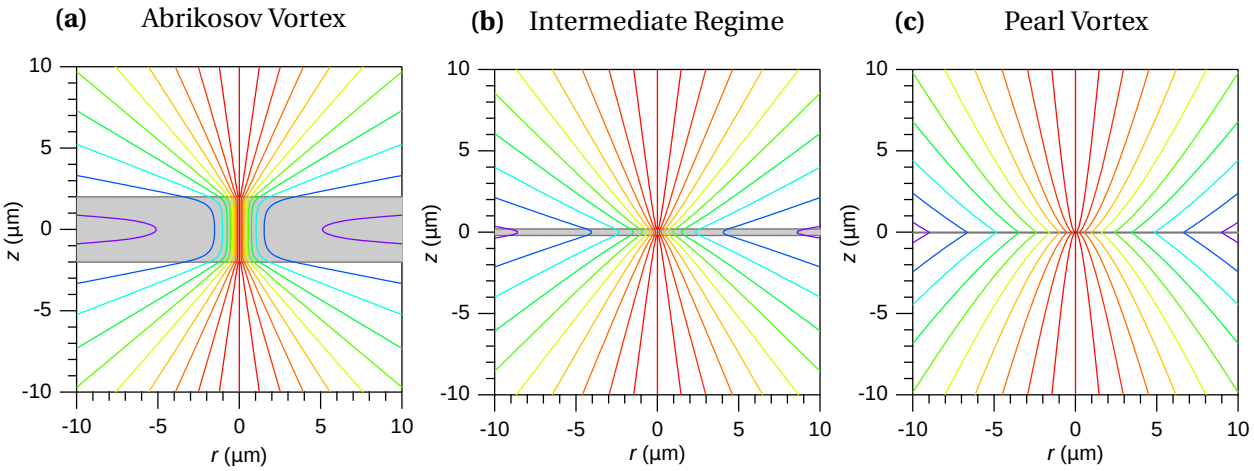

Figure 1.4: Lines of magnetic field (colored for clarity) resulting from a vortex in a superconductor (grey) calculated from the formulation presented by Carneiro and Brandt.[7] Each panel depicts calculations of a vortex in a superconductor with $\lambda = 0.6\,\mu$m in various thickness regimes: **(a)** $d \gg \lambda$ ($d = 4\,\mu$m), **(b)** $d \sim \lambda$ ($d = 0.4\,\mu$m), and **(c)** $d \ll \lambda$ ($d = 0.04\,\mu$m).

The thickness of the superconductor also influences the spatial dependence of vortices which may exist in the Abrikosov, intermediate, or Pearl regimes. The magnetic field of these vortices from the Abrikosov to Pearl limits can be calculated by the method presented by Carneiro and Brandt where field profiles are plotted as contour lines of $r\mathbf{A}$, where $\mathbf{A}$ is the magnetic vector potential.[7] Figure 1.4a depicts the field profile for a well-localized vortex in the Abrikosov regime in the limit that the material thickness d is much larger than λ ($d \gg \lambda$). As was previously discussed, the fields and currents of a standard Abrikosov vortex fall off as $\sim e^{-r/\lambda}$ (see Equations 1.1 and 1.2) in bulk superconductors.[4,5] As d becomes comparable with λ ($d \sim \lambda$), the fields and currents of the vortex begin to spread out and the vortex is considered to be in the *intermediate regime* and is shown in Figure 1.4b. Pearl showed that in the thin-film limit of $d \ll \lambda$, the vortex fields and currents are even further dispersed.[8] Pearl defined a thin-film penetration length $\Lambda = 2\lambda^2/d$ and showed that the two-dimensional vortex sheet current $\mathbf{K}_s$ in films at a distance r from the center of the vortex is[8]

$$\begin{aligned} \mathbf{K}_s &\approx \hat{\Phi}\frac{\Phi_0}{\pi}\frac{d}{2\lambda^2 r} \quad \text{for } r \ll \Lambda \\ \mathbf{K}_s &\approx \hat{\Phi}\frac{\Phi_0}{\pi}\frac{1}{r^2} \quad \text{for } r \gg \Lambda. \end{aligned} \tag{1.3}$$

Figure 1.4c depicts a vortex in the Pearl regime and shows the dispersed field where the vortex field and current fall off as $\sim 1/r^2$. Equation 1.3 combined with the representation of the vortex fields of Figure 1.4 dictate that Pearl vortices within a thin superconductor are inherently larger in diameter than the Abrikosov vortex and so the thickness of superconducting samples plays a significant role in determining vortex properties.

1.1.2 Vortex Interactions

Many of the interesting phenomenon in vortex physics are due to interactions between vortices and their environment. There are three main methods by which vortices within a type-II superconductor interact. Figure 1.5 illustrates the vortex-vortex interaction that results in the formation of a vortex lattice, the vortex-current interaction that results in a transverse vortex

motion in response to an applied current, and the recently tunable vortex-potential interaction which allows vortices to interact with an artificially imposed potential landscape. Each of these interactions are discussed in further detail in this section.

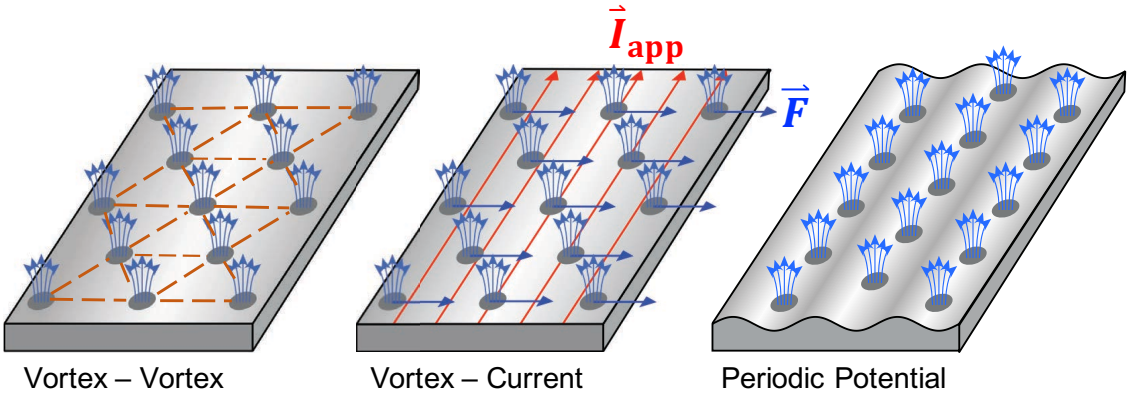

Figure 1.5: A cartoon depicting the three main vortex interactions in a type-II superconducting film (grey). Vortices (blue) interaction with one another (orange), with an applied current (red), or with a potential landscape that is imposed by a modulated sample thickness.

Vortex-Current and Vortex-Vortex Interactions

It can be shown that vortices can interact with supercurrents via a Lorentz-type force. The force per unit length on a vortex is given by

$$\mathbf{f} = \mathbf{J}_s \times \frac{\mathbf{\Phi}_0}{c} \tag{1.4}$$

where $\mathbf{\Phi}_0$ is a vector that represents the magnetic field in a single vortex with a magnitude of a single flux quantum and $\mathbf{J}_s$ is the total supercurrent density at the core of the vortex and is due to the currents from other vortices along with any additional applied currents.[4] Equation 1.4 can be used to describe the vortex-vortex repulsive interaction depicted in Figure 1.5 as this interaction is a result of the current from one vortex interacting with the flux of another vortex. Since this interaction is repulsive, the vortices will arrange themselves into a triangular lattice (given a sufficient applied field) in the absence of defects that would trap or *pin* the vortices at the defect site.

The Lorentz-type force of Equation 1.4 also indicates that vortices within a superconductor can be pushed by an applied transport current. If a transport current is applied to the sample as shown in Figure 1.5, then Equation 1.4 indicates that this current will cause vortex motion transverse to the applied current in the superconductor. This vortex-current interaction is commonly employed to experimentally study vortex dynamics.

Vortex-Potential Interactions

Recent developments in lithographic fabrication techniques have introduced the possibility of fabricating and tuning artificial potential landscapes in superconducting samples, which provides another method of probing vortex dynamics. These *pinning potentials* can be realized in numerous ways such as an array of holes,[9–14] magnetic arrays,[15–19] or by a thickness modulation in the sample[20–22] as depicted in the third interaction in Figure 1.5. Dröse *et al.*,[20] Morrison *et al.*,[21] and Yu *et al.*[22] have shown that vortices can be confined to a narrow channel simply by thinning the sample material in the channel. In general, thinner sample regions correspond to local minima in the potential landscape because the free energy of a vortex is proportional to its line length. The free energy of a vortex (per unit length) f_{v} is due to the normal material free energy in the core (per unit length) f_{n}, the magnetic field energy of the vortex, and the kinetic energy of charge carriers in the vortex current. Therefore, f_{v} is given by

$$f_{\mathrm{v}} = f_{\mathrm{n}} + \frac{1}{8\pi}\int \left(h^2 + \lambda^2 |\nabla \times \mathbf{h}|^2\right) dS \tag{1.5}$$

where h represents the microscopic field density and the integral that describes the energy contributions from the vortex field and current (per unit length) is evaluated over a surface S.[4] Equation 1.5 indicates that a longer vortex will result in a larger vortex energy since the longer vortex will suppress more superconducting material via the vortex core and will be accompanied by higher contributions from the field and current. As a result, vortices will tend to thinner sample regions to minimize the vortex line length.

1.1.3 Vortex Dynamics in Surface Potentials

The effects of various periodic surface potentials on the transport properties of type-II superconductors has been of significant experimental and theoretical interest, arising from the prospective use of surface-modified samples as fluxonic devices[23–30] such as a relativistic-flux-quantum-based diode,[23] logic elements,[26,28] or even as a nondestructive readout random access memory (RAM) cell.[29] One of the tools available to researchers to create these fluxonic devices is to intentionally induce an asymmetry in the potential landscape to create a "vortex ratchet" that possesses an easy and hard direction to flux-flow. These vortex ratchets can also be employed to clean a film of vortices,[27] or as a landscape to study and image vortex dynamics.[9,31–35]

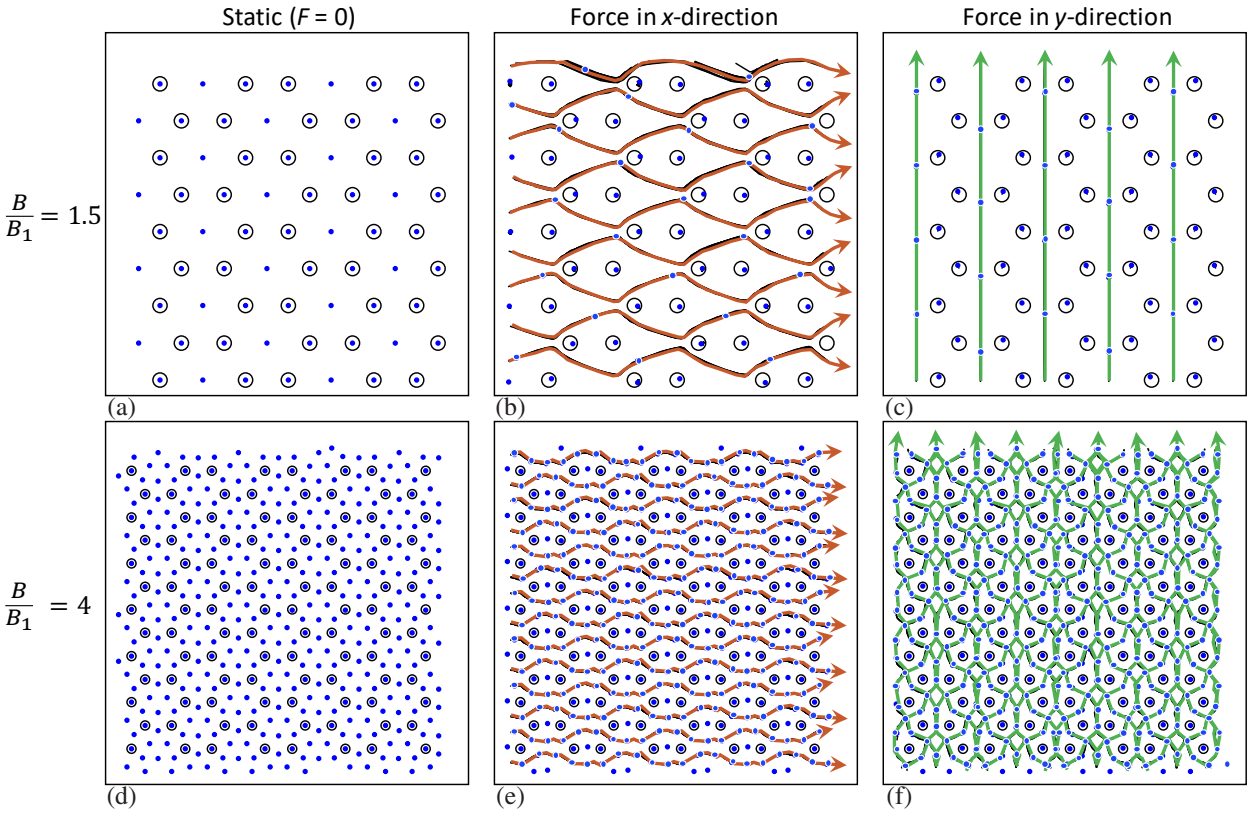

Figure 1.6: Flux-flow simulations for a honeycomb lattice adapted from Figure 23 of Reichhardt *et al.*;[36] colored arrows highlighting vortex trajectories were added. The static configurations at the applied fields of $B/B_1 = 1.5$ and $B/B_1 = 4$ are shown in **(a)** and **(d)** respectively. Vortices are depicted as blue dots, with moving vortices forming flux-flow channels (orange and green) in the regions between the potential wells (black circles). Simulations were performed for the **(b, e)** x (orange) and **(c, f)** y (green) directions of flux-flow at applied fields of **(a-c)** $B/B_1 = 1.5$ and **(d-f)** $B/B_1 = 4$.

Vortex motion in periodic potentials has been the subject of numerous simulations[15,17,27,30,36–52] and experimental studies[9–17,17–22,37,53] that seek to understand the effects of these potentials on vortex dynamics. In particular, simulations performed by Reichhardt *et al.* indicate that the vortex dynamics in arrays of periodic pinning potentials is incredibly complex.[36] Figure 1.6 depicts simulations of vortex motion in a honeycomb lattice of potential wells (black circles) at various normalized applied fields B/B_1. Here, B_1 represents the applied field required to populate each potential well with one vortex.[36] These simulations reveal flux-flow trajectories that result in anisotropies in the current-voltage response when driving vortices in the x and y directions with respect to the honeycomb lattice, as denoted by the orange and green paths in Figure 1.6, respectively.

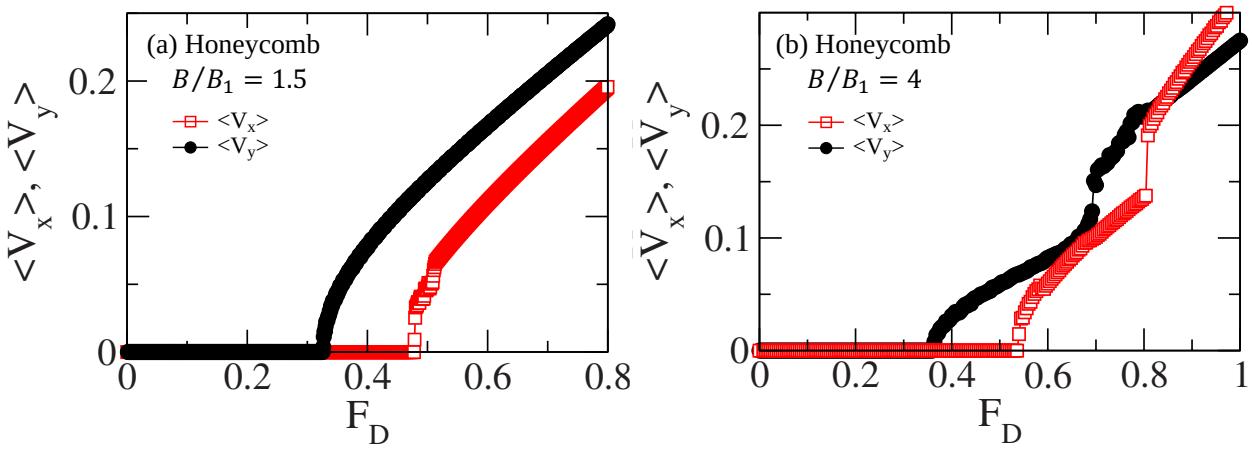

Figure 1.7: CVC simulations depicting the average voltage that is generated by vortex motion plotted against an applied current (or force) for a honeycomb lattice adapted from Figure 24 of Reichhardt *et al.*[36] The average voltage response to a driving force (or current) **(a)** CVC simulation for $B/B_1 = 1.5$. **(b)** CVC simulation for $B/B_1 = 4$.

Moving vortices generate a voltage $V = vBl$ where v is the vortex velocity, B is the average field, and l is the width of the sample. Thus, V can be used as a probe of the global motion of vortices in a superconductor. This voltage is measured with current-voltage characteristics (CVCs) where the average voltage that is generated by vortex motion in response to an applied current (or force) is recorded. The CVC curves corresponding to the simulations performed with the honeycomb lattice of potential wells are shown in Figure 1.7. While there is a clear differ-

ence in the driving current that is required to elicit a non-zero voltage response, or the *critical depinning current*, in the CVCs for $B/B_1 = 1.5$ displayed in Figure 1.7a there is also an interesting reversal in the anisotropy for these same driving directions that emerges at the larger applied field of $B/B_1 = 4$ depicted in Figure 1.7b. These results indicate that flux-flow within a 2D periodic pinning potential is complex and depends subtly on a wide variety of parameters, which is to be expected for the complicated potential landscape that is produced by the honeycomb array.

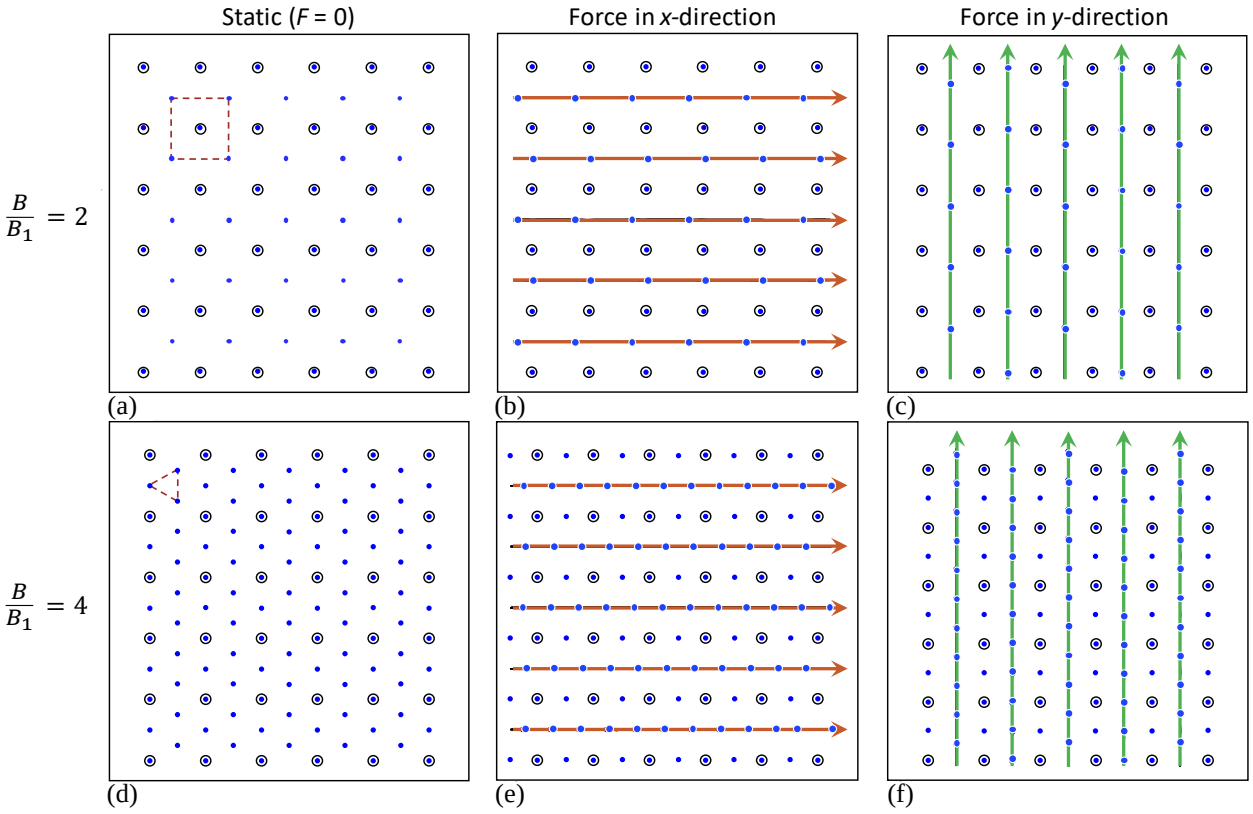

Figure 1.8: Flux-flow simulations for a square lattice adapted from Figures 17 and 19 of Reichhardt *et al.*;[36] colored arrows highlighting vortex trajectories were added. The static configurations at the applied fields of $B/B_1 = 2$ and $B/B_1 = 4$ are shown in **(a)** and **(d)** respectively, along with the unit cell of the resulting vortex lattice that is formed. Vortices are depicted as blue dots with moving vortices forming flux-flow channels (orange and green) in the regions between the potential wells (black circles). Simulations were performed for the **(b, e)** x (orange) and **(c, f)** y (green) directions of flux-flow at applied fields of **(a-c)** $B/B_1 = 2$ and **(d-f)** $B/B_1 = 4$.

Reichhardt *et al.* also simulated the effects of a simple square lattice of potential wells on vortex dynamics. Figure 1.8 depicts the flux-flow trajectories in the x and y driving directions for this square lattice at various applied fields.[36] As expected, the flux-flow channels in the x (orange paths) and y (green paths) directions are identical with respect to the 90° symmetry of the square lattice. However, the CVC simulations performed at larger applied fields exhibit anisotropy even for these seemingly equivalent driving directions. Figure 1.9 depicts the CVC simulations for applied fields of $B/B_1 = 2$ and $B/B_1 = 4$.[36] Figure 1.9a, corresponding to $B/B_1 = 2$, illustrates the expected reversible flux-flow for both driving directions. However, Figure 1.9b, corresponding to $B/B_1 = 4$ depicts an anisotropy with larger depinning currents required for the y driving direction which is caused by a "pseudo-triangular-lattice" that is formed by the interstitial vortices (see Figure 1.8d). The simulations shown in Figure 1.9b also exhibit reversible slopes in the CVC curves, or flux-flow resistances, at larger currents so that the anisotropy is solely described as a depinning anisotropy, unlike the simulations for the honeycomb lattice which displays anisotropies in the depinning current as well as in the flux-flow resistance.

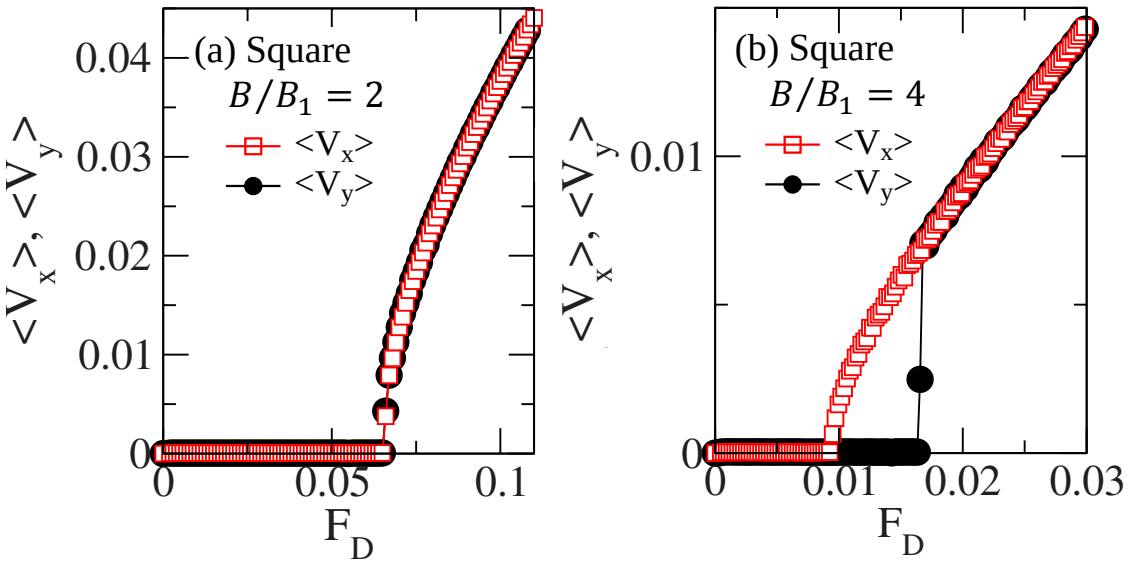

Figure 1.9: CVC simulations depicting the average voltage that is generated by vortex motion plotted against an applied current (or force) for a square lattice adapted from Figure 18 of Reichhardt *et al.*[36] **(a)** CVC simulation for $B/B_1 = 2$. **(b)** CVC simulation for $B/B_1 = 4$.

An experimental and theoretical understanding of one-dimensional periodic potentials is desired since the details of flux-flow in two dimensional pinning potentials is complicated and subtle. There has been theoretical interest in the flux-flow response for one dimensional washboard potentials and we seek to experimentally explore these one dimensional potentials.[33,54–58] Chapter 2 presents experimental work in which we study the rectification in the flux-flow dynamics in asymmetric and in symmetric one-dimensional washboard potentials by studying the vortex dynamics in thickness-modulated granular aluminum films.

1.2 The Effects of the Sample Edges

Vortex motion in flat thin-film superconductors is a complex problem that is dependent on several factors. The previously discussed simulations assumed an infinite film, but experimental superconductors have edges that have been experimentally[59–62] and theoretically[63–85] shown to directly affect how vortices enter and move within a superconductor. If the energy barrier to vortex entry that is created by the existence of the sample edges becomes comparable to or larger than the bulk pinning, then bulk and surface effects can be obscured by the sample edges. Therefore, it is necessary to understand the details of vortex nucleation, including the effects of the sample edges, so that a complete model for vortex motion can be established.

1.2.1 Edge Barriers to Vortex Nucleation

Vortex nucleation into thin-film superconductors is heavily influenced by the details of the film geometry. The existence of the sample edges creates an *edge energy barrier* to vortex nucleation that arises from two distinct sources: the Bean-Livingston barrier (BLB) and the geometric barrier (GB).[63,65–68,70–74,76,77,79–81,85] The BLB can be thought of as an attraction of a nascent vortex to an image antivortex outside of the sample that is necessary to satisfy the zero-normal-current boundary condition at the surface of the superconductor. This leads to an attractive force between a vortex and the sample edge, which tends to push vortices toward the superconducting edges and out of the film.[86]

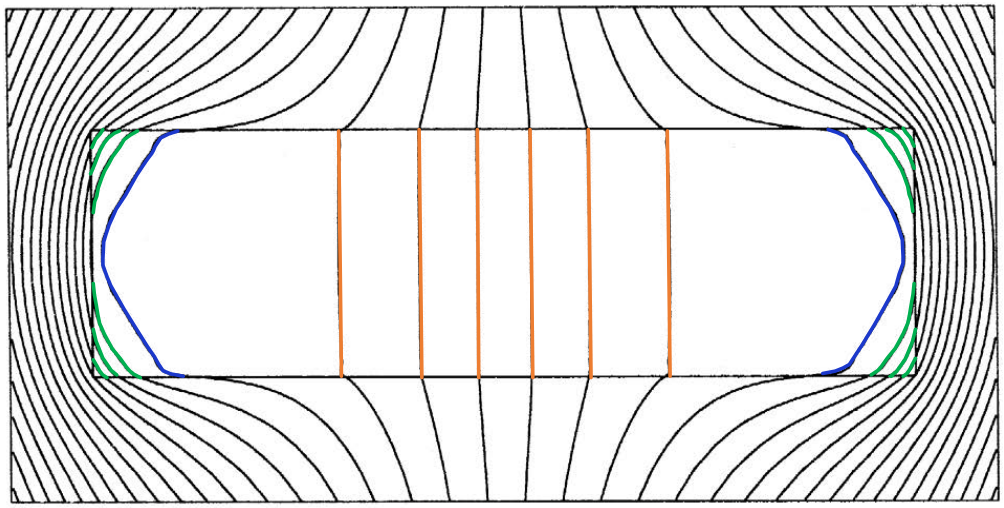

Figure 1.10: The calculated flux penetration in a superconductor with squared edges in a perpendicularly applied field, adapted from Figure 1 from Brandt.[70] Nucleating vortices (green) are bifurcated in the corners of the square edges. The two halves join at the center of the thickness of the sample and become one, continuous vortex (blue). The nascent vortex is then swept to the interior of the sample (orange).

This BLB is distinct from the geometric barrier, which is an expulsive barrier that is created by the cross-sectional shape of a superconducting sample. Recall that a longer vortex has a larger vortex energy (see Equation 1.5). Therefore, the GB is caused by the line-length increase that a nascent vortex must undergo during the nucleation process.[84] Figure 1.10 shows the effects of a squared edge shape on the line-length increase for nucleating vortices.[70] As a nascent vortex nucleates in a sample with squared edges the flux must penetrate through each edge corner, splitting the vortex into two halves represented by the green field lines in Figure 1.10. This bifurcated vortex incurs a large line-length increase as it further penetrates into the sample edges until both halves of the vortex join at the center of the sample thickness, represented as the blue field lines in Figure 1.10. The vortex is then swept to the center of the superconductor, denoted by the orange field lines in Figure 1.10, by the Lorentz force generated by the Meissner screening currents. The GB of a sample with squared edges is large as a result of the steep line-length increase that is caused by the bifurcation that a nascent vortex must experience to fully penetrate a squared-edge sample. However, it is possible to fabricate superconductors with tapered or prism edge geometries that minimize or completely eliminate the GB.[61] It is important

to note that the BLB still exists despite reducing or eliminating the GB and so an edge barrier will still be present for these samples.

1.2.2 The Vortex Dome

The entrance of vortices into a thin-film superconducting strip can be complex because of the presence of the edge barriers. There are numerous theoretical treatments that have calculated the profiles of the currents and fields within a type-II superconductor in the presence of externally applied fields and currents in order to understand the effects of the superconducting edges on flux penetration.[7,61,67–71,74,76,84,85,87,88]

Consider a magnetic field that is applied perpendicularly to a superconducting strip of width $2W$, thickness $d \ll W$, and with a penetration depth $\lambda \ll d$ in the absence of vortices. A superconductor in this state will form Meissner screening currents that are parallel to the strip edges. These currents are large and positive at one edge, fall to zero at the center of the strip, and become large and negative at the opposing strip edge. This Meissner current density J_{M} for a location x along the strip is given by

$$J_{\mathrm{M}} = -\frac{2H_{\mathrm{a}}x}{d\sqrt{W^2 - x^2}} \tag{1.6}$$

where H_{a} is the applied field.[68] Several Meissner screening current distributions are shown in Figure 1.11a at various applied fields that are normalized to a field H_{s}, which we will show is related to the vortex entry condition at the edges.

An applied current I within the superconductor in the absence of an applied field will flow on the surfaces of the superconductor. The applied current is also labelled as a *transport current* since any applied current will exert a perpendicular force on each vortex (see Equation 1.4), moving them across the strip in the absence of pinning. The resulting applied current density has the same directional sense at all locations in the strip, but is largest near the edges of the strip and lowers to a nominal (but non-zero) minimum value at the center of the strip. This transport current density J_{t} within the superconductor is given by[68]

$$J_t = \frac{I}{\pi d\sqrt{W^2 - x^2}} \tag{1.7}$$

and is shown in Figure 1.11b at several applied currents that are normalized to I_s, which we will show is also related to the vortex entry condition at the edges. The total current density within the strip in the presence of an applied field and current, but without vortices is then the sum of Equations 1.6 and 1.7 given by[68]

$$J(x) = J_M + J_t = -\frac{2H_a x}{d\sqrt{W^2 - x^2}} + \frac{I}{\pi d\sqrt{W^2 - x^2}}. \tag{1.8}$$

A treatment of the onset of flux penetration into a superconducting strip requires a model of the edge barrier. We begin by postulating that no vortices will enter the superconducting strip until the current density at one of the edges reaches a critical value J_s, which will therefore depend on the details of the edges. Consider the superconducting strip of width $2W$ and thickness d once again in the presence of an increasing applied field with edge currents J_{edge}. As H_a is increased from zero field, the Meissner currents at the edges will be of magnitude $J_{edge} < J_s$ and the superconductor exhibits the full Meissner state. Eventually, H_a will increase to a point such that $J_{edge} = J_s$ and the first vortices will begin to enter the strip over both edges. Additionally, vortices may be coaxed into the strip by increasing an applied transport current I_t. Consider a value of H_a such that the Meissner screening currents result in $J_{edge} < J_s$. Then, a transport current I_t is applied and is increased until eventually $J_{edge} = J_s$. At this value of I_t, vortices nucleate into the strip over one of the edges since, from the Equations 1.6 and 1.7 which are plotted in Figure 1.11, J_t and J_M are in the same direction at one edge but are in opposing directions at other other edge.

From these observations we can define a critical current density and a critical field. The *critical current density* J_s is defined as the edge current density that is required to first pull a vortex into the strip and the *critical field* H_s is the field at which the Meissner edge-current density is equivalent to J_s. We may also define a *critical current* I_s which is the applied current

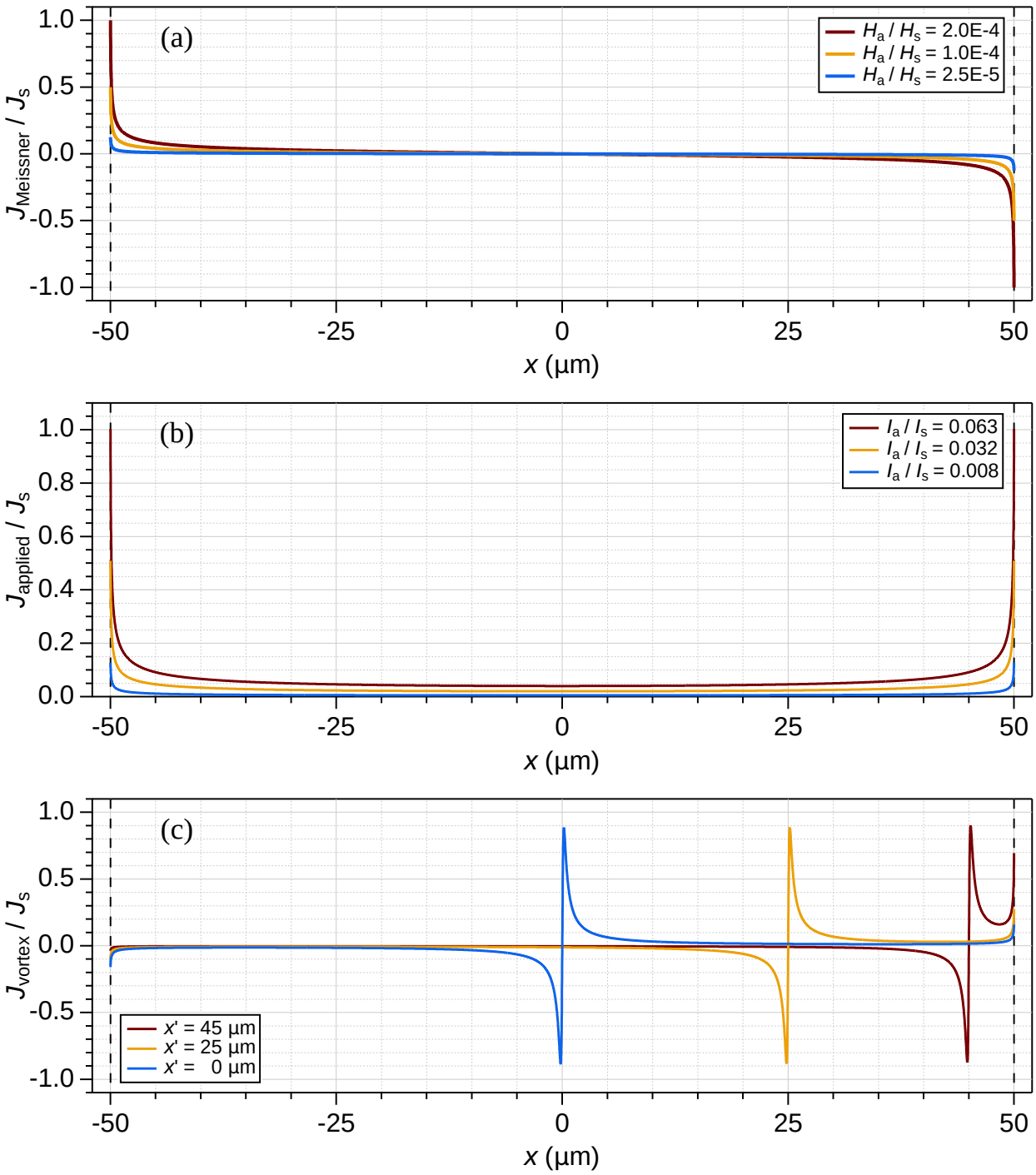

Figure 1.11: Calculations of the various currents present in the Meissner state described by Equation 1.6 from Benkraouda *et al.*[68] **(a)** The surface screening currents resulting from the Meissner response to various applied fields. **(b)** The current density profiles for various applied transport currents. **(c)** The current densities of three strips of vortices at various locations x' in the strip for $H_z/H_s = 0.005$. The film parameters used to obtain these solutions were $W = 50\,\mu$m (where W = width/2 and the sample boundaries are denoted by the dashed lines) and a film thickness of $d = 0.5\,\mu$m. The edge singularities were treated by implementing a cutoff length of $\Lambda = 2\lambda^2/d$[74] where $\lambda \sim 700\,$nm. Note that H_s is defined by the critical current by Equation 1.9.

that is required to reach J_s in the sample edges at $H_a = 0$. These critical definitions are related to J_s by

$$J_s = \frac{H_s}{W} = \frac{I_s}{2Wd}. \tag{1.9}$$

Here, I_s is the applied current for which a vortex can first overcome the edge energy barrier and enter the strip at $H_a = 0$ and H_s is determined by J_s, which in turn depends on the BLB and GB. We note that H_s is distinct field from H_{c1} and these two fields should not be considered synonymous. The currents and fields in this discussion are normalized with respect to the critical definitions of Equation 1.9.

We have just considered the case of $H_a < H_s$, but we will now consider what happens when H_a is increased slightly above H_s. At this point, $J_{edges} > J_s$ and vortices will spill into the strip. The Meissner currents create a potential minimum for vortices at the center of the strip, so these nucleating vortices cluster near the center of the strip and form a *vortex dome*. As vortices enter the superconductor, they repel additional vortices from entering as a result of their own currents adding to the edge currents. The current contribution due to a strip of vortices dJ_v of width dx' and located at x' is given by

$$dJ_v = \frac{2H_z(x')\sqrt{W^2 - x'^2}}{\pi d\,(x - x')\sqrt{W^2 - x^2}}dx' \tag{1.10}$$

where $H_z(x') = B_z(x')/\mu_0$ for a flux field distribution $B_z(x')$.[68] The currents resulting from various vortex locations x' within the strip are plotted in Figure 1.11c which shows that the current from a strip of vortices extends to the edges of the superconducting strip with current directions that oppose the Meissner screening currents. Therefore, the current from each vortex acts to *lower* the edge current, preventing more vortices from entering. This feedback mechanism ensures that J_{edge}/J_s never exceeds 1. If H_a is further increased, then vortices will once again enter the superconductor, which then causes J_{edge} to decrease below J_s. In this way, a slowly widening vortex dome forms as the magnetic field is increased[68] as shown in Figure 1.12.

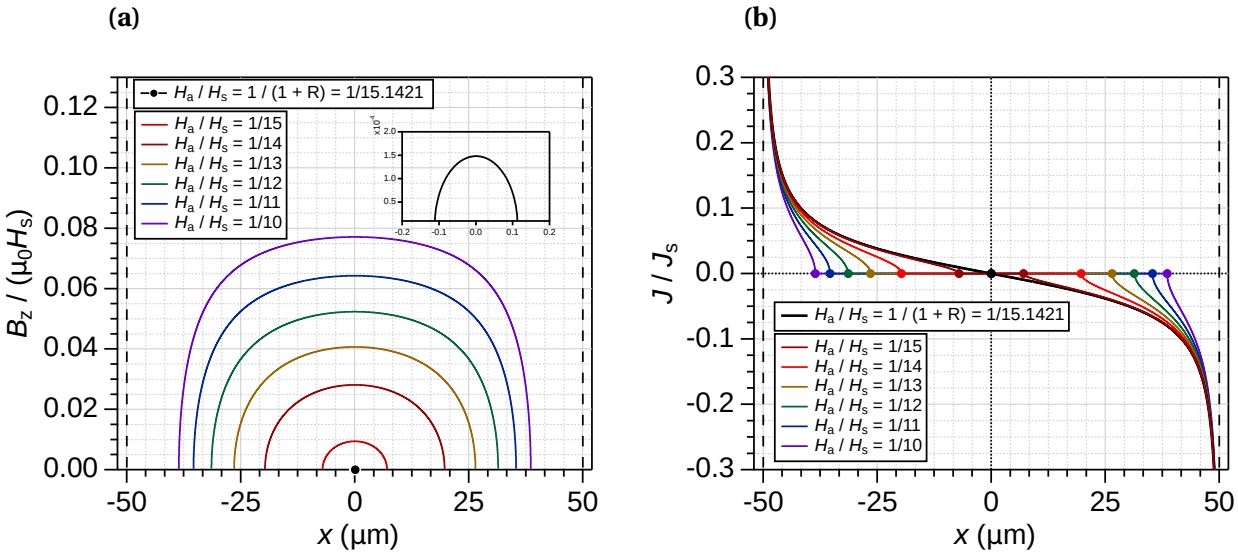

Figure 1.12: A superconducting film in the dome state for various applied fields and no transport current calculated using the formulation of Benkraouda *et al.*[68] **(a)** The flux dome at various applied fields with respect to the edge entry field. The flux dome at the entry condition (when $H_a/H_s = 1/(1+R)$, see text) is also displayed and magnified in the subfigure. **(b)** The corresponding current densities, normalized to J_s, for each flux dome. Recall that $J/J_s = 1$ at the edges (dashed lines). The film parameters used to obtain these solutions are $W = 50\,\mu$m (a film width of $100\,\mu$m) and a film thickness of $d = 0.5\,\mu$m.

Thus a superconducting film in the mixed state will have a *flux dome* in the sample interior caused by the vortex lattice that is formed at the center of the film in the absence of a transport current.[68] This flux dome, or a dome of vortex density n, is the average field of the vortices within the strip, $B_z \sim n\Phi_0$ and is described by

$$B_z(x) = \begin{cases} B_0 \dfrac{\sqrt{(x-a)\,(b-x)}}{\sqrt{W^2 - x^2}} & a < x < b, \\ 0 & \text{otherwise}, \end{cases} \tag{1.11}$$

where B_0 is related to the applied field by $B_0 = \mu_0 H_a$ and W is half of the sample width.[68] The parameters a and b determine the boundaries of the flux dome within the sample where no current flows interior to a and b.[68] The dome boundary parameters are given by

$$a = W\left[\frac{I}{2\pi W H_a} - \sqrt{\left(1 + \frac{I}{2\pi W H_a}\right)^2 - \left(\frac{H_s - H_a}{R H_a}\right)^2}\right], \tag{1.12}$$

$$b = W\left[\frac{I}{2\pi W H_a} + \sqrt{\left(1+\frac{I}{2\pi W H_a}\right)^2 - \left(\frac{H_s - H_a}{R H_a}\right)^2}\right], \tag{1.13}$$

where $R = \sqrt{(2W)/d}$ is the square root of the aspect ratio of the strip and can be used to describe the sample edges.[68] The condition on H_a required for first flux entry can be obtained by considering the limit of vanishing dome width which corresponds to Equation 1.12 in the limit of $a = 0$ or $b = 0$ with no transport current (we arbitrarily choose to consider the case of $a = 0$ with Equation 1.12). Simple rearrangement in this limit yields the relationship between the applied field H_a and the edge entry field H_s of

$$H_a = H_s\left(\frac{1}{1+R}\right) \tag{1.14}$$

that is required to nucleate vortices into the film. The parameter R can therefore be used as a modeling tool to constrain the relationship between H_a and H_s. The minimal vortex dome that is formed for an applied field that just satisfies the criterion described by Equation 1.14 is depicted in Figure 1.12a as the small black curve (magnified in the inset) and represents the first few vortices entering the sample. As the applied field is increased beyond the criterion condition of Equation 1.14, vortices begin to nucleate into the superconductor and contribute to the interior flux dome as shown in Figure 1.12a. These vortices also contribute to the net current density in the dome state,[68] shown in Figure 1.12b. The current densities corresponding to each vortex dome are zero wherever vortices exist (or equivalently where the vortex dome exists) since any nonzero current would cause the vortices within the dome to move. Also, recall that the current at the strip edges can never exceed $|J_{edge}/J_s| = 1$ since the current from each vortex that nucleates lowers the currents at the edge.

The addition of a transport current will alter the dome shape.[68] Figure 1.13 shows the flux dome and corresponding current densities in the presence of various transport currents. These transport currents are normalized to $I_c(H_a)$, which is another critical current defined as the applied current that is required to cause vortices to exit the strip at a given applied field. The terms

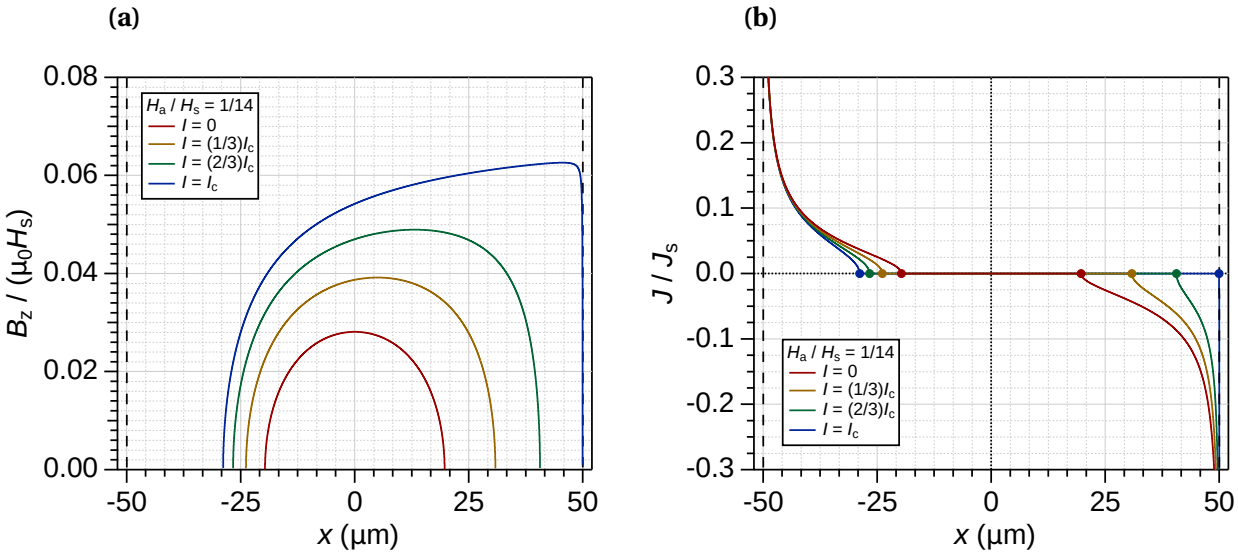

Figure 1.13: A superconducting film in the dome state for an applied field of $H_a/H_s = 1/14$ for various transport currents.[68] **(a)** The effects of several transport currents on the flux dome. **(b)** The corresponding current densities, normalized to J_s, for each flux dome. Recall that $J/J_s = 1$ at the edges (dashed lines). The film parameters used to obtain these solutions are $W = 50\,\mu$m (a film width of $100\,\mu$m) and a film thickness of $d = 0.5\,\mu$m.

in Equations 1.12 and 1.13 that depend on the applied current I cause the dome shape to be asymmetric and "pushed away" from the vortex nucleation edge. For larger transport currents, the dome is heavily distorted until the right dome edge (determined by b of Equation 1.13) overlaps with the right edge of the strip. At this point, the vortices that comprise the flux dome begin to exit the superconductor via the overlapped, right edge. As they do so, new vortices enter over the left edge, and a continual flow of vortices across the sample begins and the superconductor has entered the flux-flow regime in which the dome model is no longer valid.

These considerations of the flux dome formed within a superconducting strip required the inclusion of the effects of the sample edges. This implies that the sample edges heavily influence vortex nucleation and vortex dynamics. The effect of the sample edges on flux properties within granular aluminum superconductors will be the subject of Chapter 3.

Chapter 2

Superconductivity in Modulated Granular Aluminum Films

Exploiting Abrikosov vortices in type-II superconductors to create fluxonic devices such as relativistic-flux-quantum-based diodes,[23] logic elements,[26,28] or even as nondestructive read-out random access memory (RAM) cells[29] has lead to a significant amount of research on the effects of various surface potentials on vortex transport properties. One method of influencing and exploiting vortices is with a *vortex ratchet* that *rectifies* vortex motion by preferentially restricting flux-flow in one direction. These vortex ratchets are typically fabricated by imposing a two-dimensional potential landscape with magnetic pinning potentials[17,56–58,89] or with magnetic and hole dot arrays[14,90,91] (for a review see Ref. 33). Other ratchets have been realized via modification of the sample edges that alter the vortex nucleation environment[60,62] rather than imposing a surface potential.

In Chapter 1, we argued that the vortex dynamics in two-dimensional surface potentials can be complex and so surface potentials that impose a one-dimensional washboard potential are an ideal testing ground. For example, experiments by Morrison *et al.* and Dobrovolskiy *et al.* exploit an asymmetry in the magnetization of type-II superconductors by pressing or milling grooves into the sample to modulate the surface which induces an asymmetry in the surface potential landscape.[21,24,92,93] Additionally, there have been numerous theoretical works that show how rectification can be achieved by considering asymmetry from washboard potentials.[27,33,91,94,95] We, therefore, aimed to fabricate and study vortex ratchets by imposing a periodic thickness variation, and thus a direct washboard potential, in superconducting films.

In order to understand the vortex dynamics in ratchet systems, it is first useful to briefly revisit the details of vortex entry within a flat superconducting strip, which was thoroughly discussed in Chapter 1. Recall that a thin type-II superconducting strip that is in the presence of

an applied field H_a will exist in the mixed state where vortices penetrate the sample since we assume that the first critical field $H_{c1} \approx 0$ for thin-film geometries. In this mixed state, vortices nucleate over either sample edge and are pushed towards the center of the strip by a Lorentz force that is generated from the Meissner screening currents at the edges of the sample. This process is repeated for subsequent nascent vortices creating a dome-like field distribution in the interior of the sample along with a triangular vortex lattice that is caused by the repulsive vortex-vortex interaction. An applied transport current I_t will then create a preference for vortex nucleation to occur at one of the two strip edges, as well as alters the vortex dome shape into a form such that the dome is "pushed away" from the nucleation edge.[68] As I_t is further increased, the dome will eventually be skewed such that one of the dome edges reaches one of the film edges. At this point vortices begin to spill out of and flow across the strip, generating a voltage as each one exits.[68] The system is now in a dynamic state where the dome model no longer applies.

One way to influence the previously described vortex dynamics is by creating a symmetric, washboard potential landscape in a superconducting sample. Consider a superconducting thin-film strip that possesses a potential of this kind with a sinusoidal thickness modulation that is in the presence of an applied field H_a, represented in Figure 2.1. For small H_a, only a few vortices enter the strip and the vortex density inside the sinusoidally modulated superconductor is lower than what is required to fill each of the potential minima with a vortex.* In this case, as shown in Figure 2.1a, the vortices will reconfigure themselves so that each vortex sits as low as possible within this potential landscape. Since there is no commensurability between the vortices and the potential wells, vortices with no neighbors and vortices that are surrounded by neighbors will sit at the potential minima while vortices with only one neighbor will be marginally pushed up in the potential wells by the repulsive vortex-vortex interaction. Therefore, the critical current I_c that is required to liberate these vortices from the potential wells, cause flux-flow across the strip, and produce a voltage will be large since all the vortices

*We assume that $H_{c1} \approx 0$ for strips and thin-films.

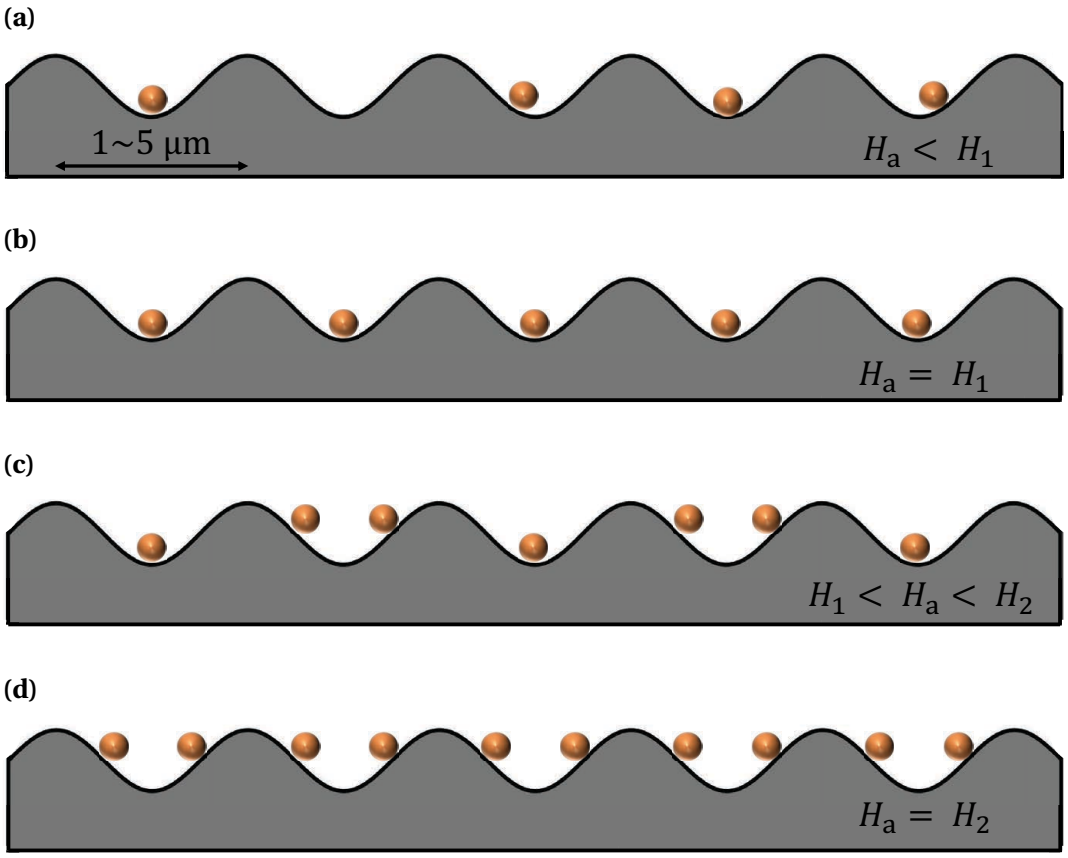

Figure 2.1: A cartoon depiction of the arrangements of vortices (orange balls) in a symmetric, one-dimensional washboard potential (grey modulation) for several applied fields. H_n will be used to denote the n^{th} matching field. **(a)** $H_a < H_1$. **(b)** $H_a = H_1$. **(c)** $H_1 < H_a < H_2$. **(d)** $H_a = H_2$.

in the film sit fairly low within the potential (although some are not sitting at the minima). A symmetric potential will yield the same critical current for leftward and rightward moving vortices since the force required to push these vortices up the symmetric potential walls is identical in both directions.

The effects of the thickness modulation further influence vortex motion as the applied field is increased. Once H_a reaches the *first matching field* H_1, the vortex density is commensurate with the period of the washboard potential and each potential minima is occupied by a single vortex as shown in Figure 2.1b. The vortices in this case experience the same landscape potential created by the sample as in the previous case depicted in Figure 2.1a, but each vortex is symmetrically influenced by the repulsive vortex-vortex interaction. The critical current re-

quired to liberate the entire vortex lattice from the washboard potential at this matching field will be larger than is required in the $H_a < H_1$ case since each vortex in the strip now sits at local minimum within the potential (as opposed to some vortices sitting slightly higher in the wells in the case of Figure 2.1a). In Figure 2.1c, H_a is increased above H_1 such that the vortex density is higher than in the $H_a = H_1$ case. For example, consider a density such that every other well in the washboard is occupied by two vortices. In this case, the vortex-vortex interaction prevents some of the vortices from occupying the local minima and the vortices are pushed up in the potential wells so that the distance between the vortices is uniform. Now, the critical current required for vortex motion is less than what is required for the first matching field since some of the vortices sit higher in the potential wells as a result of the repulsive vortex-vortex interactions. Finally, the field is increased such that there are exactly two vortices allowed per well as shown in Figure 2.1d. At this second matching field H_2, we notice an increase in the required critical current compared to the situation described in Figure 2.1c since the vortices are sitting lower (on average) in the potential wells than they do when the field is not at a matching field. In this way, a symmetric washboard potential alters the details of vortex motion when compared to a flat strip. However, the critical currents for leftward and rightward vortex motion in this symmetric potential are identical at all applied fields following from the previous considerations of the symmetric potential wells.

Vortex dynamics can also be influenced by an asymmetric potential landscape. Now, consider a superconducting strip that possesses a potential of this kind with a sawtooth thickness modulation that is in the presence of an applied field, as shown in Figure 2.2. The previous general considerations that were made at each applied field in the case of the symmetric potential apply to the case of the sawtooth potential in that certain applied fields will cause matching effects within the asymmetric potential, resulting in an increase in the corresponding critical currents. However, these critical currents will no longer be reversible due to the difference in the slopes that rightward and leftward moving vortices experience. Vortices that are driven rightward in the sawtooth potential of Figure 2.2 will require a lower critical current to liber-

ate vortices than leftward driven vortices due to the shallower rightward slope which creates an "easy" and a "hard" direction to flux-flow. In this way, vortex ratchets can be realized by causing a *rectification* in the vortex dynamics in which there is a preferential direction of vortex motion.

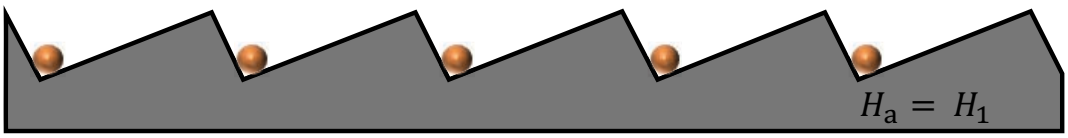

Figure 2.2: A cartoon depiction of the arrangements of vortices (orange balls) in an asymmetric, one-dimensional washboard potential (grey modulation) at an applied field that is equivalent to the first matching field, $H_a = H_1$.

Both symmetric and asymmetric washboard potential landscapes can be fabricated by influencing either the line length of a vortex or by creating pinning sites that preferentially trap vortices. Recall that previous studies have created asymmetric potentials by grooving the sample surface[20–22,93] or by introducing artificial pinning sites into the sample in the form of an array of holes or defects.[14,33,90,91] In our work, we used a combination of substrate surface modifications and sputter techniques to elegantly fabricate both an asymmetric and a symmetric modulation in the thickness of superconducting granular aluminum films. These thickness modulations influence the vortex line-length and therefore the vortex energy (see Chapter 1) which will result in a corresponding asymmetric or symmetric surface potential landscape.

In order to properly study these modulation effects, a material with inherently low pinning properties must be chosen so that the effects of the thickness modulations are not obscured. In general, vortices within a superconductor are not necessarily mobile since defects such as grain boundaries, can restrict flux motion by trapping or *pinning* vortices within the superconductor. These pinning effects may obscure vortex motion within these potentials if the pinning forces exceed the effects of the washboard potentials. Therefore, the superconductors studied in this work are granular aluminum films since this material is known to have extremely low inherent pinning as a result of minuscule grain sizes.[96]

2.1 Film Fabrication and Characterization

The study of superconducting films requires a fabrication technique that reliably and repeatably produces film samples. In general, a photolithographic lift-off process was employed to pattern granular aluminum films on glass substrates in a four-probe geometry, shown in Figure 2.3. In this geometry, an alternating current (AC) can be applied with the current leads while simultaneously measuring the voltage response between the voltage leads so that accurate resistance measurements of the sample can be made by mitigating contact resistance effects. Standard four-probe films that were studied in this work, shown in Figure 2.3, are typically ~100 μm wide by ~200 μm long between the voltage leads and were grown with a magnetron sputter system to be ~0.5 μm thick.

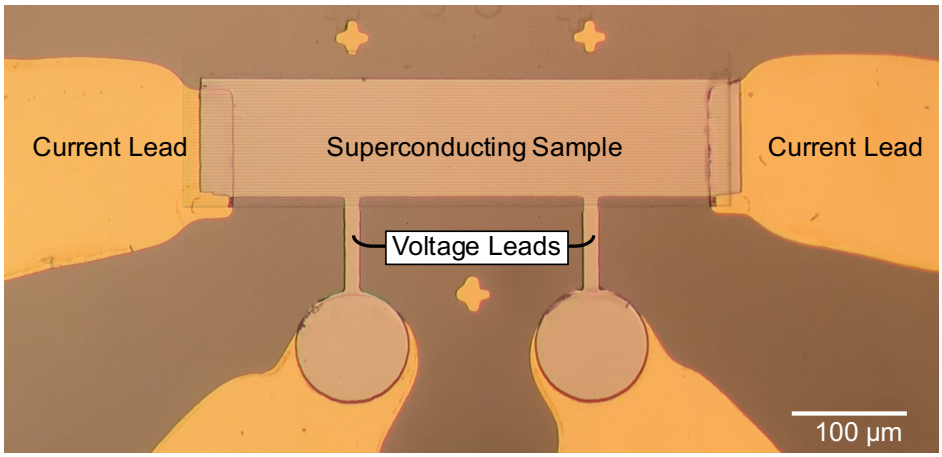

Figure 2.3: An optical image of a granular aluminum film sample in a four-probe geometry. The sample is grown on a soda-lime glass substrate on top of gold current and voltage leads. The gold crosses were used to align the various lithographic layers to one another.

2.1.1 Lift-Off Photolithography

Lift-off lithography is a versatile and widely used sample fabrication technique[97–104] that utilizes a resist mask that is sensitive to either ultraviolet light[105] or to an electron beam[106] to pattern microstructures in a wide variety of surface and sample geometries. Figure 2.4 depicts a general lift-off lithographic process. First, the substrate is cleaned with a 3-solvent rinse. Then

lift-off resist, which is not light sensitive but is soluble in the photoresist developer, is spun and baked onto the clean substrate. The light-sensitive photoresist is then spun and baked on top of the lift-off resist resulting in the resist layering that is depicted in Figure 2.4a. The sample may now be patterned by exposing the photoresist with the desired sample geometry. After the exposure is completed, the substrate is developed and the exposed area is developed away. Figure 2.4b shows the resulting post-development resist layer geometry in which an undercut is formed in the lift-off resist beneath the developed photoresist. This undercut forms since the lift-off resist is dissolved by the photoresist developer during the development step. In order to achieve an appropriate undercut, the photoresist must be slightly overdeveloped to allow the developer to dissolve the lift-off resist that is protected by the photoresist. For some lift-off resists, the extent of the undercut can be tuned by increasing or decreasing the bake time and temperatures.[107]

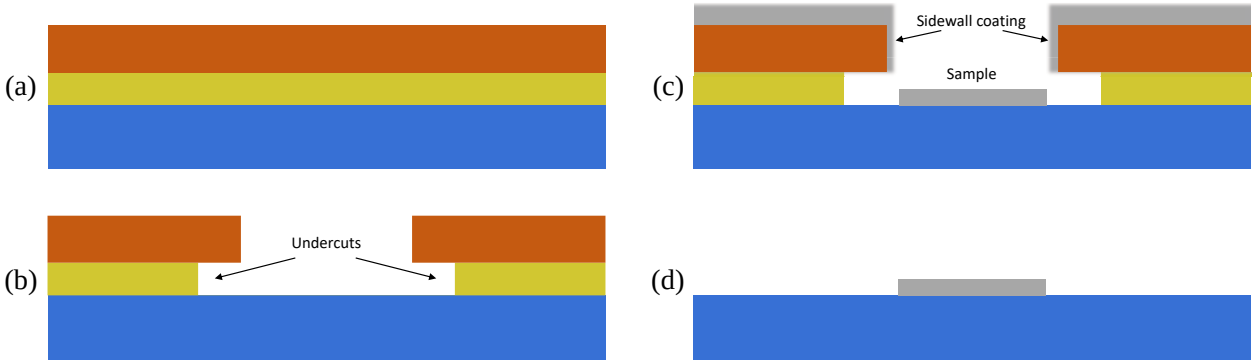

Figure 2.4: A cartoon depicting the lift-off process. **(a)** Lift-off resist (yellow) is spun on a substrate (blue). Then, photoresist (red) is spun on top of the lift-off resist. **(b)** The photoresist is exposed and developed, creating an undercut in the lift-off resist. **(c)** The substrate is metalized (grey). Note that the resist sidewall coatings are disconnected from the sample. **(d)** The resist is washed away, leaving only the sample.

At this stage, the substrate and resist layers are prepared for sample growth and subsequent lift-off. The resist stack is metalized with the sample material via a choice of any number of deposition techniques such as thermal evaporation or magnetron sputtering. Figure 2.4c depicts the substrate after the sample deposition is completed; the extreme advantage of producing an undercut becomes apparent. The resist sidewalls inevitably become coated with the sample

material, shown in Figure 2.4c, as a result of the diffusive components that are typically present during sputter growth techniques or as a result of the solid angle subtended by the material trajectories from thermal evaporation sources. The desired sample material could therefore be connected to these sidewall coatings in a monolayer resist geometry and the quality of the lift-off would suffer. The presence of the undercut ensures that it is impossible for the sidewall coating to be continuous with the desired sample area for film growths that are less than the lift-off resist thickness. The final lift-off step is performed, depicted in Figure 2.4d, by soaking the substrate in a solvent (typically remover PG or acetone) to dissolve the resist layers, leaving behind the metalized material defined by the patterned area.

Several lithographic parameters such as resist type, layer structure, and spin speeds must be carefully considered to obtain the highest quality lift-offs. The thickness of each resist layer is vital and is determined by both the choice of resists and spin speed. The desired resist thicknesses will ultimately be constrained by the desired sample thickness. If the lift-off resist layer is comparable to or thinner than the desired sample thickness then the sidewall coatings may become connected to the sample and lift-off will likely be unsuccessful. If the lift-off resist is too thick then the incoming ballistic sample material can be occluded from the substrate surface by shadowing from the photoresist layer. We found that a lift-off layer that is $\sim 3\times$ the thickness of the sample reliably produces successful lift-offs. Additionally, the success of the lift-off requires a delicate balance between the exposure dose and the development time. Underexposed resists will not yield a successful liftoff since the substrate surface will be partly covered in the sample region and the sample geometry may be altered as a result. An overexposure will also be unsuccessful as overexposed photoresist tends to have sloped sidewalls which will increase the likelihood that the sample and sidewall coatings will be connected during sample growth. The over- and under-development of the resist tends to present itself in a similar manners as incorrect exposure doses. So, a proper exposure dose balanced with an appropriate development time along with an optimized resist layer geometry is vital in obtaining high-quality samples.

2.1.2 Sample Growth by Magnetron Sputtering

The granular aluminum films that were studied in this work were grown by magnetron sputtering which is a widely implemented sample deposition technique that offers uniformity, reliability, and ease of control of the growth rate. An adaptation from Knittel *et al.*[108] was used to accurately represent the details of the sputter gun in the schematic representation of the sputter system that was used, shown in Figure 2.5. The magnetic field that is created from the permanent magnet in the sputter gun upon which an aluminum target sits traps stray electrons in tight helical orbits near the sputter gun. When a voltage is applied between the anode and the cathode in the sputter gun, the electrons that are trapped by the magnetic field are accelerated and inelastically collide with an argon atom and ionize it. This argon cation is then accelerated towards the target by the voltage applied between the cathode and anode where it ejects $1 \sim 2$ target atoms. The exact amount of ejected material for a given ion fluence depends on the voltage and the material-dependent sputter yield, or the number of ejected atoms for each incident ion. The material ejected from the sputter target is purely ballistic in an ideal system. However, random collisions with the un-ionized argon gas in the vacuum environment creates a diffusive component to the incident sputtered material.[108] This diffusive material can impinge on the substrate at relatively large angles that exceed the solid angle subtended by the target diameter, which will become an important detail when growing granular aluminum films.

The sputter deposition of granular aluminum films with this system yields reliable and repeatable superconducting samples. This reliability is crucial since we will show that the oxygen pressure and growth rate heavily influence the critical temperatures of the superconducting films. To deposit a film, the system is first pumped to a base pressure near 0.5 µTorr. Then, 6.5 mTorr of argon along with a partial oxygen pressure of $\sim$ 50 µTorr are introduced into the chamber directly near the sputter gun via a gas inlet ring and are controlled with Alicat mass flow controllers. This argon pressure is required to ignite a plasma to begin the sputtering process while the optional oxygen pressure is used to tune the superconducting properties of the sputtered films. Once the gases have been introduced into the vacuum chamber, the argon

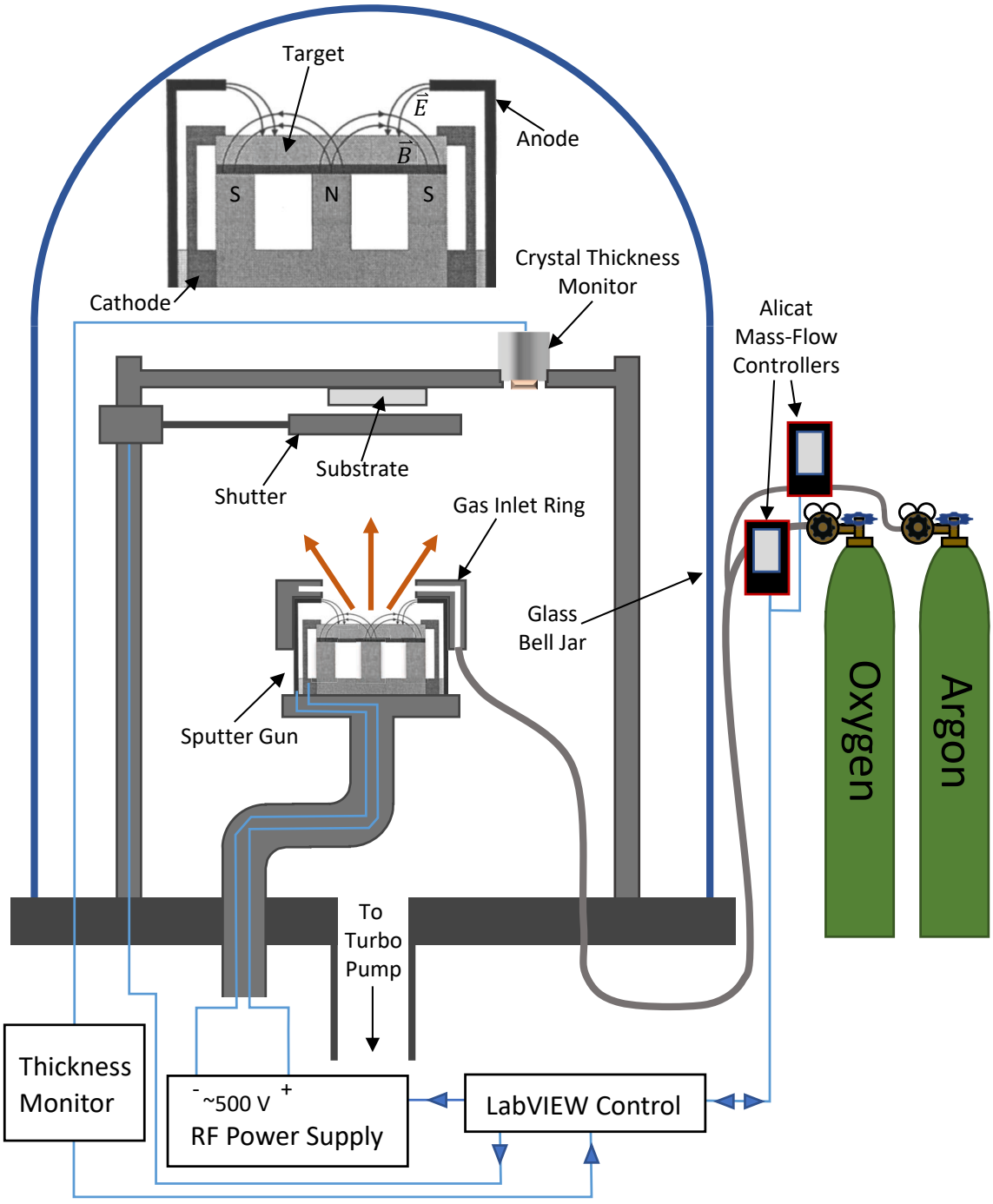

Figure 2.5: A schematic representation of the bell jar sputter system used to deposit granular aluminum films and gold contacts. Sample substrates are mounted to the sample stage near a crystal thickness monitor and are shielded by a LabVIEW controlled shutter. The inset shows an enhanced view of the magnetron sputter head adapted from Knittel *et al.*[108] An arrangement of magnets induces the magnetic field that traps stray electrons near the target and an RF power supply creates a potential that accelerates ionized argon towards the target, ejecting the desired material (orange arrows). A gas ring is outfitted onto the sputter head to vent mass-flow controlled pressures of argon and oxygen directly near the target.

plasma is ignited and the aluminum target material begins to sputter at an initially non-uniform rate. So, the sample is occluded by a LabVIEW-controlled shutter to protect the substrate while the sputter rate stabilizes. Both the sputter rate and film thickness are measured with a crystal thickness monitor that is not obscured by the shutter so that these parameters may be recorded by LabVIEW for the entire duration of the growth. Once the rate stabilizes to a desired value that is typically $\sim 10\,\text{Å}\,\text{s}^{-1}$ (for the aluminum films studied in this work), the shutter is opened, exposing the substrate to the sputter target and the sample growth begins. The shutter is closed once the desired thickness has been grown and the sample is lifted-off as previously described.

2.1.3 Why Granular Aluminum?

The superconducting properties of granular aluminum films are ideal for studying vortex dynamics within modulated surface potentials with the available cryogenic measurement equipment. The cryostat used to measure the superconducting films has an optimum operating temperature range between $1.3\,\text{K} < T < 2.0\,\text{K}$.[109] So, materials with critical temperatures that are too low (such as pure Al) or that are too high (such as Pb or Nb) are not ideal. However, the critical temperature of granular aluminum can be tuned by adjusting the oxygen content during sample growth so that the transition temperature is about $\sim 1.75\,\text{K}$, which allows for an optimal operating temperature range of the cryostat.[96, 109]

In addition to possessing an attractive and tunable critical temperature, granular aluminum is ideal since this material is also a low-pinning superconductor. As previously discussed, a superconductor with inherently low bulk pinning properties is required so that the surface modulation effects on vortex motion are not obscured. Recall that even vortices within a superconductor with no modulation are not necessarily mobile since certain material properties can trap or pin vortices and restrict vortex motion within the superconductor. For example, the inherent material pinning in "pure" Al films with minimal oxygen content is caused by large grains ($> 100\,\text{nm}$[110]) within the material which tend to pin vortices since the line energy of a vortex will be affected by the local variations in the superconducting properties near the inhomogeneities

that are induced by these grain boundaries.[4] The pinning within the material can mask the effects of the washboard thickness modulations on vortex motion if the inherent pinning is sufficiently large. Therefore, the ideal material to study flux flow within thickness-modulated superconductors is a material that possesses minimal pinning properties.

The low pinning properties of granular aluminum results from the small size-scales of grains that arise from the incorporation of oxygen within this material. The introduction of oxygen during film growth creates a nearly amorphous material that is composed of grains of aluminum surrounded by insulating oxide boundaries that have a length scale of $\sim 10\,\text{nm}$.[96,110] These nanometer-scale grains weakly interact with vortices within granular aluminum films since the vortex sizes (defined by ξ) are typically much larger than these grains. Therefore, vortices are unlikely to be trapped or pinned by the small grains.

Granular aluminum is considered to be a *dirty superconductor* since the electronic mean free path l is much smaller than the BCS coherence length ξ_0 as a result of the minuscule grain sizes in these materials. To show this, we find the mean free path in a granular aluminum film from the resistivity, which are related by[96]

$$\rho l = 0.4 \times 10^{-11}\,\Omega \cdot \text{cm}^2. \tag{2.1}$$

and the granular aluminum BCS coherence length is obtained by scaling the pure aluminum BCS coherence length of $\xi_{0\,\text{Pure}} = 16\,000\,\text{Å}$ by the ratio of the critical transition temperatures of these materials,[96]

$$\xi_0 = 16\,000\,\text{Å}\,\frac{T_{\text{c Pure Al}}}{T_\text{c}}, \tag{2.2}$$

where $T_{\text{c Pure Al}} = 1.140\,\text{K}$.[111] Using typical granular aluminum properties of $\rho = 10\,\mu\Omega\cdot\text{cm}$[96] and $T_\text{c} = 1.75\,\text{K}$ with Equations 2.1 and 2.2 yields a mean free path of $l = 4\,\text{nm}$ and a BCS coherence length of $\xi_0 = 1042\,\text{nm}$, indicating that granular aluminum is indeed a dirty superconductor since $l \ll \xi_0$.

The vortex properties in granular aluminum are therefore determined by the Ginzburg-Landau characteristic lengths for dirty superconductors. Recall from Chapter 1 that the vortex size depends on the material dependent coherence length ξ, which is distinct from (but related to) the BCS coherence length ξ_0. Also recall that the penetration depth λ determines the vortex regime (Abrikosov, intermediate, Pearl) that vortices experience when compared to the sample thickness. In a dirty superconductor, these temperature-dependent Ginzburg-Landau characteristic lengths are given by[4]

$$\xi(T) = 0.85(\xi_0 l)^{1/2}\left(1-\frac{T}{T_c}\right)^{-1/2} \tag{2.3}$$

$$\lambda(T) = 0.62\lambda_L\left(\frac{\xi_0}{l}\right)^{1/2}\left(1-\frac{T}{T_c}\right)^{-1/2} \tag{2.4}$$

where $\lambda_L = 157\,\text{Å}$ is the London penetration depth at $T = 0$.[110] Evaluating Equations 2.3 and 2.4 with the previously noted granular aluminum properties ($\rho = 10\,\mu\Omega\cdot\text{cm}$[96] and $T_c = 1.75\,\text{K}$) yields characteristic lengths of $\xi(0.9T_c) = 174\,\text{nm}$ and $\lambda(0.9T_c) = 496\,\text{nm}$ with the temperature dependence of both lengths displayed in Figure 2.6.

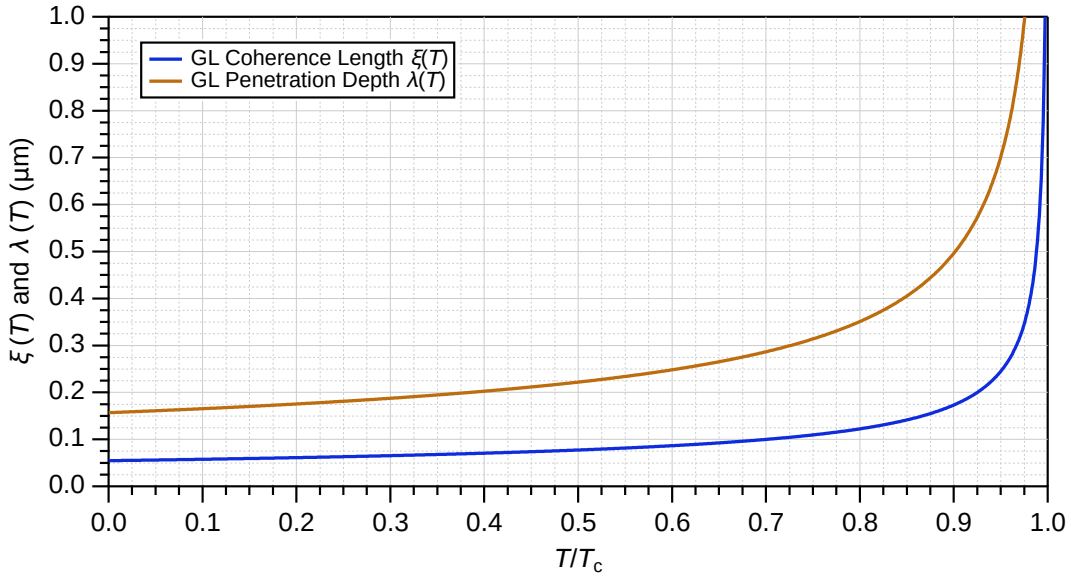

Figure 2.6: The temperature dependence of the GL characteristic lengths (Equations 2.3 and 2.4) for typical granular aluminum films. These calculations were performed with $T_{c\,\text{Pure}} = 1.14\,\text{K}$ and $\rho = 10\,\mu\Omega\cdot\text{cm}$.

The vortex properties in granular aluminum are thus ideal to study vortex dynamics in surface potentials. The sizes of vortices in granular aluminum of diameter $\sim 2\xi$ must be reasonable such that a realistic periodic potential pitch of $\sim 3\,\mu$m can be lithographically fabricated. The previously calculated value of ξ for granular aluminum is particularly attractive since vortices of diameter $\sim 2\xi \sim 348\,$nm are small enough to experience an easily fabricated washboard pitch of $3\,\mu$m while also being large enough to not be affected by the previously noted 10 nm grains that are present in these superconductors. Additionally, the granular aluminum films that were typically grown to a thickness of $\sim 0.5\,\mu$m are comparable to the previously calculated GL penetration depth indicating that vortices within these films are likely in the intermediate regime (see Chapter 1). The combination of the tune-ability of the critical temperature, the low inherent surface pinning, and the vortex size-scale makes granular aluminum an ideal material to study the vortex dynamics resulting from the modulation in the sample thickness.

2.1.4 Granular Aluminum Film Characterization

Numerous samples were tested in an attempt to empirically determine how the growth parameters influence the superconducting properties of the films. The first series of four-probe samples were grown at various deposition rates and partial pressures of oxygen to characterize the sputtering system that was used to grow granular aluminum films. Figure 2.7 reveals a dependence of the critical temperatures of the films on the ratio of the oxygen pressure to the growth rate. This can be visualized by considering the substrate surface at the atomic level during a sample growth. At a partial oxygen pressure of P_{O_2} there are n atomic layers of oxygen incident on the substrate surface per second, where n is proportional to P_{O_2}. Since the rate of sputtered aluminum is typically on order of 10 Å/s and since the atomic diameter of aluminum is 2.86 Å, then there are ~ 3.5 atomic layers of aluminum incident on the substrate per second. This will result in a ratio of oxygen to aluminum at the substrate surface that is proportional to the ratio of the oxygen pressure to to deposition rate. We also found that the room temperature resistivity is dependent on the oxygen content in the films and can therefore be used as an

initial metric of the quality of the films without needing to cool the sample to cryogenic temperatures. While there is a clear dependence on the critical temperature on the oxygen content in the granular aluminum films that is indicated in Figure 2.7, there is evidently another property that contributes to this dependence because of the imprecision in the trend of the critical temperatures.

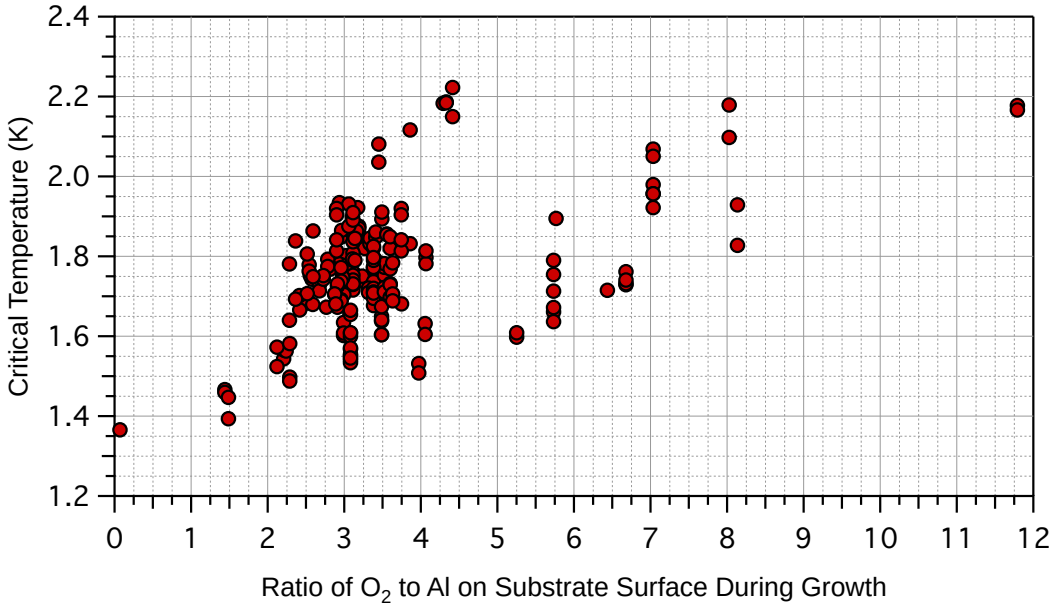

Figure 2.7: Critical temperature measurements for approximately 200 granular aluminum samples grown via magnetron sputtering in a partial pressure of oxygen. The critical temperature location trends with the ratio of the number of oxygen atoms to the number of aluminum atoms incident on the substrate surface during growth.

In addition to the dependence of the location of the transition temperature on the film growth parameters, we found that the shape of the critical transitions of the films are influenced by the sloped sample edges that are created as a result of the lift-off geometry. Various transition measurements of films that were tested without any additional fabrication steps after lift-off seemed to have wide transitions with irregular shapes. Since the sputter gun cannot be considered a point source at a typical substrate-target distance of 8 cm, there is an 8° angular variation in the incident material that can blur the sample edges. However, this geometry alone could not explain the micron-sized blurring of the sample edges that we repeatedly observed. Our

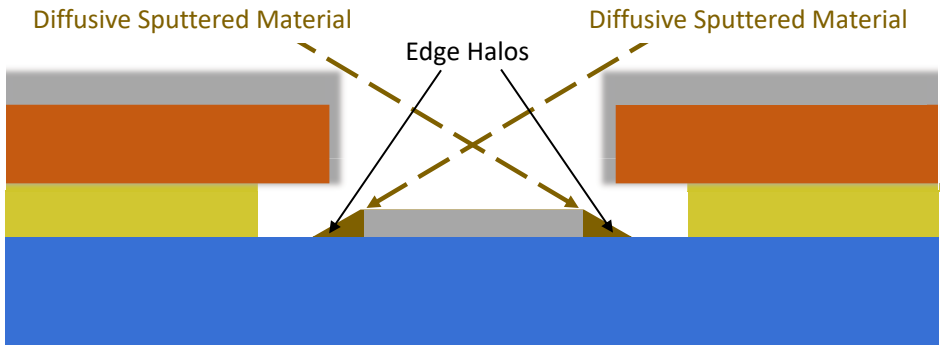

Figure 2.8: The lift-off undercut geometry created by the lift-off resist (yellow) and the photoresist (red) along with the diffusive component of the sputtered material (orange dashed arrows) can create an edge halo in the sample (orange edges).

hypothesis was that the "haloed" film edges were caused by an interplay between the undercut geometry and the non-negligible diffusive component of the incident sputtered aluminum[108] as shown in Figure 2.8. These "haloed" or irregular edges have been known to cause broadened critical transitions in other superconducting films which were remedied by trimming the film edges.[112,113] Therefore, a touch up wet-etch in Trasene moly etchant (which is a phosphoric-acetic-nitric acid solution) was performed after the lift-off step to create an edge geometry that is closer to a squared edge by using photoresist as an etch mask. Figure 2.9 contrasts the transitions of two granular aluminum samples before and after the touch-up edge etch is performed

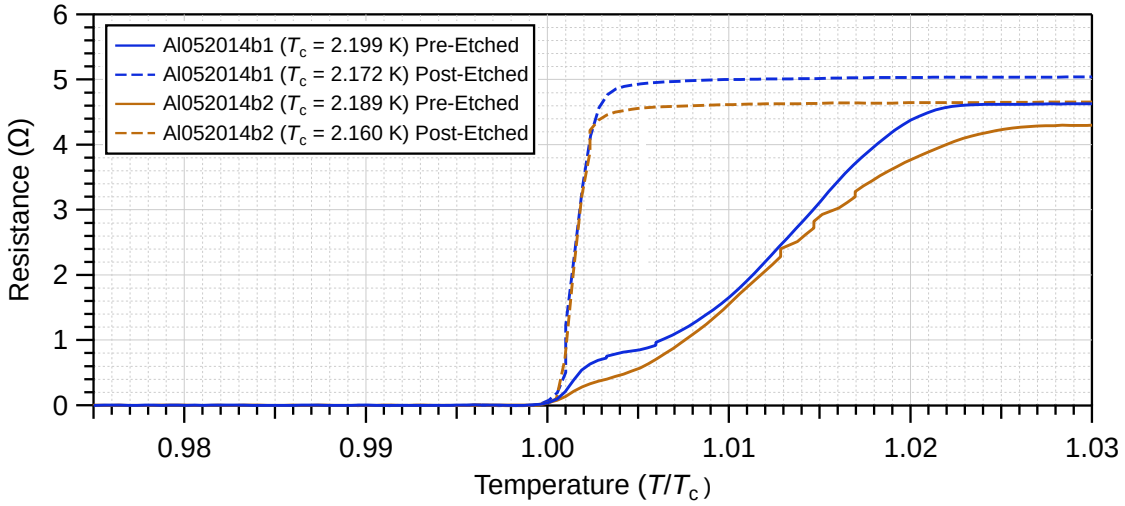

Figure 2.9: Transition curves of two granular aluminum films before (solid) and after (dashed) trimming the edges via a wet etch. The transition widths (defined as ΔT_c between $0.9R_{\text{Normal}}$ and $0.1R_{\text{Normal}}$) are $\Delta T_c \sim 4\,\text{mK}$ for the post-etched films and are $\Delta T_c \sim 38\,\text{mK}$ for the pre-etched films.

and shows that the wet-etched films have much sharper transitions. This clearly demonstrates that the sample edges influence the shape of the superconducting transitions.

2.2 Fabrication of Modulated Granular Aluminum Films

In order to study vortex motion within vortex ratchets, we fabricated granular aluminum film samples with either a symmetric (sinusoidal) or an asymmetric (sawtooth-like) thickness modulation with a ~ 3μm pitch similar to the representation in Figure 2.1. These thickness-modulated films were fabricated by first etching a square wave grating into the surface of a glass substrate followed by an annealing step to smooth the grating. Then, a granular aluminum sample was sputtered at a large angle (~40°) relative to the glass substrate surface and lifted-off. As we will show, this leads to a superconducting film with a periodic thickness modulation. Finally, the edges of the films were trimmed with a wet etch to remove any edge haloing effects that were previously discussed. This is an attractive technique to fabricate thickness-modulated films since the washboard potential is highly tunable via adjustment of the square grating pitch, the grating depth in the glass substrate, the annealing time, and the film growth geometry.

2.2.1 Fabrication of Modulated Glass Substrates

The fabrication of a modulated granular aluminum film began by creating a thickness-modulation in the surface of a glass substrate. An ultraclean soda lime glass substrate that was pre-coated with a 120 nm chromium layer (which will eventually serve as a wet etch mask) was spun with 950K A3 poly(methyl methacrylate) (PMMA) resist to a thickness of ~ 120 nm. Next, the PMMA resist was patterned with a ~ 3μm pitch square grating using a JEOL 6500F scanning electron microscope (SEM) equipped with a Nabbity controlled beam blanker. The PMMA was developed in a 3 : 1 mixture of isopropyl alcohol (IPA) : methyl isobutyl ketone (MIBK) for 1 minute and 30 seconds. The sample was then submerged in a Trasene chromium etchant solution for 1 minute and 30 seconds to etch away the exposed chromium, which transferred the square grating from the PMMA into the chromium layer. Next, the remaining PMMA was re-

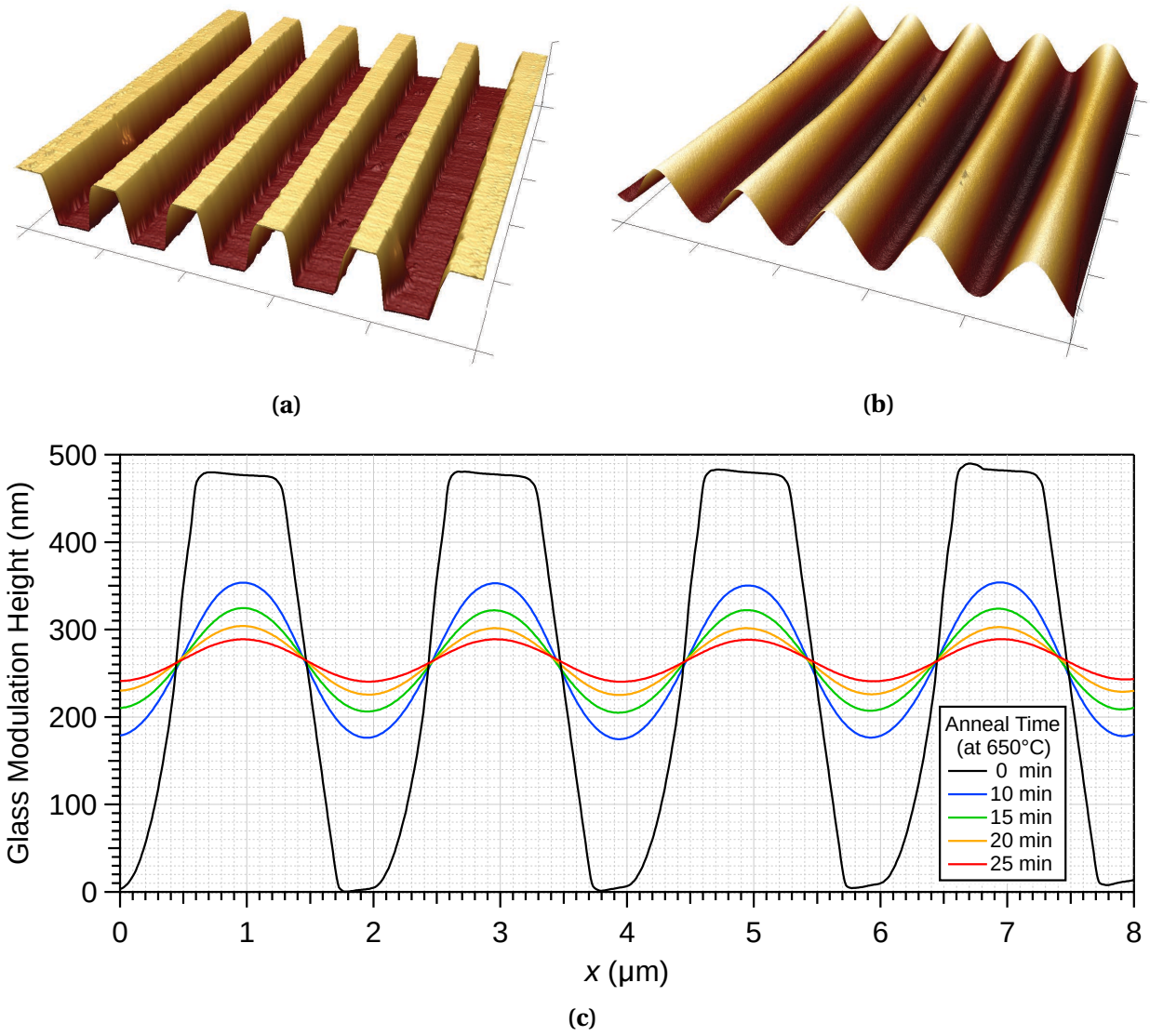

Figure 2.10: **(a)** An AFM scan of a square grating etched into a glass substrate. **(b)** An AFM scan of the final modulation in a glass substrate after annealing the square grating. **(c)** AFM scans of the glass substrate at various stages during the annealing process, which was performed in a 650 °C tube furnace.

moved with acetone and the glass substrate was etched in a buffered hydroflouric acid solution to transfer the square grating from the chromium layer into the glass. The remaining chromium was removed with another submersion in chromium etchant, resulting in a glass substrate with a square wave etched into the surface that is shown with the atomic force microscopy (AFM) scan in Figure 2.10a. This square wave in the glass substrate was then annealed in a tube furnace at 650 °C to smooth the square wave grating as shown in Figure 2.10b. Figure 2.10c shows

the AFM scans of the modulation in the glass substrate at various stages during the annealing process. This annealing step must be done incrementally so that the substrate surface can be checked with AFM to avoid over- or under-annealing in order to achieve the desired waveform in the glass surface (the choice of the desired waveform depends on several process parameters and will be discussed in the next section).

2.2.2 Deposition of Modulated Granular Aluminum Films

Thickness-modulated granular aluminum films were deposited via magnetron sputtering in a partial pressure of oxygen with the sputter system that was previously described and characterized. The sputter deposition of granular aluminum at an angle relative to a previously fabricated surface-modulated glass substrate results in a film with a periodic variation in the thickness of the sample. Areas of the substrate with normal vectors that are parallel, or close to parallel, with the incident material will become the thickest regions of the sample. In contrast, the portions of the substrate with normal vectors that are perpendicular to the incident material will become the thinnest regions of the sample. The differential dependance of the thickness modulation during a growth, where a discrete layer dt of material is deposited onto the substrate, is represented by

$$dt = \frac{dx}{\cos(\gamma)} \frac{\cos\left(\text{atan}\left(\frac{dh}{dx}\right) - \gamma\right)}{\cos\left(\text{atan}\left(\frac{dh}{dx}\right)\right)} \tag{2.5}$$

where x is the lateral distance along the modulation, h is the modulation height, and γ is the deposition angle relative to the normal of the unmodulated substrate surface. Figure 2.11 depicts this geometry where the resulting thickness variation in the sample is given by the difference between the sample surface modulation and the underlying substrate modulation.

It is possible to obtain virtually any desired modulation in a film sample with the proper choice of initial grating spacing in the PMMA, chromium etch time, glass etch depth, substrate anneal time, and deposition angle. In particular, asymmetric gratings with different forward

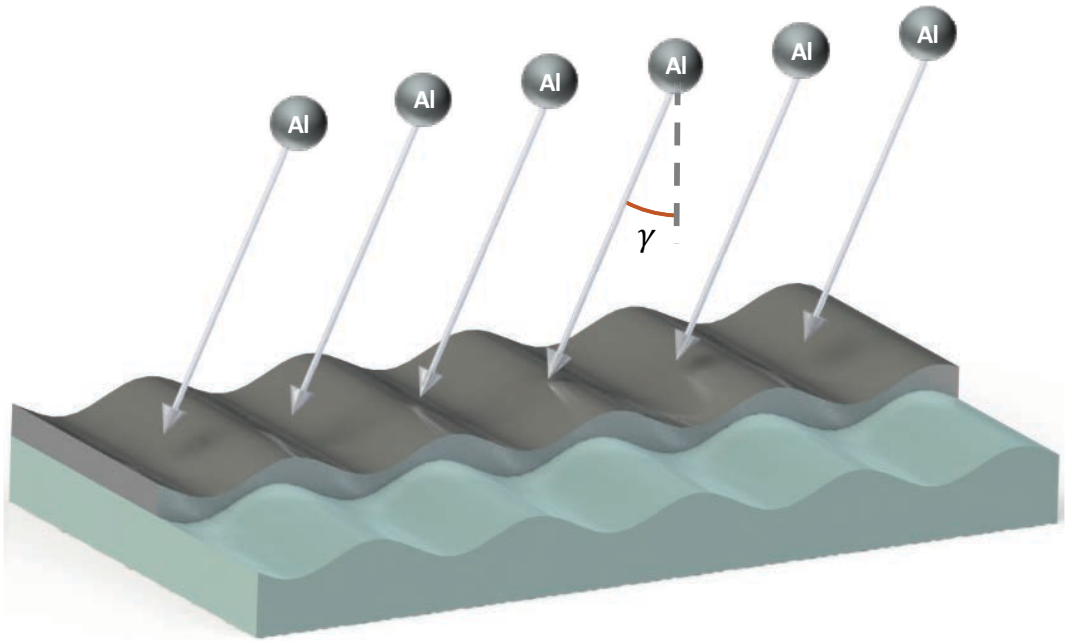

Figure 2.11: Angle deposition of granular aluminum (grey) at an incident angle of γ onto a modulated glass substrate (teal). The vertical scale is greatly exaggerated for clarity.

and reverse slopes can be fabricated with the proper initial choice of the previously enumerated fabrication parameters. Figure 2.12 depicts calculations of the ratio of the forward and reverse slopes or *the rectification ratios* of a simulated thickness-modulated film sample that is grown to a nominal thickness of $d = 0.5\mu$m at a deposition angle of 40° on substrate modulation waveforms resulting from various initial square wave grating widths and etch depths. Contour lines of constant modulation amplitudes represented as percentages of the sample thickness, called *percent modulations*, are also depicted in Figure 2.12 with the red lines. These results were calculated with Equation 2.5 combined with a wet-etch model that predicts the grating achieved in the chrome and glass layers along with a mathematical representation of annealing that filters out higher Fourier coefficients in a given wave. These calculations were performed in order to choose waveforms in the glass substrate (by determining which square grating fabrication parameters to use combined with the annealing time) that would produce a symmetric (sinusoidal) and an asymmetric (sawtooth-like) sample thickness modulation with non-negligible and comparable percent modulations when depositing granular aluminum with the previously noted deposition parameters.

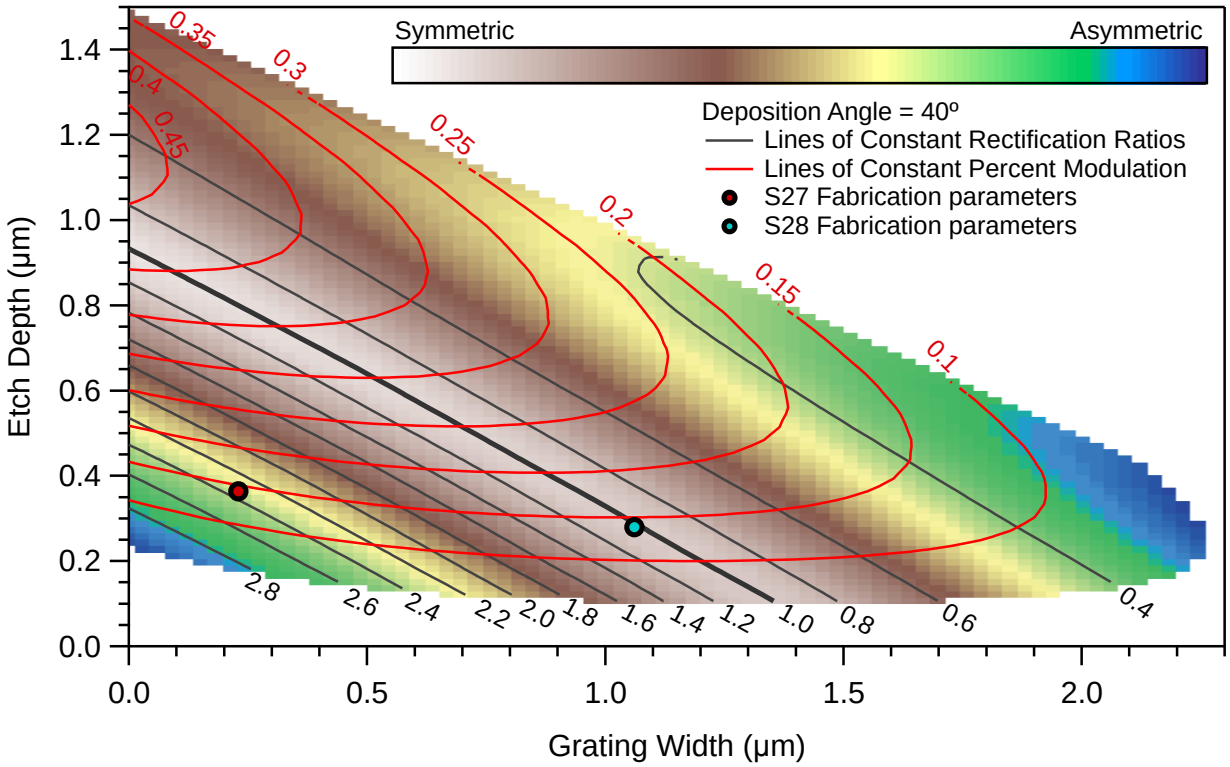

Figure 2.12: Ratios (represented with the colored image) of the forward slope to the reverse slope of various film thickness modulations calculated from the initial grating width and etch depth for a growth angle of 40 degrees using Equation 2.5. Lines of constant percent modulation (red contours) and lines of constant rectification ratios (grey contours) are also plotted. The parameters used to fabricate the asymmetrically and symmetrically modulated samples Al060315c and Al060315d are shown as the red and blue circles.

2.3 Rectification Measurements of Modulated Films

2.3.1 Sample details

Two modulated substrates, designated S27 and S28, were fabricated using the previously described method so that a sample grown on S27 will have an asymmetric thickness modulation and a sample grown on S28 will have a symmetric thickness modulation. These two substrates were fabricated to compare the effects of an asymmetric and of a symmetric vortex potential to one another. The fabrication parameters that were used to create S27 and S28 are marked in Figure 2.12 by the red and blue dots respectively. Both substrates were fabricated with a 3 µm pitch and were designed to yield modulated-films with similar percent modulations of 15 % ~ 20 % of the film thickness.

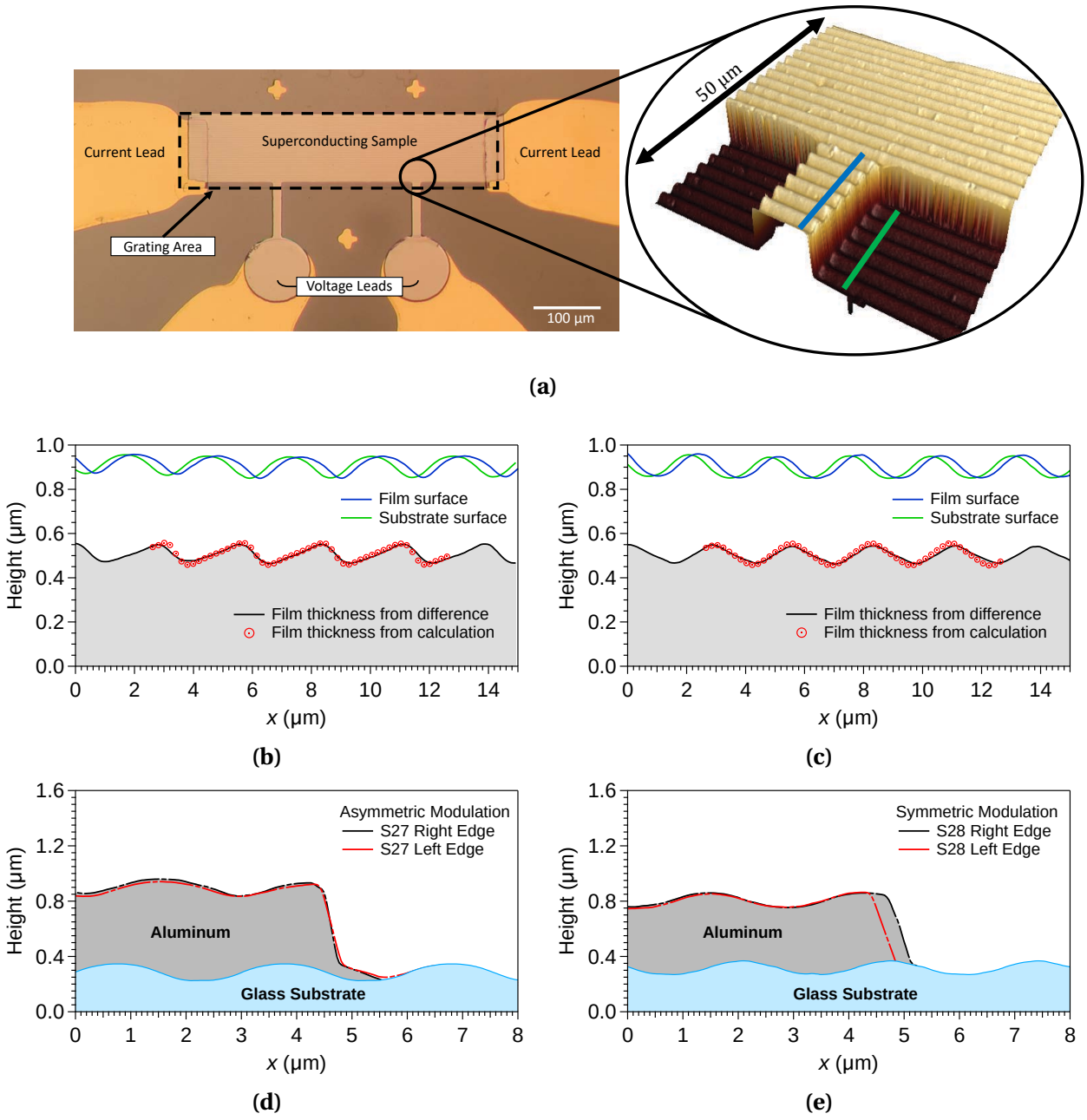

Figure 2.13: **(a)** Image of a modulated granular aluminum sample where the black dashed line represents the area of the substrate that has been modulated along with an AFM scan of a 50 µm area around a voltage lead. Also depicted are AFM scans of the sample and substrate surfaces of the **(b)** asymmetric Al060315c and **(c)** symmetric Al060315d granular aluminum samples. These AFM scans were taken along the corresponding paths in **(a)** for the modulation in the film surface (blue) and in the substrate surface (green). The sample thickness modulations (black curves) were obtained by taking the difference between the sample surface modulation and the substrate modulation. The red circles represent the expected thickness variation obtained from Equation 2.5. AFM scans depicting the edge profiles for the **(d)** asymmetric and **(e)** symmetric samples are also shown.

Thickness-modulated samples were obtained by depositing granular aluminum films onto S27 and S28 in a four-probe geometry via the previously described lift-off lithographic techniques. First, gold contacts were patterned and lifted-off onto the modulated substrates. Then, granular aluminum samples labelled Al060315c and Al060315d were simultaneously sputtered onto S27 and S28 respectively at an angle of 40° in a 33.16 μTorr partial pressure of oxygen and at a rate of 11.2 Å/s to a thickness of 428 nm as measured by a crystal thickness monitor. As was previously discussed, these growth parameters were chosen to obtain critical transitions that could be measured with the available cryostat. Additionally, the simultaneous sample growths ensured uniformity between the sputtering and superconducting parameters of the films which implies that the only difference between the samples was the modulation geometry. Figure 2.13a shows an optical image of one such sample along with a 50 μm AFM scan of the area near a voltage lead. Figures 2.13b and 2.13c show the sample thickness modulations resulting from the difference between the sample and surface modulations. These waveforms were obtained by performing AFM scans along the corresponding blue and green paths in Figure 2.13a to ensure that the AFM profilometry of the film surface and substrate modulations were properly aligned. The resulting thickness-modulation waveforms of the asymmetric and symmetric samples agreed well with the thickness modulations that were predicted with Equation 2.5 for samples grown on each substrate at an angle of 40°, shown as the red circles in Figures 2.13b and 2.13c. This indicates that the desired asymmetric and symmetric thickness-modulated films with reasonable percent modulations were achieved.

The sample edges were also characterized to ensure that any observed rectification effects were caused by the film thickness modulations rather than by any differences in the sample edges. After the sample lift-off was completed, the sample edges were wet-etched in Trasene Moly etchant to remove the previously discussed sputtered edge halo that might be present. During the edge-etch step, great care was taken to define the wet-etched edges at similar locations in the thickness modulation in each film. Figures 2.13d and 2.13e depict AFM scans of both film edges for the asymmetric and symmetric samples respectively. These scans show

that both films possess comparable edges that terminate at equivalent locations in the sample thickness modulations which indicates that each pair of sample edges are similar.

2.3.2 Cryogenic Measurements

The vortex dynamics in the asymmetrically (Al060315c) and symmetrically (Al060315d) thickness-modulated samples were measured in a home-built closed-cycle pulse tube cryocooler with an rms temperature stability of 25 μK and a base temperature near 1.2 K.[109] The samples were mounted on a copper sample plate with Apiezon N thermal grease to thermally anchor the samples to a liquid helium pot. The temperatures of the films were monitored by a Cernox thermometer and controlled with a manganin wire resistive heater. First, the samples were cooled to 3 K where standard resistivity and the ratio of resistivity to room temperature (RRR) measurements were performed. Table 2.1 contains many of these measurements along with various film, conductivity, and superconducting properties for these samples (see Equations 2.3 and 2.4 for the calculation of ξ and λ).

Table 2.1: Properties of Al060315c,d

Sample	T_c (K)	$\xi(0.9T_c)$ (nm)	$\lambda(0.9T_c)$ (nm)	R_{RT} (Ω)	R_{3K} (Ω)	ρ_{RT} (μΩ·cm)	ρ_{3K}	RRR ρ_{RT}/ρ_{3K}
S27-c Unpolished	1.887	108	740	1.28	1.12	27.5	23.9	1.149
S28-d Unpolished	1.905	105	751	1.33	1.16	28.5	24.9	1.146
S27-c Polished	1.884	106	754	1.34	1.15	28.7	24.8	1.156
S28-d Polished	1.893	98	812	1.56	1.35	33.3	28.9	1.149

The superconducting transitions of the asymmetric and symmetric films, shown in Figure 2.14 with the dashed curves, were then recorded by applying an AC current between the current leads while simultaneously measuring the voltage leads with an SR830 lock-in amplifier. The critical transitions are sharp for both films with transition widths of 3 mK occurring at critical temperatures of 1.905 K for the symmetric sample and at 1.887 K for the asymmetric sample. As was previously noted, the sharp transitions are likely a result of the careful treatment

of the film edges while the commensurate critical temperatures are a result of the simultaneous film growths. These properties indicate that both samples nominally have similar oxygen contents and therefore possess similar superconducting properties.

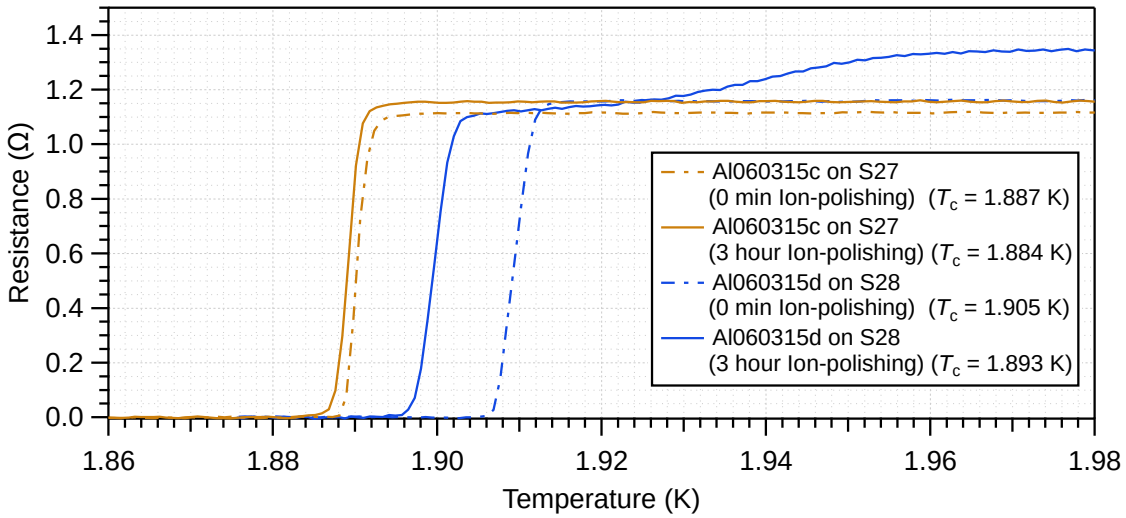

Figure 2.14: Transition curves for the asymmetrically (orange) and symmetrically (blue) modulated granular aluminum films for pre- (dashed) and post- (solid) polishing by RF ion argon impingement at a power of 40 W for 3 hours.

The effects of the surface modulations in the asymmetrically (Al060315c) and symmetrically (Al060315d) modulated samples were then studied by probing the vortex dynamics within these films. This was done by performing transport measurements in the form of current-voltage characteristics (CVCs) which are schematically represented in Figure 2.15. In these CVC measurements, vortices are driven at 100 Hz in each direction (blue arrows) across the films by sweeping both senses of a transport current I_t (red arrows) that is applied between the current leads of the sample. This driving is performed in the presence of an applied magnetic field H_a, which was generated by coil magnets consisting of copper wire and were mounted at room temperature outside of the cryostat. The voltage response to I_t that is generated by vortices exiting over the sample edges (black dashed lines in Figure 2.15) is then recorded. This process is repeated at various temperatures between $0.85T_c < T < 0.99T_c$ and at various applied fields between $0\,\mathrm{G} < H_a < 25\,\mathrm{G}$.

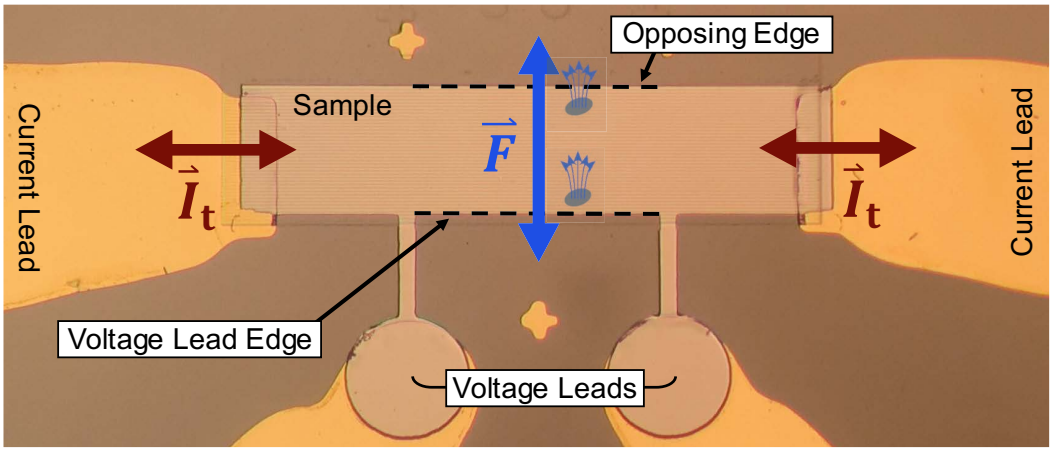

Figure 2.15: A schematic depicting the details of vortex motion during a typical CVC measurement. A current (red) is driven in either direction between the current leads which generates a transverse force on the vortices (blue), driving them over one of the sample edges (dashed lines) with each one generating a voltage pulse as it exits the sample.

Representative CVC measurements performed on the symmetrically-modulated sample (Al060315d) at a constant temperature of $0.9T_c$ and at various applied fields are shown in Figure 2.16. These CVC measurements were performed by gradually increasing the amplitude of a 100 Hz single-sided square wave current while simultaneously measuring the voltage response with an SR830 lock-in amplifier that was locked to the 100 Hz current driving frequency. This waveform of I_t was chosen because an AC lock-in technique can be used to drastically reduce the noise of an inherently DC measurement while additionally filtering out any DC offsets that may be present in these measurements. Here, we define negative values of I_t to correspond to vortices that are driven over the voltage-lead-side edge of the sample while positive values of I_t correspond to driving vortices over the opposing edge (see Figure 2.15). Note that the previously discussed matching effects are observed in these CVC measurements depicted in Figure 2.16 near $H_a \approx 11.0\,\mathrm{G}$ and $H_a \approx 23.5\,\mathrm{G}$ as the constriction of the CVC curves.

The CVC measurements shown in Figure 2.16 reveal the details of vortex motion across a modulated film. For small values of I_t, the vortices within the sample are pinned and form a flat-topped vortex dome in the interior of the sample for moderate applied fields which is deformed by I_t. Recall from Chapter 1 that an applied current pushes and distorts the vortex dome towards the sample edge opposing vortex nucleation.[68] As the current is increased, new vortices

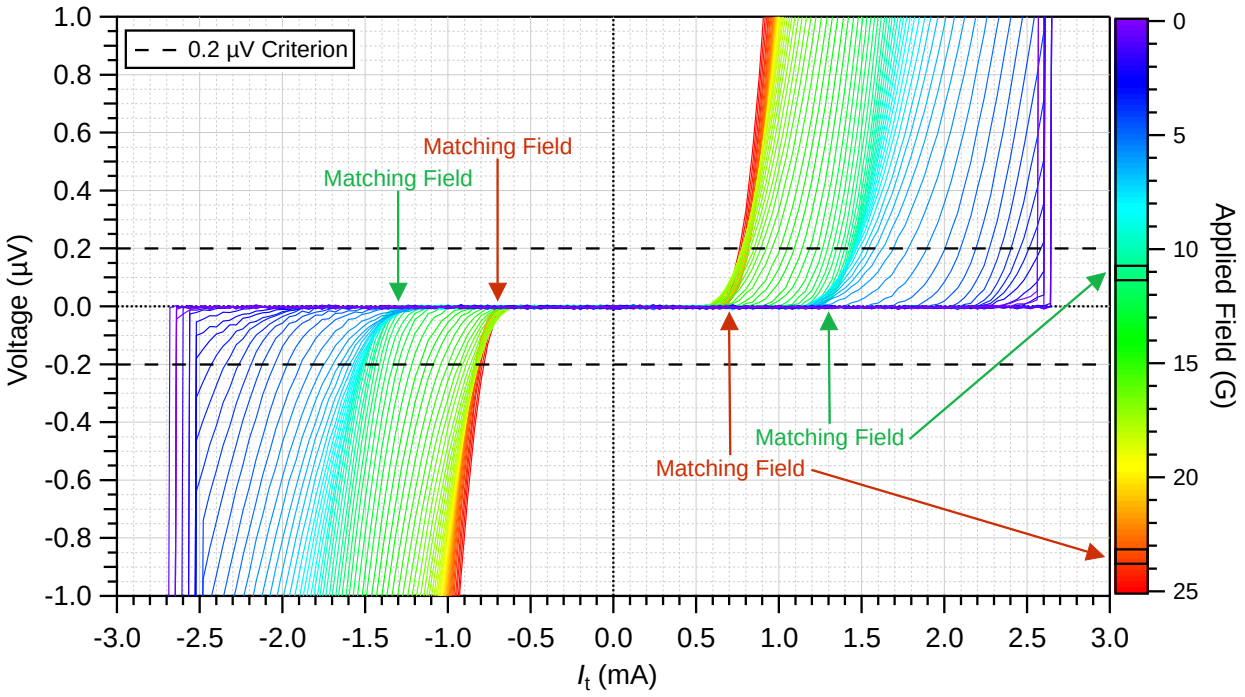

Figure 2.16: Typical current-voltage characteristics (CVC) for a modulated granular aluminum sample at various applied fields at $T = 0.9T_c = 1.719\,\mathrm{K}$. The current amplitude is gradually increased while recording the voltage at each applied magnetic field (rainbow colors). A 0.2 μV criterion was used to determine the critical currents. Matching effects are also observed near $H_a \approx 11.0\,\mathrm{G}$ and $H_a \approx 23.5\,\mathrm{G}$ (indicated).

begin to nucleate into the sample and contribute to the vortex dome which is further skewed by the increased current. As the applied current continues to increase beyond the *critical depinning current* I_c one of the vortex dome edges overlaps with a sample edge and vortices begin to flow across the sample with each vortex generating a voltage pulse as it is exits. Here, I_c is experimentally defined as the current required to elicit a *criterion voltage* of 0.2 μV between the voltage leads; this criterion voltage corresponds to the average voltage of $\sim 10^7$ vortices/s flowing across the sample and is represented by the black dashed lines in Figure 2.16. The vortices within the film are now in the *flux-flow regime* where vortices continue to flow across the superconductor and larger voltages are measured for correspondingly larger I_t. At very large I_t, the voltage response suddenly jumps, which is only observed in Figure 2.16 at very low fields (purple CVC curves) and is a result of the dynamic vortices entering the Larkin-Ovchinnikov (LO) phase where a runaway effect causes an immediate transition into the normal state.[114,115] This runaway effect is qualitatively described as a positive feedback between the reduced core size

of faster moving vortices causing a reduction in the effective drag that the vortices experience within the superconductor, which in turn causes an in increase the vortex velocity. The applied driving current that is required to cause this effect is less than the large depinning critical currents at low applied fields, so vortices immediately enter the LO phase when the depinning current is reached at these low fields.

While there are numerous details of vortex motion that are represented in Figure 2.16, the vortex rectification effects that we seek to study are best shown by plotting the critical depinning currents at each applied field. The previously described CVC measurements were repeated

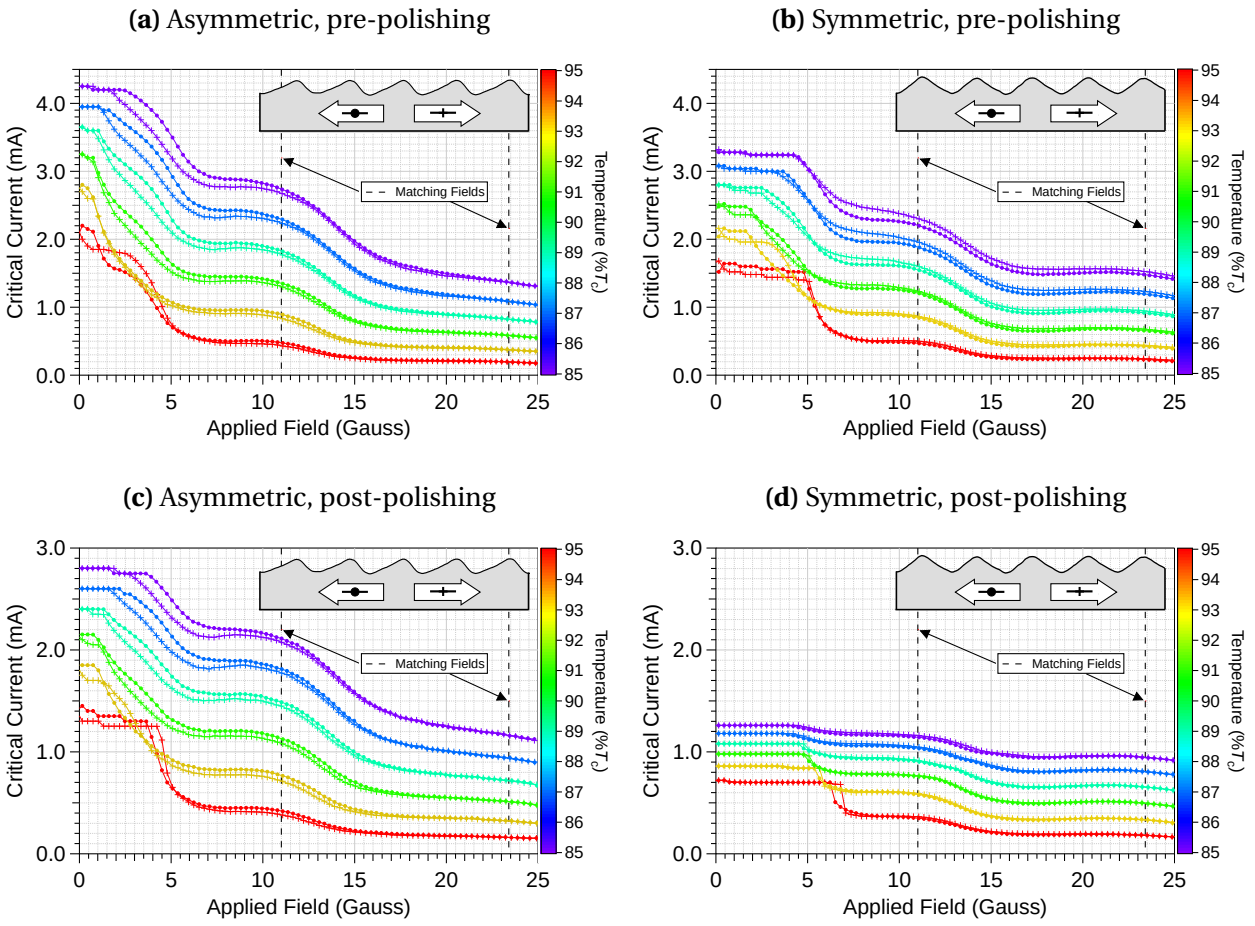

Figure 2.17: Transport curves obtained by using a 0.2 μV criterion for the un-polished **(a)** asymmetrically and **(b)** symmetrically modulated samples. Transport measurements were repeated after polishing the sample surfaces for 3 hours at 40 W in an RF argon plasma for the **(c)** asymmetric and **(d)** symmetric samples.

on both the asymmetrically (Al060315c) and symmetrically (Al060315d) modulated samples at various temperatures in the range of $0.75T_c < T < 0.98T_c$ and at various applied magnetic fields in the range of $0\,\mathrm{G} < H_a < 25\,\mathrm{G}$. The critical depinning currents that were required to achieve the $0.2\,\mu\mathrm{V}$ criterion voltage response in each direction at each applied field and at several temperatures are shown in Figures 2.17a and 2.17b for both the asymmetric and symmetric samples. Unsurprisingly, the previously observed matching effects in the CVC measurements also appear in the critical currents shown in Figure 2.17 as several local maxima where vortices are strongly pinned near the same applied fields because both samples have a $\sim 3\,\mu\mathrm{m}$ pitch thickness modulation.

The details pertaining to this representation of the critical currents are as follows. For simplicity and transparency, we define I_{c+} as the critical current for leftward moving vortices and I_{c-} as the critical currents for rightward moving vortices in the insets of Figure 2.17. In the low field region (less than $2 \sim 5\,\mathrm{G}$), larger values of I_c are required to observe the criterion voltage and low-field plateaus are observed in the critical currents. These plateaus are a result of the large critical currents causing vortices to immediately enter the LO regime since this transition occurs near the same current for a given film at a constant temperature. Therefore, these low-field measurements display the physics pertaining to the LO regime which is different from the flux flow rectification effects that we seek to study. As the field is increased, the I_t that is required to elicit the $0.2\,\mu\mathrm{V}$ criterion is now less than the current that is required to caused the vortices to enter the LO regime. These critical currents at moderate and large fields now correspond to the criterion voltages from vortices in the flux flow regime and therefore are a measurement of the rectification within these samples.

2.3.3 Discussion of Results

The rightward and leftward driving directions measured in Figure 2.17 and schematically represented in Figure 2.15 can be compared to determine the resulting rectification characteristics of the samples. For example, consider an unmodulated sample with a symmetric vortex

potential. In this case, the measured values of I_{c+} and I_{c-} corresponding to vortices exiting over each sample edge at a constant field and temperature should be identical. If, however, an asymmetry exists in the sample, such as an asymmetry in the sample edges or by a thickness modulation such as in the asymmetric sample, then these critical currents will exhibit an *irreversibility* or *rectification* in these vortex transport measurements, indicated as an inequality between I_{c+} and I_{c-}.

The initial transport measurements of the asymmetrically-modulated sample (Al060315c) shown in Figure 2.17a shows a mild asymmetry for applied fields less than ~ 11 G. As was previously noted, the rectification of a sample is determined by the inequality between I_{c+} and I_{c-}, which we will discuss via the deviation from unity in the ratio of these critical currents I_{c+}/I_{c-}. As an initial hypothesis, we expected that the observed I_{c+}/I_{c-} ratio would be similar to the ratio of the leftward and rightward slopes in the thickness modulations (and therefore in the washboard potential) since the force (and therefore current) that is required to move vortices in each direction should be proportional to the potential slopes. However, we observed a maximum ratio of $I_{c+}/I_{c-} \approx 1.1$ for the asymmetric sample, which is not at all similar to the ratio of the slopes in each direction within the asymmetric modulation of ~ 2.4, as determined by Equation 2.5 (see S27 fabrication parameters in Figure 2.12) and verified by the previously discussed profilometry shown Figure 2.13b. This marginal observed rectification at applied fields less than ~ 11 G did, however, correctly coincide with the "easy" and "hard" directions in the thickness modulation since the measurements of I_{c+} (represented by the filled circles in Figure 2.17a) corresponding to vortices moving over the steeper slopes were larger than the measurements of I_{c-} (represented by the crosses) corresponding to vortices moving over the shallower slopes.

The corresponding measurements of the symmetrically-modulated sample (Al060315d) contradicted our expectations. The predicted rectification ratio in the thickness modulation slopes as calculated by Equation 2.5 (see S28 fabrication parameters in Figure 2.12) is extremely close to 1. However, the critical current measurements shown in Figure 2.17b show that this symmetrically-modulated sample exhibits rectification that is similar to the asymmetrically-

modulated sample. Additionally, the direction of the rectification was opposite to the asymmetric sample in that I_{c+} was smaller than I_{c-}. This indicates that there are other contributions to the vortex potential beyond the thickness modulation of the film that are influencing the rectification of the sample and are therefore obscuring the effects of the thickness modulation.

2.3.4 Surface Roughness and Edge Effects

We believe that possible causes of the discrepancy in the transport measurements that were discussed in the previous section shown in Figures 2.17a and 2.17b are due to a combination of the sample edges and/or surface granularity. Since the edge wet-etch lithographic mask was aligned manually with a light mask positioned in the light path of a standard optical microscope, an exact edge placement with respect to the thickness modulation was initially difficult. Therefore, the edges of films that were tested previous to the asymmetric and symmetric samples (Al060315c and d) were defined at different thicknesses, which could influence the vortex nucleation environment and therefore contribute to the rectification in CVC measurements. However, great care was taken to define the sample edges at similar locations in the thickness modulations of Al060315c and d so that the opposing sample edges are nominally identical. This presumably mitigates any rectification that would arise from a variation in the two edges of the samples. Recall that Figure 2.13 shows the AFM scans of the both sample edges for both Al060315c and d and indicates comparable edge geometries for both samples. These edge scans also illustrate that there are no appreciable differences in the sample edges that could be the culprit of the discrepancy in the transport measurements.

Another factor that could be masking the surface characteristics of the thickness modulation could be the grain sizes in the samples. Recall that granular aluminum is known to have incredibly small grain boundaries ($\sim 10\,\text{nm}$) which are essentially invisible to vortices of size $\sim 2\xi \approx 348\,\text{nm}$. However, aluminum films that are grown at high angles of incidence may develop a surface roughness[116] that could serve as unforeseen pinning centers. Surface AFM scans of the asymmetrically- and symmetrically-modulated samples are shown in Figures 2.18a and

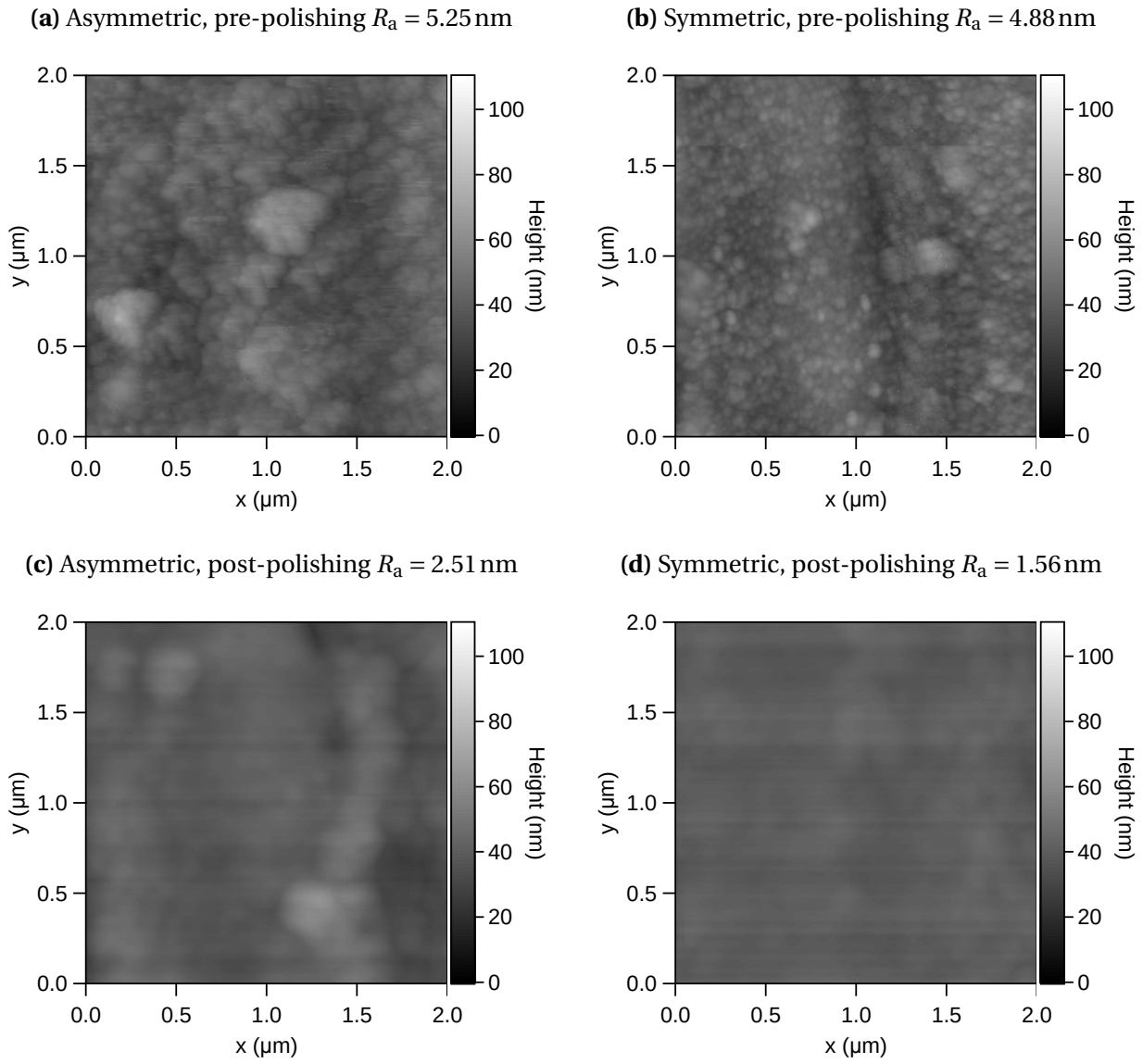

Figure 2.18: Surface AFM scans of the samples pre- **(a)** and **(b)** and post- **(c)** and **(d)** polishing in an RF argon plasma for 3 hours at 40 W.

2.18b which reveal RMS roughness factors R_a of 5.25 nm and 4.88 nm respectively, which are in agreement with the roughness factors that were observed by Leem *et al.* in AZO films that were deposited at similar angles.[116] Note that the RMS roughness factor is not a measurement of the grain size. These AFM profilometry measurements reveal surface variations that are ~ 10× the size of the 10 nm grains that were expected in these granular aluminum films.[96,110] There-

fore, the commensurate size-scales between the observed surface roughness and the vortex size within these films could plausibly influence vortex motion.

In order to test the hypothesis that artificial sample grains caused by the oblique sample deposition angle were responsible for the unexpected transport results, the sample surfaces were ion-polished to make them smoother. This was accomplished by placing the samples in the presence of an RF argon plasma at 40 W for 3 hours. The resulting AFM scans of the sample surfaces after plasma polishing both samples are shown in Figures 2.18c and 2.18d and reveal reduced R_a values of 2.51 nm and 1.56 nm respectively and indicates that the roughness was more than halved for both samples. The critical temperature transitions of the asymmetric and symmetric samples were re-measured; the results are shown in Table 2.1 and in Figure 2.14 as the solid curves. These T_c measurements indicate that the polishing had minimal or no affect on the superconducting properties of the samples since the observed changes are commensurate with the changes observed in previous films. These previously observed changes are believed to be a result of increased sample oxidation that slowly occurs over time as the samples are exposed to air.

Once the sample properties were verified, CVC transport measurements were retaken to determine if this polishing and decreased surface roughness affected the critical currents. These re-measured critical currents, shown in Figures 2.17c and 2.17d, were obtained with the same 0.2 μV criterion. The post-polishing measurements show the same qualitative low field behavior as the un-polished measurements, but the zero field I_c is reduced for the asymmetric sample and drastically reduced for the symmetric sample. The matching field effects remain unaffected by the polishing and are clearly portrayed in the transport measurements of both polished samples. Additionally, the post-polishing measurements of the symmetric sample shown in Figure 2.17d indicates that the rectification shown Figure 2.17b was completely eliminated by the polishing process, which solved one of the mysteries presented in the un-polished measurements. We hypothesize that the initial surface roughness of these samples could plausibly contribute to the rectification of the samples since the large evaporation angles could cause

asymmetrically shaped roughness features. In contrast, the newly measured critical current rectification for the asymmetric sample shown in Figure 2.17c remains unaffected when compared to the pre-polishing measurements in Figure 2.17a. This indicates that the rectification that was observed with the asymmetric sample was caused by the asymmetric thickness modulation, although this rectification was not as large as expected which suggests that another source of vortex pinning was obscuring the surface asymmetry in this sample.

2.4 Conclusions

In conclusion, we explored the rectification effects of thickness modulations on vortex motion by cryogenically measuring superconducting granular aluminum films which were fabricated by sputtering granular aluminum on modulated glass substrates at large angles. The large deposition angles caused an unforeseen surface roughness that plausibly contributed to the potential that the vortices experienced, which induced rectification in the symmetrically thickness-modulated sample. This unexpected rectification was completely eliminated by reducing the surface roughness via smoothing the sample with Ar^+ ion impingement. Additionally, the rectification exhibited by the asymmetrically modulated sample remained unaffected by this smoothing process. However, this rectification that was observed in the asymmetric sample was much less than what we expected by considering the force on the vortex line-length resulting from the slopes of the asymmetric thickness modulation. This indicates that another contribution to the vortex potential landscape could still be obscuring the rectification effects within these samples. We therefore postulate that the film edges may affect these measurements in a more subtle manner than we initially hypothesized, despite the films possessing similar edge geometries. Even commensurate and symmetric film edges could obscure surface effects if vortex nucleation over these edges dominates the vortex motion within these films. In order to address this question, the effects of the edges in granular aluminum films will be explored in more detail in the next Chapter to determine if and to what extent the edges affect rectification.

Chapter 3

Edge Barriers to Vortex Nucleation in Granular Aluminum

Considering the effect of the sample edges is crucial in order to fully understand the various methods of realizing vortex ratchets for applications in fluxonic devices.[28,30,117] Vortex ratchets that influence the surface pinning environment can be achieved by inducing artificial pinning centers with magnetic and hole arrays,[19,90] magnetic pinning potentials,[17,56–58,89] or by modulating the sample thickness.[21,24,92,93] Chapter 2 explored the effects of thickness modulations in granular aluminum superconductors on vortex transport properties to determine if rectification can be realized in this way. It became apparent from the measurements of the thickness-modulated films and from other experimental[59–62] and theoretical[63–85] studies that the sample edges may also significantly contribute to the overall rectification in flux flow within these samples. Therefore, we aim to study and explore the effects of the film edges to determine if unique edge geometries can also be exploited to fabricate high quality vortex ratchets and rectification effects.

Vortex nucleation and dynamics are influenced by the existence of the sample edges. As was previously discussed in Chapter 1, the edges of superconducting films impose an *edge energy barrier* which prevents vortices from readily nucleating into superconducting samples. Theoretical descriptions of vortex nucleation and penetration describe the energy barrier for vortex entry as a consequence of two distinct phenomena: the Bean-Livingston barrier (BLB) and the geometric barrier (GB).[63,65–68,70–74,76,77,79–81,85] The BLB is an expulsive barrier that results from the attraction between a penetrating vortex to an image antivortex outside of the sample that is required to produce vortex currents near the sample edge that satisfy the zero-normal-current boundary condition at the surface of the superconductor.[86] Several experiments have been performed to probe the effect of the sample edges on vortex nucleation by perturbing the

BLB such as by creating pinning centers via irradiating[118–120] patterning,[60] or removing[96] the sample edges. While the BLB can never be totally suppressed as long as the sample edges exist, these studies indeed show a reduction in the BLB contribution to edge barrier.

The BLB is distinct from the GB, which is an expulsive barrier that is created by the non-elliptical shape of a superconductor[84] and can also influence the asymmetry in the vortex motion within a superconducting film. This GB arises from a force that pushes vortices out of the sample that is caused by the vortex line-length increase as the vortex nucleates into a superconducting film.[84] Recall from Chapters 1 and 2 that longer vortices have more energy than shorter vortices and so there is an energy penalty associated with the line-length increase of a vortex. For a sample with an elliptical cross-section, the expulsive force of the GB on a vortex is exactly balanced against the inward force from the Meissner surface currents that tend to push the vortex towards the interior of the sample, indicating that the edge barrier is solely caused by the BLB.[84] Sabatino *et al.*[62] have explored the GB in a thin Nb sample with wedged edges of differing slopes on both sides and observed rectification in the voltage response in the transport measurements of this sample. However, they observed no rectification in the μV criterion critical currents corresponding to the onset of flux flow across the sample, indicating that the wedged edges affected flux flow but did not affect the vortex nucleation into this sample.[62] The GB has also received experimental and theoretical attention in the high critical temperature superconductor arena[61,76,85] since vortex pinning is crucial to the performance and quality of these materials. The GB was found to be eliminated in samples with a thickness variation over the entire sample width that resulted in a prism sample geometry.[61] These superconductors exhibit fully reversible magnetization further showcasing the importance of the sample edge geometry.[61]

The shape of the sample edges can drastically alter the conditions for vortex nucleation by directly influencing the geometry of the vortex line-length within the edges. To better understand this, we studied the details of vortex nucleation over a squared and tapered edge geometry in an externally applied field with simulations using FREEFEM, which is a program that is

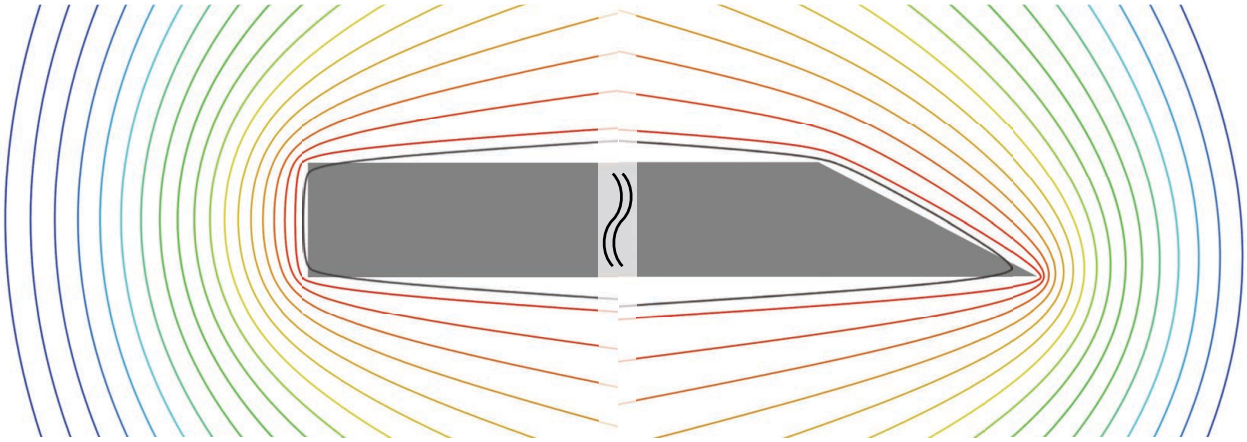

Figure 3.1: FREEFEM simulations of the expulsion of an applied field (colored for clarity) from a superconducting film (grey) with squared and tapered edges and with a thickness d and width w such that $d \ll w$. A nascent vortex is depicted as the penetrating field line (black). The middle region of the film has been omitted so that the details near the film edges can be represented more clearly.

used to solve partial differential equations via a finite element method and is ideal for modeling the vector potential solutions to the London equation near a superconductor. Figure 3.1 depicts these simulations which were performed on a superconducting film of thickness d and of width w where $d \ll w$ and are two-dimensional results of how the field would penetrate a superconducting strip, but presumably, vortex penetration behaves similarly. As a vortex enters over the squared edge, the magnetic flux penetrates each corner of the squared edges which splits the nascent vortex into two halves.[70,71,76,88] The two halves of the vortex increase in line-length as the vortex continues to enter into the sample until both halves of the vortex meet at the center of the thickness of the sample.[70,71,76,88] The vortex is then pushed towards the interior of the superconductor by the Lorentz force from the screening currents in the sample edges. Recall from Chapter 1 that this results in a large energy barrier to vortex entry since the line-length increase of the bifurcated vortex during nucleation is rapidly increasing as each vortex half contributes to the total line-length of the vortex. In contrast, a vortex nucleating over the tapered edge in Figure 3.1 only penetrates the superconductor once and does not bifurcate since this taper geometry effectively presents one "corner" in the knife-edge that the field must overcome. Therefore the line-length increase experienced by the vortex in this case is simply equivalent to the slope of the taper and the resulting GB is reduced when compared to the squared edge case.

The effects of the geometric barrier in superconducting films were tested in this work by studying the effects of several taper lengths on vortex transport measurements. As we previously noted in Chapter 2, granular aluminum is once again used to study the effects of the sample edges for the attractive and tunable critical temperature and because granular aluminum is a low-pinning material. Recall that vortices are not necessarily mobile in a generic superconductor since any number of material properties or inclusions can trap or *pin* vortices within the sample. Therefore, using a superconducting material with inherently low pinning is required so that the edge effects of interest are not obscured or convoluted by the inherent pinning of the material.

There are various methods of fabricating a tapered edge in superconducting films, such as taking advantage of lift-off undercut geometries during sample growth.[62] In this work, we created tapered samples possessing tapered edges on one side with a common, reference edge on the opposing side to study and compare the effects of various taper geometries on vortex motion referenced to the common edge. The tapered edges were fabricated by employing greyscale lithographic techniques to create tapered structures in photoresist; these structures were then transferred into a granular aluminum film via ion bombardment. This fabrication technique allows for the control and tunability of the slope in the tapered edges and in the lengths of the tapers. We hypothesize that longer tapers will result in lower critical currents since longer taper geometries more closely emulate prism geometries,[61,76] which are theorized to eliminate the GB.[61,76,84]

3.1 Tapered Sample Fabrication

The process of fabricating a superconducting film with tapered edges requires numerous lithographic steps and careful preparation. In general, a photolithographic lift-off process that was previously described in Chapter 2 was implemented to pattern an oxide-coated silicon substrate with gold measurement contacts followed by granular aluminum films in an 8- or 14-lead multi-probe geometry, shown in Figures 3.2a and 3.2b respectively. Silicon wafers with a

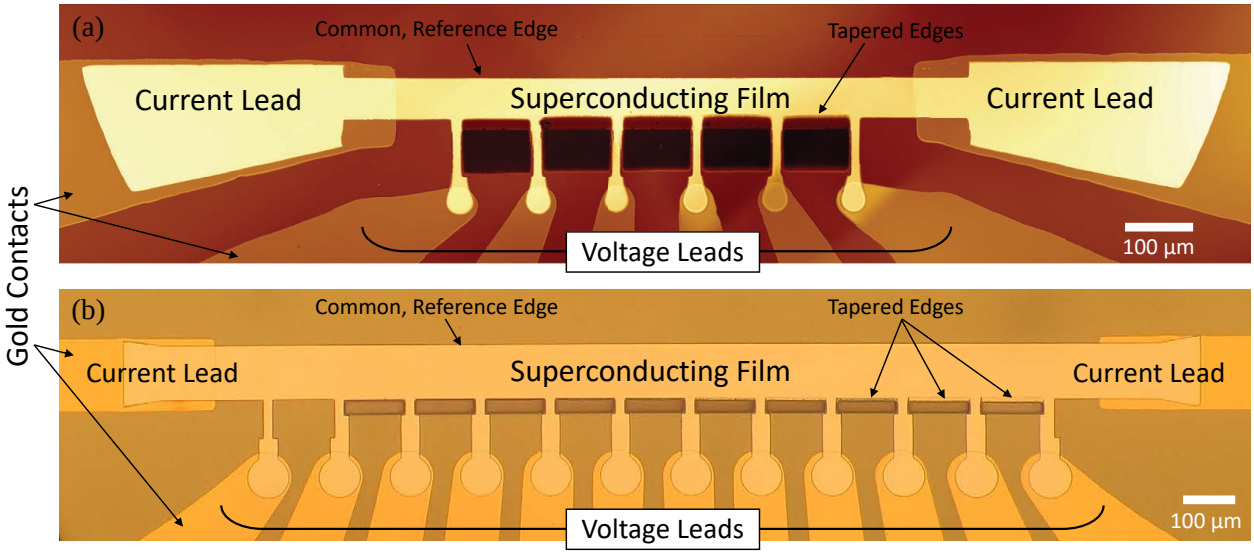

Figure 3.2: (a) A white light interferometric image of a granular aluminum film with tapered edges in an 8-probe geometry. **(b)** An optical image of a granular aluminum film with tapered edges in an 14-probe geometry. Both films were grown on the surface of a silicon substrate with an insulating oxide coating on top of gold current and voltage leads.

200 nm – 300 nm thick insulating oxide coating were chosen as the substrate material because these wafers can be easily obtained, are electrically insulating on the surface, and retain the good thermal conductivity of standard silicon materials.* Each adjacent pair of voltage leads defines a *sample segment* that can be measured with a standard 4-probe technique. These multi-probe sample segments are therefore measured in a similar manner to the 4-probe samples that were discussed in Chapter 2 in that an AC current is applied between the current leads while simultaneously measuring the voltage response between any two adjacent voltage leads. Typical tapered-edge granular aluminum films were designed to be 120 µm long between adjacent pairs of voltage leads, ~ 60 µm wide between opposing film edges, and were grown to be ~ 0.5 µm thick with the Magnetron sputter system that was described in Chapter 2.

The multi-probe geometries, depicted in Figure 3.2, were chosen so that the effects from numerous taper geometries could be simultaneously measured and then compared to a common, vertical reference edge that is shared by all segments. Additionally, the superconducting prop-

*We will see that fabricating a tapered superconducting sample on thermally conductive substrates is a vital detail in the fabrication process since the samples must be cooled during an ion milling step.

erties (such as the critical temperature, coherence length, penetration depth, and the normal state resistivity) that belong to a multi-segment sample are expected to be uniform across each sample segment since each segment belongs to the same film. This ensured that the artificial edge geometries were the only difference between each segment and therefore any difference that was observed in the measurements of these segments were caused by the differences in the edges.

3.1.1 Greyscale Lithography

The fabrication of tapered edges in superconducting films requires the use of a greyscale lithographic technique in which photoresist is partly exposed to produce multilevel resist structures. When used in standard binary lithographic applications, S1800 series resists are fully exposed at a *clear dose* of 82 mJ cm^{-2}.[105] However, the exposure curve for S1800 series resists,[105] shown in Figure 3.3a along with calibrations of the optical microscope that was used to expose substrates (represented with the yellow data), indicates that partial exposures of the resist within a certain exposure range will yield remaining resist thicknesses (after development) that depends on the partial exposure dose. For example, if an S1800 series resist is exposed with a dose of $\sim 62\,\mathrm{mJ\,cm^{-2}}$, then Figure 3.3a indicates that roughly 30 % of the original resist thickness will remain after the partly exposed resist is developed. Therefore, if the exposure dose is properly varied over a sample surface, then a linear variation in the resist thickness, or a taper, can be fabricated in these resists.

In order to expose high quality tapers in S1800 series photoresist, several lithographic details that are usually inconsequential to binary lithography must be accounted for and optimized. One such detail that must be properly managed is the initial resist thickness plateau for low exposure doses, or the *resist bias*, that is observed in the data sheet exposure curve and in the microscope calibrations shown in Figure 3.3a. This plateau indicates that there is a minimum exposure dose, called a *bias exposure*, that is required to cause a change in the thickness of the resist. According to the exposure curve in Figure 3.3a, S1800 series resists require a minimum

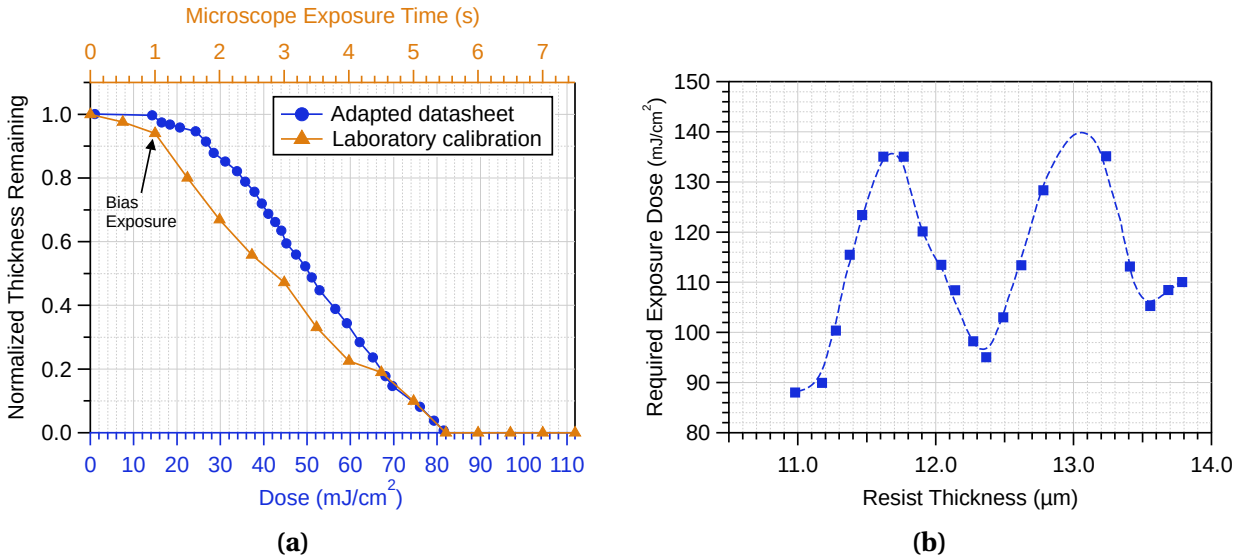

Figure 3.3: **(a)** The normalized remaining thickness of S1800 series resist for a given exposure dose adapted from the S1800 series data sheet (blue) and from an exposure calibration of the optical microscope (orange). **(b)** The exposure dose variation resulting from interference effects in the thickness of the resist also adapted from the Shipley S1800 series datasheet.[105]

bias dose of 14 mJ cm^{-2} (corresponding to a 1 s microscope exposure) to begin exposing the resist. This exposure bias is an important property to characterize and compensate for when exposing taper structures in the resist because exposures that neglect the bias properties of the resist will produce tapers that are systematically shorter in length (and therefore steeper in slope) since the top of the tapers will not be properly exposed. Therefore, a bias exposure must be performed so that accurate taper lengths can be reliably exposed in the resist.

Another property of S1800 series photoresists that hinders the quality of multilevel features is the existence of interference fringes within the resist during exposure. These resists are sensitive to 405 nm light which easily forms standing waves in a resist layer and therefore creates a variation in the exposure dose that depends on the resist thickness* as shown in Figure 3.3b. Normally, these exposure variations are not detrimental to the quality of binary exposures. However, in greyscale lithography, these standing waves hinder the fabrication of smooth tapers as they cause post-development thickness variations that are superimposed on the taper

*The resist thickness is dependent on the spin speed (see Chapter 2). The thickness of the resist that was used to fabricate tapered structures in this work is on order of ~ 0.5 µm.

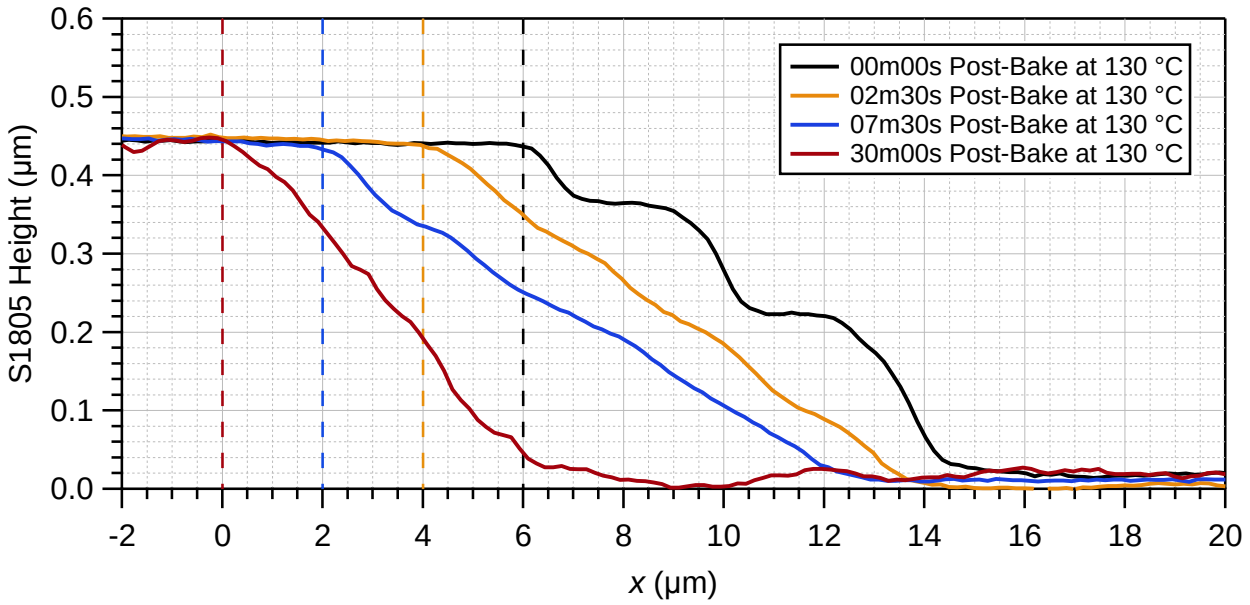

Figure 3.4: The effect of various post-bake times on the profile of a resist taper. The post-bake was performed at 130 °C immediately after exposure and before development. The colored dashed lines represent the beginning of the corresponding resist tapers. These resist profiles were arbitrarily horizontally offset from one another by 2 µm for clarity.

slope which creates "steps" in the resist taper as shown in the profilometry scan represented by the black curve in Figure 3.4. When the photoresist is exposed with ultraviolet light, a chemical reaction occurs that produces indene carboxylic acid which increases the dissolution rate in the resist developer.[121] The concentration of this acid within the resist is therefore higher where standing waves artificially increase the exposure and lower where the standing wave nodes lower the exposure. Post-baking the resist after exposing but before developing allows the indene carboxylic acid to isotropically diffuse within the resist layer, smoothing out the effects of the standing waves.[121] Therefore, the greyscale-exposed resist was post-baked on a 130 °C hotplate for 2–30 minutes before development in order to reduce the amplitude of this modulation.[122] Figure 3.4 also shows profilometry scans of resist tapers which were post-baked in this way to smooth the tapers. While this post-bake definitely improved the taper quality, it did not completely eliminate the interference effects since remnant steps can still be observed in the post-baked resist profiles.

We also found that uniformity in the resist thickness is paramount in achieving successful greyscale structures in the resist. Photoresist that is spun on a substrate with pre-patterned features (such as pre-defined contacts or films) will have large variations in the resist thickness near the edges of the pre-existing features due to the similarity in thicknesses between the resist and the pre-patterned structures. This thickness variation makes greyscale lithography in the area near the edges of the structures nearly impossible due to the previously discussed dependance of the exposure dose on resist thickness. In order to promote resist uniformity and to achieve successful and repeatable greyscale tapers in the photoresist, it was vital to either spin photoresist on top of flat and uniform sample sheets or to lift-off large pre-patterned structures so that tapers could be safely exposed away from pre-patterned edges where the resist profile was likely nonuniform. The final desired sample geometry can then be defined by wet-etching away any unwanted material after the tapers have been properly transferred into the sample.

Additionally, the thickness of the photoresist is a critical parameter to consider before tapering a superconducting sample. The slope of the taper in the resist determines the slope of the taper in the sample edges which we hypothesize directly influences the nucleation energy barrier to vortex entry. Thicker resists will yield steeper slopes in the sample edges than thinner resists for tapers with comparable lengths indicating that thinner resists will provide a wider range of accessible taper slopes. However, the resist must also be thick enough to protect the bulk of the film when transferring the taper from the resist into the sample edges. The resist that was used to taper the samples presented here was Shipley S1805 photoresist that was spun at 3000 rpm – 4500 rpm which yielded a 0.5 µm thick resist layer. This resist thickness is comparable to the desired sample thickness and therefore ensured that the slopes of the tapers that were fabricated in the S1805 resist would be comparable to the slopes of the tapers in the sample edges, while also adequately protecting the sample when transferring the resist taper into the edges of the film.

While there are numerous details to consider and pitfalls to avoid when performing greyscale lithography, the mechanisms to vary an exposure dose across the surface of a sub-

strate must also be characterized. Therefore, two greyscale exposure methods were developed to perform the previously described greyscale lithography. The first method varied the exposure dose by moving a light mask in the light path of an optical microscope and the second method utilized a direct write maskless laser system to expose the substrate with varying laser intensities. The details of both greyscale exposure techniques are discussed in further detail in the following sections.

3.1.2 Exposure Method I: "Dynamic" Optical Lithography

An attractive method of varying the exposure dose incident on a layer of photoresist is to use dynamic optical lithography by *moving* a mask during an exposure to gradually increase the amount of light incident on the substrate surface. A schematic of the dynamic lithographic process used to fabricate tapers in photoresist layers is shown in Figure 3.5. The area to be tapered is gradually exposed as a mask is moved above the substrate such that the left edge of the mask (green bar) begins at point "A" which defines the knife-edge of the taper where the resist is fully exposed and ends at point "B" which defines top of the taper where the resist has had no exposure. This method is controllable and smoothly varies the intensity of light which produces smooth tapers in the photoresist.

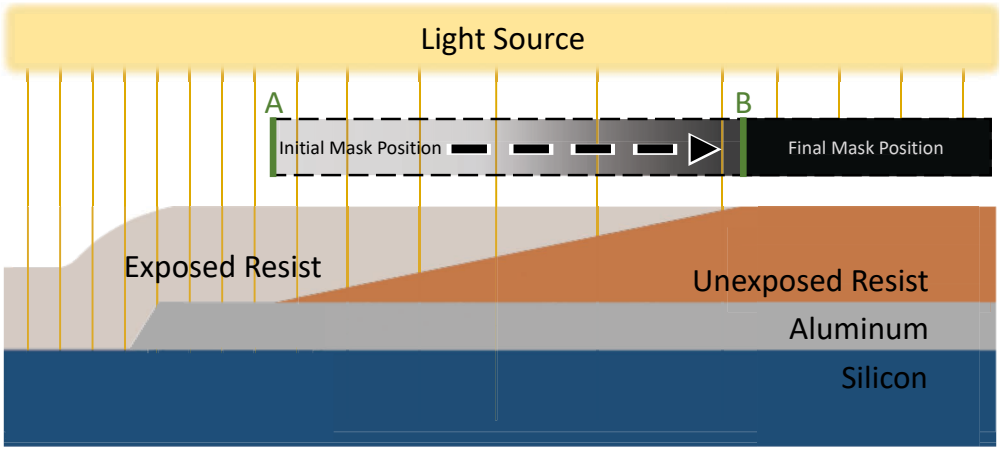

Figure 3.5: A schematic of dynamic optical lithography. The left edge of a light mask (green line) begins at position "A" and is moved to the right to position "B". This varies the intensity of light (represented by the density of light beams) along the resist (orange) spun on top of the aluminum film (grey) which creates a taper in the resist after development.

Several modifications to a Nikon Optiphot 66 optical microscope, shown in Figure 3.6, were required in order to controllably and repeatably move a light mask. For binary lithographic applications, a mask that was fabricated via standard monochrome film photography is rigidly placed in the light-path of the microscope and is projected onto the substrate surface with an objective lens. Dynamic lithography was performed by modifying this binary exposure method with the addition of a 3-axis micro-stage positioner that was driven by several Arduino-

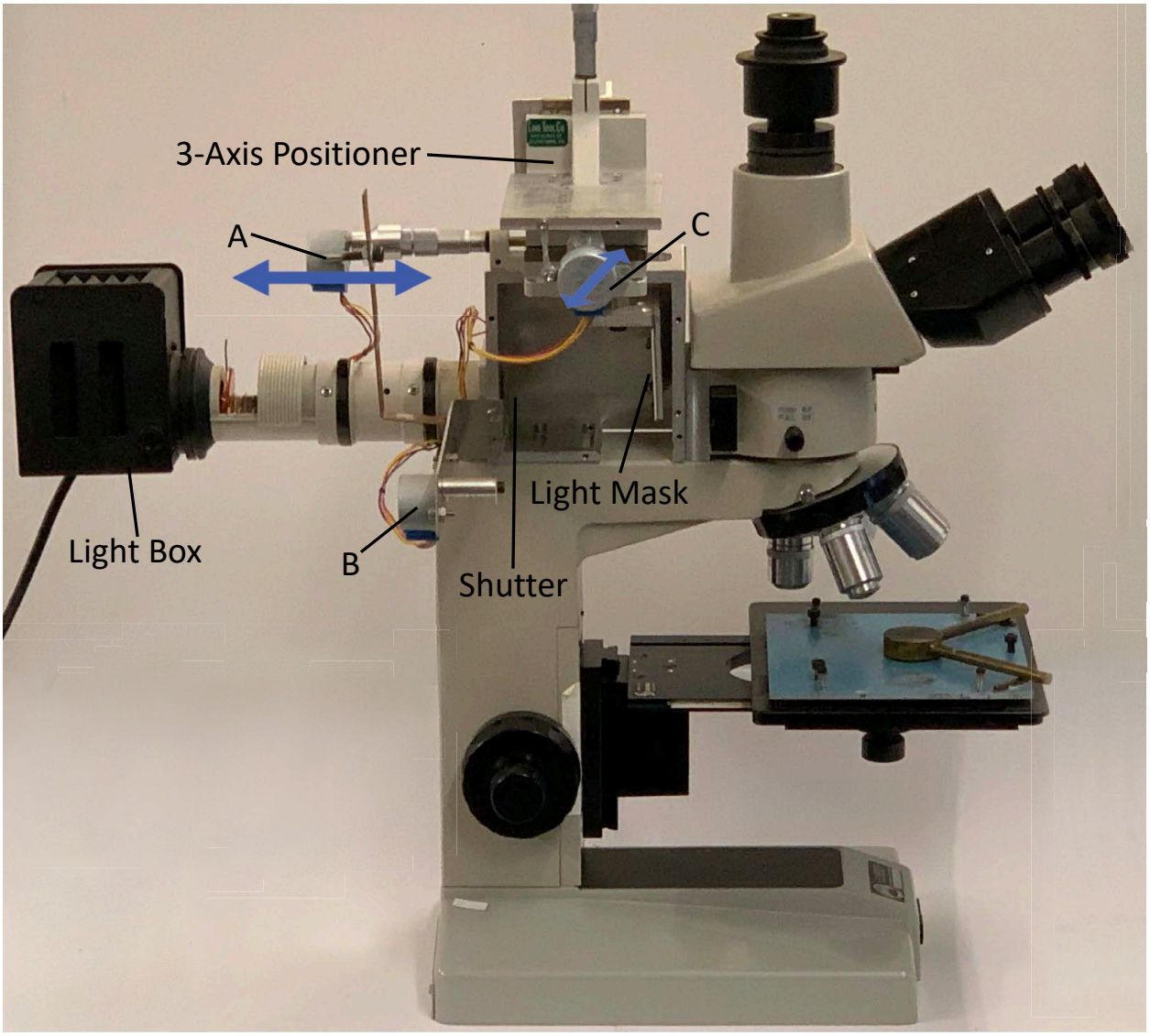

Figure 3.6: The modified Nikon Optiphot 66 microscope that was used to perform dynamic optical lithography to fabricate tapers in photoresist. Motor **A** controls the pattern defocus corresponding to left and right movement, motor **B** controls the shutter, and motor **C** controls the motion of the light mask during the tapering process corresponding to motion that is either into or out of the page.

controlled stepper motors. Two stepper motors were mounted to the micrometers of the positioner stages that controlled the mask motion along with a third stepper motor that controlled an amber filter shutter as indicated in Figure 3.6. The motor labelled **A** controls the forward and reverse motion of the light mask which controls the defocus of the pattern that is projected onto the substrate surface. This defocus step is crucial since the focal plane of the ultraviolet light that will expose the resist is in a different plane than the focal plane of white light that is used to align and focus the light mask. Exposures that are performed without a defocus will be exposed with an incorrect focal plane which will result in a blurred exposure. The motor labelled **B** controls the shutter, enabling an accurate exposure time which in turn reliably exposes the resist with the correct dose. This accuracy in the exposure time is also vital since over- or under-exposing tapered structures will result incorrect taper lengths (and slopes). Finally, the motor labeled **C** is used to align the mask horizontally, but also controls the speed that the mask travels when partly exposing tapers in the photoresist. This motor is responsible for fabricating the tapers and its speed and driving distance determine the length of the resulting taper for optimized defocus and exposure dose parameters.

Dynamic lithography was performed with the modified optical microscope to expose repeatable and controllable tapers in photoresist. Several tapers of varying lengths, shown in the profilometry scans in Figure 3.7a, were created in S1805 resist and were used to calibrate the relationship between the mask travel distance and the resulting taper length as was determined from the most linear region of each taper. These tapers were created by first spinning S1805 photoresist on a silicon substrate that was uniformly coated with granular aluminum which promoted uniformity in the resist thickness as was previously discussed. Then, the tapers were exposed in the resist by aligning and defocusing the light mask on the substrate surface and then opening the amber shutter. Stepper motor **C** then smoothly moved the light mask across the surface of the photoresist to vary the exposure dose along the tapers. In order to correct for the bias exposure, the mask must be moved further than the desired taper length to artificially increase the exposure in the desired taper region. This indicates that the calibration shown

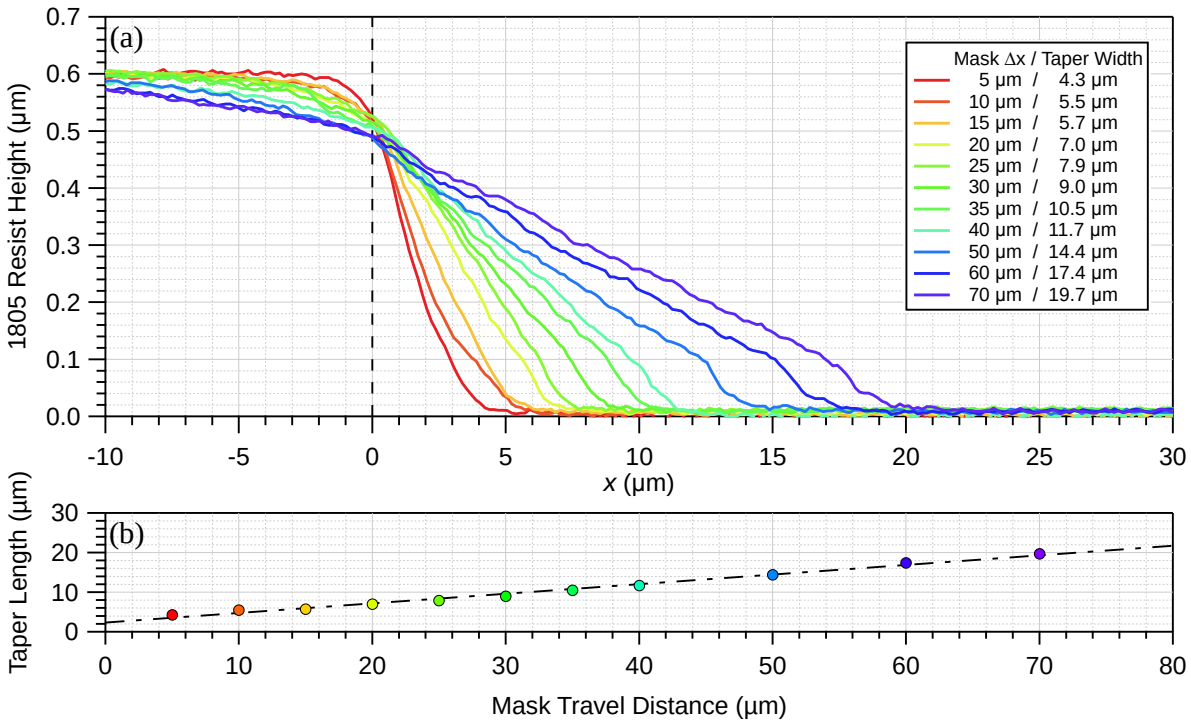

Figure 3.7: **(a)** Profilometry scans of tapers with various lengths ranging from 4.3 µm to 19.7 µm fabricated in S1805 resist. The lengths were determined from the most linear regions in the tapers. **(b)** The relationship between the distance that the light mask is moved at the sample surface to the resulting taper length in the photoresist which effectively calibrates the bias exposure.

in Figure 3.7b is, in essence, a calibration of the bias exposure. The shutter was then closed once the dynamic exposure was completed which was followed by post-baking the exposed photoresist at 130 °C for 3 minutes to reduce the effects of the previously described interference fringes.[122] The resist was next developed in AZ 917 photodeveloper* for 1 minute which resulted in the smooth tapers in the photoresist that are shown in Figure 3.7a. Therefore, this dynamic optical lithographic technique allows for the repeatable and reliable fabrication of a wide range of taper geometries in photoresist layers.

*It is important to note that AZ 917 is a Tetramethylammonium hydroxide (TMAH) based developer and therefore attacks aluminum samples, even when the sample is only marginally overdeveloped.

3.1.3 Exposure Method II: Direct Write Multilevel Laser Lithography

The use of an LW405C maskless laser writer developed by MICROTECH and equipped with a GaN laser provides another method to expose photoresist with greyscale doses. This instrument is capable of 0.5 µm binary lithographic linewidths with a stage spatial resolution of 10 nm relative to the laser position which is made possible by the simultaneous monitoring of an interferometric system along with an optical encoder. Greyscale patterns with a minimum design spatial resolution of 0.2 µm × 0.2 µm are exposed by rastering a 405 nm laser at a nominal frequency of 3200 Hz while modulating the laser power to turn the laser on or off, or to reduce the laser intensity, while the sample is moved beneath the laser. During a line raster, the laser power is modulated at the desired locations in the raster according to a CAD file pattern for binary exposures or according to a multilevel bitmap for greyscale patterns. In this way, a greyscale pattern may be exposed without the need of a mask.

The various lithographic parameters of the laser writer were calibrated so that the laser writer could optimally expose greyscale taper patterns in photoresist. The bias and clear exposure doses of S1805 photoresist were gauged by exposing and developing several features in the resist at varying bitmap grey values between 0 and 255. Here, a grey value of 0 corresponds to 0 % of the desired dose while 255 corresponds to 100 % of the dose. The bias dose was determined by noting the percentages of the desired exposure dose that first caused a thickness change in the photoresist in profilometry scans. Typical bias values ranged between 25 % – 35 % of the clear dose which was near $\sim 180\,\mathrm{mJ\,cm^{-2}}$ as calculated by the laser writer. This clear dose differs quit significantly from the clear dose indicated by the S1800 series data sheet[105] value of $82\,\mathrm{mJ\,cm^{-2}}$ that is shown in Figure 3.3a. However, several factors such as humidity, resist shelf life, spin speed, bake temperature, bake time, and ambient temperature during an exposure as well as the assumptions made by the laser writer software during the dose calculation could affect the reported dose.

Although this instrument appears to be well-suited for greyscale lithography, one unfortunate feature posed an obstacle to exposing high quality taper structures. The computers that

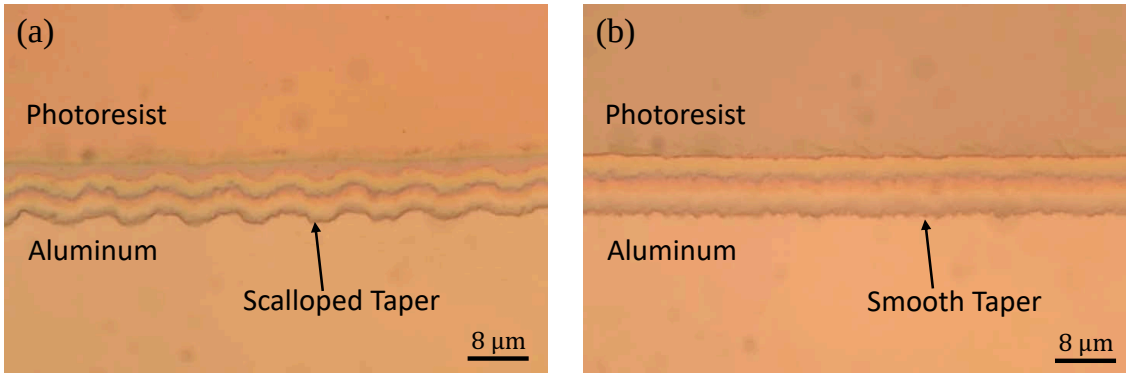

Figure 3.8: Optical images of **(a)** a scalloped and of **(b)** a smooth taper in S1805 photoresist on top of a granular aluminum film. Each taper is ~ 8µm in width and was post-baked before developement as previously described.

control the sample stage periodically pause to read the stage position which causes a minor lag in the stage sweep and resulted in an apparent intermittent lateral scalloping of the resist, shown in Figure 3.8a. This resist scalloping is not detrimental to binary exposures since the exposure variations are on order of 1 %. However, this variation in the exposure results in an extremely problematic scalloping in the knife-edge of the resist tapers as scalloped edge geometries also influence vortex dynamics.[60] Since this readout was impossible to suppress, this scalloping was overcome by exposing the same taper pattern numerous times in the same spot on the sample at lower exposure doses that added up to the correct single-shot clear dose, resulting in the taper shown in Figure 3.8b. The multiple exposures averaged out the effects of the scalloping since the scalloping occurred at random locations in the pattern at each of the exposures.

Multilevel patterns were fabricated in the resist with the laser writer by using the appropriately calibrated bias and clear doses. Several taper calibrations were performed to optimize the taper length which included fine adjustments of the bias and clear doses as well as the post-bake and development times. Similar to the dynamic lithographic process, standing waves still formed interference modulations in the resist tapers. So, tapers that were exposed with the laser writer still required a predevelopment post-bake to reduce the effects from the interference fringes within the resist during the exposure step. By properly characterizing the various

lithographic exposure parameters combined with performing multiple lower dose exposures to mitigate resist scalloping, the laser writer could also be used to reliably create tapers in photoresist layers.

3.1.4 Ion Milling to Transfer Tapers Into the Sample Edges

Once tapers have been fabricated in photoresist, these structures must be transferred into the underlying granular aluminum film in order to create a superconducting sample with tapered edges. One way to transfer multilevel structures from one sample layer into an underlying layer is to dry-etch or mill the surface of the sample via ion bombardment. The way in which argon ion bombardment transfers a taper from a resist layer into a granular aluminum film is depicted in Figure 3.9, where each transparency step represents a different stage in the milling process and is separated by an equal time interval. As argon cations impinge (at ideally normal incidence) on the surface of the layered substrate, a discrete layer of material is etched away within a small time interval. The knife-edge of the resist taper begins to "pull back", revealing previously protected granular aluminum. After another small time interval passes, an additional layer of material is etched away and the taper is partly transferred into the previously protected granular aluminum. This logic that describes this etching geometry can be continued until the sample layer has been milled through completely and the taper has been fully transferred. The slope of the resulting taper in the granular aluminum layer is then determined by

$$\frac{S_{\mathrm{Al}}}{S_{\mathrm{PR}}} = \frac{R_{\mathrm{Al}}}{R_{\mathrm{PR}}} \tag{3.1}$$

where R_{Al} and S_{Al} are the etch rate of and slope in the taper in the granular aluminum and similarly, R_{PR} and S_{PR} are the etch rate of and slope in the taper in the photoresist.

One bombardment method that was explored to transfer tapers was to use a Kaufman and Robinson (K & R) AJA ion mill equipped with a KDC 40 ion source. This ion mill produces a neutralized beam of argon atoms by first ionizing argon via inelastic collisions with stray electrons that are accelerated by a *beam voltage* within the ion gun. Then, the ionized argon is acceler-

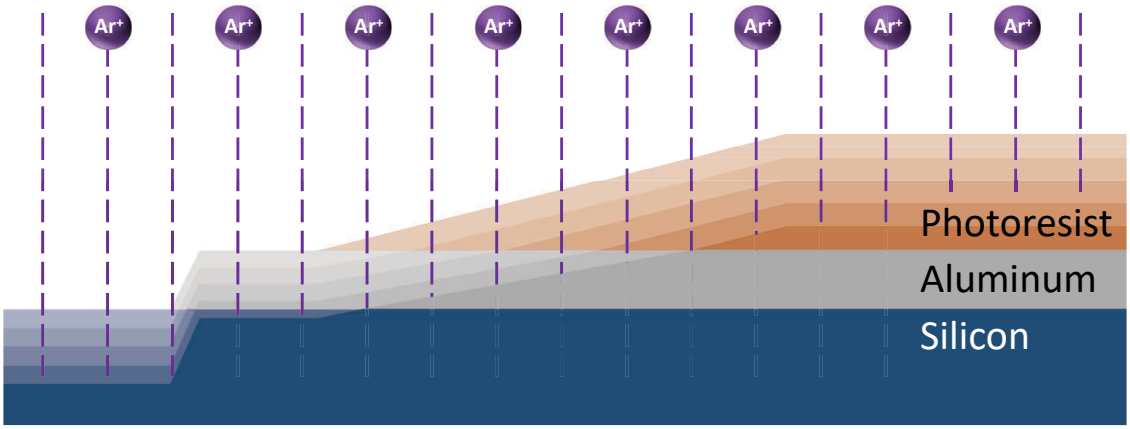

Figure 3.9: A cartoon depicting ion bombardment with normally incident Ar^+ ions (purple) to transfer a taper from a layer of resist (orange) into a layer of granular aluminum (gray) on a silicon substrate (blue). Each transparency step is separated by equal time intervals.

ated toward an accelerator grid by an *accelerating voltage* which creates a collimated beam of argon ions. As the argon cations leave the accelerating grid, they become neutralized by passing though a cloud of electrons that is generated from a nearby neutralizer filament. In this way, a beam of collimated and neutral argon atoms can be used to mill substrate surfaces.

Characterization of this ion mill with S1805 photoresist and granular aluminum was required before tapered structures could be bombarded and transferred. First, the milling etch rates of S1805 photoresist and of granular aluminum were characterized to determine an appropriate etch time. Additionally, the etch rate characterization was necessary to ensure that the taper slopes that were transferred into the granular aluminum layer were comparable to the tapers that were fabricated in the resist layer (see Equation 3.1). If the etch rate of the photoresist is too slow when compared to the etch rate of granular aluminum, then the taper in the aluminum layer would be too steep. Conversely, if the etch rate of the photoresist is comparatively too fast, the photoresist would fail to protect the un-tapered region of the granular aluminum film. Therefore, a balance between the etch rates of these materials is required to reliably transfer tapered structures into underlying layers.

The etch rate characterization was performed with the K & R AJA ion mill at a beam voltage of +500 V, an accelerating voltage of −300 V, and a beam current of 56 mA. Typically, the

etch rates of materials depend on each of these parameters since the difference between the beam and accelerating voltages determines the energies of the bombardment species (here, $E = eV_{\text{Beam}} - eV_{\text{Accel.}} = 800\,\text{eV}$) while the beam current determines the ion fluence that impinges on the substrate. Milling with the previously noted parameters revealed that the etch rates of the photoresist and of the granular aluminum layer were extremely similar and were both close to 10 nm/minute, indicating that the transferred tapers should have similar slopes. This granular aluminum etch rate also indicated that an etch time of ~ 50 minutes was required to just barely mill through the typically ~ 500 nm thick granular aluminum films.

An unfortunate side effect of the long mill times that were required to mill through the aluminum layer indicated that this ion mill could not be used to transfer tapers. When aluminum test samples that were coated with resist were milled for longer than ~ 10 min, the resist layer burned and bubbled. This resist damage could be plausibly caused by two different sources. One possibility was that the substrate was significantly heating over the course of the lengthy mill, which was effectively burning the resist. Several attempts were made to promote substrate cooling to mitigate the possible resist burning by decreasing the sample stage temperature, by thermally anchoring the sample and the sample stage to the cold head with conductive vacuum grease, and by decreasing the ion power by lowering the beam voltage. Each of these attempts resulted in the same resist damage before the granular aluminum film could be entirely milled. Another possible cause of the resist damage was that a reactive etch by oxygen contamination in the argon line was occurring during the mill. We attempted to remedy this by milling with higher purity argon as well as by upgrading the gas plumbing to no avail. In every attempt, we repeatedly found that the photoresist could be milled for a maximum of 10 minutes with this particular instrument before the pitting and burning of the resist became problematic, indicating that a different milling technique was required.

In order to circumvent the challenges associated with damage to the photoresist caused in the K & R AJA ion mill, we employed an alternative milling technique by using a Magnetron sputter system as an ion source. This implementation of a sputter system has been realized in

an elegant way by Hindmarch *et al.* by reversing the roles of the sputter gun anode and cathode.[123] However, a simpler approach was employed in this work by directly mounting samples to a copper sputter target and then sputtering the sample (see Chapter 2 for a schematic of the sputter system). The characterization of milling with the sputter system was required as previously described and was accomplished by performing several rate tests to determine the optimum milling parameters. We found that controlling the sputter gun to a current of 0.01 A (yielding a power of 3 – 5 W and a voltage of 300 – 400 V) was vital to successfully mill with the sputter gun since the ion fluence depends on the current. Milling in this way once again resulted in similar etch rates between the photoresist and granular aluminum and were typically near 1.0 ~ 1.5 nm/s. From these rates, a mill time of ~ 8.3 min was required to just barely mill through a 500 nm thick layer of granular aluminum.

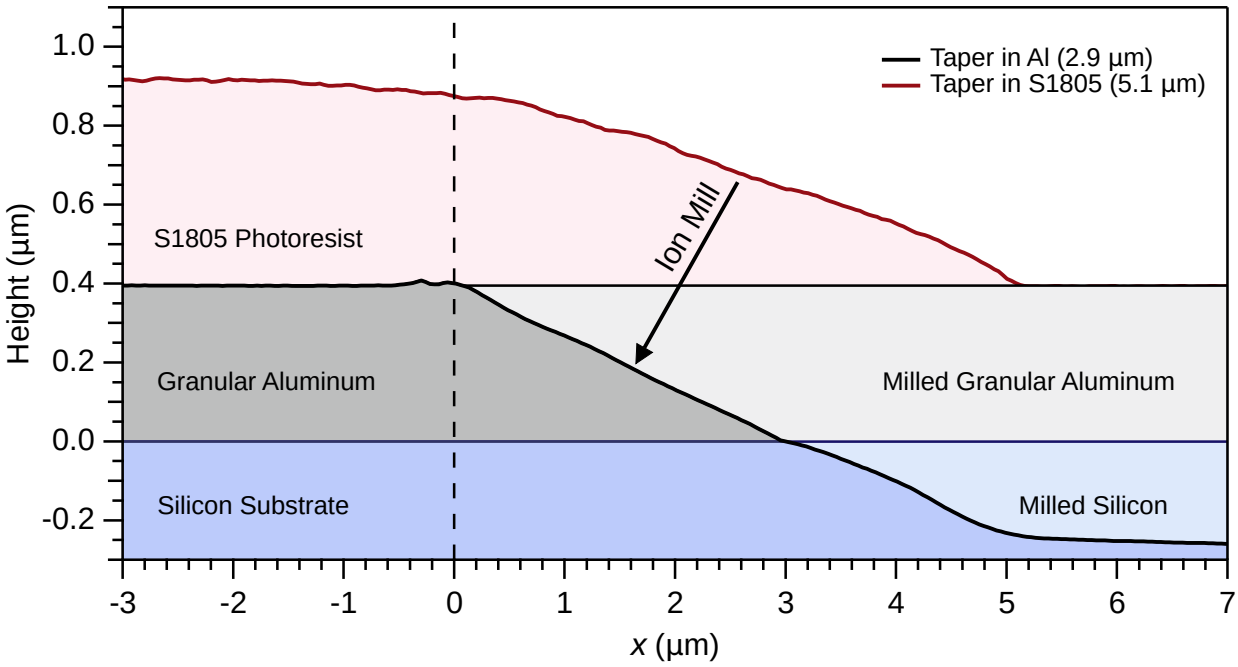

Figure 3.10: AFM scans of a taper in S1805 resist (red) and the resulting taper that was transferred into the aluminum sample (grey) after milling the substrate with the sputter system. The sample was over-milled which partly transferred the taper into the silicon substrate (blue).

We also found that properly grounding the sample to the sputter cathode was imperative to avoid charge buildup on the substrate in order to achieve a uniform etch. Substrate charging can occur because the argon ions are not neutralized in a sputter system and can build up on the silicon substrate since there is no available path to the sputter cathode through the insulating silicon oxide layer. Therefore, the samples were attached to the sputter target with conductive copper tape and the connections between the granular aluminum film, copper tape, and sputter cathode were rigorously verified with a multimeter. By carefully ensuring the electrical connections in this way, the charge buildup of samples was mitigated and uniform dry etches were commonly achieved. Figure 3.10 shows AFM scans of a 5.1 µm taper in 0.53 µm thick S1805 resist and the resulting 2.9 µm taper that was transferred into a 0.4 µm thick granular aluminum film by milling a properly grounded sample with the sputter system. It is important to note that pre-patterned films grown on top of gold contacts required individual checks of the connections between each lead to the sputter cathode while samples that were deposited as sheets that covered the entire substrate surface were much simpler to ground since the entire surface was conducting. Taper structures were successfully and reliably transferred into granular aluminum samples that were milled with this implementation of the sputter system, pending that the samples were properly grounded to the copper sputter target.

3.2 Rectification Measurements with a 5-Segment Sample

3.2.1 Sample Details

The effects of five distinct tapers of differing lengths on vortex nucleation were simultaneously measured and compared with a 5-segment sample that was fabricated in an 8-probe geometry, shown in Figure 3.11, by using the previously described lift-off and tapering methods. The extreme advantage of studying the effects of tapered edges in a multi-segment sample is that each segment belongs to the same film so that the only difference between the segments is the length of taper. The 5-segment sample, designated Al091616b1, was grown on top of pre-patterned gold contacts by Magnetron sputtering granular aluminum at a rate of 10 Å/s and in

an argon pressure of 6500 mTorr with a 50 µTorr partial oxygen pressure which were both controlled by Alicat mass flow controllers. The sample was grown to a thickness of 427 nm and was initially patterned in a bulk, 5-segment geometry that was 100 µm wide and 120 µm between each pair of voltage leads.

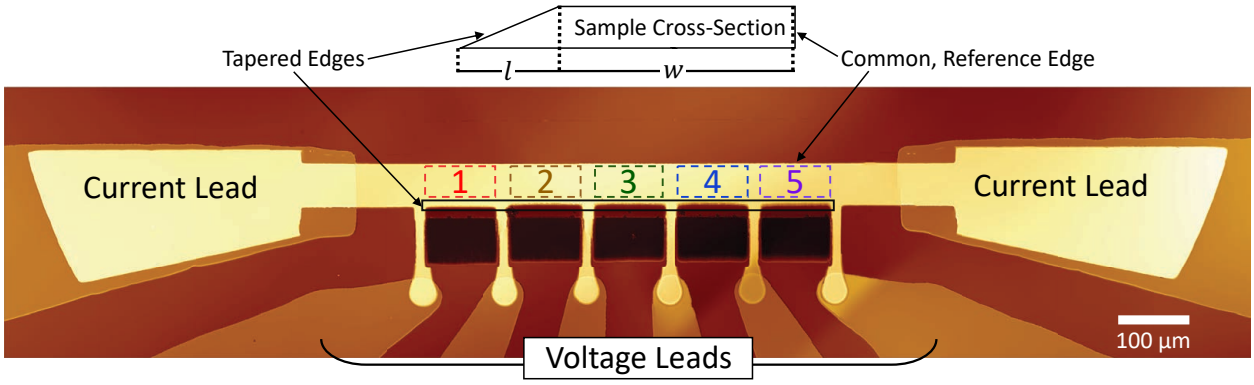

Figure 3.11: A white light interferometry image of the 5-segment sample Al091616b1. There are two current leads and 6 voltage leads that define 5 sample segments (labelled $1-5$). Each sample segment is 120 µm long and 55 µm wide (w). The tapered edges exist between each pair of voltages leads with the common edge on the opposite side with no voltage leads. The resulting cross-sectional film geometry is shown with the schematic where l is the taper length and w is the width of the film. The dark areas between the voltage leads are areas of the silicon substrate that were milled during the tapering process.

Pre-Tapered Film Characterization

Before tapering the edges between the voltage leads, the 5-segment sample was measured to characterize the uniformity of the film after all of the sample edges were wet-etched to a sample width of 77.5 µm, which defined sharp edges on both sides of each sample segment. The superconducting properties of each of the identical and pre-tapered sample segments of Al091616b1 were characterized with critical transition measurements, shown in Figure 3.12 as the colored curves. The identical critical temperatures of $T_c = 1.718$ K between each sample segment indicates that the 5-segment film was grown uniformly and that the five segments are comparable to one another. These critical measurements also reveal that the transitions of each sample segment are narrow with transition widths of $\delta T_c = 2$ mK, which suggests that the wet-etched edges of each segment are identical.

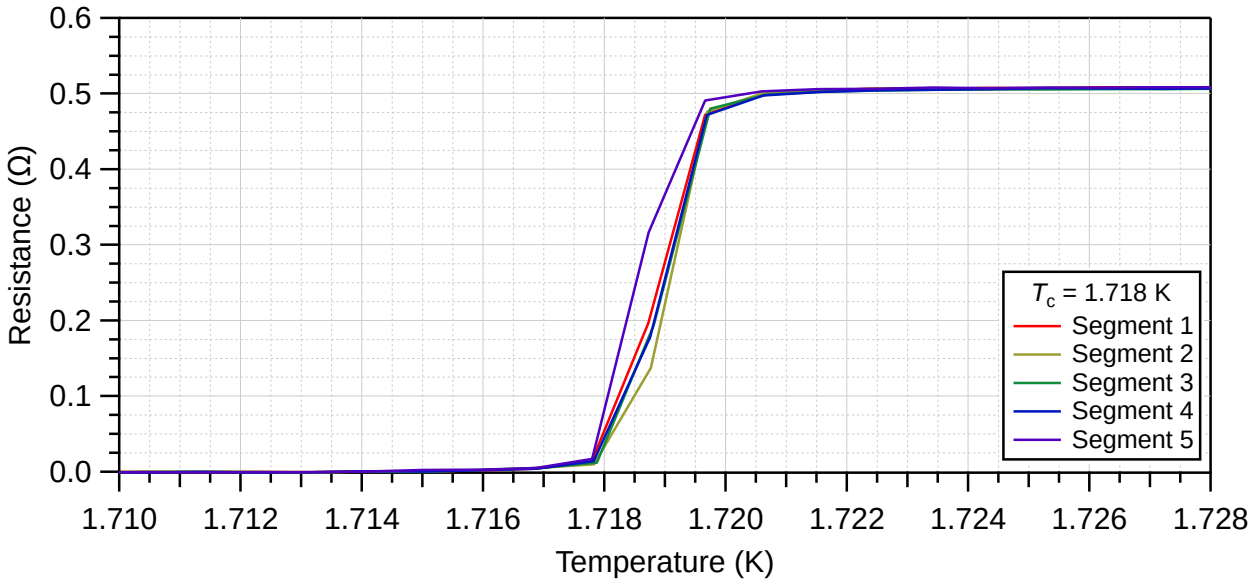

Figure 3.12: Transition measurements for the 5-segment sample Al091616b1 before tapering the sample edges. The nearly identical critical transitions of all of the sample segments indicates that the film is uniform and the narrow transition widths ($\delta T_c = 2$ mK) indicates sharp wet-etched edges. Note that the temperature axis only extends over a range of 18 mK to show the subtle differences between the five transitions.

Tapered Edge Characterization

The sample edges between the voltage leads were tapered after confirming the uniformity in the film properties across each of the segments. Photoresist was spin-coated on the sample and then tapered by using the dynamic optical lithography technique that was previously described. The resist was then post-baked for 3 minutes at 130 °C to reduce exposure interference effects and then developed. Then, the tapers were transferred from the resist into the aluminum sample by mounting the sample onto a copper sputter target and then milling the sample in the sputter system. The sample was milled for 12 minutes by controlling the current to 0.01 A which yielded a power of 4 W and a voltage of ~ 300 V. The final width of the post-milled sample was 55 µm with the top of each taper aligned to the edges of the current leads.

The sample and tapered edge geometries were quantified with a combination of profilometry techniques. An optical interferometric image of the sample, shown in Figure 3.11, was recorded to determine the sample width and to visualize the 5-segment geometry. Each segment (numbered) of the aluminum sample (yellow) was individually measured with a 4-probe

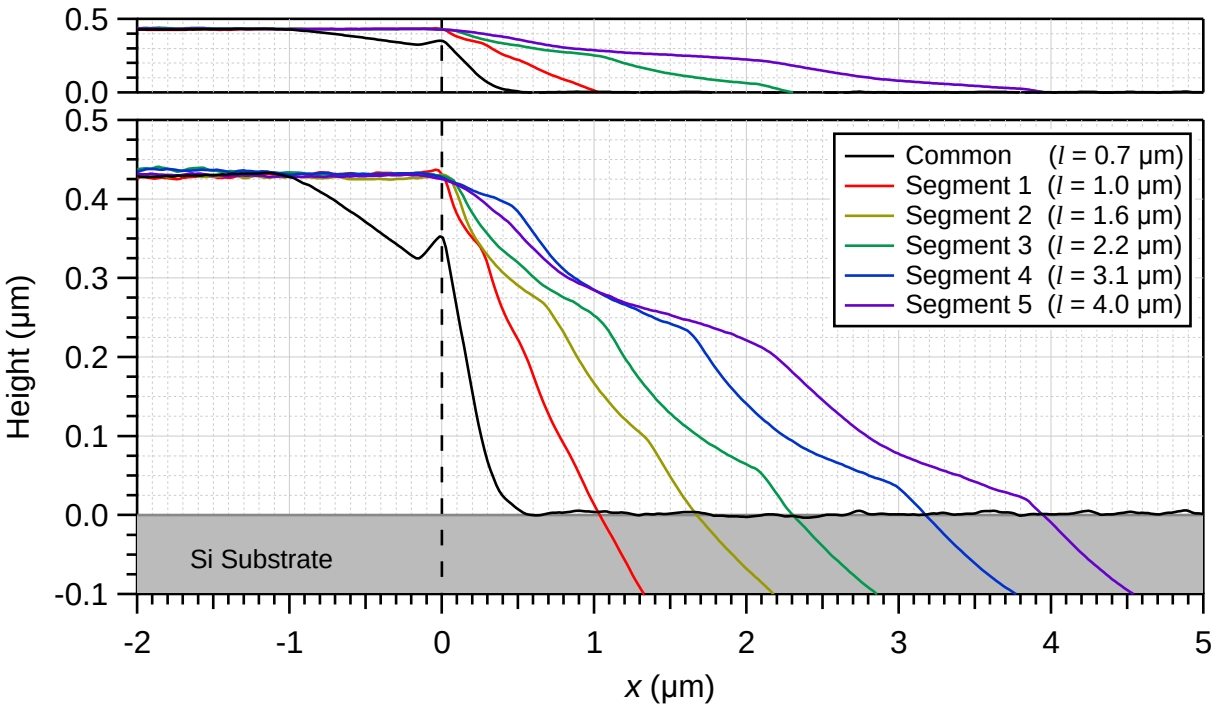

Figure 3.13: AFM profilometry scans of the tapers and common edge of the 5-segment sample Al091616b1. The upper figure depicts the common edge and the tapers of segments 1, 3, and 5 with a 1:1 scaling between the axes so that the taper length may be directly compared to the thickness. Since the tapers were milled into the silicon substrate, the sample thickness and termination of each taper were determined with the AFM scan of the common edge, which was wet-etched. Refer to Figure 3.11 for a schematic that defines the taper length parameter l.

measurement by applying a current between the current leads and then measuring the voltage between each pair of adjacent voltage leads. The sample and gold contacts rest on a silicon substrate (dark red) and the darkest areas between each pair of voltage leads are areas where the milling process etched into the underlying silicon substrate. The profile of tapered edges and of the common, reference edge on the edge opposing the voltage lead side were measured by tapping mode atomic force microscopy (AFM) scans shown in Figure 3.13. The thickness of the film was obtained from the AFM scans taken over the wet-etched sample edges since the tapered edges were mildly over-milled into the silicon substrate to ensure that the tapers were completely transferred. The resulting lateral taper lengths l for the relevant sample edges were determined to be 0.70 μm for the common edge resulting from the geometry of a wet-etch and 1.00 μm, 1.56 μm, 2.21 μm, 3.07 μm, and 3.95 μm for the other five tapered segments. Addition-

ally, the effects of the interference fringes during the taper exposure were observed in the AFM scans of Figure 3.13 as the periodic variation in the thickness of the tapers. The AFM scan of the common edge revealed a mostly sharp edge with a slight rounding near the top. This artifact was caused by the partial transfer of the non-uniform thickness variation in the photoresist near the sample edge resulting from spinning the resist over a structure of comparable thickness. We found that the details of the experiment were unaffected by this artificial inclusion since the initial slope in the common edge was unaffected and remained much steeper than any of the taper slopes.

3.2.2 Cryogenic Measurements

The effects of the tapered edges on vortex nucleation in the 5-segment sample were measured in a home-built closed-cycle pulse tube cryostat.[109] The sample was mounted to a copper sample plate with Apiezon N thermal grease and the temperature of the film was monitored and controlled as previously described in Chapter 2. First, the sample was cooled to 3 K where standard resistivity measurements were recorded for each sample segment. Next, the superconducting transitions for each sample segment, shown in Figure 3.14, were recorded by applying an AC current between the current leads while measuring the voltage between each pair of adjacent voltage leads with an SR830 lock-in amplifier as the sample was cooled. These measurements reveal a striking difference between the transitions for the pre-tapered and tapered segments, which we will discuss in a later section. However, we define T_c to be the temperature at which the transitions become vertical where the tapered transitions all match. The small discrepancy between the pre-tapered and post-tapered critical transition locations has been previously observed in other granular aluminum film samples that were grown and tested in our lab and is a consequence of the sample film and not of the tapering process. Since the film is kept at room temperature between runs, we believe that this drift in the critical temperature is caused by either surface oxidation or stress and strain factors that are changing within the film after the sample growth. Additionally, segments 1 and 2 exhibit a mild increase in the

normal state resistance just before the critical transition which will also be discussed in a later section for a similar sample. The various superconducting properties that were measured for the segments of this sample are enumerated in Table 3.1.

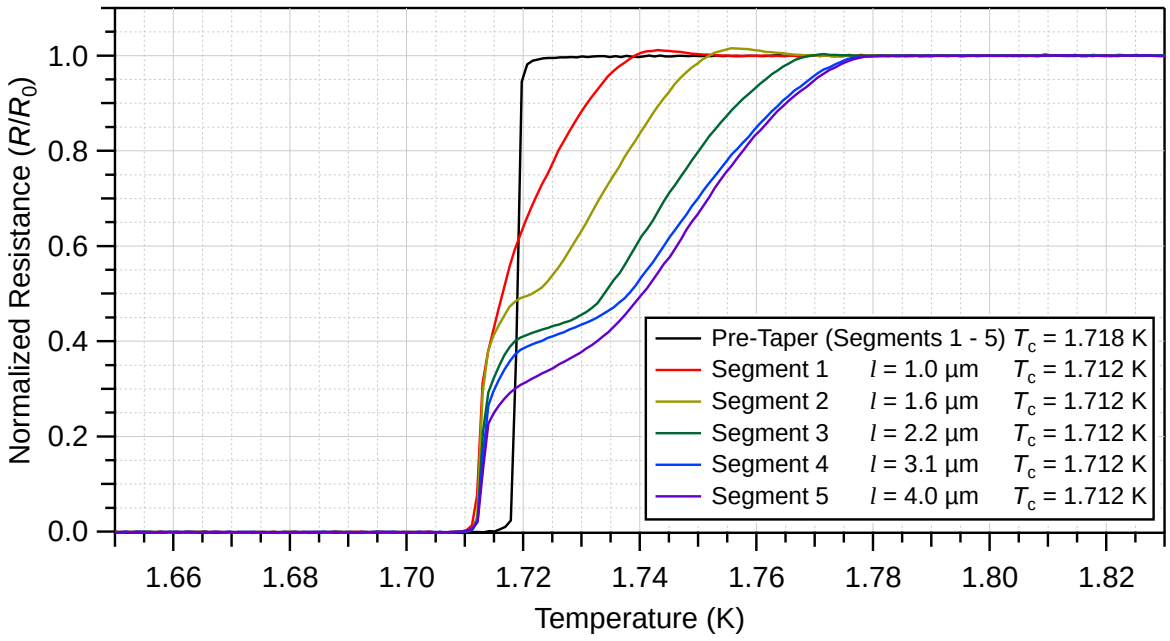

Figure 3.14: Transition measurements for the 5-segment sample Al091616b1. The pre-taper measurements of the critical transitions (black) were identical for all five sample segments and are shown in Figure 3.12 with a narrower temperature axis. Then, the transitions were re-measured after tapering the edges between the voltage leads (colored) where a widening in the transition is observed that depends on the taper length. Refer to Figure 3.11 for a schematic that defines the taper length parameter l.

The dirty-limit Ginzburg-Landau (GL) characteristic lengths were inferred from the characterizations in Table 3.1 to elucidate the vortex properties within the 5-segment sample. Recall from Chapter 2 that granular aluminum is a dirty superconductor with inherently low pinning properties, so the dirty-limit expressions in the GL theory must be used. The dirty-limit coherence lengths ξ for the sample segments were calculated at $T/T_c = 0.9$ (see Chapter 2) and are much smaller than the effective hard edge taper length of $\sim 0.7\,\mu$m (recall that the vortex core diameter is approximated as $\sim 2\xi$). The dirty-limit penetration depths λ of the sample segments were also calculated at $T/T_c = 0.9$ and are all near $\lambda = 600\,$nm. Recall from Chapter 1 that the size-scale of the vortex fields and currents are determined by λ and thus a perfectly vertical

edge will be smeared out on this scale. So, a wet-etched reference edge with an effective taper width of 0.7 μm may be considered vertical since it is similar to λ for this film. Additionally, the shortest tapered edge of width 1.0 μm is just beginning to exceed λ, so vortices will interact with the taper slopes in the film edges.

Table 3.1: Properties of the 5-segment sample (Al091616b1)

Segment	Taper (l)	T_c	$\xi(0.9T_c)$	$\lambda(0.9T_c)$	R_{RT}	R_{3K}	ρ_{RT}	ρ_{3K}	RRR
	(μm)	(K)	(nm)		(Ω)		(μΩ·cm)		ρ_{RT}/ρ_{3K}
Pre-Taper	–	1.718	149	591	0.594	0.504	16.3	13.9	1.17
1	1.0	1.712	152	579	0.734	0.628	15.5	13.3	1.17
2	1.6	1.712	149	590	0.804	0.690	16.0	13.8	1.16
3	2.2	1.712	151	584	0.805	0.692	15.7	13.5	1.16
4	3.1	1.712	150	586	0.796	0.683	15.8	13.6	1.16
5	4.0	1.712	151	584	0.789	0.675	15.8	13.5	1.17

The characteristic lengths also determine the size regimes that vortices experience. Recall from Chapter 1 that the sample thickness d significantly affects the length scales of the fields and currents of vortices and that vortices can exist in the Abrikosov ($d \gg \lambda$), intermediate ($d \sim \lambda$), or Pearl ($d \ll \lambda$) regimes. Therefore, the film penetration depths of ~ 0.6 μm for the sample segments indicate that vortices in the interior of the film are likely not in the Abrikosov or Pearl regimes but are rather in the intermediate regime since the sample thickness is similar to λ. It is important to note, however, that vortices that are nucleating into a tapered edge are initially in the Pearl regime until the thickness at the location of the vortex within the taper becomes non-negligible when compared with λ. Therefore, emerging vortices are only in the Pearl regime while immediately nucleating into the knife-edge of the taper but then rapidly localize into a vortex that is in the intermediate regime.

The effects of the tapered edges on the rectification properties and therefore on the vortex nucleation in the 5-segment sample were studied by probing the vortex dynamics within each of the five sample segments. Recall from Chapter 2 that vortex transport measurements are performed in the form of current-voltage-characteristics (CVCs). In these CVC measurements,

vortices are driven across both sample edges by sweeping both senses of a transport current I_t that is applied between the current leads of the sample while in the presence of an applied field H_a which was generated by coil magnets that were mounted outside of the cryostat at room temperature. The voltage response to the driving current that corresponds to vortices exiting over the edges of the sample segments is then recorded by measuring each pair of adjacent voltage leads of the 5-segment sample. This process* is repeated at various temperatures and applied fields until a complete picture of the vortex dynamics within each sample segment is obtained.

Representative CVC measurements of each of the five sample segments performed at a constant temperature of $0.75\,T_c = 1.29\,\mathrm{K}$ and at a single applied field of $H_a = 11.5\,\mathrm{G}$ are shown in Figure 3.15. As described in Chapter 2, these measurements were obtained by gradually increasing the amplitude of a 100 Hz single-sided square wave current while simultaneously measuring the voltage between two adjacent voltage leads with an SR830 lock-in amplifier that was locked to the 100 Hz current driving frequency. This waveform of I_t allows for lock-in techniques that are typically reserved for AC measurements to be exploited to reduce the noise in this inherently DC measurement. We define positive values of I_t in Figure 3.15 to correspond to currents that nucleate vortices over the tapered edges on the voltage lead side while negative values of I_t correspond to currents that nucleate vortices over the common, reference edge on the opposing side.

The transport measurements depicted in Figure 3.15 reveal the details of vortex motion in the 5-segment sample with tapered edges. First consider negative senses of I_t that nucleate vortices over the common, reference edge. For small and negative values of I_t, vortices are prohibited from nucleating over the steep common edge due to the existence of the Bean Livingston barrier (BLB) but also due to the large geometric barrier (GB) that is associated with squared edge geometries. The current magnitude is then increased, but no voltage is observed since the large edge barrier belonging to the common edge continues to exclude vortices from

*Refer to Figure 2.15 in Chapter 2 for a schematic representation of the details of these measurements.

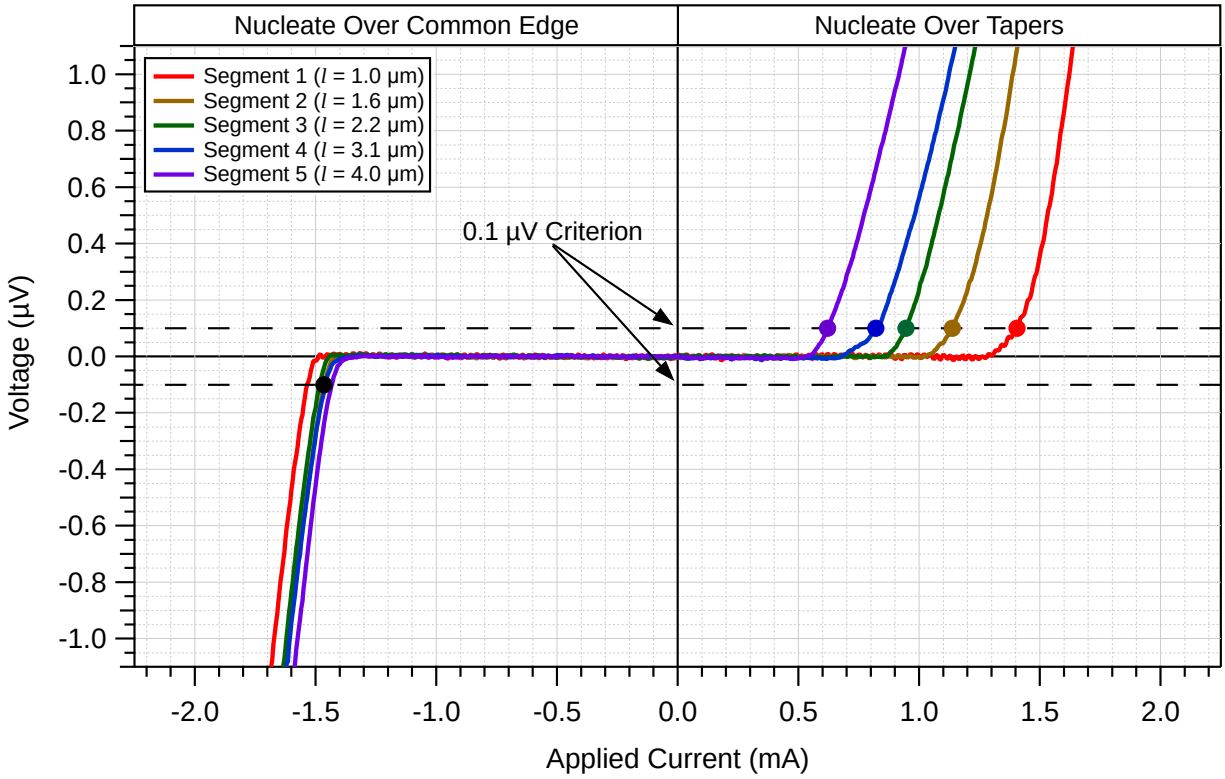

Figure 3.15: Current voltage characteristics (CVCs) for the 5-segment sample Al091616b1 recorded at $H_a = 11.5\,\mathrm{G}$ and $T = 0.75T_c = 1.29\,\mathrm{K}$ for each sample segment (colored). A $0.1\,\mu\mathrm{V}$ criterion was used to define the critical currents for each tapered edge (colored dots) of the segments. The common, reference edge critical current was obtained by averaging the five common edge measurements (black dot). Refer to Figure 3.11 for a schematic that defines the taper length parameter l.

the interior of the film. As the current magnitude continues to increase, the inward force on the expelled vortices eventually exceeds the edge barrier and vortices begin to enter over the shared reference edge, forming a flat-topped vortex dome in the interior of the 5-segment sample for the applied fields that were tested (the domes that were previously discussed in Chapter 1 were considered in the case of low fields). Recall that this vortex dome is "pushed" toward the tapered edges by the applied current. Once the applied current reaches the *critical depinning current* I_c, one of the dome edges overlaps the tapered edges and vortices being to flow across each segment of the film with each vortex generating a voltage pulse as it exits between a pair of voltage leads. Here, I_c is experimentally defined to be the applied current that is required to elicit a *criterion voltage* of $0.1\,\mu\mathrm{V}$ (represented by the black dashed lines in Figure 3.15) between any pair of adjacent voltages leads. CVC measurements with this negative sense of I_t result in

extremely similar measurements of I_c for each sample segment, indicating that the common, reference edge influences the vortex nucleation dynamics identically for each sample segment and also indicates that the tapered edges have no effect on vortices exiting the film.

At this point, we have considered the case of negative I_t corresponding to vortex nucleation over the common edge, but we will now consider the case of positive I_t corresponding to vortex nucleation over the tapered edges. For small and positive values of I_t, vortices are once again prohibited from nucleating over the tapered film edges due to the BLB and GB. As the current is increased, vortices first begin to nucleate over the shallowest and longest taper since the GB is most suppressed for longer tapers (purple). As the current continues to slightly increase, the vortices are driven across the sample and exit the film indicating that I_c has been achieved.

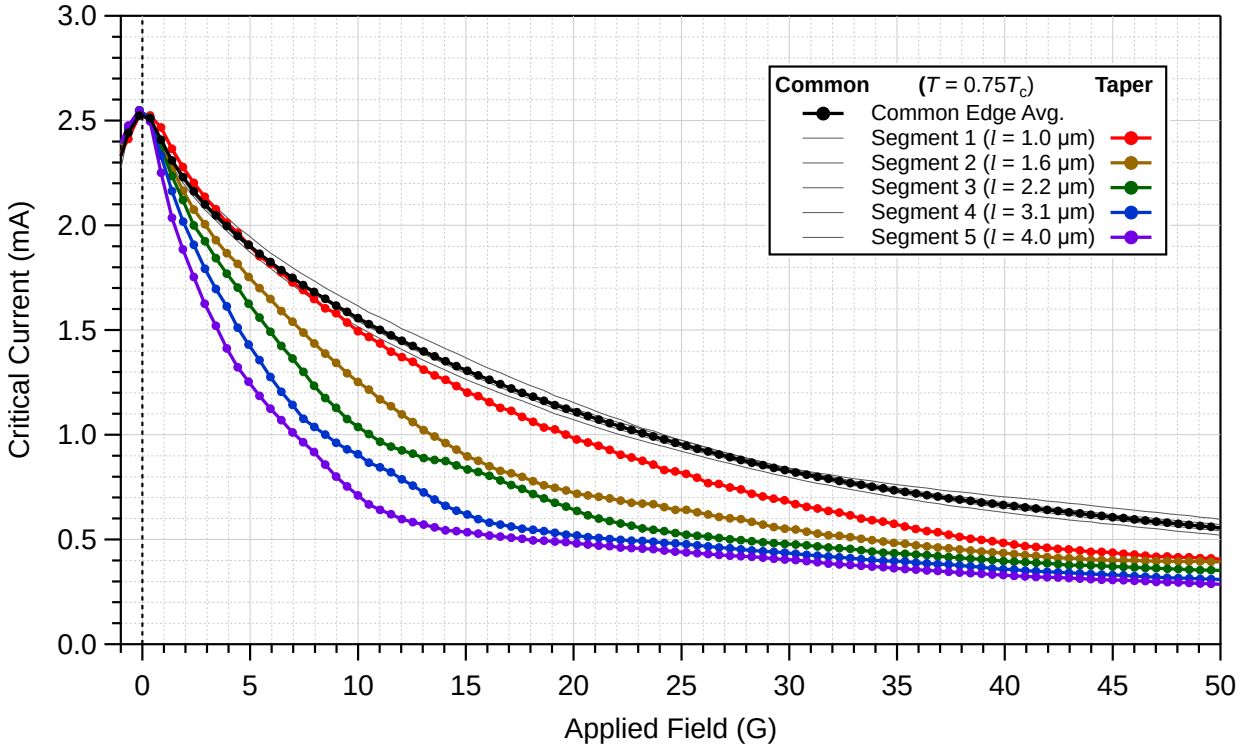

Figure 3.16: Transport measurements of the 5-segment sample after tapering the edges at $0.75T_c$ = 1.29 K. The measurements performed corresponding to vortex nucleation over the tapers for each sample segment are colored, with the average of the common edge measurements displayed in black. Each individual set of common edge data for each segment that were used to compute the common edge average are also displayed with grey lines. The critical currents measured at 11.5 G were obtained from the CVC measurements portrayed in Figure 3.15 as the colored and black dots. Refer to Figure 3.11 for a schematic that defines the taper length parameter l.

This results in a significantly reduced measurement of I_c when compared to the measurements corresponding to nucleating vortices over the common edge. This trend continues for each sample segment where the applied currents that are required to both nucleate vortices into the sample as well as drive them completely across the sample are lower for longer (and shallower) tapers. Thus we observed that all of the tapered edges that were tested exhibited a suppression in the measurements of I_c when compared to the common edge, indicating that forming any taper in one edge of a granular aluminum film will result in rectification.

The 5-segment sample displayed the previously described rectification for a wide range of applied fields and temperatures, which are most clearly represented by recording the critical currents at each field and temperature. These CVC measurements were repeated for temperatures between $0.75T_c < T < 0.98T_c$ and for applied fields ranging between -1 G and 50 G. The current was zeroed before changing the applied field, but the sample was not zero field cooled between each measurement and the connections to the sample were switched with an Arduino-controlled multiplexer switching circuit. Once all of the CVC measurements were completed, the critical currents required to elicit a 0.1 μV criterion voltage were determined for each field and temperature. This representation of the critical currents, depicted in Figure 3.16 at a temperature of $0.75T_c$, allows for the comparison of the rectification effects from each taper length (and slope) over the entire range of applied fields for a specific temperature.

3.2.3 Discussion of Results

The aim of measuring a multi-segment sample both pre- and post-tapering the film edges was to verify that the fundamental superconducting properties of the film were unaffected by the tapered edges as well as to probe the nature of the geometric barrier (GB). The previously discussed resistive and critical temperature characterizations of the sample segments, listed in Table 3.1, determined that the superconducting properties belonging to each segment both before and after forming tapers in the sample edges were extremely uniform. Indeed, these

characterizations also determined that the superconducting properties as well as the locations of the critical temperatures were unaffected by the tapering process.

While tapering the edges of the 5-segment sample appeared to be largely benign in regards to the properties of the film, one superconducting feature was altered in each segment. The post-tapered critical transition measurements (colored) displayed in Figure 3.14 exhibited a widening in the critical transition widths of the tapered segments when compared to the pre-tapered measurements (black) where longer tapers seemed to create wider transitions. Since only the sample edges were changed between measuring the critical transitions of the pre- and post-tapered segments, we attribute these widened transition shapes to edge effects resulting from the tapered edges. One possible explanation for this widening is that thinner granular aluminum geometries have higher critical temperatures than thicker geometries which indicates that the thinnest regions in the tapered edges transition into the superconducting state before the bulk material for granular aluminum.[124] As the temperature of the film is initially lowered, the narrow edges of the tapers become superconducting first and a reduction in the measured resistance of the film is observed. Since the applied current is larger than the effective critical current of the superconducting "wires" in the taper tips, an intermediate state structure forms in which diamond-shaped domains of superconducting material are surrounded by normal material.[4] Therefore, only a decrease in the resistance will be observed since only some of the applied current is shorted through these intermediate regions of the tapers. As the temperature continues to decrease, slightly thicker regions of the tapers become superconducting and the resistance drops once again. This process is repeated as the sample is cooled and thicker portions of the tapers become superconducting. Eventually the bulk critical temperature is reached at which point the entire film exhibits superconductivity. Therefore, the critical temperatures of each tapered segment are identical regardless of the broadened transitions because they belong to the same bulk film.

Other possible explanations for the effects of the sample edges on superconducting transitions have been experimentally explored. Delano claims that imperfections in the sample edges

cause broadened transitions and that wet-etching the edges eliminates this dependence.[112] Behrndt *et al.* has also explored this phenomenon and posits that an interplay between the material granularity and the edges may cause similar effects.[125] However, this explanation cannot explain the observations in Figure 3.14 since granular aluminum has inherently small grain sizes as was discussed in Chapter 2.

After verifying the minimal effects of the tapered edges on the film properties, the effects of the tapered edges on vortex nucleation can be probed with rectification measurements of each sample segment. A previous study[62] has shown a rectification in the high-current voltage response in the flux low regime corresponding to similar tapered edge geometries in a thin Nb film. This result only showed that vortex motion was affected rather than showing that the onset of flux flow was altered since the critical currents required to first observe a voltage response were identical for both edges. However, similar transport measurements of the tapered edges in the 5-segment granular aluminum film shown in Figure 3.15 clearly indicates that tapered edge geometries are also capable of directly influencing the criterion voltage critical currents that correspond to the onset of flux flow and therefore to vortex nucleation into the sample. Additionally, Figure 3.16 indicates that the critical currents of the 5-segment sample exhibit similar rectification effects across the entire applied field range that was tested, except in the low field regime.

One important feature of these critical currents is that the zero-field critical currents are independent of the taper length between samples and are identical to the critical currents measured for the common edge. This is because the bulk pinning of the material dominates the edge pinning at low fields, despite the low bulk pinning properties of granular aluminum. At larger applied fields, the rectification effects for the tapered edges become more apparent with a maximum in the edge effects occurring near 11.5 G. Rectification effects are also observed at higher applied fields, however, these effects are reduced in magnitude and seem to become less dependent on the taper length.

Matching effects are also observed in Figure 3.16 by the increase in the critical currents as the field is increased for each segment. Recall from the discussions in Chapter 2 that when the applied field becomes commensurate with a periodic potential in a superconductor, then a *matching field* is reached and vortex motion is inhibited. In Chapter 2, these matching effects were expected since the surface of the superconductors were intentionally thickness-modulated with a 3 μm pitch to induce a washboard potential. However, the 5-segment sample does not have a modulation in the film surface, but rather possesses thickness modulations in the tapered edges. Recall that standing waves that are formed in the resist during the exposure of the tapers results in a thickness modulation in the resist tapers. Although these thickness modulations were mitigated by post-baking the resist after exposure and before development, the thickness modulations could not be entirely eliminated from the tapers in the resist and were therefore transferred into the edges of the superconducting film (see Figure 3.13). Since the pitch of the modulations depends on the taper length, matching effects were observed at different fields for the sample segments with longer tapers. These matching effects are observed in Figure 3.16 near 24 G for segment 2, 16 G for segment 3, 11.5 G for segment 4, and near 7.5 G for segment 5. We hypothesize that matching effects were not observed in the shortest taper since the pitch of the modulations became smaller than the average vortex size within that taper. While these matching effects marginally influence the vortex transport properties for each taper, the qualitative rectification results remain unchanged.

So far, rectification within the 5-segment sample has only been discussed in the context of the measurements that were performed at $0.75T_c$, but similar rectification properties resulting from the tapered edges were observed for a wide range of temperatures in the measurements of each segment. For clarity, we define I_{c-} as the critical current for nucleating vortices over the common, reference edge while I_{c+} is defined as the critical current for vortices nucleating over the tapered edges. Figure 3.17 displays the difference in the critical currents $|I_{c-} - I_{c+}|$ at each applied magnetic field and at various percentages of T_c for each of the five sample segments. For reference, Figure 3.16 can be reconstructed from the $0.75T_c$ measurements from each panel

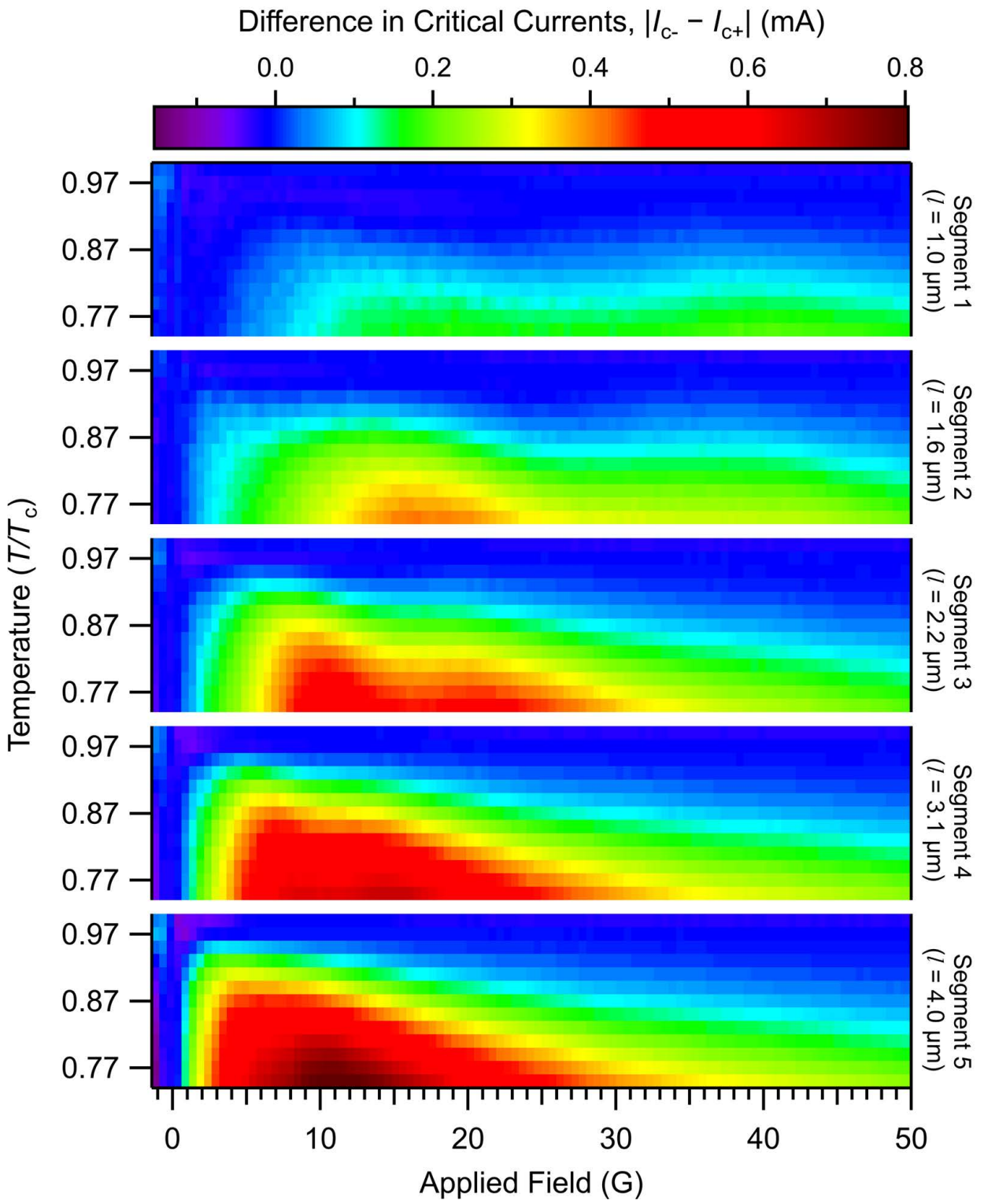

Figure 3.17: Differences in the critical currents $|I_{c+} - I_{c-}|$ (colormap) obtained for temperatures in the range of $0.75T_c < T < 0.98T_c$ and for applied fields in the range of $-1\,\mathrm{G} < H_a < 50\,\mathrm{G}$ for each segment of Al091616b1. Refer to Figure 3.11 for a schematic that defines the taper length parameter l.

corresponding to each sample segment where the critical current axis in Figure 3.16 is related to the color scale axis in Figure 3.17. Segment 1 with the shortest taper begins to exhibit rectification in the critical currents for temperatures lower than $\sim 0.9T_c$. However, segments 2, 3, 4, and 5 with longer tapers begin show rectification effects at warmer temperatures when the sample is cooled below $\sim 0.96T_c$. The matching effects from the modulations in the taper thicknesses are also be observed in Figure 3.17 for each of the segments as the lateral dips in the critical current differences. While these measurements depicted in Figure 3.17 indicate that rectification properties in the critical currents are more pronounced at colder temperatures for each taper length, the general suppression in the critical currents indicates that the GB was reduced by the existence of the tapered edges for a wide range of applied fields and temperatures.

The observed suppression in the critical currents for the tapered edges depends on the length (and therefore the slope) of the tapered edge. Recall that a reduction in the GB is hypothesized for longer and shallower taper geometries since the expulsive force corresponding to the line-length increase of a nucleating vortex is proportional to the slope of the taper. To show this, Figure 3.18 displays the rectification of each tapered segment as the ratio of I_{c-}/I_{c+} at various applied fields and at a constant temperature of $0.75T_c$. Recall that I_{c-} corresponds to the critical currents belonging to vortex nucleation over the common, reference edge while I_{c+} corresponds to the critical currents for the vortices nucleating over the tapered edges. The critical currents are reversible and display no rectification for each taper length at low fields (red) as expected following from the previous discussion of the dominant low-field bulk pinning properties. As the field is increased, a linear dependence between the taper length and the observed rectification emerges where the slope of this dependence is seemingly determined by the applied field. This slope increases as H_a is increased until a maximum value is achieved in this representation between 10 G and 15 G. Then, the slope begins to decrease as H_a continues to increase (blue). These results corroborate the hypothesis that an increase in taper length (and therefore shallower tapers) results in an increase in the rectification for non-zero fields which corresponds to a reduction in the GB for the tapered edges.

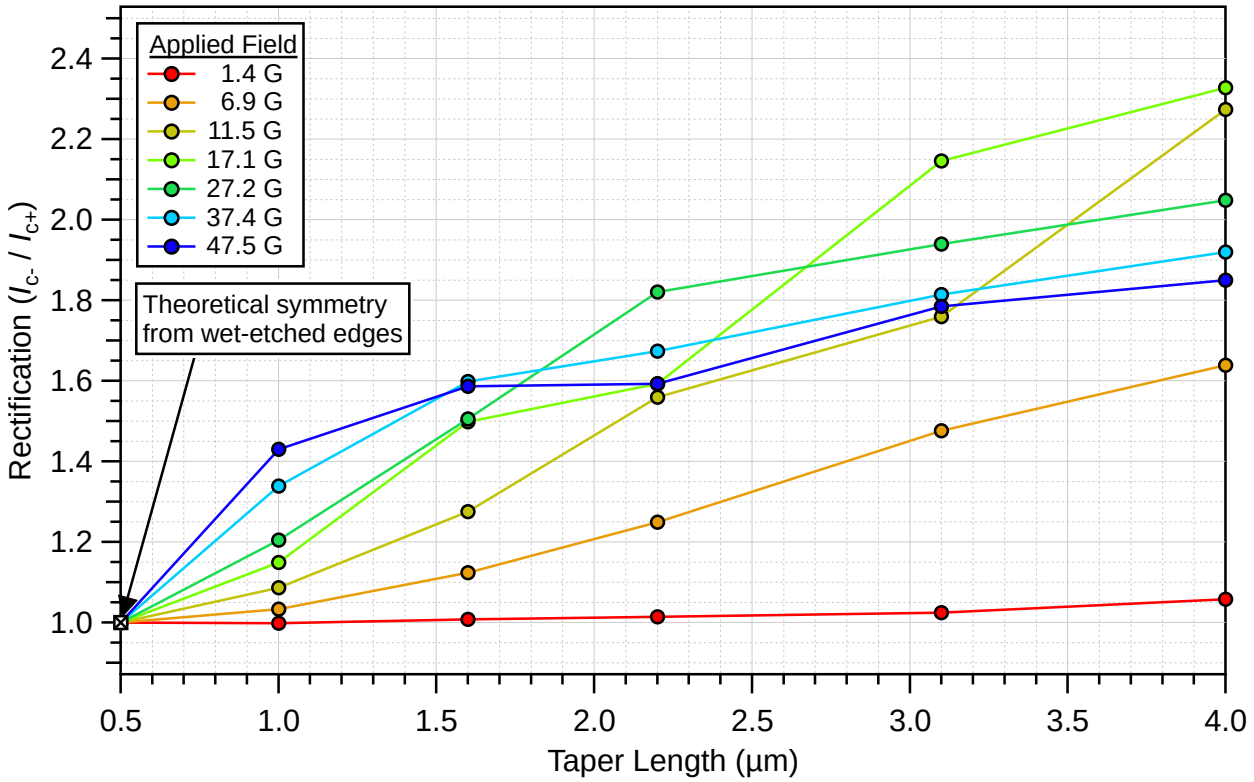

Figure 3.18: The dependence of the ratio of the critical currents in each direction (I_{c-}/I_{c+}) on the taper length at various applied fields (colored) at $0.75T_c$. Refer to Figure 3.11 for a schematic that defines the taper length parameter l.

Rectification effects are also present once the vortices are moving in the flux flow regime of the CVC measurements, as were seen in Figure 3.15. Recall that once I_t reaches I_c, vortices are nucleated on one sample edge and are driven across the sample where they exit on the opposing edge and generate a voltage. However, vortex dynamics continue as I_t is increased beyond I_c. For $I_t > I_c$, vortices are driven across the film at a rate that is roughly proportional to $I_t - I_c$ and will therefore generate larger average voltages that correspond to larger I_t. This creates an effective *flux flow resistance* R_{ff} of the superconductor that is determined by the slope of the CVC curves. Measurements of the flux flow resistances from the CVC measurements that were recorded at $0.75T_c$ and sampled in the region near two criterion voltages of 0.1 μV and 1.0 μV are shown in Figures 3.19a and 3.19b respectively. For clarity, we define R_{ff-} to be the flux flow resistance from vortices that are driven over the common edge and exit over the tapered edges and R_{ff+} is the flux flow resistance from vortices that are driven over the tapered

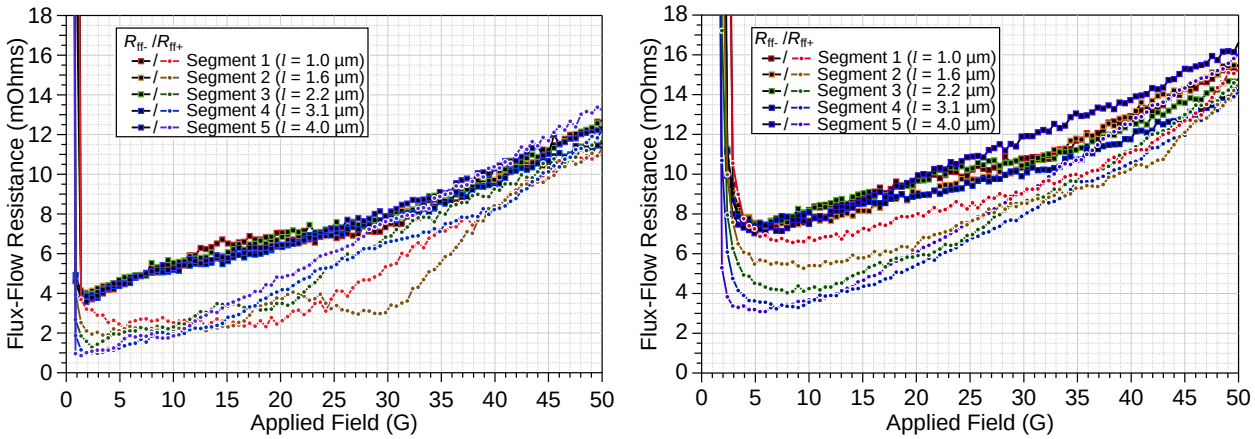

Figure 3.19: Measurements of the flux flow resistance R_{ff} for each sample segment at each applied field in the region near two criterion voltages of **(a)** 0.1 μV and **(b)** 1.0 μV. These measurements were obtained by sampling the slopes of the CVC curves that were recorded at $0.75\,T_c$ near the respective criterion voltages. Resistances that correspond to vortex motion over the common, reference edge, R_{ff-}, are labelled as squares while resistances that correspond to vortex motion over the tapered edges, R_{ff+}, are labelled as circles. Refer to Figure 3.11 for a schematic that defines the taper length parameter l.

edges and exit over the common edge. Both Figures 3.19a and 3.19b show a suppression in R_{ff+} when compared to R_{ff-}, however, Figure 3.19a corresponding to the lower criterion voltage implies that the flux flow resistance is not dependent on the taper length while Figure 3.19b that corresponds to the larger criterion voltage indicates a trend between the flux flow resistance and the taper length.

We hypothesize that the rectification effects on the flux flow resistance should be considered with the larger criterion voltage. The smaller criterion voltage is the correct metric to determine the critical currents that are required to first move vortices within the film. However, the critical current for each sample segment is physically distinct from the apparent resistance that corresponds to vortex motion. Therefore, it seems that the flux flow resistance should be considered at a slightly larger criterion voltage that corresponds to the flux flow regime rather than using the criterion voltage that corresponds to the onset of flux flow. In either case, it is clear that the tapered edges affect flux flow and that a trend exists between the flux flow resistances and the length of the taper when sampling R_{ff} after the vortices have been moving for a while.

The measurements of the critical currents along with the measurements of the flux flow resistances unequivocally demonstrate that the sample edges have a significant influence on vortex nucleation and on vortex dynamics. We found that the geometric barrier was generally suppressed in all five tapered segments of the 5-segment multi-lead sample for a wide range of temperatures and fields as evidenced by the widely suppressed critical currents corresponding to vortex nucleation over the tapered edges. The flux flow resistances were also suppressed when driving vortices from the tapered edge and over the common, reference edge. Therefore, we have shown that vortex nucleation and transport are dependent on the sample edge geometry and can be influenced in granular aluminum by tapering the sample edges.

3.3 Rectification Measurements with an 11-Segment Sample

3.3.1 Sample Details

In an effort to further expand upon the conclusions made with the 5-segment sample, a 14-probe sample in an 11-segment geometry was fabricated using the direct write laser lithography system. The advantages of using an 11-segment sample geometry, shown in Figure 3.20, are identical to the previously described advantages of the 5-segment design along with the added benefit of simultaneously studying a wider range of taper lengths. Rather than lifting-off a bulk film and then tapering the pre-patterned structure as was done for the 5-segment sample, the 11-segment sample (designated Al121119b) was initially sputtered as a sheet of granular aluminum, with no lithographic patterning, that completely covered pre-patterned gold contacts. Recall that exposing tapers in resist covering a uniform aluminum layer is vital in producing high quality tapers. This granular aluminum film was grown by sputter deposition at a rate of 8 Å/s to a thickness of 516 nm in an Alicat mass-flow controlled argon pressure of 6500 µTorr with a partial oxygen pressure of 50 µTorr in order to achieve the desired superconducting properties (see Chapter 2). The multi-segment sample geometry will be defined in later fabrication steps since the granular aluminum film is a sheet that covers the entire substrate and is not in a pre-patterned geometry.

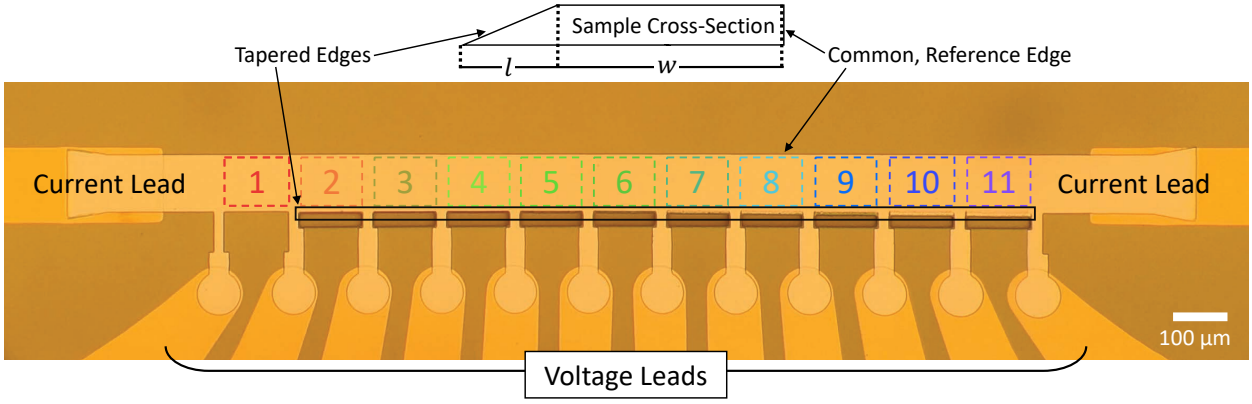

Figure 3.20: An optical image of the 11-segment sample Al121119b. There are two current leads and 12 voltage leads that define 11 sample segments (labelled $1-11$). Each sample segment is 120 µm long and 78.8 µm wide (w). The tapered edges exist between each pair of voltages leads for segments $2-11$ with a reference segment with a wet-etched edge between the voltage leads of segment 1. The common, reference edge is on the opposite side with no voltage leads. The resulting cross-sectional film geometry for the tapered segments is shown with the schematic where l is the taper length and w is the width of the film. The darker areas between the voltage leads are areas of the milled silicon substrate that were milled as an artifact of the lithographic tapering process.

The 11-segment geometry was defined in the granular aluminum sheet with a combination of tapering the sample edges and with multiple wet-etches. First, ten tapers ranging from 2 µm − 20 µm in length were exposed in S1805 photoresist with the direct write laser writer by exposing the same greyscale pattern 20 times at a dose of 7.05 mJ cm^{-2} with a bias and clear dose of 34 % and 87 % respectively. This multiple exposure method of creating tapers with the laser writer is necessary in order to avoid the previously discussed resist scalloping that is detrimental to the quality of resist tapers. The photoresist was then post-baked for 30 minutes at 135 °C to mitigate the effects of the interference fringes in the tapers and then developed. These resist tapers were next transferred into the granular aluminum sheet with the Magnetron sputter system. The sample was milled for ∼ 7 min by controlling the sputter current to 0.01 A which yielded a power of 4 W and a voltage of ∼ 300 V. Once the tapers were transferred into the granular aluminum layer, a wet-etch using S1813 photoresist as an etch mask was performed to define the common, reference edge as well as the 11-segment, 14-probe geometry. Both edges of the remaining un-tapered sample segment were also wet-etched during this step to produce an 11-segment sample with one symmetric, control segment and ten tapered segments. Then,

the remaining sheet aluminum was wet-etched away in a separate step to finish defining the 11-segment sample geometry. This resulted in the 11-segment sample, shown in Figure 3.20, which was 516 nm thick, 78.8 µm wide, and 120 µm long between each pair of voltage leads.

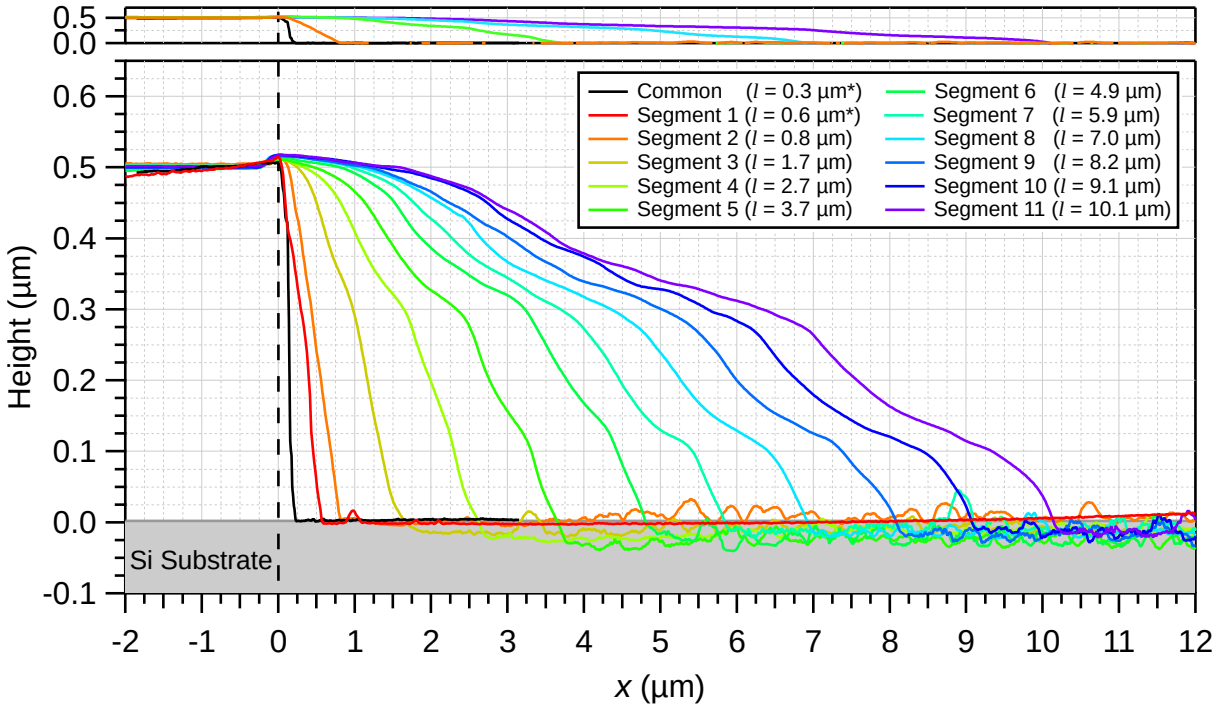

Figure 3.21: AFM profilometry scans of the tapers and common edge of the 11-segment sample Al121119b. The upper figure depicts the common edge and the tapers of segments 2, 5, 8, and 11 with a 1:1 scaling between the axes so that the taper length may be directly compared to the thickness. The segment numbers (and trace colors) match the labelling in Figure 3.20. Since the tapers were milled into the silicon substrate, the thickness and termination of the each taper was determined with the AFM scan for the common, wet-etched edge. Refer to Figure 3.20 for a schematic that defines the taper length parameter l. *These edges were defined via a wet-etch.

The sample and edge geometries were quantified with atomic force microscopy (AFM) profilometry. The profile of the tapered edges and of the common, reference edge were measured by tapping mode AFM scans and are shown in Figure 3.21. The thickness of the film was determined from scans obtained over the wet-etched sample edges since the tapered edges were mildly over-milled into the silicon substrate to ensure that the tapers were completely transferred into the granular aluminum film. The tapers were exposed to be 2 µm – 20 µm long in

the resist and the AFM scans revealed that the tapers were transferred into the aluminum to be between 0.8µm – 10µm in length. The modulation in the photoresist taper thickness that was caused by the interference fringes during the exposure were transferred into the aluminum film and are observed in the AFM scans of each tapered edge.

3.3.2 Cryogenic Measurements

The impacts of longer tapers on vortex nucleation and dynamics were probed at cryogenic temperatures with the cryostat and methods that were described previously for the 5-segment sample. First, the 11-segment sample was characterized by performing resistivity measurements on each sample segment. Then, critical temperature measurements, shown in Figure 3.22, were performed and revealed that the critical temperature locations for each of the sample segments are all identical, although we will discuss the resistance anomaly belonging to segment 2 later. The resistivity characterizations and critical temperatures, shown in Table 3.2, indicate that the film and superconducting properties of the sample segments are uniform.

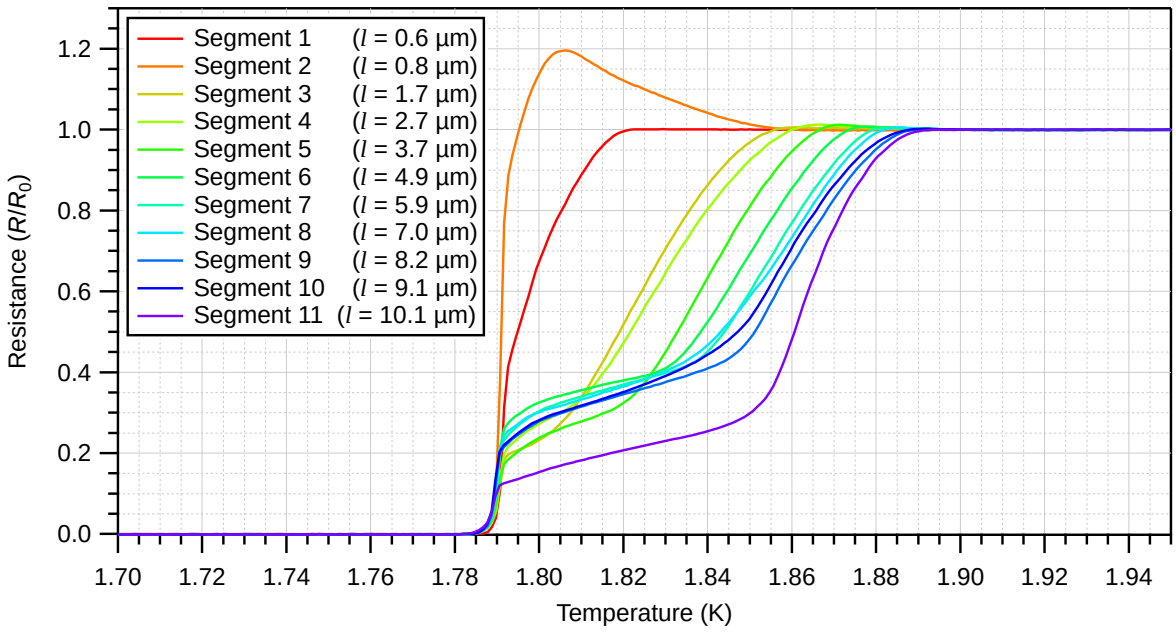

Figure 3.22: Superconducting transition measurements of each segment in the 11-segment sample Al121119b. The transition for the reference segment with no tapering is shown in red. The T_c for each of the segments is 1.784 K. Refer to Figure 3.20 for a schematic that defines the taper length parameter l.

Additionally, these characterizations were used to determine the dirty-limit Ginzburg-Landau (GL) characteristic lengths at $T/T_c = 0.9$ in order to understand the shapes and sizes of vortices within the film. As expected, the calculated coherence length ξ and penetration depth λ in each segment are all commensurate and also agree with the properties of the 5-segment sample (see Table 3.1) since both of these films were grown with similar sputtering conditions. Therefore, the qualitative shape and behavior of vortices within the 11-segment sample are identical to the previously discussed vortices within the 5-segment sample.

Table 3.2: Properties of the 11-segment sample (Al121119b)

Segment	Taper (l)	T_c	$\xi(0.9T_c)$	$\lambda(0.9T_c)$	R_{RT}	R_{3K}	ρ_{RT}	ρ_{3K}	RRR
	(μm)	(K)	(nm)		(Ω)		($\mu\Omega\cdot$cm)		ρ_{RT}/ρ_{3K}
1	0.6	1.784	136	621	0.560	0.467	19.0	15.9	1.20
2	0.8	1.784	137	617	0.552	0.461	18.8	15.7	1.20
3	1.7	1.784	138	615	0.545	0.455	18.7	15.6	1.20
4	2.7	1.784	138	615	0.541	0.452	18.6	15.6	1.20
5	3.7	1.784	138	615	0.539	0.450	18.7	15.6	1.20
6	4.9	1.784	138	615	0.534	0.446	18.7	15.6	1.20
7	5.9	1.784	138	615	0.532	0.443	18.7	15.6	1.20
8	7.0	1.784	138	615	0.529	0.441	18.7	15.6	1.20
9	8.2	1.784	138	615	0.525	0.438	18.7	15.6	1.20
10	9.1	1.784	138	615	0.523	0.436	18.7	15.6	1.20
11	10.1	1.784	142	595	0.486	0.406	17.5	14.6	1.20

The effects of the tapered edges on the vortex transport properties in each of the eleven sample segments were studied by performing CVC measurements as was described for the 5-segment sample. Representative CVC measurements of the 11-segment sample performed at a constant temperature of $0.72T_c = 1.28$ K and at an applied field of 10.9 G are shown in Figure 3.23. These measurements were obtained by measuring the voltage response between a pair of adjacent voltage leads to a 100 Hz single-sided square wave transport current I_t while in the presence of an applied magnetic field which was generated by coil magnets mounted outside of the cryostat and at room temperature. Recall that negative senses of I_t correspond to

currents that nucleate vortices over the tapered edges while positive senses of I_t correspond to currents that nucleate vortices over the common edge on the opposing side.

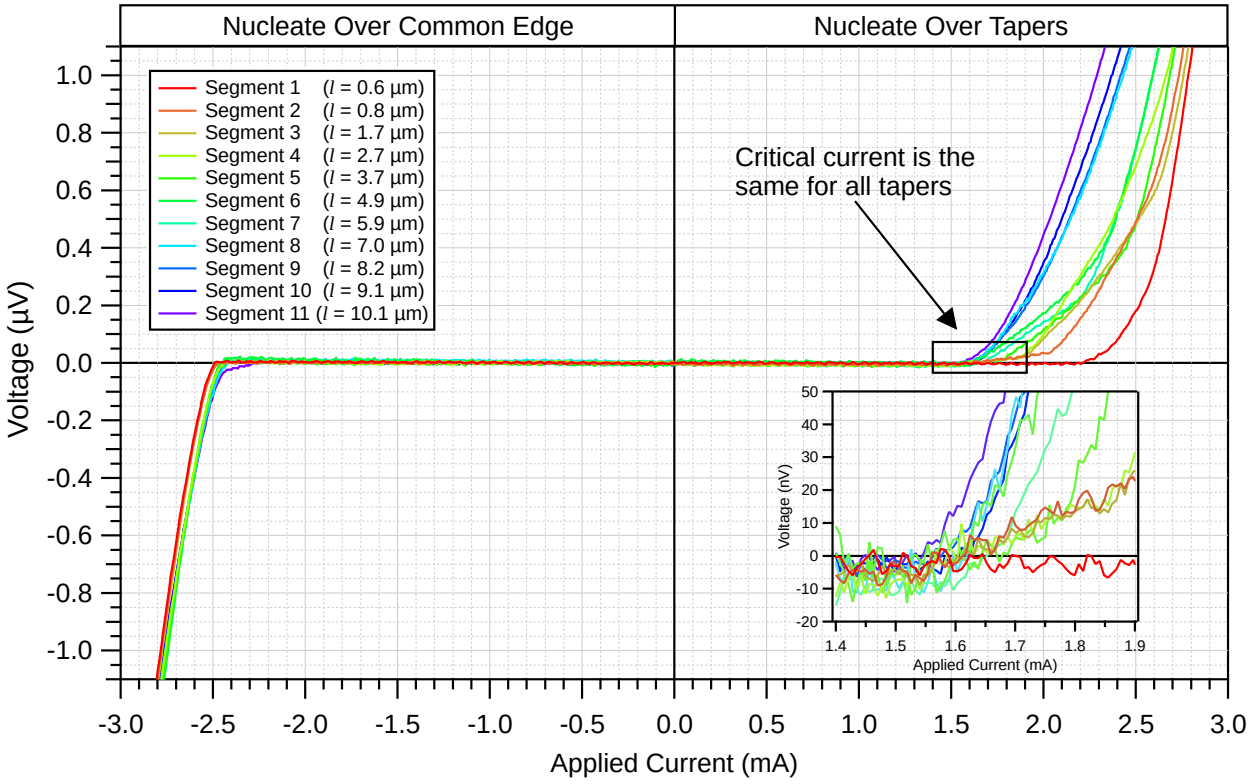

Figure 3.23: Current voltage characteristics for the 11-segment sample Al121119b recorded at H_a = 10.9 G and $T = 0.72T_c$ for each sample segment (colored). The inset shows an enlarged area denoted by the black box to depict the critical currents of the sample segments. Refer to Figure 3.20 for a schematic that defines the taper length parameter l.

3.3.3 Discussion of Results

The purpose of measuring the 11-segment sample was to expand upon the measurements of the 5-segment sample by exploring a wider range of taper geometries. The resistivity and critical temperature characterization measurements, listed in Table 3.2, showed that the 11-segment film was uniform across all eleven segments. While each sample segment exhibited a uniform critical temperature of T_c = 1.784 K, the shapes of the critical transitions shown in Figure 3.22 were widened by the tapered edges as was observed in the 5-segment sample. How-

ever, the transition measurements of segment 2 within the 11-segment sample revealed an unexpected resistance anomaly as an apparent increase in the normal state resistance just before the temperature was lowered below T_c. This resistance increase has been the subject of several studies and is explained with a non-equilibrium charge imbalance model,[126] by applying sufficiently large DC currents,[127] or by measurement in the presence of radiation.[128] The resistance anomaly observed with the 11-segment sample is most likely due to a charge imbalance model since Park *et al.* also measured these effects in a multi-segment sample with geometries that are similar to the 11-segment sample.[126]

After characterizing the uniformity of the 11-segment sample, the effects of the tapered edges on vortex nucleation and transport were probed with rectification measurements in the form of CVCs of each sample segment. However, the CVC curves shown in Figure 3.23 did not exhibit a rectification in the critical currents contrary to the measurements performed with the 5-segment sample. Recall that the CVC measurements for each taper of the 5-segment sample exhibited critical currents that were distinct from one another when using a 0.1 μV criterion current and these CVC curves clearly emerge off of the zero voltage axis at different currents. Although a similar difference in the critical currents could be obtained with a 0.1 μV criterion with the 11-segment sample, the CVC curves for the tapered segments 2–11 all emerge off the zero voltage axis at the same critical current of 1.575 mA, which is highlighted with the inset in Figure 3.23 for clarity. Rectification effects, however, still clearly exist in the flux flow regime of the 11-segment sample as evidenced by the differences in the slopes of the CVC curves. It is important to note that the shared critical current of 1.575 mA is only shared by segments 2–11 and is not observed in segment 1 because the edges belonging to segment 1 were both defined by a wet-etch and should nominally be identical. However, segment 1 still exhibits rectification in the slopes of the CVC measurements, indicating that this segment is not entirely symmetric. Therefore, the rectification portrayed with the 11-segment sample more closely emulates the observations made by Sabatino *et al.* in thin Nb films as differences in the flux flow regime.[62]

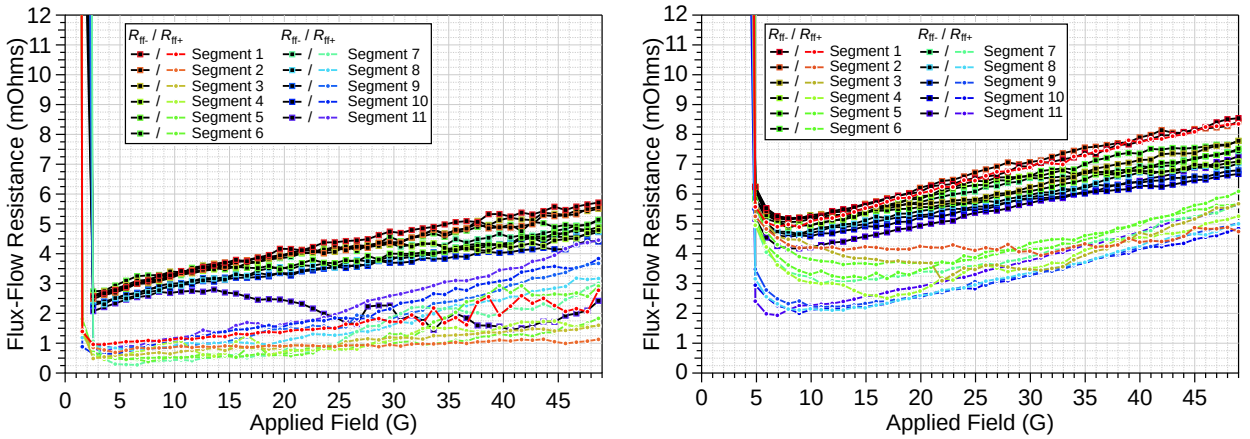

(a) **(b)**

Figure 3.24: Measurements of the flux flow resistance R_{ff} for each sample segment at each applied field in the region near two criterion voltages of **(a)** 0.1 µV and **(b)** 1.0 µV. These measurements were obtained by sampling the slopes of the CVC curves that were recorded at $0.72\,T_{\mathrm{c}}$ in the region near each criterion voltage. Resistances that correspond to vortex motion over the common, reference edge, $R_{\mathrm{ff}-}$, are labelled as squares while resistances that correspond to vortex motion over the tapered edges, $R_{\mathrm{ff}+}$, are labelled as circles.

As was previously discussed, the rectification effects of the tapered edges in the 11-segment sample are observed in the flux flow resistances for the sample segments. Recall from the discussions of the 5-segment sample that as the applied current I_{t} exceeds the critical current I_{c}, vortex dynamics continue within the film since larger values of I_{t} will drive more vortices over the sample edges, and so a larger voltage will be observed. Also recall that these dynamics result in a flux flow resistance R_{ff} within the superconductor that is determined by the slope of the CVC measurements. For simplicity, we define $R_{\mathrm{ff}-}$ to be the flux flow resistance corresponding to nucleating vortices over the common edge and $R_{\mathrm{ff}+}$ to be the flux flow resistance corresponding to nucleating vortices over the tapered edges. These flux flow resistances for the 11-segment sample are displayed in Figures 3.24a and 3.24b which were obtained by sampling the slopes of the CVC curves that were obtained at $0.72\,T_{\mathrm{c}}$ near criterion voltages of 0.1 µV and 1 µV respectively for each sense of I_{t}. Once again, both Figures 3.24a and 3.24b show a suppression in $R_{\mathrm{ff}+}$ when compared to $R_{\mathrm{ff}-}$. However in contrast to the 5-segment sample, the flux flow resistances near both criterions shown in Figure 3.24a and Figure 3.24b indicate a trend between the flux flow resistance and the taper length. One important feature to note is that the flux flow resis-

tance of the reference segment with wet-etched edges on both sides exhibits rectification when sampling near the 0.1 μV criterion, which is surprising since both edges were nominally identical and should therefore exhibit no rectification. However, at the larger 1.0 μV criterion, the flux flow resistance of this reference segment showed no difference between the two current directions as was initially expected. As in the case of the 5-segment sample, we hypothesize that the rectification effects on the flux flow resistance should be considered with the larger criterion voltage, but the 11-segment sample exhibits a trend in the rectification in the flux flow resistances sampled at both criterion voltages.

3.4 Discrepancies Between the 5- and 11-Segment Samples

The 5- and 11-segment multi-lead samples allowed for the effects of multiple tapered edges on vortex transport properties to be simultaneously studied within a uniform granular aluminum film. However, these transport measurements in the form of critical currents (the applied current required to elicit a non-zero voltage response in each sample segment) between the 5- and 11-segment samples revealed discrepant rectification effects. The measurements performed with the 5-segment multi-lead film corroborate our initial hypothesis that longer and shallower tapers lower the edge barrier for vortex nucleation as evidenced by a decrease in the critical currents that trended with the length of the tapered edge when compared with the critical currents for a common, reference edge. In contrast, the transport measurements that were performed on the 11-segment multi-lead sample indicate that there is a reduction in the critical currents for tapered edges, but shows no trend between this reduction and the length of taper. This is a surprising result since we previously observed a trend with the 5-segment sample, and therefore expect to observe a similar trend with the wider range of taper lengths belonging to the 11-segment sample because there are no obvious differences between the physical properties of these multisegment samples (aside from the number of sample segments).

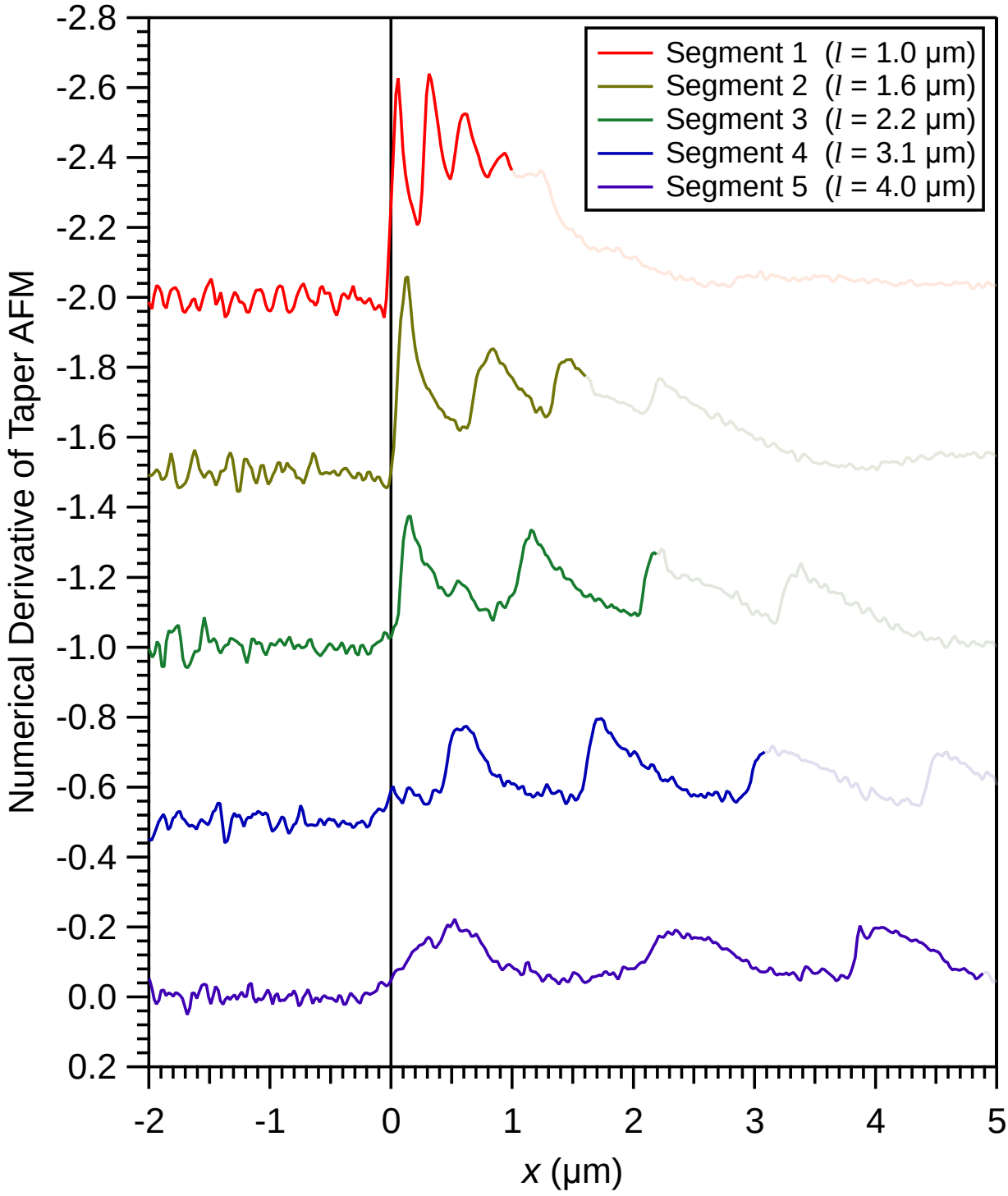

Figure 3.25: The numerical derivatives of the AFM scans of each tapered edge of the 5-segment sample presented in Figure 3.13. The portions of these curves that correspond to the tapers are colored solid while the areas of the derivative that correspond to the scans over the silicon substrate are muted. Each derivative is vertically offset by 0.5 for clarity. Refer to Figure 3.11 for a schematic that defines the taper length parameter l.

The vortex nucleation environment created by each tapered edge in the 5- and 11-segment samples were carefully considered to gain insight into the inconsistency in the rectification measurements between these samples. Recall that the force a vortex experiences when nucleating into a superconductor is proportional to the change in the vortex line-length, and thus, the derivative or slope of the film thickness at the sample edge is proportional to the force that a nucleating vortex experiences. Therefore, the numerical derivatives of the AFM profilometries of the tapered edges in the 5- and 11-segment samples (see Figures 3.13 and 3.21) were calculated and are displayed in Figures 3.25 and 3.26 respectively. These derivatives are displayed with a solid color for locations that correspond to granular aluminum and become muted for locations that correspond to the tapers that were transferred into the silicon substrate as an artifact of the milling process. The locations where each granular aluminum taper becomes a taper in the silicon substrate in the AFM derivatives were determined from the taper lengths which were obtained from comparing the profilometry of a wet-etched edge to the milled tapered edges.

First, we considered the derivatives of the tapered edges in the 5-segment sample, shown in Figure 3.25. The effects of the previously discussed interference fringes that formed in the photoresist layer during the taper exposures are observed as oscillations in the taper slopes. Of particular interest, however, is that the derivatives of the tapered edges in the granular aluminum film each terminates at a different slope, which are each coincidentally close to the average slope of the taper (as determined by the solid portions of the derivatives). Therefore, the derivatives of the tapered edges in the 5-segment sample indicate that the initial and average slopes that a nucleating vortex experiences are different for each tapered edge, which is consistent with the transport measurements of this sample.

We will now consider the slopes of the tapered edges in the 11-segment sample that are shown in Figure 3.26. Once again, the effects of the interference fringes that occur during the taper exposure of the photoresist are observed as the oscillations in the slopes of each tapered edge. However, the derivatives of the AFM profilometry of this 11-segment sample reveal another feature that is common to all the tapered edges and is not present in the tapers of the

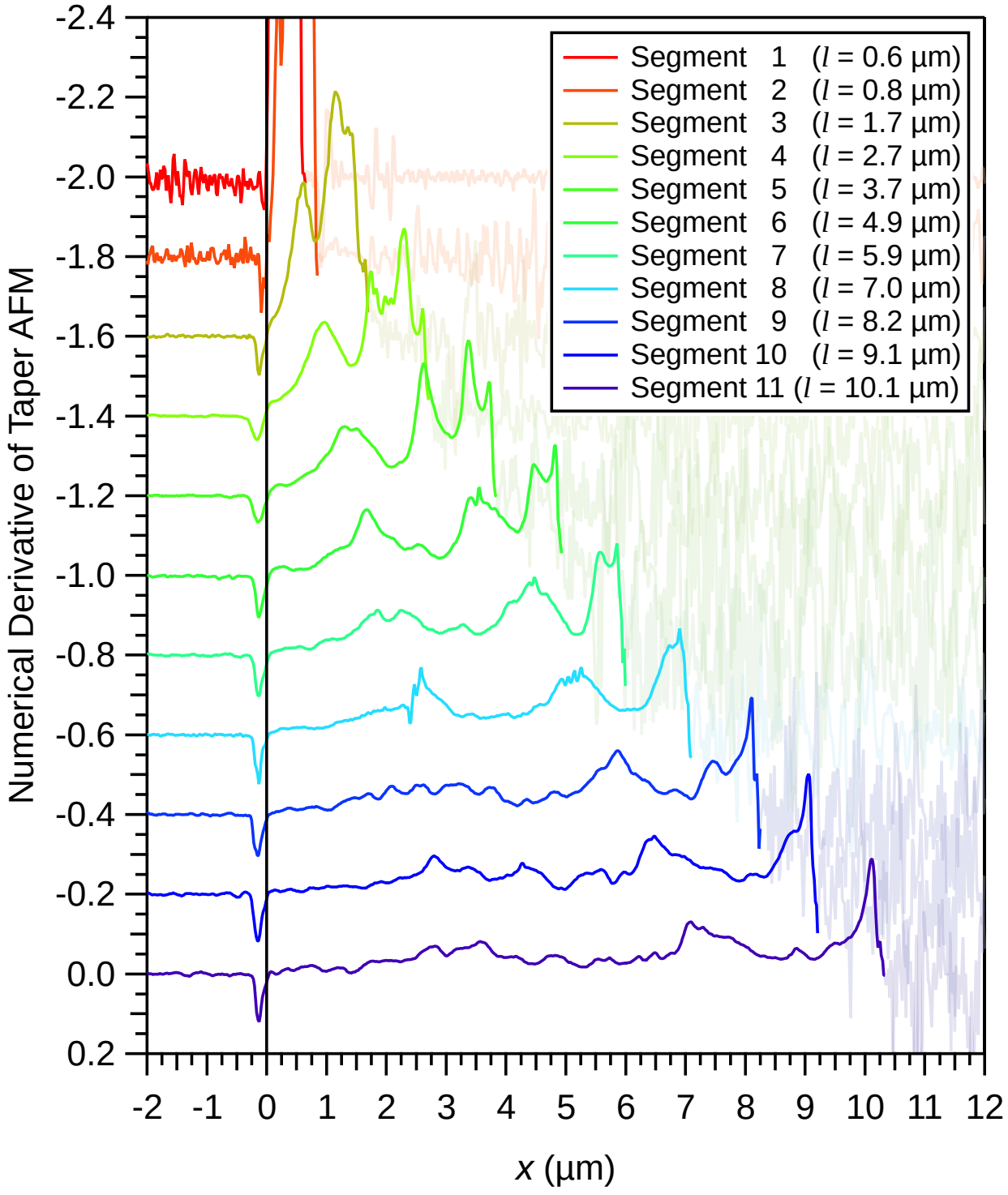

Figure 3.26: The numerical derivatives of the AFM scans of each tapered edge of the 11-segment sample presented in Figure 3.21. The portions of these curves that correspond to the tapers are colored solid while the areas of the derivative that correspond to the scans over the silicon substrate are muted. Each derivative is vertically offset by 0.2 for clarity. Refer to Figure 3.20 for a schematic that defines the taper length parameter l.

5-segment sample. A large increase in the slope of the tapers is observed in Figure 3.26 at the knife-edge of each taper just as the profilometry transitions from the granular aluminum to the silicon substrate, which appears to be roughly uniform in magnitude for each taper length. Therefore, similar applied currents are required to nucleate vortices over the initially large geometric barrier imposed by the common large slope in the knife-edge of the tapers, which agrees with the critical current measurements of the 11-segment sample (see Figure 3.23). It is still plausible that the differing taper slopes affect vortex motion once vortices nucleate into the tapered edges over the common knife-edge slope as was observed with the flux-flow resistances (see Figure 3.24).

We conclude that an important, but subtle, difference in the sample fabrication processes between the 5- and 11-segment films caused the uniform knife-edge slope in the 11-segment film. The tapers were transferred from a layer of S1805 photoresist via argon ion bombardment for both films using a magnetron sputtering system as previously described. However, the 5-segment film was bombarded for a longer time, which resulted in the partial transfer of the tapered edges into the underlying silicon substrate while the 11-segment film was bombarded for a shorter time which resulted in a minimal transfer of the tapered edges into the silicon substrate. Therefore, if the knife-edge of the tapers in the S1805 photoresist layer have a common and steep slope, then this feature would be transferred into the silicon substrate in the case of the 5-segment sample but would appear in the tapers in the case of the 11-segment sample as a result of the shorter mill time.

3.5 Conclusions

In conclusion, we explored the effects of tapers of varying lengths on the transport and nucleation properties of vortices with two multi-segment films of granular aluminum. These multi-segment films were fabricated in either a 5- or an 11-segment geometry to allow for the study of various taper lengths referenced to a common hard edge while ensuring that the film properties between each sample segment were uniform so that the only difference between the

sample segments were the taper lengths. The transport measurements performed with the 5-segment sample in the form of 0.1 μV criterion critical currents showed that the tapered edge geometry reduced the critical currents when nucleating vortices over the tapered edges when compared to the opposite driving direction that nucleated the vortices over the common, reference edge. Additionally, we observed a trend in the suppression of the critical currents with the taper length and therefore with the slope in the taper. Then, we fabricated an 11-segment multi-lead sample with longer tapers in order to explore the rectification effects from a wider range of taper lengths. The transport measurements that were performed on this sample indicated that the critical currents of the tapered edges were reduced when compared to the critical currents of the common, reference edge. However, we did not observe a trend in the suppression of the critical currents with the taper length. This discrepancy between the measurements of the 5- and 11-segment samples was evidently caused by an artifact that is present in the knife-edge slope of each taper in the 11-segment sample which was caused by a short milling time when transferring the tapers from a photoresist layer into the sample layer. So, it is entirely plausible that each taper within the 11-segment sample, will exhibit similar critical currents since the initial slope a nascent vortex experiences is similar in each tapered edge. Therefore, we have shown with the transport measurements of the 5-segment sample that the geometric barrier may be influenced by forming tapers into the sample edges where shallower tapers result in a larger suppression of the edge barrier while the uniform critical currents that were observed with the 11-segment sample are most likely a result of an unintentional uniformity in the slopes at the knife-edge of the tapers.

Chapter 4

Superconductivity in One-Dimensional Systems

The details of flux vortices within granular aluminum films were explored beginning in Chapter 1, with thickness-modulated films in Chapter 2, and with a consideration of the film edges in Chapter 3. We will now shift our focus to the details of dissipation within one-dimensional granular aluminum nanowires from this point forward.

The study of superconductivity in nanoscale geometries is particularly interesting since restricting the sizes of superconductors results in unique and emergent physics that does not manifest at larger length scales. One such property that has become the subject of significant interest is the apparent non-zero resistance of superconductors in a one-dimensional nanowire geometry where the cross-sectional dimensions of the superconductor are confined. Typically, the critical transition of a bulk superconducting material is sharp, meaning that as the material is cooled below the critical temperature T_c the resistance changes from the normal state value to zero over a narrow temperature range as the material enters the superconducting state. However, the transition of the same superconducting material in a one-dimensional nanowire geometry will not be sharp as in the case of the bulk geometry, but will rather exhibit a significantly broadened transition. For example, Figure 4.1 depicts the contrast in the critical transition widths between a superconducting In nanowire and a co-deposited superconducting In thin film; the transition belonging to the nanowire geometry is broadened when compared to the transition of the thin-film geometry.[129] This broadened transition that is characteristically observed in numerous nanowire experiments[129–164] (for a review, see Ref. 165) indicates that there exists dissipation in these superconducting systems well below T_c.

The physics of superconducting nanowires has been the focus of several early theoretical studies. In order to quantitatively characterize this dissipative phenomenon Little,[166] Langer and Ambegaokar,[167] and McCumber and Halperin[168] (LAMH) formulated a model to describe the apparent resistance of a superconducting nanowire in the framework of the time-

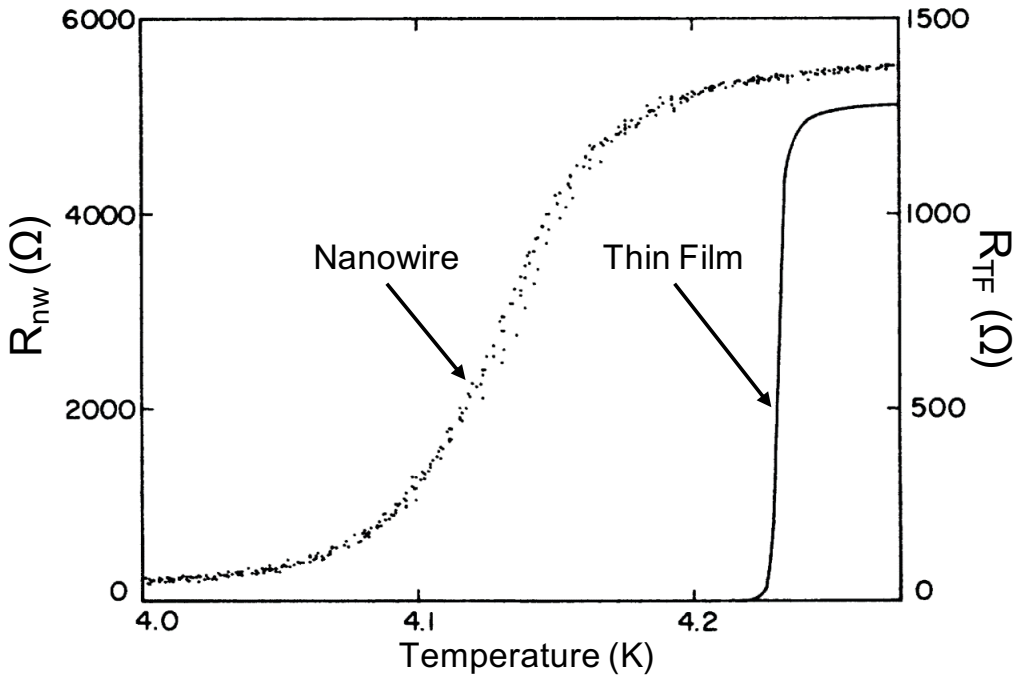

Figure 4.1: Transition measurements of a co-deposited In nanowire and thin film adapted from Figure 2 from Giordano.[129]

dependent Ginzburg-Landau (TDGL) theory. Recall that according to Ginzburg-Landau (GL) theory, the superconducting electrons within a superconducting material belong to a macroscopic many-body state that is characterized by a pseudo-wavefunction $\psi(\mathbf{r})$ called *the superconducting order parameter*. This order parameter is a complex quantity such that $|\psi|^2$ is proportional to the local density of superconducting charge carriers. Further, a change in time of the complex phase ϕ is related to a voltage within the nanowire. With these GL tools, LAMH showed that superconductors in a one-dimensional nanowire geometry exhibit dissipation in the superconducting state via *thermally activated phase slip* (TAPS) events of the order parameter. Thus, the apparent nanowire resistance can be thought of as an activation of the superconducting nanowire system over free energy barriers by thermal fluctuations within the nanowire. The GL theory and the results derived by LAMH will be discussed in further detail in later sections.

Recent advancements in nano-fabrication techniques and processes have reduced the accessible size scales of laboratory fabricated nanowires, facilitating the study of the dissi-

pation theorized by LAMH. One commonly employed nanowire fabrication technique that achieves the smallest nanowires involves scribing a channel into a substrate and then bridging the groove with carbon nanotubes. Then, the carbon nanotube bridges are coated with a superconducting material, resulting in a nanowire with a "U-shape" cross section.[130–132,135–137,139,144,145,148,151–154] Other works have attempted to produce extremely small nanowires by utilizing and combining various lithographic techniques.[133,156,169–172] For example, Morgan-Wall *et al.*[171] fabricated sub-15 nm Al nanowires via a controlled mild wet-etch with *in situ* resistance measurements of an initially 200 nm nanowire fabricated with lift-off electron beam lithography. The etching process was terminated when the nanowire achieved the desired resistance and therefore the desired cross-section. Other nano-fabrication techniques include depositing nanowires after fabrication via solution chemistry,[173] relief dry etching,[174] and even exploiting unique substrate geometries to create a dry-etch shadow.[175,176]

Experimental observations of recently developed small-scale nanowires have revealed interesting details that are not predicted by the LAMH model which generated considerable interest in these superconducting nanowires. In particular, transition measurements performed by Giordano[129,140–142] on indium nanowires with right-triangular cross sections were found to be well-described by the LAMH theory for temperatures close to T_c. However, Giordano found that at lower temperatures and for narrower wires the effective nanowire resistance deviates from the LAMH model as these nanowires exhibited larger resistances than what this model predicts.

The exact cause of the excess nanowire resistance observed by Giordano is thought to be a result of one of two possibilities. One hypothesis, phenomenologically proposed by Giordano, is that the resistance deviations are caused by the nanowire system macroscopically quantum tunneling (MQT) through a free energy barrier[129,140–142] as opposed to contributions solely from thermal activations over a barrier as proposed by LAMH. If the excess resistance observed by Giordano in superconducting nanowires are a result of MQT events, then these nanowires would be extremely impactful since there are few physical systems that truly exhibit

macroscopic quantum tunneling phenomena. However, another possible cause of the excess nanowire resistance at colder temperatures is that inhomogeneities in the cross section of the nanowire serve as preferential TAPS sites.[177–179] Inhomogeneities in the nanowire could mimic the resistance from MQT events since the phase slip rate may be influenced by constrictions in the cross section of the nanowire as a result of the dependance of the free energy barrier on the nanowire cross section. Therefore, an experiment is required to map the locations of phase slips along a nanowire to determine if a correlation between nanowire inhomogeneities and the phase slip rate exists.

The goal of the last 3 Chapters of this dissertation is to experimentally elucidate the relationship between the phase slip rate and inhomogeneities in superconducting nanowires to provide insight into the origins of low-temperature phase slips that are not well-described with the LAMH model. This Chapter will introduce the details and background of superconductivity in one-dimensional systems followed by framing the scientific importance of determining the cause of the low-temperature behavior of superconducting nanowires. Chapter 5 will present and discuss the home-built cryogenic atomic force microscope (cryo-AFM) that was used to scan nanowires as well as methods of cryogenically locating a nanowire sample with an AFM tip. Finally, Chapter 6 will present the various nanowire fabrication techniques that were implemented to create granular aluminum nanowires and the scanning experiments that were performed to locally perturb superconductivity in these nanowires to map phase slips.

4.1 Resistance in Superconducting Nanowires

As was previously discussed, one-dimensional superconducting nanowires exhibit a non-zero resistance below T_c with critical transitions that are broadened when compared to larger geometries of the same material. An expression that describes the apparent resistance in superconducting nanowires was first formulated by Little,[166] Langer and Ambegaokar,[167] and McCumber and Halperin[168] (LAMH) by considering thermal fluctuations in a one-dimensional superconductor with the time dependent Ginzburg-Landau (TDGL) theory. A similar expression

will be derived in this section by following in the footsteps of LAMH; however, in the interest of transparency and clarity, the treatment of dissipation in one-dimensional superconducting nanowires presented in the following sections will largely be performed using the Ginzburg-Landau (GL) theory rather than using the more complicated TDGL theory.

4.1.1 The Ginzburg-Landau (GL) Theory for One-Dimensional Systems

The formulation for the apparent resistance in superconducting nanowires requires a theoretical framework that describes the superconducting free energy which was developed by Vitaly Ginzburg and Lev Landau. This "triumph of physical intuition,"[4] now referred to as the Ginzburg-Landau (GL) theory, proposes that the superconducting electrons within a superconducting material belong to a macroscopic many-body state that is characterized by a complex pseudo-wavefunction $\psi(\mathbf{r})$ called *the superconducting order parameter*. Since this proposed order parameter is inherently complex, $\psi(\mathbf{r})$ at a position $\mathbf{r}$ within the superconductor can be generally expressed as

$$\psi(\mathbf{r}) = |\psi(\mathbf{r})|e^{i\phi(\mathbf{r})} \tag{4.1}$$

where $|\psi(\mathbf{r})|^2$ is proportional to the local density of superconducting electrons and where $\phi(\mathbf{r})$ represents the complex *phase* of the order parameter.[4] Additionally, note that the "pseudo-wavefunction" described in Equation 4.1 is not a true quantum mechanical wavefunction since the order parameter describes superconductivity at a local position $\mathbf{r}$ within the superconductor and does not depend on the individual positions of each of the superconducting charge carriers, that is, $\psi(\mathbf{r}) \neq \psi(r_1, r_2, r_3, ..., r_n)$.

The Ginzburg-Landau theory of superconductivity begins with the expansion of the free energy of a superconducting system in powers of the slowly varying* order parameter ψ. In the absence of an applied field, the free energy of the superconducting state is expanded as

$$f_s = f_n + \alpha|\psi|^2 + \frac{\beta}{2}|\psi|^4 + \frac{1}{2m^*}\left|\frac{h}{i}\nabla\psi\right|^2 \tag{4.2}$$

*This is required to validate the free energy expansion.[4]

where f_s and f_n denote the free energy per unit volume of the superconducting and normal states respectively and m^* denotes the effective superconducting charge carrier mass of $2m_e$.[4] Note that when $|\psi| = 0$, then $f_s = f_n$ as expected.

The signs of the parameters α and β in Equation 4.2 are determined by considering Equation 4.2 in the absence of the electron kinetic energy term and by initially assuming positive signs for α and β. Under these conditions, Equation 4.2 becomes

$$f_s - f_n = \alpha|\psi|^2 + \beta|\psi|^4 \tag{4.3}$$

and it is clear from inspection of Equation 4.3 that β must be positive to avoid arbitrary minimization of the free energy. This results in either positive or negative values of α.[4] Positive values of α allows for Equation 4.3 to be minimized at a single location at $|\psi|^2 = 0$, which only describes the material in the normal state. However, the negative α case allows for minimizations at two distinct, nonzero locations corresponding to[4]

$$|\psi|^2 = -\alpha/\beta \tag{4.4}$$

which indicates that increasingly negative α solutions leads to larger $|\psi|^2$, and therefore $\alpha \sim T - T_c$. Because positive α solutions describes the normal state and negative α yields nonzero $|\psi|^2$, then α must change from positive to negative as the superconductor is cooled below T_c which leads to a second order phase transition that occurs at T_c.

The last term of Equation 4.2, which depends on $\nabla\psi$, represents the contributions from the kinetic energy of the superconducting charge carriers. The dependence of this kinetic energy term on $\nabla\psi$ indicates that rapid spatial changes in ψ are energetically unfavorable which implies that there is a length scale associated with spatial fluctuations in the order parameter. In other words, the GL theory implies that spatial changes in ψ occur over a material-dependent length scale known as the *coherence length* ξ of the superconductor.[4] For example, Figure 4.2 depicts how $|\psi|$ changes from unity in a normalized representation to $|\psi| = 0$. One way this

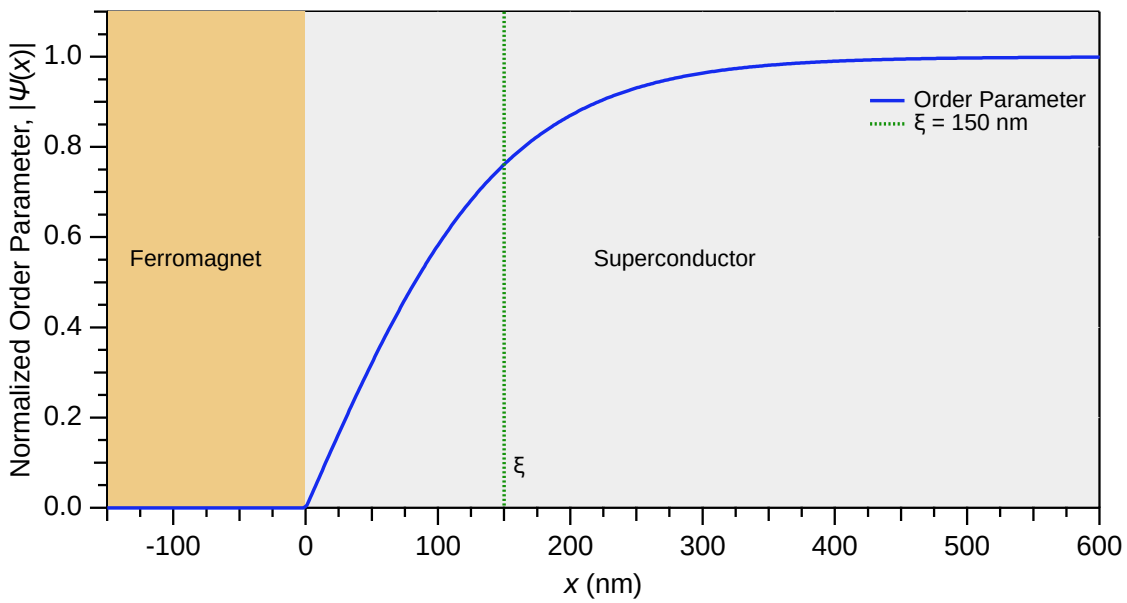

Figure 4.2: A schematic representation of the behavior of the normalized order parameter within a superconductor ($x > 0$) with $\xi = 150\,\text{nm}$ when the order parameter is pinned to $|\psi| = 0$ at $x = 0$ by a ferromagnet ($x < 0$). The order parameter magnitude changes from $|\psi| = 1$ to $|\psi| = 0$ over a length of $\sim \xi$.

may occur is if a boundary of a superconducting material (located at $x > 0$ in Figure 4.2) is adjacent to a region of ferromagnetic material (located at $x < 0$ in Figure 4.2). In this case, the order parameter must change in magnitude from $|\psi| = 1$ to $|\psi| = 0$ over a length that is similar to ξ and superconductivity becomes suppressed in this region. Therefore, the order parameter and superconductivity can be thought of as "spatially rigid" quantities where fluctuations in $|\psi|$ suppress superconductivity.

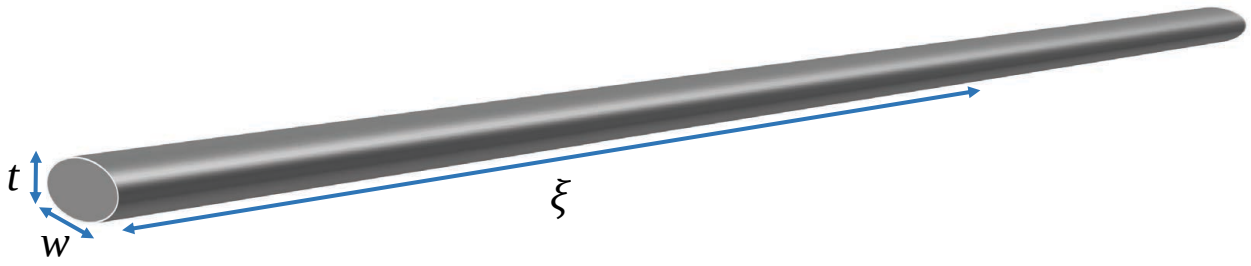

Figure 4.3: A schematic representation of a generic nanowire where the cross-sectional dimensions (t and w) are small when compared to the coherence length ξ of the superconductor.

The energetic restrictions on spatial fluctuations in $|\psi|$ results in unique superconducting behaviors in one-dimensional nanowire systems. For a superconducting system to be considered one-dimensional, the cross-sectional dimensions (the thickness t and the width w) of a superconductor must be small when compared to ξ, as depicted in the schematic of a nanowire in Figure 4.3. A superconducting system with this geometry is essentially one-dimensional because ψ must be constant across the width and thickness of the wire since these dimensions are smaller than ξ. Fluctuations in ψ, however, may still occur along the length of the wire. Therefore, to decide if a given wire should be considered as one-dimensional, it is important to carefully consider the dimensions of a superconducting wire with respect to the coherence length of the superconducting material. For example, the cross-sectional dimensions that would classify a granular Al wire as a nanowire would not necessarily classify a Nb wire as a nanowire since the coherence length of Nb ($\xi = 38\,\text{nm}$)[111, 165] is much shorter than that of granular Al ($\xi = 150\,\text{nm}$).* Typical superconducting properties of various common low-temperature superconductors are enumerated in Table 4.1.

Table 4.1: Superconducting Properties of Typical Nanowire Materials

Material	ξ_0 (nm)	λ_L (nm)	T_c (K)
Granular Al*[4, 110]	150	600	1.2–3.0**
Al[4, 110, 111, 165]	1600	157	1.14
In[141, 165]	260	65	3.4
Pb[111, 140, 165]	83	16	7.2
Sn[111, 165]	230	34	3.73
$NbSn_2$[173]	8	–	2.0–2.3
Nb[111, 165]	38	39	9.25
Ti[165]	6200	–	0.40
MoGe (film)[165]	5	720	5.5

*The dirty limit was used to obtain these results for typical granular aluminum films that were studied in this work.
**Observed in this work.

*See Chapter 2 for the calculation of the GL characteristic lengths in granular Al.

4.1.2 Winding of the Order Parameter Helix

The energetic restrictions on fluctuations in the superconducting order parameter ψ in the minuscule cross-sectional dimensions of a one-dimensional superconductor results in unique behaviors of ψ within a nanowire. In order to quantitatively describe these behaviors, it is useful to consider the current in a superconducting nanowire by using the quantum mechanical probability current **J** of the superconducting charge carriers that are represented by ψ with

$$\mathbf{J} = \frac{ihe}{2m^*}\left(\psi\nabla\psi^* - \psi^*\nabla\psi\right). \tag{4.5}$$

Substitution of the generic complex form of ψ represented in Equation 4.1 into Equation 4.5, while also noting that ψ is energetically restricted to fluctuations along the length of a nanowire x so that the gradient in the phase $\nabla\phi$ becomes one dimensional, yields an electric current in a superconducting nanowire given by

$$J = \frac{eh}{m^*}\left|\psi\right|^2\frac{d}{dx}\phi(x). \tag{4.6}$$

Equation 4.6 reveals that an applied current within a superconducting nanowire is proportional to gradients in the phase ϕ of the order parameter along the length of the nanowire. Therefore, if a constant current is applied along a superconducting nanowire then the phase must increase linearly, leading to an *order parameter helix* forming in the complex plane along the length of the wire as depicted in Figure 4.4.

The order parameter of a superconducting nanowire is also influenced by an externally applied voltage across the length of the nanowire. The influence of an applied voltage V on the order parameter phase is succinctly described with the Josephson relation,

$$\frac{d\Delta\phi}{dt} = \frac{2eV}{\hbar}, \tag{4.7}$$

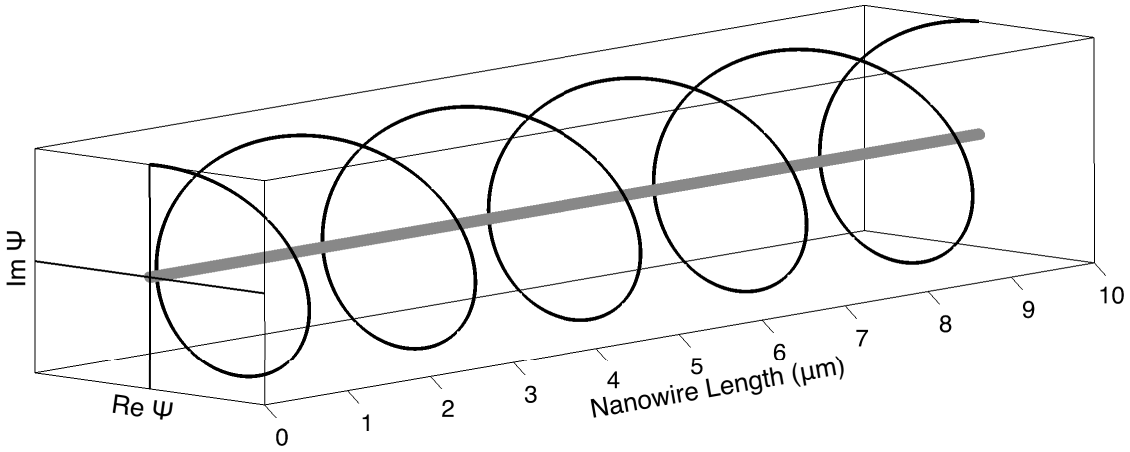

Figure 4.4: A representation of the complex superconducting order parameter (black helix) plotted along the length of a nanowire (grey) by superimposing the complex plane on the nanowire. This particular depiction represents a 5-turn helix ($\Delta\phi_{\text{ends}} = 10\pi$) for a constant applied I (or a constant $\nabla\phi(\mathbf{x})$).

which indicates that an applied voltage will result in a time rate of increase in $\Delta\phi$ between the ends of the nanowire. The Josephson relation represented in Equation 4.7 in conjunction with Equation 4.6 suggests a *winding* of the order parameter helix in the case of a constant applied voltage, which in turn corresponds to an *increasing current* within the nanowire.

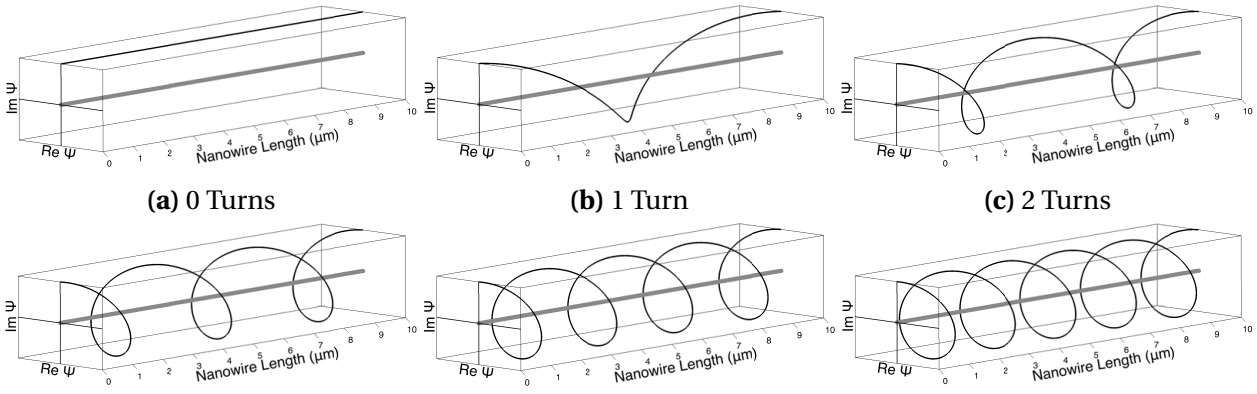

(a) 0 Turns **(b)** 1 Turn **(c)** 2 Turns

(d) 3 Turns **(e)** 4 Turns **(f)** 5 Turns

Figure 4.5: The winding of the order parameter helix (black) in a superconducting nanowire (gray) in the case of a constant applied voltage (and increasing current).

This order parameter winding is represented in Figure 4.5 as an increase of the density of turns in the helix with time when a constant voltage is applied to the ends of the nanowire. Figure 4.5a depicts the initially complex order parameter for a nanowire in the absence of current at

the instant a constant applied voltage is imposed on the nanowire. Equation 4.7 then indicates that the order parameter will begin to wind up by one turn, portrayed in Figure 4.5b. Now, Equation 4.6 dictates that an increasing current is present within the nanowire since $\nabla\phi \neq 0$. The order parameter helix continues to wind with the same constant voltage applied to the nanowire, reaching two turns in Figure 4.5c, corresponding to a further increase in the nanowire current. This trend of a constant applied voltage winding more turns in the complex order parameter helix (and therefore increasing the nanowire current) continues in Figures 4.5d-4.5f until the order parameter helix has wound by five turns along the nanowire. The order parameter helix will continue to wind by increasing the density of helix turns for as long as the superconducting nanowire is subjected to the constant applied voltage until a *critical current* is reached where superconductivity is destroyed in the nanowire.

4.1.3 Dissipation from Phase Slips - The LAMH Model

Now that the basic principles and theories of superconductivity in one-dimensional nanowire geometries has been described, the origin of the apparent resistance in these nanowires can be discussed. As mentioned previously, the critical transitions of superconductors in a nanowire geometry are broadened when compared to the critical transitions of the same material in film geometries (see Figure 4.1). This onset of resistance in superconducting nanowires below the critical temperature T_c was first theoretically described by Little,[166] Langer and Ambegaokar,[167] and McCumber and Halperin[168] (LAMH) who theorized that thermal fluctuations within the nanowire could cause the magnitude of the order parameter ψ to vanish, allowing the phase of ψ to slip in a *thermally activated phase slip* (TAPS) event which is accompanied by a voltage pulse. The time average of these pulses gives rise to an effective resistance V_{avg}/I.

Before the details of TAPS are explored, it is first useful to consider the resistance in a superconducting nanowire from a qualitative perspective. We showed in the previous section that the order parameter forms a helix in the complex plane with a constant magnitude when a volt-

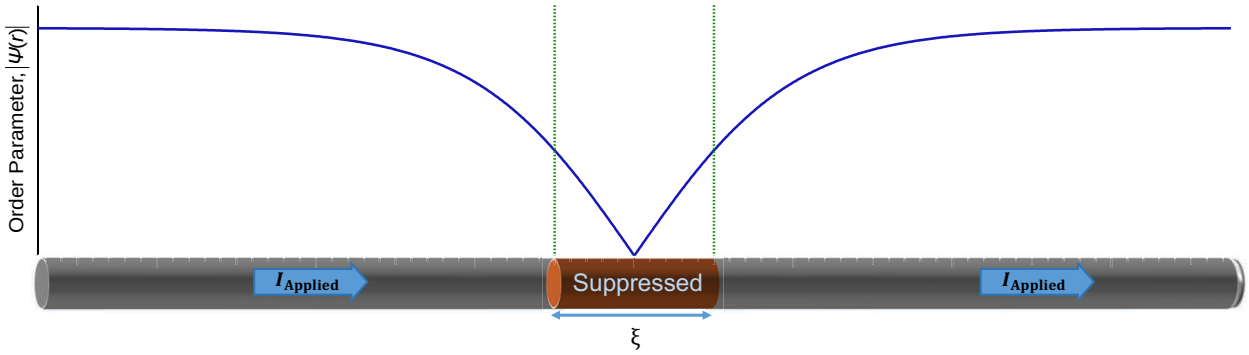

Figure 4.6: A cartoon representation of the qualitative model of the dissipation in superconducting nanowires. The superconductivity in a segment of superconducting nanowire (grey) of width $\sim \xi$ becomes suppressed (orange) by a thermal fluctuation. The order parameter magnitude in this case is superimposed on nanowire; the total fluctuation of ψ requires a distance of $\sim 2\xi$ to completely recover. Note that the order parameter magnitude only vanishes at a single, distinct point along the wire.

age is applied on the nanowire. Now consider a thermal fluctuation in the superconducting nanowire that causes $|\psi|$ to vanish somewhere in the order parameter helix. The total length along the nanowire where $|\psi|$ is changing spans a distance of $\sim 2\xi$ since each change in $|\psi|$ occurs over a length scale of $\sim \xi$. This fluctuation in $|\psi|$ is modeled as a segment of the nanowire of length $\sim \xi$ with suppressed superconductivity as shown in Figure 4.6. Therefore, the change in the free energy that is required to cause a suppression in superconductivity for such a wire segment is given by

$$\Delta F_0 = \text{Energy Density} \times \text{Volume} = uA\xi \tag{4.8}$$

where $u = \frac{8\sqrt{2}}{3}\frac{H_c^2}{8\pi}$ (see *Introduction to superconductivity*[4]) represents a superconducting energy density and the volume of the suppressed wire segment is $V = A\xi$, where A is the cross-sectional area of the wire.

The phenomenon responsible for the suppression of superconductivity in segments of nanowires that was just qualitatively discussed is the *phase slip*. When the magnitude of ψ vanishes, then the complex phase of the order parameter (see Equation 4.1) is undefined and may "slip" by $\pm 2\pi$ (to preserve continuity) to add $(+2\pi)$ or remove (-2π) windings from the order parameter helix. In the absence of an applied current, $+2\pi$ or -2π events are equally likely. We will later show that if a current exists within the nanowire, then phase slips that remove a turn

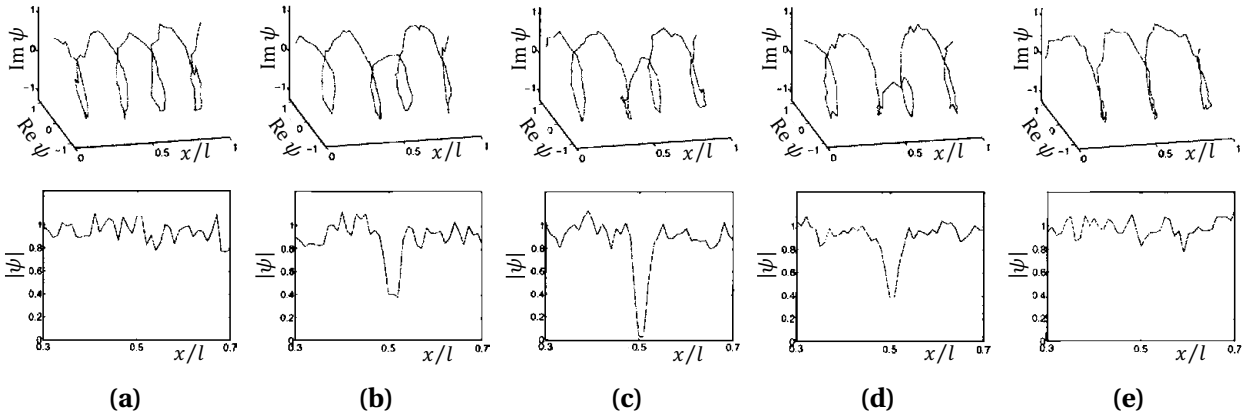

Figure 4.7: Simulations performed by Qian *et al.* of a thermally activated phase slip event in a superconducting nanowire ring with periodic boundary conditions.[180] The order parameter magnitude at each stage is plotted beneath the corresponding complex helix. The order parameter helix is initially wound by 4 turns (**(a)** and **(b)**) and then has 3 turns (**(d)** and **(e)**) after the phase slip event **(c)**.

from the helix (-2π) are favored. Figure 4.7 depicts numerical modeling performed by Qian *et al.* of the magnitude and complex components of the order parameter along a superconducting nanowire ring* of length $l = 32\pi$ during a TAPS event.[180] These simulations were performed via a saddle-point minimization method and employed the time dependent Ginzburg-Landau (TDGL) formulation using a Langevin noise term.[180] Figure 4.7a shows the 4-turn order parameter helix plotted in the complex plane overlaid along the length of the nanowire ring, represented by the z-axis. A companion plot of the normalized magnitude of ψ is also shown below the order parameter helix plot at each stage during the phase slip. In this configuration (Figure 4.7a), the normalized order parameter magnitude is constant (on average) and non-zero implying that the entire length of the nanowire ring is in the superconducting state. The order parameter magnitude becomes suppressed in Figure 4.7b as a thermally activated phase slip begins. Once $|\psi|$ vanishes at $x/l = 0.5$ in Figure 4.7c, the phase becomes undefined and unwinds by 2π. The order parameter magnitude recovers after the phase slip event and the resulting helix now has one fewer turn as shown in Figures 4.7d and 4.7e.

*A superconducting nanowire ring is simply a nanowire with cyclic boundary conditions, so, these results are still largely applicable to the case of nanowire systems without cyclic boundary conditions.

Each phase slip event is accompanied by a Josephson voltage pulse that is described by Equation 4.7 resulting from the change in the phase of ψ. Therefore, the resulting voltage pulse may be understood by integrating Equation 4.7

$$\int d\Delta\phi = \int \frac{2eV(t)}{\hbar} dt \tag{4.9}$$

and since the phase changes by $\Delta\phi = \pm 2\pi$ to wind (+) or unwind (−) the order parameter helix, the left hand side becomes

$$2\pi = \frac{2e}{\hbar}\int V(t)\,dt \quad \longrightarrow \quad \int V(t)\,dt = \frac{h}{2e} = \Phi_0 \tag{4.10}$$

which indicates that the integral of the voltage pulse from each phase slip event is equivalent to the flux quantum Φ_0.

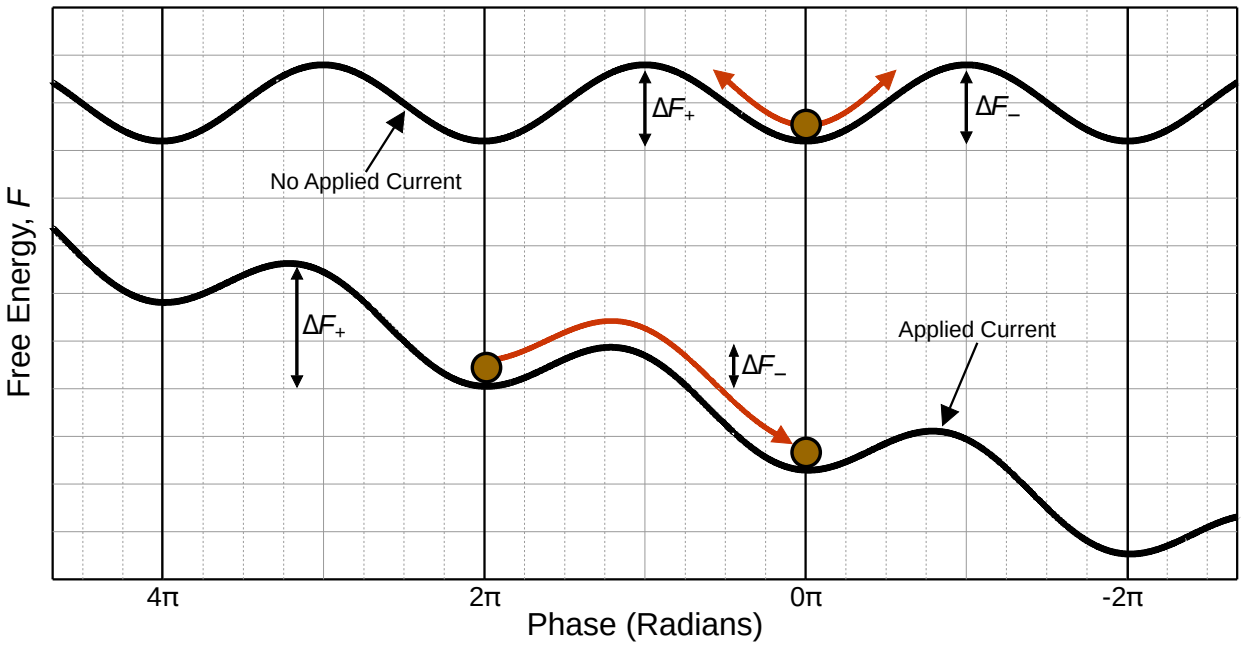

Figure 4.8: A schematic depiction of the free energy landscape (black sinusoidal curves) experienced by a superconducting nanowire system (orange ball) in the absence of (upper) and in the presence of (lower) an applied current. The relative right and left barrier heights are labelled as ΔF_- and ΔF_+ respectively with the red arrows denoting the path that the superconducting system may take in this space resulting from a thermal activation over one of these barriers.

A TAPS event requires a thermal activation of the superconducting nanowire system from a local free energy minima to another, nearby local minima over a free energy barrier. Schematic representations of examples of free energy landscapes are illustrated in Figure 4.8 for the case of no applied current (upper) and with an applied current I (lower), where adjacent local minima are separated by a phase difference of $\Delta\phi = 2\pi$ and the superconducting state within these landscapes is represented by the orange ball. In this representation, leftward minima are arbitrarily chosen to correspond to an increase in the phase difference while rightward minima correspond to a decrease in the phase. In the absence of an applied current (upper landscape in Figure 4.8), the potential landscape is horizontal and the energy barrier difference for rightward and leftward adjacent local minima, denoted by ΔF_- and ΔF_+ respectively, are equivalent and equal to ΔF_0 (see Equation 4.8). Therefore, a thermal fluctuation is equally likely to activate the superconducting state (orange ball) over either ΔF_+ or ΔF_-. This indicates that phase slips that either wind or unwind the order parameter helix are also equally likely to occur in the absence of a current in the nanowire which results in a voltage noise.[4] However, this potential landscape will become tilted if a current I exists within the nanowire,[4] depicted by the lower energy landscape in Figure 4.8. In this case, $\Delta F_- < \Delta F_+$ where

$$\Delta F_\pm = \Delta F_0 \pm \frac{hI}{4e}, \tag{4.11}$$

which indicates that TAPS that activate the system rightward in Figure 4.8 and over ΔF_- to unwind the order parameter helix by $\Delta\phi = -2\pi$ are much more likely to occur.[4] Also note that each TAPS event that unwinds a turn from the order parameter helix will also lower the current within the nanowire (see Equation 4.6).

The resistance observed in nanowires below the critical temperature is a result of a time-average of the Josephson voltages that are generated from numerous unwinding TAPS events that preferentially occur when a current is present within a superconducting nanowire. In the presence of a current, the relative free energy barrier height difference δF between the two phase slip directions (unwinding and winding) for a tilted free energy washboard landscape is

given by

$$\delta F = \Delta F_+ - \Delta F_- = \frac{hI}{2e} \tag{4.12}$$

where $\Delta F_\pm = \Delta F_0 \pm \delta F/2$ (see Equation 4.11). LAMH assumed that the phase slip rate in either direction is exponentially dependent on the corresponding free energy barrier heights. This assumption yields an expression for the phase slip rate at a temperature T of

$$\frac{d\left(\Delta\phi\right)}{dt} = \Omega\left[\exp\left(-\frac{\Delta F_0 - \delta F/2}{kT}\right) + \exp\left(-\frac{\Delta F_0 + \delta F/2}{kT}\right)\right] \tag{4.13}$$

where Ω is a phase-slip attempt frequency.[167,168] McCumber and Halperin qualitatively described Ω as a ratio of the number of independent segments that can experience a phase slip N_w in a nanowire of length L to a characteristic time τ which is typically on order of 10^{-9} s and inversely proportional to $\Delta T = T - T_\mathrm{c}$.[168] Recall that the superconductivity in a segment of wire of length ξ becomes suppressed during a phase slip which indicates that N_w may be approximated as $N_\mathrm{w} \approx L/\xi$ and gives an attempt frequency of

$$\Omega \approx \frac{N_\mathrm{w}}{\tau} \approx \frac{L}{\xi\tau}. \tag{4.14}$$

McCumber and Halperin continue to evaluate the attempt frequency via the TDGL theory to obtain a more accurate, temperature-dependent form of Ω.[168] However, these details are inconsequential to the experiments that are performed in this work since the arguments that we will make rely on the functional form of the nanowire resistance rather than on the exact prefactors. Therefore for clarity, we will use the previously described qualitative model that is represented by Equation 4.14.

LAMH then compared the phase slip rate to the Josephson relation (Equation 4.7) to obtain an expression for the apparent resistance in superconducting nanowires in the presence of a current. We now equate Equation 4.13 to Equation 4.7 and employ a hyperbolic sine identity to obtain

$$\frac{d\left(\Delta\phi\right)}{dt} = \frac{2eV}{\hbar} = 2\Omega e^{-\Delta F_0/kT}\sinh\left(\frac{hI}{4ekT}\right). \tag{4.15}$$

In the limit of small applied currents ($I \ll 4ekT/h$) we may rewrite the hyperbolic sine as

$$\sinh\left(\frac{hI}{4ekT}\right) \approx \frac{hI}{4ekT}, \tag{4.16}$$

which allows us to solve for V/I and indicates an ohmic resistance. After one final rearrangement, the effective resistance resulting from numerous TAPS in a superconducting nanowire with a current becomes

$$R_{\mathrm{TAPS}} = \frac{V}{I} = \frac{\pi\hbar^2}{2e^2kT}\Omega e^{-\Delta F_0/kT} \tag{4.17}$$

which reveals an exponential dependence of the nanowire resistance on ΔF_0 and therefore on the cross-sectional area and on ξ (see Equation 4.8).[4,167,168] This exponential dependence of the nanowire resistance on the cross-sectional area of the nanowire indicates that TAPS are more likely to in narrower nanowires, resulting in an exponentially enhanced resistance when compared to a wider nanowire. It is also important to note that the above formalism is not valid very near T_c since the free energy barrier and the attempt frequency both go to zero when the wire becomes normal.[4]

4.2 Evidence of Phase Slips in Superconducting Nanowires

Numerous experimental observations of superconducting nanowires of various materials have reported a non-zero nanowire resistance below T_c.[129–164] However, some of these experiments exhibit resistances that cannot be explained by the LAMH model alone.[129–131,141,142,145,147,154,156,157,159] One such experiment that is of particular interest is the work performed by Giordano on In nanowires[129,141,142] which showed that narrow In nanowires at very low temperatures possess an excess resistance that is not predicted by the LAMH model. This deviation from the LAMH model, first observed by Giordano, has spurred significant experimental and theoretical interest in an attempt to determine the origin of this excess resistance.

These studies have proposed that this excess resistance is caused, at very low temperatures, by direct quantum tunneling of the superconducting nanowire system through the barrier separating different winding numbers.[130,131,145,147,154,156,159,164,181–184] These one-dimensional systems would be highly interesting since there are few systems that truly exhibit macroscopic quantum tunneling phenomena. However, a more mundane explanation that must be considered in light of the exponential dependence of the TAPS rate on thickness is that the resistance at low temperatures is dominated by ordinary TAPS events in unintended narrow regions of the wires.[136,151,164,177,178,185] It is thus important to determine which of these theories is the cause of the LAMH deviation to fully understand the dissipation in superconducting nanowires.

The study of narrow superconducting nanowires poses a technically difficult fabrication challenge that has recently experienced several avenues of success. There are three main fabrication techniques that have been used to create nanowires. The first is to employ a lift-off technique by metalizing a high-resolution resist after exposing a nanowire pattern. Then, the resist is washed away to leave behind a nanowire in the desired pattern and size scale.[133,156,169–172] Another class of fabrication techniques uniformly metalizes a substrate followed by wet- or dry-etching to remove any unwanted material while protecting the nanowire with an ultranarrow etch mask such as poly(methyl methacrylate) (PMMA) resist[174] or a predefined geometry in the substrate[175,176] that creates a shadow when ion milling at an angle. The final fabrication category that is capable of producing the narrowest nanowires first forms trenches in the surface of a substrate. Then, these trenches are bridged by carbon nanotubes and then metalized resulting in nanowires with a "U-shape" cross-section.[135,145,151,186] Although this final method is capable of fabricating ultra-narrow nanowires, in our experiments we will primarily focus on employing scanning electron microscope (SEM) lithography in combination with dry- and wet-etch techniques. The details of SEM lithography and the various nanowire fabrication techniques that were explored in this work are discussed in Chapter 6.

4.2.1 Evidence for TAPS and MQT Regimes

The experiments performed by Giordano were among the first studies to observe a deviation from the LAMH model in superconducting nanowires. In these experiments, Giordano measured the critical transitions of various In nanowires with right-triangular cross-sections and discovered that the narrowest wires exhibited an excess resistance that could not be explained by the TAPS model formulated by LAMH.[129,141,142] Giordano attempted to explain this excess resistance via phase slips that are cause by a macroscopic quantum tunneling (MQT) of the nanowire system trough a free energy barrier in addition to the LAMH model.[129,141,142] Therefore, we will present the experiments and findings made by Giordano in order to understand the nature of the TAPS and proposed MQT resistance regimes.

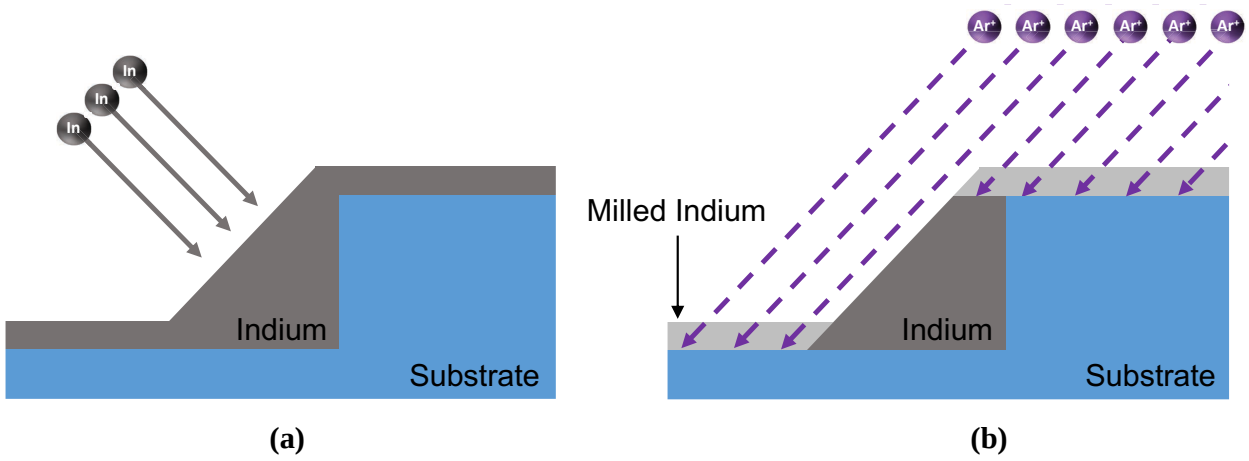

Figure 4.9: An illustration of the step-edge milling method for the fabrication of roughly right-triangular cross-section nanowires used by Giordano.[175,176] **(a)** Indium is deposited at an angle with respect to the step-edge in the substrate. **(b)** The metalized step-edge is milled at an angle such that the step-edge forms a shadow that protects the indium within the shadow.

One of the first examples of a successful nano-scale fabrication technique is the dry-etch process employed by Giordano to fabricate right triangular cross-sectional nanowires.[175,176] In this technique, a sharp step-edge is first patterned and transferred into a substrate and then metalized with the desired material (in this case In), shown in Figure 4.9a. Then, the metal-coated substrate is milled at a large angle so that the step-edge in the substrate creates a shadow

that protectes the nanowire material, shown schematically in Figure 4.9b. This technique results in a right-triangular cross-sectional nanowire with an effective width of $W_{\text{eff}} = \sqrt{A_\Delta}$, where A_Δ is the area of the right-triangular cross-section. The effective widths of nanowires that were fabricated by Giordano with this technique were typically on order of $40 \sim 70\,\text{nm}$.[129,141,142]

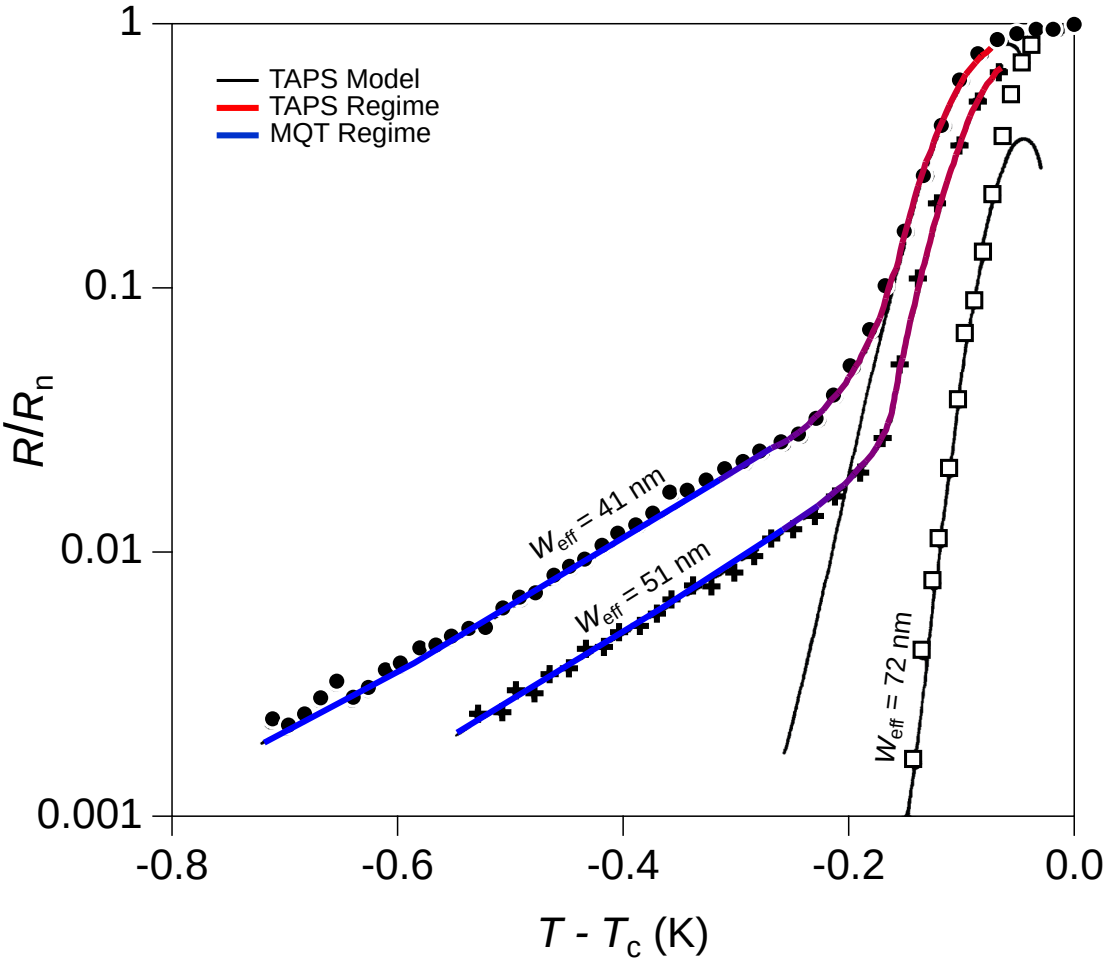

Figure 4.10: Transition measurements of right-triangular In nanowires adapted from Figure 1 from Giordano.[141] The solid black curves are fits to the LAMH model while the red and blue curves utilize both the MQT and TAPS terms. The data is well described by the LAMH model close to T_c; however, the resistances of the thinner wires significantly deviates at colder temperatures and is described by the inclusion of the MQT term to the nanowire resistance.

Cryogenic measurements performed by Giordano of the right triangular cross-sectional In nanowires revealed two distinct resistance regimes. Figure 4.10 plots the transitions of three In nanowires of various effective widths W_{eff} on a normalized log scale.[141] The LAMH the-

ory (Equation 4.17) is fit to the resulting data as the solid black curves. The widest wire exhibited good agreement with the LAMH model (Equation 4.17), indicating that the resistance below T_c is entirely caused by TAPS for this wire.* However, the narrower wires revealed an unexpected deviation from the LAMH model. The transition measurements of these wires close to T_c are well described by the LAMH model, but as the temperature was lowered below $T - T_c \gtrsim -0.25\,\mathrm{K}$, the wire resistance strongly deviates from the TAPS model predicted by LAMH, resulting in two distinctive regimes.[129,141,142]

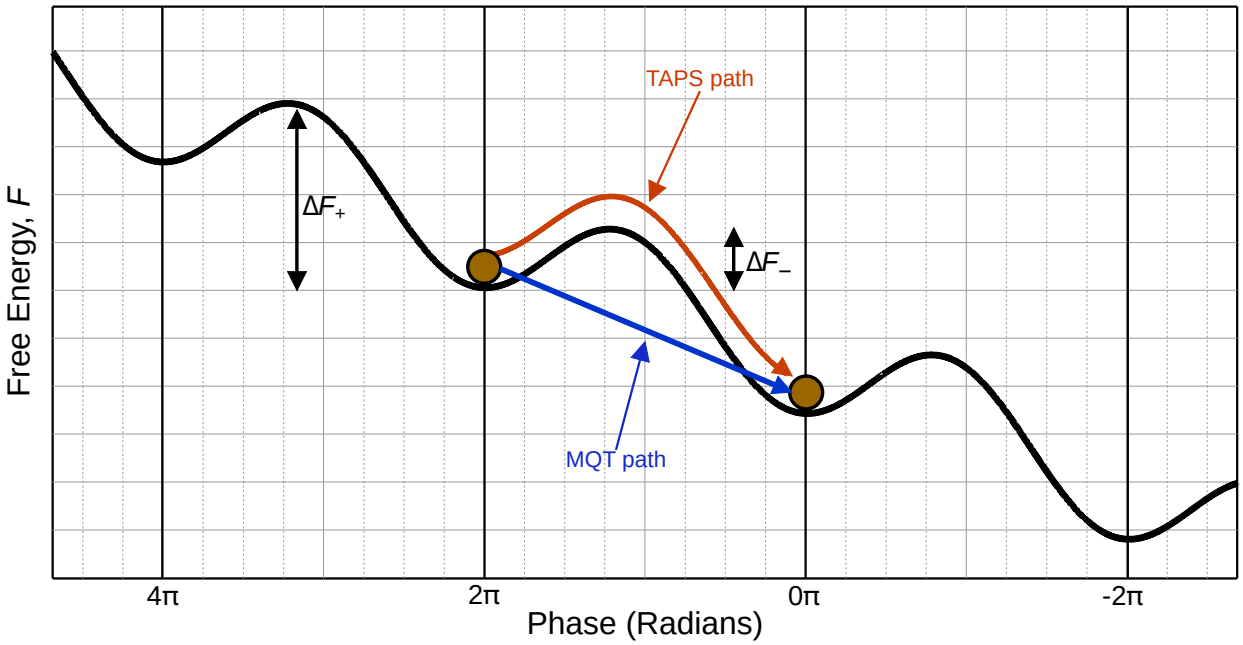

Figure 4.11: A schematic representation of free energy washboard potential for a superconducting nanowire with an applied current. Thermally activated phase slips are represented by the red path and the proposed tunneling phase slips are represented by the blue path.

In order to explain the unexpected behavior of the low-temperature nanowire resistance for the narrower samples, Giordano proposed another type of phase slip. At low temperatures where TAPS become less likely, Giordano suggests that rather than a thermal activation *over* a free energy barrier, the order parameter tunnels *through* the free energy barrier result-

*Recall that the LAMH model fails near T_c since $\Delta F_0 \to 0$ at T_c by definition. This is why there is a nonphysical turn over in the wire resistance near T_c.

ing in a quantum tunneling phase slip (QTPS) via a macroscopic quantum tunneling (MQT) event.[129,141,142] Figure 4.11 represents the distinction between TAPS and MQT events with respect to the qualitative free energy landscape. Since each minimum in the free energy landscape is separated by $\Delta\phi = 2\pi$, the phase will unwind by 2π when the nanowire system tunnels though ΔF_{-}. The form of the resistance that was proposed by Giordano resulting from QTPS is given by

$$R_{\mathrm{MQT}} = A\frac{l}{\xi}\left[\frac{\Delta F_0}{\hbar\tau}\right]^{1/2} e^{-B\Delta F_0\tau/\hbar} \tag{4.18}$$

where A and B are phenomenological fitting parameters and τ is a characteristic Ginzburg-Landau timescale.[129,141,142] MQT events that would wind the phase by 2π corresponding to the system tunneling through ΔF_{+} (in the presence of an applied current) are extremely unlikely since the tunneling probability is exponentially dependent on the barrier height. Since TAPS and MQT events can occur concurrently, Giordano proposes that the resistance in a nanowire is generally the sum of Equations 4.17 and 4.18 which is given by

$$R_{\mathrm{Total}} = R_{\mathrm{TAPS}} + R_{\mathrm{MQT}} = \frac{\pi\hbar^2}{2e^2kT}\Omega e^{-\Delta F_0/kT} + A\frac{l}{\xi}\left[\frac{\Delta F_0}{\hbar\tau}\right]^{1/2} e^{-B\Delta F_0\tau/\hbar}. \tag{4.19}$$

One important result of Equation 4.19 is that both the MQT and TAPS terms are exponentially dependent on ΔF_0 and therefore on the cross-sectional area of the nanowire. Giordano then fit Equation 4.19 to the transition measurements of the narrower nanowires. This combined fit is depicted as the blue-red curve in Figure 4.10 where the blue portion of the fit represents the MQT regime and the red portion represents the TAPS-dominated regime. Giordano found that this combined MQT and TAPS model well-described the transition measurements of the narrower nanowires, indicating that QTPS that were caused by MQT events are a plausible explanation for the observed deviation from the LAMH model.[129,141,142]

4.2.2 What is the Origin of the Low-Temperature Regime?

The discovery of the low-temperature deviation from the LAMH model observed by Giordano[129,141,142] has resulted in an extensive theoretical and experimental exploration aimed at elucidating the origin of the observed discrepancy. Numerous superconducting nanowire experiments have observed similar nanowire resistance behaviors below T_c as observed by Giordano and have also attributed the results of these studies to quantum tunneling phase slip (QTPS) events caused by a macroscopic quantum tunneling (MQT) of the nanowire system.[130,131,136,145,147,154,156,159,164] The phenomenological hypothesis of MQT and QTPS proposed by Giordano[129,141,142] to explain the discrepancy between the nanowire transition measurements and the LAMH model are corroborated by several theoretical works on homogeneous[181,184] and inhomogeneous[182] superconducting nanowires and are in good agreement with nanowire transition measurements.

While there appears to be substantial evidence that supports the claim that MQT and QTPS are responsible for the low-temperature deviation from the LAMH model, there is still speculation and disagreement about the cause of this discrepancy. Rather than MQT causing QTPS events resulting in the low-temperature resistance, other theoretical treatments[177–179] suggest that wire inhomogeneities or wire defects can exponentially affect the superconducting nanowire resistance. At low temperatures, TAPS become "frozen out" since random thermal fluctuations become too small (even in the presence of an applied current) to reliably activate the system over an adjacent free energy barrier. However, recall that ΔF_0 is proportional to the cross-sectional area of the nanowire A. Thus, at low T, TAPS may still occur at a constriction in the nanowire, represented by the cartoon in Figure 4.12, leading to an enhancement of the effective nanowire resistance compared to its uniform wire value (see Equation 4.17). Therefore, TAPS occurring at a weak point in the nanowire could plausibly explain the contribution to the wire resistance that differs from the standard LAMH model at colder temperatures.

Defects in nanowires that are fabricated in a laboratory are more subtle and complicated than the single, artificial inclusion represented in Figure 4.12. Examples of homogeneous

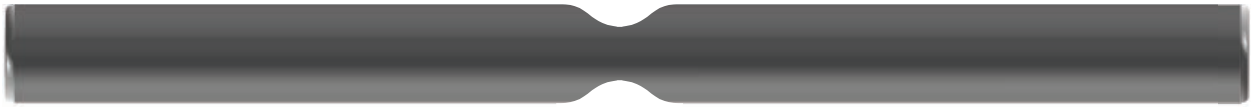

Figure 4.12: A cartoon representation of a possible defect in a nanowire. This particular defect is represented as a constriction in the cross-section of the nanowire.

nanowires fabricated by Lehtinen *et al.*[147] are portrayed in Figures 4.13a and b and of inhomogeneous nanowires fabricated by Bezryadin[135] are portrayed in Figures 4.13c and d. Both of these studies observed a low-temperature deviation from the LAMH model below a cross-over temperature. The nanowire fabricated and measured by Bezryadin[135] (Figures 4.13c and d) possesses a non-uniform cross-section, indicating that weak points along this nanowire could plausibly induce low-temperature TAPS events. However, it is unlikely that inhomogeneities in the nanowire cross-section caused the deviation from the LAMH model that was observed in the nanowire that was fabricated by Lehtinen *et al.*[147] (Figures 4.13a and b) since this nanowire is extremely uniform. Therefore, this nanowire is either exhibiting the previously discussed QTPS events that are caused by MQT or there are other forms of inhomogeneities that can influence the wire resistance. In addition to fabrication details affecting wire uniformity, nanowire inhomogeneity can also be introduced by the material granularity,[177] the wire geometry,[177,178] or by the existence of measurement electrodes.[148]

In contrast to the MQT model proposed by Giordano, the observed resistance deviation from the LAMH model has also been well-described by theoretical formulations that include wire inhomogeneities. Pai *et al.*[177] fit a power-law temperature dependence obtained via a wire inhomogeneity formulation in each temperature regime to the nanowire transitions presented by Giordano[129] and Tian *et al.*[159] and found that this formulation well-described the low-temperature regime with reasonable exponents, indicating that the dissipation in this regime for these studies are plausibly caused by wire inhomogeneities rather than QTPS. Additionally, Duan claims that MQT events could not have been observed by Giordano as a result of several discrepancies between the In nanowires that were studied and the presented theoretical formulation.[185] Duan proposes that "Josephson weak links" caused by the material granularity

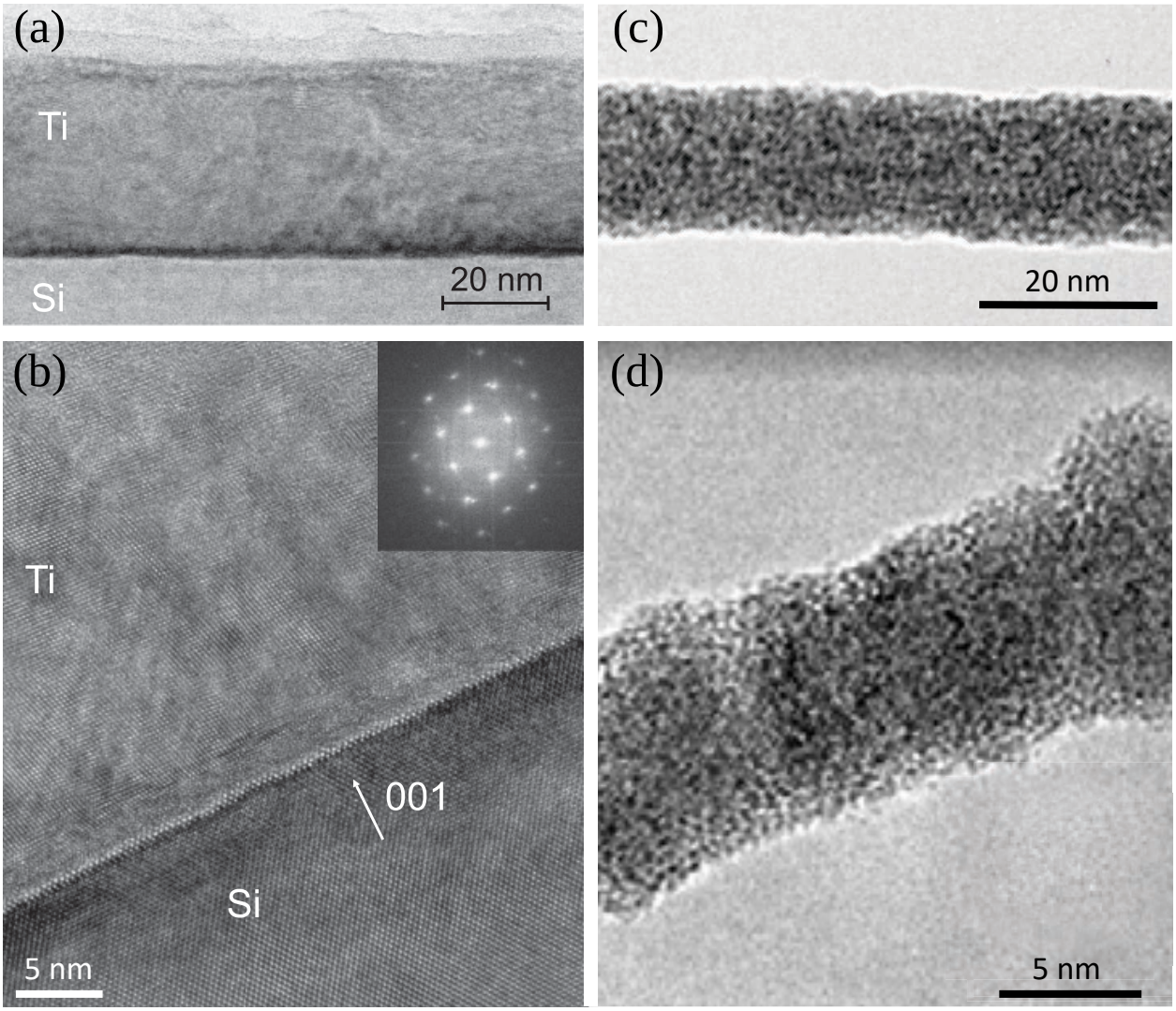

Figure 4.13: Low **(a)** and high **(b)** resolution Transmission Electron Microscopy (TEM) images of a uniform Ti nanowire fabricated using conventional liftoff and e-gun evaporation techniques adapted from Lehtinen *et al.*[147] Low **(c)** and high **(d)** resolution TEM images of a MoGe nanowire fabricated by deposition onto a carbon nanotube bridge adapted from Bezryadin.[135]

of the In nanowires are more likely the cause of the unexpected low-temperature dissipation that Giordano observed.[185] There has also been spirited debate between Zaikin *et al.*[184] and Duan[185,187] regarding the theoretical treatment of QTPS in superconducting nanowires and the scope of the observable QTPS regime.

There are additional experimental findings that further obfuscate the nature of superconductivity in one-dimensional nanowire systems. A study performed by Rogachev *et al.* on 7 nm – 15 nm diameter Nb nanowires found no evidence of a QTPS regime and found that

the nanowire transitions are well-described by the LAMH model.[151] This is possibly a result of the extremely small coherence length of pure Nb of $\xi = 38\,\text{nm}$,[111,165] implying that these nanowires are not narrow enough with respect to ξ to observe QTPS. Another study performed by Zgirski *et al.* states that previous experiments that have claimed to observe the QTPS regime performed by Sharifi *et al.*,[155] Giordano,[142] Bezryadin[136] , and Lau *et al.*[145] did not in fact observe the QTPS regime since the wire diameters in these studies were too large.[164] However, Zgirski *et al.* claims to have observed MQT events in nanowires that are below this size limit.[164] Finally, an extensive characterization of the homogeneity of Ti nanowires performed by Lehtinen *et al.* revealed that these nanowires were incredibly uniform in geometry (Figure 4.13) and in composition. This characterization ruled out any contributions from wire inhomogeneities and indicated that the observed deviations from the LAMH model were caused by QTPS at low temperatures.[147] Therefore, the cause of the low-temperature resistance regime observed by these studies is uncertain since there seems to be ample evidence that supports both the MQT and the wire inhomogeneity hypotheses.

4.3 An Experiment to Cryogenically Map Phase Slips

The uncertainty of the origin of the low-temperature phase slips demands an experiment that can determine if a correlation exists between constrictions or other inhomogeneities in a nanowire and the local phase slip rate. We postulate that if superconductivity were to be *locally* influenced in the region near a defect or inhomogeneity, then the phase slip rate would also be influenced. The previously discussed theories indicate that phase slips preferentially occur at constrictions in a nanowire since the apparent wire resistance is exponentially dependent on ΔF_0 (see Equation 4.19) and is therefore exponentially dependent on the local cross-sectional area A of the wire. So, if superconductivity is locally suppressed/enhanced in the region of a nanowire near a defect, then the local phase slip rate at the constriction will exponentially increase/decrease and cause a sharp increase/decrease in the nanowire resistance.

These ideas suggest that it may be possible to experimentally explore the contributions of local inhomogeneities to the phase slip rate and provide insight into the seemingly discrepant results between the LAMH model and the findings presented by Giordano. To do so, we propose an experiment to *map* the locations of phase slips along a superconducting nanowire using a cryogenic atomic force microscope (cryo-AFM). In this experiment, an AFM tip is scanned very near (but not necessarily in contact with) the surface of a nanowire to locally influence the superconductivity, either by using a dielectric tip that alters the capacitance per unit length and therefore the local energy density near the nanowire defect[177,181,183–185] which may either suppress or enhance superconductivity or by using a magnetically coated tip which suppresses superconductivity.* If the resistance of the nanowire is simultaneously recorded while scanning such a tip above the nanowire, then a sharp increase/decrease in the wire resistance will be observed resulting from the increase/decrease in the phase slip rate (see Equation 4.19).

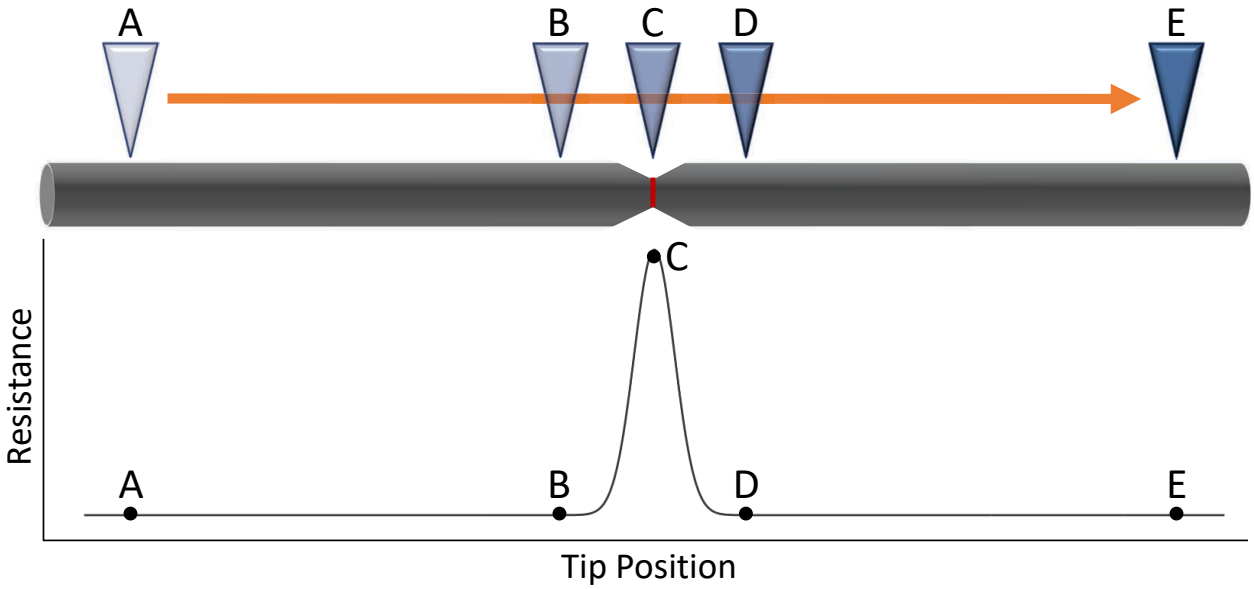

Figure 4.14: A schematic representation of scanning a superconducting nanowire (grey) with an AFM tip (blue). The corresponding resistance that is plausible from locally perturbing superconductivity within the nanowire is plotted below the scanning schematic and the tip positions A, B, C, D, and E are highlighted with the black dots. A maximum in the resistance should be observed when a tip that suppresses superconductivity is directly over a nanowire defect where phase slips are most likely to occur (red).

*There has been no theory developed that determines how a nanowire would react to a locally applied magnetic field. However, it is well known that applied magnetics fields suppress superconductivity.

Figure 4.14 schematically depicts the process of a cryogenic scanning experiment performed on a nanowire with a single defect site, which is similar to the situation considered by Vanevic *et al.*[183] As the tip is scanned above the wire from position A to position B at a constant temperature that is just below the critical temperature, then a resistance should be observed since phase slips are presumably occurring at the defect site. The tip then comes into close proximity with the defect as the tip is scanned from B to C. For example, consider that this tip suppresses superconductivity, and recall from Equation 4.19 that the resistance observed from phase slips is exponentially dependent on the free energy barrier ΔF_0 between the superconducting and normal states of the nanowire. In this case, once the tip reaches position C, the tip suppresses superconductivity enough to strongly increase the TAPS or QTPS rates at the defect due to the lower energy barrier height from the constriction. This would lead to a measurable increase in the resistance that is measured concurrently between the two ends of the wire. The tip then continues to position D and the initial resistance is once again observed as the tip is scanned from D to E. In this way, the locations of phase slip events may be indirectly imaged as changes in the overall resistance of the nanowire, and may be potentially correlated to nanowire inhomogeneities.

In order to successfully perform a cryogenic scanning experiment of this kind, two key components are required. First, we require a cryogenic scanning technique that is capable of both directly imaging a substrate surface to locate the nanowires and that is capable of indirectly scanning the nanowire. Chapter 5 will focus on the construction, details, and implementation of a home-built cryogenic atomic force microscope (cryo-AFM) which was used in combination with a unique mapping scheme to locate the nanowires at cryogenic temperatures. Second, we need to fabricate nanowire samples that can be measured with the available cryostat that also exhibit dissipation below the critical temperature. This will require delicate sample fabrication using techniques that are capable of producing nanometer-scale features to create granular aluminum nanowires. The fabrication and scanning experiments that were performed on these nanowires will be discussed in detail in Chapter 6.

Chapter 5

The Cryogenic Atomic Force Microscope (Cryo-AFM)

As outline in Chapter 4, the origin of the apparent resistance in one-dimensional superconducting systems is not entirely understood and requires an experiment that is capable of providing additional insight into the nature of this dissipation. We also saw in Chapter 4 that the dissipation exhibited in superconducting nanowires can be thought of as *thermally activated phase slip* (TAPS) events of the superconducting order parameter ψ that occur within the nanowires. These TAPS events cause discontinuous slips of $\pm 2\pi$ in the phase of ψ that may occur when a thermal fluctuation causes the magnitude of ψ to locally vanish. However, experiments performed by Giordano on narrow indium nanowires (which were discussed in detail in Chapter 4) exhibited larger sub-T_c resistances that could not be explained by only this TAPS model within a nanowire.[129,140–142] In an attempt to interpret the observed excess nanowire resistance, Giordano proposed that phase slips may also be caused by macroscopic quantum tunneling (MQT) events of the nanowire system in addition to TAPS events[141] and found that the inclusion of these *quantum tunneling phase slip* (QTPS) events explained the excess resistance in narrow indium nanowires.

The discrepancy between the observations made by Giordano and the TAPS model has caused considerable experimental[130,131,136,145,147,154,156,159,164] and theoretical[177–179,181,182,184] investigation of these low-temperature phase slips. While there seems to be evidence that MQT events are the cause of the low-temperature nanowire dissipation, other theories propose that constrictions or defects in the nanowires could elicit TAPS events at a different rate. These competing theories therefore demand an experiment that can provide insight into the nature of these phase slips by determining if a correlation exists between the locations of phase slip events and any inhomogeneities in the nanowire.

It is useful to briefly describe the proposed phase slip mapping experiment that employs a cryogenic atomic force microscope (cryo-AFM), which was discussed in detail in Chapter 4.

First, an AFM tip is scanned very near the surface of the nanowire (but not necessarily in direct contact with the sample), then superconductivity may be plausibly influenced by either a dielectric or magnetic AFM tip. The four-probe nanowire resistance is simultaneously recorded as the cryo-AFM tip is scanned above the nanowire and an exponential increase or decrease in the resistance should be observed resulting from the change in the phase slip rate as the AFM tip passes near a defect along the nanowire. In this way, the locations of preferential phase slip events may be indirectly imaged along a superconducting nanowire. An experiment of this kind requires an indirect imaging technique that can be performed at cryogenic temperatures and that is capable of influencing superconductivity over a small region of the nanowire, such as contactless cryogenic atomic force microscopy.

We therefore require an instrument that is capable of scanning an AFM tip at cryogenic temperatures in order to perform the proposed scanning experiment. So, we built a cryogenic atomic force microscope (cryo-AFM) scan head that is compatible with the available home-built cryostat. This cryo-AFM is capable of performing coarse positioning of a sample substrate above a self-sensing AFM probe with a three-axis stick-slip positioner. Then, the cryo-AFM scan head may perform fine movements of as well as scan the self-sensing AFM probe with various piezo actuators. Additionally, the self-sensing AFM probe may be replaced on the scan head to allow for multiple scanning experiments that utilize a dielectric or a magnetized tip to perturb superconductivity.

Each scanning experiment to influence the local superconductivity of a nanowire will also require the precise placement of the cryo-AFM tip with respect to the nanowire sample at cryogenic temperatures. Therefore, the superconducting nanowire samples must also be designed and fabricated in such a way that the substrate surface is uniquely mapped in order to facilitate finding the nanowire sample with the cryo-AFM. This Chapter will focus on the home-built cryogenic atomic force microscope (cryo-AFM) that was used to scan superconducting nanowires. Then, the methods and experiments that were implemented to locate the superconducting nanowire samples at cryogenic temperatures will be discussed.

5.1 Cryogenic Atomic Force Microscope (Cryo-AFM) Hardware

An experiment that probes the locations of phase slip events along superconducting nanowires requires a method of cryogenically scanning a tip over a nanowire to perturb superconductivity. In order to accomplish this, we built a cryogenic atomic force microscope (cryo-AFM) that is mounted onto a cryostat with a base temperature near $\sim 1.2\,\mathrm{K}$ with $25\,\mu\mathrm{K}$ stability.[109] The home-built cryogenic scanning instrument is shown in Figure 5.1 and is composed of two main assemblies that are mounted to the final stage of the cryostat. The sample stage assembly assembly (denoted with the blue bracket in Figure 5.1) consists of the sample stage that is mounted to three orthogonal ANPxyz100 stick-slip Attocube positioners,[188] which control the coarse positioning of the sample. The scan head assembly (denoted with the orange bracket in Figure 5.1) of the cryo-AFM consists of the scan head where a self-sensing AFM tip is scanned in the x–y plane with S-bender piezos and is scanned in the z plane with another piezo bender. The following sections will discuss the details of these cryo-AFM components.

5.1.1 Coarse Positioning of the Sample Stage

The silicon substrates on which the granular aluminum nanowire samples were fabricated (in a four-probe configuration) are mounted on a gold-plated copper sample stage. Figure 5.2 shows this sample stage assembly portion of the scanner. The gold-plated copper sample stage is mounted on three orthogonal ANPxyz100 stick-slip Attocube positioners which enables the coarse positioning of the nanowire substrates with respect to the cryo-AFM tip. A calibrated Cernox resistive thermometer is also mounted to the sample stage to ensure accurate temperature measurements of the nanowire sample. The sample substrates are mounted to a copper spacer block on the sample stage with gold contact fingers* which both firmly hold the substrate on the sample stage and makes four-probe electrical measurement connections to the nanowire samples.

*These fingers were harvested from a standard micro-USB connector and then soldered to a circuit board.

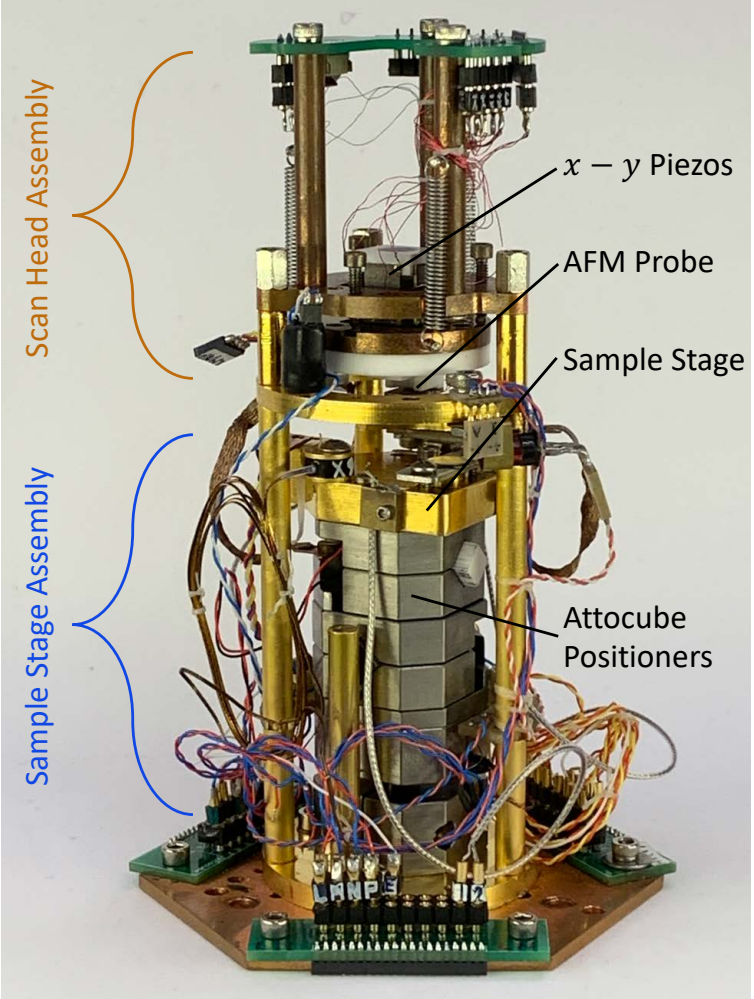

Figure 5.1: An image of the scanning instrument which is composed of an upper scan head assembly (orange) and a lower sample stage assembly (blue).

The three-axis inertial xyz Attocube positioner is a vital component when performing cryo-AFM scanning experiments. This inertial positioner controls the coarse x, y, and z positions of the sample stage with three orthogonal ANPxyz100 stick-slip Attocube positioners, which are labelled in Figure 5.2. Each Attocube positioner is composed of two titanium blocks with V-shaped channels that are lightly clamped around a square titanium rod that is attached to a piezoelectric stack. A *piezoelectric* is a material that generates a voltage when exposed to stresses or strains, or conversely, expands or contracts in the presence of an externally applied electric field.[111] Piezoelectric materials are typically composed of many permanently polarized microscopic domains. These dipole domains will either expand in the presence of an externally

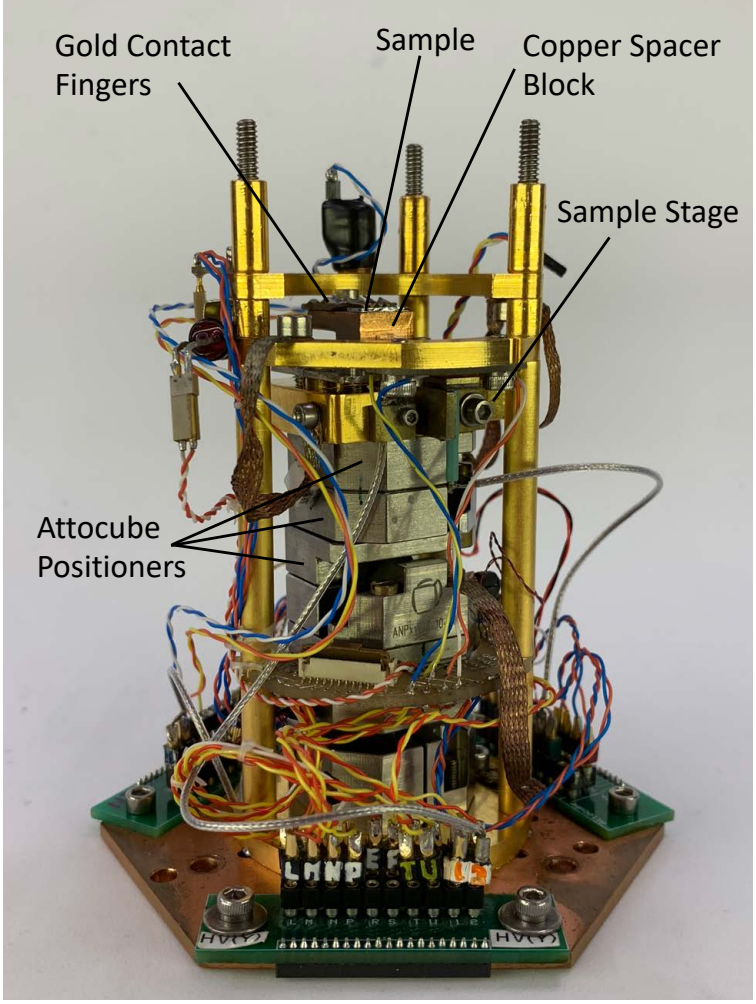

Figure 5.2: The sample stage assembly where the nanowire samples are mounted on a copper spacer block with gold contact fingers. The gold-plated copper sample stage is moved with three orthogonal xyz stick-slip Attocube positioners.

applied anti-parallel electric field or will contract in the presence of an externally applied parallel electric field. Therefore, layering multiple piezo materials and then applying a voltage will cause the stack to expand or contract depending on the poling of the dipole domains and the applied voltage.

The piezo stack voltage is controlled by an ANC150 driving controller which provides a sawtooth voltage with an amplitude of 30 V – 70 V at a frequency of 500 Hz[188] to the piezo stack at room or cryogenic temperatures respectively. This waveform allows the Attocube axis to *step* in the desired direction by smoothly expanding the piezo stack during the "ramp" of the saw-

tooth wave. Then, the voltage is very quickly reduced in magnitude back to 0 V, which rapidly contracts the piezo stack, pulling back rapidly on the titanium rod. The force with which each titanium block half is clamped to the titanium rod is calibrated to balance the friction between these pieces such that the titanium blocks "stick" to the titanium rod during the slow ramp phase, but "slip" when the piezo stack is rapidly retracted. Therefore, the titanium blocks are moved by a single step for each sawtooth pulse.

The sample stage position is controlled at room and cryogenic temperatures by stepping each Attocube axis in either a forward or a reverse direction as was previously discussed. The step sizes of the Attocube positioners change with temperature since the capacitance of the piezos depends on the temperature and the step size depends on the piezo capacitance.[189] As a result, the step size for each positioner is drastically reduced at cryogenic temperatures when compared to room temperature. For reference, we found that the x and y Attocubes have step sizes of $\sim 0.55\,\mu$m at room temperature which are reduced to $0.07\,\mu$m at 4.2 K. The z Attocube also has reduced step sizes when cooled; however, this axis is either moved with or against gravity so the step sizes in each direction are not identical. At room temperatures, the step sizes of the z Attocube are $0.96\,\mu$m (with gravity) and $0.78\,\mu$m (against gravity) which are reduced to $0.15\,\mu$m (with gravity) and $0.08\,\mu$m (against gravity) at 4.2 K. Understanding the relationship between the step sizes of each Attocube positioner and the temperature is essential in properly positioning the sample stage with respect to the cryo-AFM tip to scan nanowire samples.

The position of the sample stage is determined from a capacitive position sensor[190] as the Attocube drives the sample stage. The lower electrodes of the position sensor are fixed to the scanner frame (which does not move) and are segmented into quadrants. To measure the lateral position of the sample stage, each quadrant is driven with a different sine wave voltage of uniform frequency and amplitude, but are sequentially phase-shifted by 90° from one another. The upper position sensor electrode is then attached to the virtual ground of the current input of a lock-in amplifier and is attached to the Attocube stack. When the Attocube moves, the upper electrode also moves above the lower electrode quadrants and the resulting injected cur-

rent from each quadrant phase are measured by a two-phase lock-in amplifier to determine the x and y positions of the upper electrode with respect to the lower electrodes. Since the lower quadrant electrodes are attached to the scanner frame, the position sensor may also be used as a sensor for the z Attocube motion as well by driving the lower four quadrants with a single phase. Then, a simple capacitive measurement determines the distance between the upper and lower electrodes when moving the z Attocube. In this way, the x, y, and z position of the sample stage (and therefore of a mounted sample) can be determined.

5.1.2 The Scan Head

In addition to a movable sample stage, contactless scanning of superconducting nanowires at cryogenic temperatures also requires a cryo-AFM scan head that can precisely position an AFM tip above a nanowire sample after coarse sample positioning has been performed. The cryo-AFM scan head, shown in Figure 5.3, is composed of two parallel pairs of S-bender piezos that drive the tip in the x and y dimensions.[191] The x and y piezos are then attached to a z piezo via machined macor glass ceramic which controls the tip height above the substrate and is also where the AFM tip is mounted. The various piezos were attached to machined macor parts via superglue, since macor has similar thermal expansion properties as the piezo ceramic. Matching the thermal contractions of glued pieces is crucial since this instrument is subjected to extremely large changes in temperature ($300\,\mathrm{K} - 1.2\,\mathrm{K}$). For example, a glue joint between the piezos and machined copper would fail as a result of the vastly different thermal expansions and contractions of these materials. The machined macor components were then attached to the copper frame of the scan head with 4–40 screws, omitting the issues caused by thermal expansions or contractions between the macor and copper pieces. We will discuss the various components of this scan head except for the unique self-sensing AFM tips that were used, which will be discussed in the next section.

The cryo-AFM scan head must have minimal vibrational noise. Recall that we aim to cryogenically scan an AFM tip above a nanowire sample to perturb the local superconductivity near

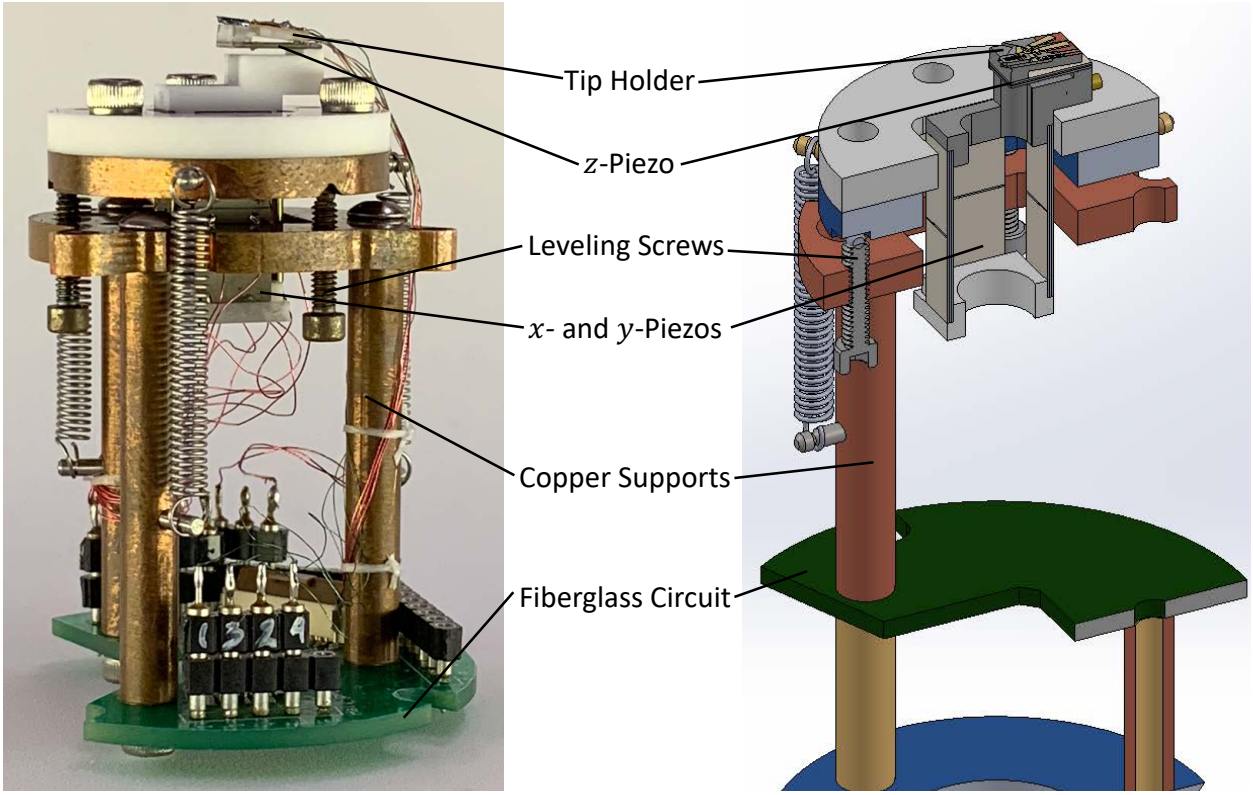

Figure 5.3: Left: An optical image and **Right:** a cutaway schematic made in SolidWorks of the cryo-AFM scan head. The macor tip holder is scanned horizontally by the x and y piezos and is glued to a z piezo which scans the tip vertically. The various macor components (white in the optical image) were built to provide gluing surfaces for the piezos. The scan head is coarsely leveled with three leveling screws and springs that are attached to copper supports.

the tip while simultaneously measuring the wire resistance in order to map phase slip locations. Since the AFM tip is intended to be scanned *above* the nanowire and not in direct contact, the various resonant modes of the scan head will result in an uncertainty in the tip height above the nanowire and therefore will affect how the tip influences the local superconductivity along the nanowire sample. Large vibrations of the tip position may therefore introduce noise in the indirect resistance imaging of the wire since either the dielectric or magnetic effects from the tip are strongly dependent on the height of the tip above the nanowire. Several properties will influence the resonant modes and frequencies of this device, such as the total mass supported by the x and y piezos, the lengths of the x, y, and z piezos, and the details of the AFM cantilever itself. Therefore, the scan head was designed to be as light as possible and to minimize the lengths of the x, y, and z piezos while maintaining adequate scan ranges.

The construction of the scan head required several Y-poled piezo actuators that were used to move the AFM tip below the sample substrate. Each piezo actuator that was implemented in the construction of the cryo-AFM scan head is composed of a brass shim core that is sandwiched between two layers of piezoelectric material with parallel poling directions (Y-poling). The piezo material on each side of the actuator is coated with a nickel contact layer, shown in Figures 5.4 and 5.5 with the blue and red areas, where electrical contact may be made to the piezoelectric. Then, these piezo actuators may be bent in an arc-like shape by applying the same voltage to each side while grounding the center brass shim. With these applied voltages, the electric field will be aligned with the poling direction (arrows in Figures 5.4 and 5.5) on one side of the shim causing that layer to contract and anti-aligned on the other side causing that layer to expand, which will result in an arc bend of the actuator.

The x and y scanning directions of the AFM tip are each controlled by two parallel pairs of Y-poled piezo actuators that were modified to move in an "S" shape, where each pair of piezos controls the x or y direction.[191] This "S" bender configuration was chosen to accommodate the fact that both ends of each piezo are glued to flat macor pieces; because both ends are fixed, arc bending is not possible as it would cause stresses at the glue joints which would result in delamination of the piezo benders from the macor. Therefore, the S-bending motion is vital to the proper realization of the scan head and commercially available Y-poled piezos must be modified to work in this way. First, the nickel contact plating on both sides of each of the x–y piezo actuators was divided into two separate segments, and shown in blue and red in Figure 5.4. This was done by very mildly grinding away a thin line of nickel halfway along the bender, using the edge of a glass cover slide and #25 aluminum grinding powder. Next, the interior brass shim was exposed on one corner of each piezo by machine milling away a small amount of the piezoelectric to enable an electrical connection to the brass shim. Now, if opposing voltages (up to $\pm 150\,\mathrm{V}$) are applied to each half of the segmented piezo with the brass shims held at ground ($0\,\mathrm{V}$) as shown in Figure 5.4, then the segmented piezo bends in an "S" shape. The piezo voltages may then be swept until the initial voltages have reversed their polarity, causing

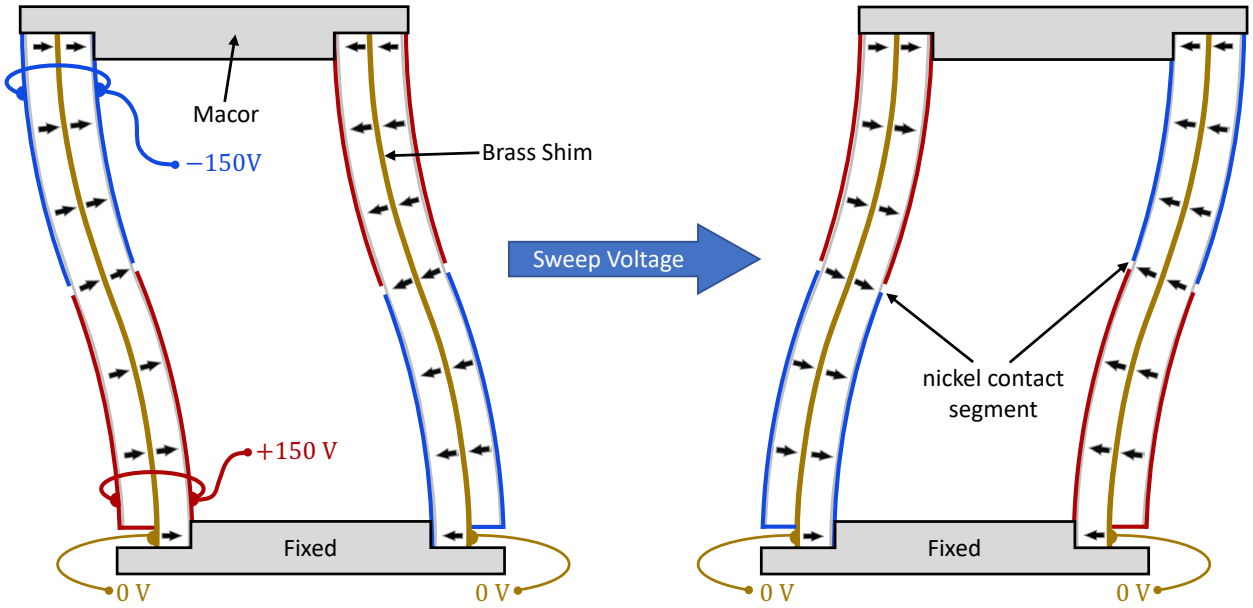

Figure 5.4: A schematic diagram of piezoelectric benders (with polarizations that are depicted with the black arrows) employed as S-benders to scan in either the x or y direction. The nickel contact layer was segmented (as indicated with the **right** figure) and then each opposing side was connected (as shown in the **left** figure) to allow for each half of the piezo to be driven with a different voltage. This way equal and opposite voltages of −150 V (blue) and +150 V (red) are applied to each piezo segment with the brass shim (orange) grounded, causing the piezos to bend in an "S" shape. The voltages may then be swept to scan the macor head as indicated.

a mirrored "S" shape bend in the piezos, which results in a nearly flat and lateral scan range. By combining two sets of these "S" benders, scanning may be performed in the x and y directions (see Figure 5.3). As was previously mentioned, a short piezo length is necessary to minimize the vibrational noise of the scan head while also maintaining a useful scan range. Therefore, the piezos were cut to a length of 0.625" to achieve an x–y scan range of 81 µm at room temperature and of ~ 16 µm when cooled to 1.2 K – 4.0 K.

The z scanning direction of the AFM tip is controlled by a single unmodified Y-poled piezo actuator. One end of the z piezo holds the AFM tip, as shown in Figure 5.5, and the other end is glued to a macor piece that is also attached to the x and y piezos. In contrast to the x and y piezos, the z piezo is not segmented and therefore does not move in an "S" shape. Rather, the z piezo is unaltered and bends in an arc, as shown in Figure 5.5, by fixing the brass shim to ground (0 V) and then applying either the same positive or negative voltage to both sides of the piezo to

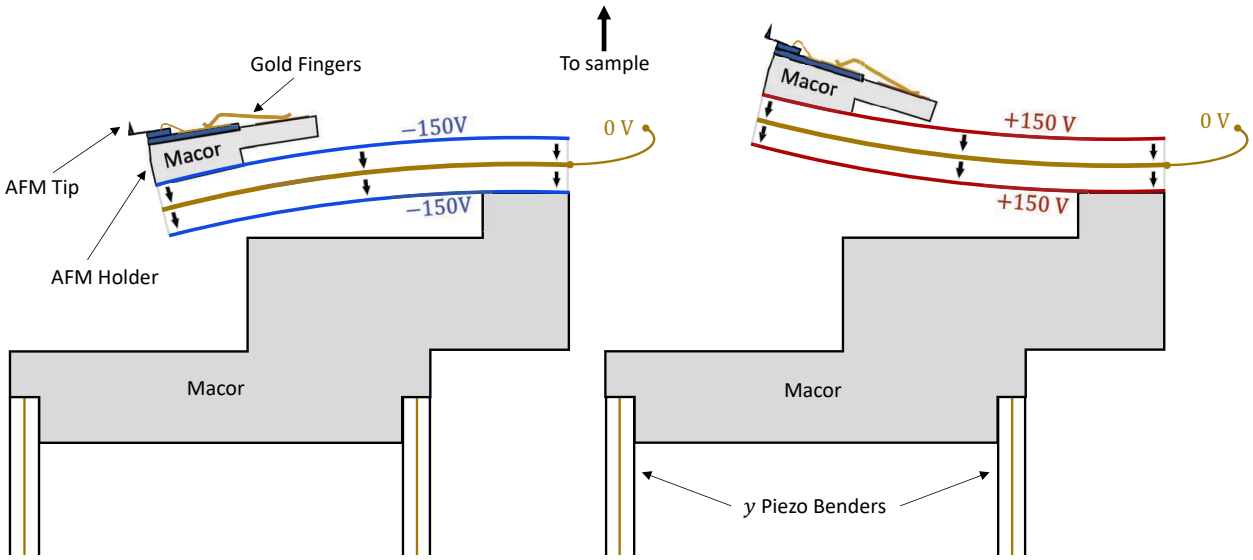

Figure 5.5: A schematic diagram of the motion of the z piezoelectric cantilever. The center brass shim is held at ground while either −150 V (blue) or +150 V (red) is applied to both faces of the piezo causing the AFM tip to be deflected either away from or towards the sample respectively. The piezo is glued on one end to a macor (gray) block that is attached to the y piezos and the macor AFM tip holder is glued to the other free end of the z piezo.

deflect the AFM tip towards or away from the sample respectively. Once again, two competing factors must be considered in order to decide an appropriate piezo length. First, the vibrational noise is minimized for shorter piezos. However, the piezo cannot be too short since an adequate z scan range is still desired in order to safely approach the sample substrate with the AFM tip and to properly perform cryogenic scanning. Additionally, the glue joints that join the z piezo to the y piezo macor block and to the macor tip holder will not bend and cannot be considered when determining the z scan range. So, the relevant length that may bend and contribute to the z scan range is confined to the unglued areas of the piezo. Therefore, we chose to cut a Y-poled piezo actuator to a length of 0.295" with an active bending length of 0.166" which yielded a z scan range of ~ 33 µm at room temperature and of ~ 4.0 µm near 1.2 K.

Attached to the free end of the z piezo on scan head is the AFM probe holder where the AFM tips are mounted. The body of this piece (see Figure 5.3) is machined from macor to allow the holder to be superglued to the piezo ceramic as previously discussed. Then, copper contacts were fabricated on the macor AFM probe holder by covering the entire upper face of the macor

part with copper tape, which was bonded to the surface with superglue. Then, four contacts were defined by cutting three channels through the copper tape with a razor blade. In order to make electrical connections to the AFM probe and to rigidly hold the probe, four gold fingers were harvested from a micro-USB cable and were soldered to the copper contacts. With this probe holder, a chip with an appropriate thickness may be slid beneath the gold fingers to hold the chip in the macor piece while also making electrical connections to any pads that the fingers are in contact with (see the probe holder in Figure 5.5).

5.2 The Self-Sensing AFM Probes

The application of a cryogenic atomic force microscope (cryo-AFM) to study phase slips in superconducting nanowires poses several challenges that are absent from traditional room temperature profilometry techniques. Atomic force microscopy (AFM) is a common method of determining the profilometry of a sample by probing the sample surface with an AFM tip that is typically $\sim 12\,\text{nm}$ in diameter. This profilometry method is therefore capable of nanometer-scale resolutions and may be implemented in numerous ways. One common technique, called *contact mode AFM*, drags an AFM tip across the surface of a substrate while measuring the deflection of the tip using a laser that is aligned to the AFM cantilever. Another common implementation of AFM profilometry, termed *tapping mode AFM*, drives an AFM tip at a constant frequency with a piezoelectric actuator which is near the resonant frequency of the AFM cantilever and the resulting amplitude of oscillation is measured with a laser. As the tip approaches the sample, Van der Waals forces between the tip and the substrate surface slightly change the resonant frequency of the cantilever as the tip begins to "tap" the surface of the substrate. In other words, the resonant curve of the cantilever shifts slightly in one way or the other and therefore causes a change in the amplitude of cantilever oscillation that is measured with a laser. Then, the tip is scanned along the surface and as the tip encounters a change in the substrate height, the corresponding changes in the strength of the Van der Waals forces causes the resonant frequency to change which in turn causes the amplitude of the cantilever to change. The AFM

then adjusts the cantilever either towards or away from the surface (depending on which way the resonant curve moved) until the original cantilever driving amplitude is recovered and the distance that the cantilever is moved is recorded as the feature height. In this way, the surface of a substrate is mapped with minimal contact between the surface and the tip. Both implementations of these commonly used AFM techniques require the use of a laser to measure the AFM cantilever deflections or oscillations, which poses challenges when attempting AFM methods at cryogenic temperatures.

Optically measuring a cantilever deflection at cryogenic temperatures poses several key difficulties. Firstly, shining a laser on instrumentation that is being precisely temperature controlled at cryogenic temperatures will result in unwanted heating of the scanning equipment which may cause temperature fluctuations of the superconducting nanowire. Secondly, aligning the laser on the AFM cantilever is crucial in performing room temperature AFM profilometry and is difficult at cryogenic temperatures, even with the use of an optical fiber to direct the laser. Thirdly, there is no easy method to sense a laser as these lasers are measured with silicon devices at room temperatures, which do not work at cryogenic temperatures. Therefore, we used commercial self-sensing AFM tips that are fabricated with a piezoresistive strain gauge on the cantilever, removing the need to optically measure the cantilever deflection. As these self-sensing tips are scanned over a substrate feature, the cantilever deflects and causes a change in the cross-sectional area of the strain gauge resistors on the end of the cantilever. This deflection therefore causes a change in the resistance in these resistors which may be measured as a deflection of the cantilever.

5.2.1 Self-Sensing AFM Probe Details

The self-sensing strain gauge AFM probes that were used to scan superconducting nanowires with the home-built cryo-AFM are commercially available and are manufactured by Sensor Tech. These tips, shown in Figure 5.6a, are formed on silicon dies and are manufactured with six aluminum contacts. Contacts H1 and H2 each connect to a resistive heater

that was not used. Contacts 1, 2, 3, and 4 each connect to the indicated locations in the strain gauge resistance balancing circuit that is schematically shown in Figure 5.6b. This strain gauge is composed of two reference resistors (R_A and R_B) which have a fixed resistance at a given temperature since they are formed on the silicon die off the cantilever and two variable resistors (R_C and R_D) which change in resistance when the AFM cantilever is deflected.

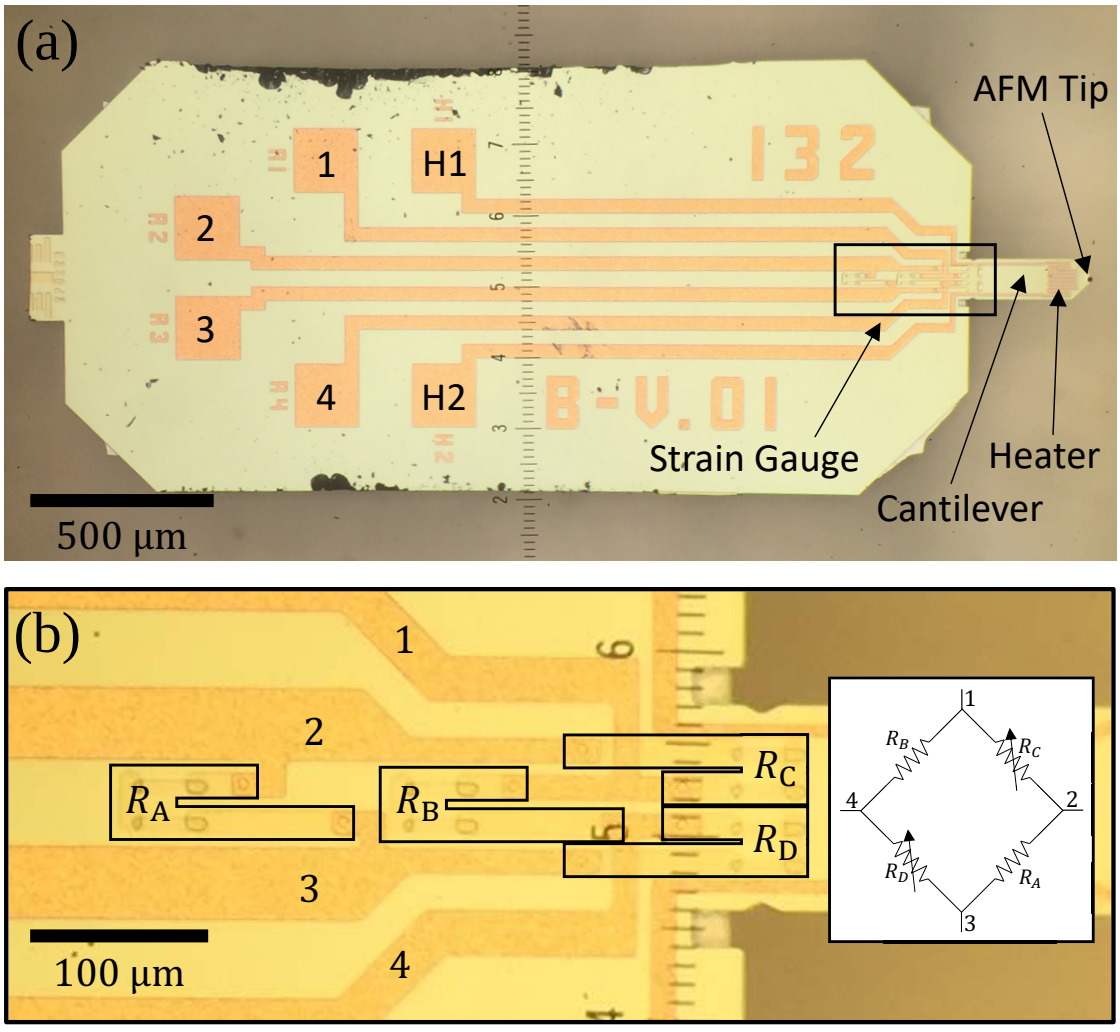

Figure 5.6: **(a)** An optical image of the self-sensing AFM tip. There are six aluminum contact pads (orange) with two pads (labelled H1 and H2) that are connected to the heater near the tip of the cantilever and the other four pads (labelled 1-4) are connected to the strain gauge at the fixed end of the cantilever, outlined with the black box. **(b)** An enlargement of the region denoted by the box in **(a)** to more clearly show the strain gauge. There are two reference resistors that are located on the silicon die (labelled R_A and R_B) and two variable resistors (labelled R_C and R_D) located on end of the cantilever. Also shown in the inset is the circuit diagram formed by the aluminum connections to the resistors.

All four connections must be used in order to accurately measure any changes in R_C and R_D. The resistors of the strain gauge are manufactured to create a Wheatstone bridge circuit which is shown in the inset of Figure 5.6b. Ideally, all four resistors are identical which indicates that if an AC voltage is applied to two opposing leads, such as leads 1 and 3, then the voltages at leads 2 and 4 will be identical and therefore there will be no measurable voltage between these leads. If the variable resistors are changed so the resistance bridge is unbalanced, then a voltage difference will be observed between leads 2 and 4.

These properties of the resistance bridge are exploited as a strain gauge to measure the deflection of the AFM cantilever. An AC voltage is typically applied between leads 1 and 3 in the diagram in Figure 5.6b, which we will call V_{13}, with the bridge response measured between leads 2 and 4 by an SR830 lock-in amplifier. A $\sim 25\,\mu$V DC voltage offset is observed when a 0.05 V driving voltage is applied to V_{13}, even when the cantilever is undeflected since the four bridge resistors are not exactly the same. As the tip is deflected and strain is introduced near the fixed end of the cantilever (where the strain gauge exists), the resistances of R_C and R_D changes, which results in a change in voltage that is measured between leads 2 and 4, which we will call V_{24}. This change in V_{24} that is observed when the cantilever is deflected is proportional to the deflection amplitude and so a tip sensitivity S that relates the deflection voltage with the motion of the AFM tip may be empirically determined, which will be discussed later.

The self-sensing probes were mounted in the cryo-AFM scan head by attaching the probes to a silicon chip with gold contacts. This was necessary to ensure that the tips could be safely mounted in the scan head of the cryo-AFM and to ensure that reliable electrical connections could be made to the strain gauge resistive balancing bridge. First, gold contacts were formed with standard lift-off lithographic techniques on a 2.5 mm × 2.5 mm silicon chip with a 200 nm insulating oxide coating, which were pre-thinned from an initial thickness of $\sim 500\,\mu$m to a thickness of $\sim 200\,\mu$m by grinding the chips with #25 aluminum grit. This final thickness is required to rigidly mount the chip in the scan head with the gold fingers that were soldered to the copper contacts on the macor AFM holder. Then, the self-sensing AFM probe was su-

perglued to the thinned silicon chip with its gold contacts, followed by making gold wire-bond connections between the four strain-gauge pads on the AFM probe to the lift-off gold contacts on the silicon chip. The AFM tip, now backed by a silicon chip with gold contacts, is mounted into the cryogenic AFM scan head by sliding the chip into the previously discussed AFM probe holder.

5.2.2 Coating AFM Tips with a Magnetic Material via Lift-Off Lithography

In the scanning experiments proposed to map phase slips in superconducting nanowires, either a dielectric or magnetic AFM tip is scanned above the nanowire to perturb the local superconductivity in the region near the tip. Since silicon is naturally a dielectric, there are no additional fabrication steps that are required on the commercially available probes when performing the scanning experiment with a dielectric tip. However, these probes are not available with a magnetic coating option. So, lift-off lithography is required to coat the tips on the self-sensing probes with a magnetic material in order to scan a nanowire to perturb superconductivity via a local magnetic field.

One way to deposit a layer of magnetic material to coat an AFM tip is to implement a lift-off technique in combination with sputter deposition of a magnetic layer. Special considerations are required to sputter magnetic materials since these magnetic targets influence the magnetic field of the sputter gun in the traditional sputter system that we commonly employ (see Chapter 2). In a collaboration with the research group of Professor Kristen Buchanan at Colorado State University, a specialized sputter system was used that is capable of depositing magnetic material, in combination with a lift-off lithographic technique. Figure 5.7 depicts optical images of the AFM cantilever at various stages in the lift-off photolithography process. This process was optimized to avoid covering and/or shorting the connections to the strain gauge bridge with the sputtered magnetic material. First, it was critical to oxygen ash the AFM probe (which was superglued to a backing glass substrate) to promote the adhesion between photoresist and polished silicon. After oxygen-ashing the probe, $\sim 0.3\mu$m-thick LOR3B lift-off resist was spun

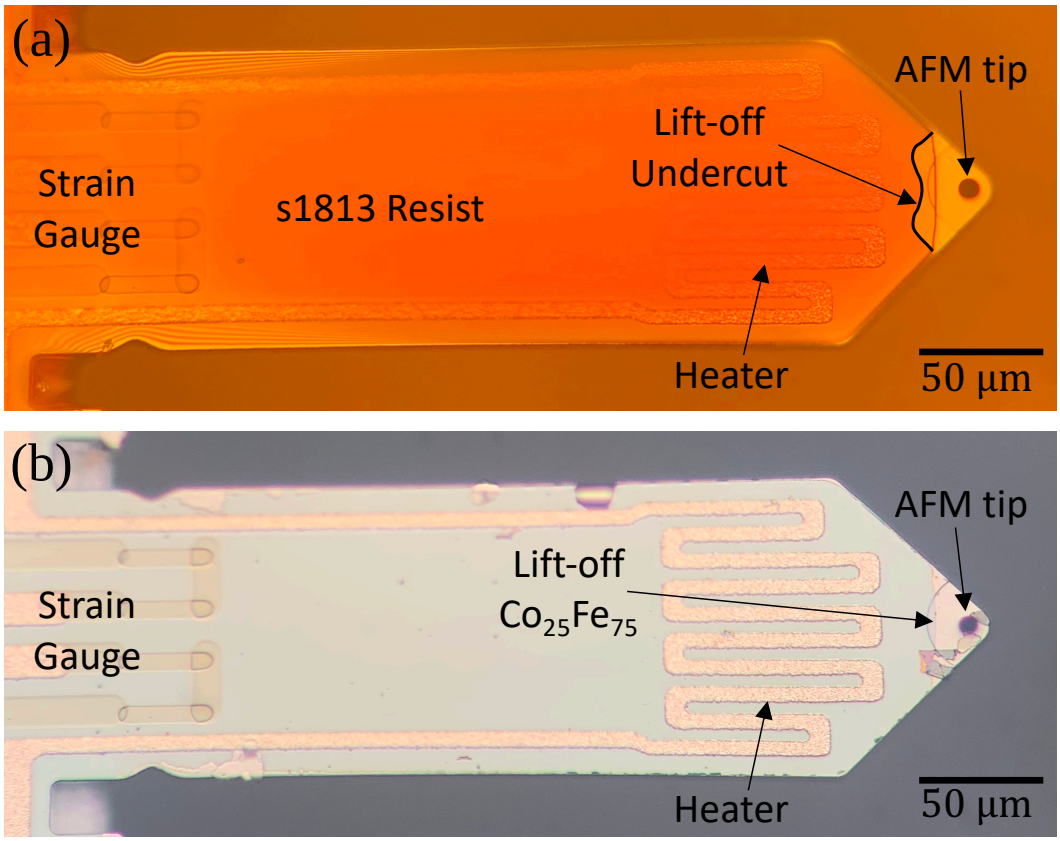

Figure 5.7: **(a)** Exposed and developed S1813 resist spun on a layer of LOR3B lift-off resist on a self-sensing AFM cantilever. The undercut that was formed during development is highlighted with the black line. **(b)** The resulting lift-off after a 40 nm magnetic layer of $Co_{25}Fe_{75}$ followed by a 10 nm layer of Ta were sputter deposited with subsequent lift-off.

and baked onto the probe.* Then, S1813 photoresist was spun and baked on top of the lift-off resist and subsequently exposed at a very high dose in the region near the AFM tip. Large exposure doses were required to properly expose the resist in this region since the combination of the surface tension of the resist and the small AFM cantilever resulted in an atypically thick photoresist layer, even with large spin speeds. The resist was then developed in a bath of AZ917 developer, a tetramethylammonium hydroxide (TMAH) based developer, which resulted in the lithography shown with the optical image in Figure 5.7a. Note that an undercut is formed under the photoresist by the lift-off resist layer. Next, the AFM probe with the exposed photoresist was metalized with a 40 nm magnetic layer of $Co_{25}Fe_{75}$ and capped with 10 nm of Ta to protect the

*We found that lift-off attempts without using a lift-off resist failed.

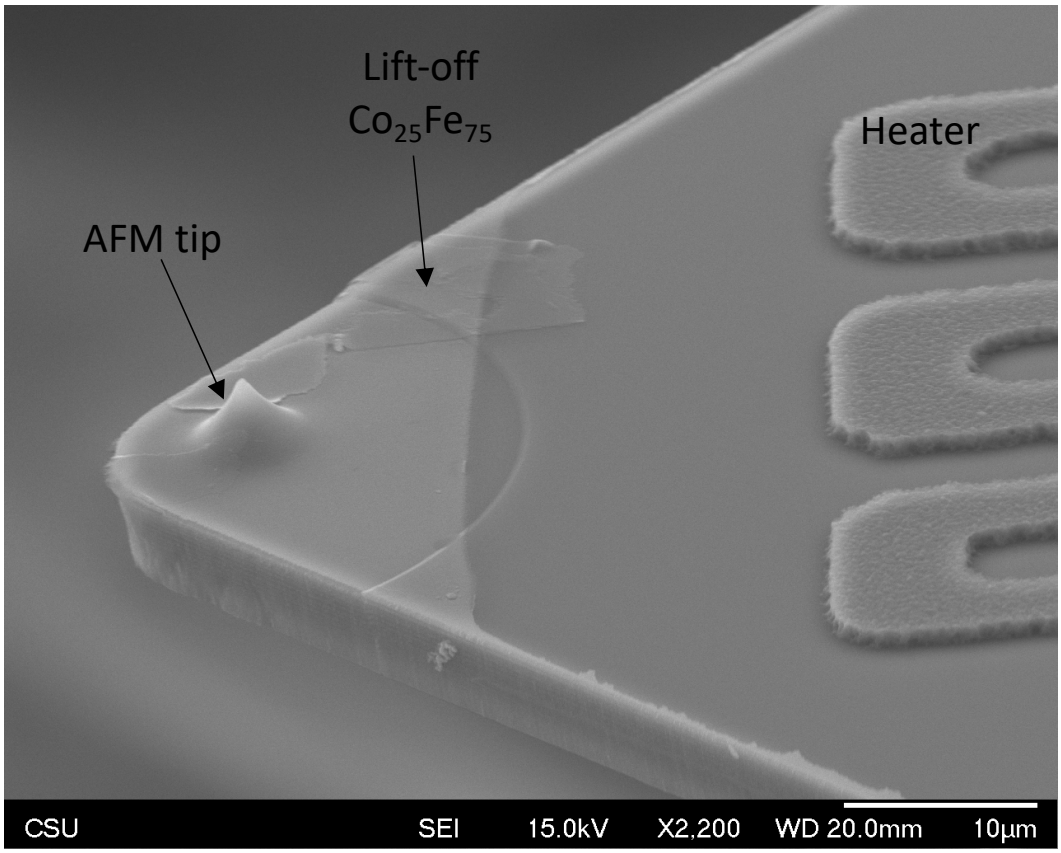

Figure 5.8: An SEM image of a self-sensing AFM tip that was coated with a 40 nm magnetic layer of $Co_{25}Fe_{75}$ followed by a 10 nm layer of Ta. This image indicates a tip radius of ~ 0.5 µm, however, the magnetic coating may influence the electron beam used to obtain this image.

magnetic layer. The magnetic layer was then lifted off in a bath of acetone and then in a bath of remover PG (RPG) followed by a 3-solvent rinse bath, yielding the self-sensing AFM probe with a magnetically coated tip shown with the optical image in Figure 5.7b.

The tip of a self-sensing AFM probe was then magnetized once the tip was successfully coated with a magnetic layer. A small D44-N52 Ni magnet was used to magnetize the $Co_{25}Fe_{75}$ coated tip by carefully lowering the tip near the surface of the magnet. After this step was completed, the tip was imaged with a scanning electron microscope (SEM), shown in Figure 5.8, to determine the physical characteristics of the coated tip. The uncoated tips are specified to have a tip radius that is < 15 nm, however, the tip radius as measured with the SEM image was found to be 0.5 µm. It is important to note that the tip is magnetic and so imaging with an electron beam may become distorted in this region as a result.

5.2.3 Cryogenic Characterizations of the Self-Sensing AFM Tips

The self-sensing AFM probes were characterized after mounting the probes on the scan head of the cryo-AFM. Table 5.1 displays the properties of the strain gauge at room and cryogenic temperatures for several of these probes. The resistances of the strain gauge bridge resistors change with temperature and so the voltage offset that is measured on the strain gauge bridge at V_{24} is also different when scanning at room or at cryogenic temperatures. Additionally, it is vital to calibrate the strain gauge sensitivity both at room and cryogenic temperatures to understand how the voltage signal from V_{24} relates to the profilometry. Therefore, patterns with ~ 50 nm features were milled into the surface of silicon substrates and were characterized with a Tencor Instruments surface profilometer. These patterns were then scanned at room and cryogenic temperatures to determine the sensitivity S of each strain gauge probe by comparing the voltage response measured from V_{24} to the surface profilometry characterizations. The resulting probe sensitivities are also displayed in Table 5.1 when V_{13} was driven with a 0.05 V excitation voltage.

Table 5.1: Properties of Self-Sensing AFM Tips

Tip ID	T	R_A	R_B	R_C	R_D	V_{Offset}	S
	(K)		(Ω)			(μV)	(μV/nm)
AFM132	296	890	891	895	888	25.5	0.070
	3.5	929	890	891	926	74.0	0.192
AFM162	294	891	905	909	886	24.0	0.069
	1.6	957	980	978	952	87.5	~ 0.200
AFM77M*	295	867	874	885	874	32.1	~ 0.070
	1.6	777	796	806	785	38.1	~ 0.200

*Magnetized tip

The frequency response of the cryo-AFM scan head and probe cantilever on AFM132 was sampled at cryogenic temperatures to determine the resonant frequency of the AFM cantilever. First, V_{13} on the strain gauge bridge was driven with a 0.05 V DC signal at ~ 4 K and the cryo-

AFM z piezo was driven with a sine-wave voltage. The frequency of the sine-wave driving to the z piezo was then swept while simultaneously recording the strain gauge voltage and phase responses from V_{24} at each frequency with an SR830 lock-in amplifier, shown in Figure 5.9. These measurements determined that this self-sensing probe mounted in the cryo-AFM scan head has a resonant frequency of $f_r = 55.593\,\text{kHz}$ which is accompanied by a characteristic 180° phase change.

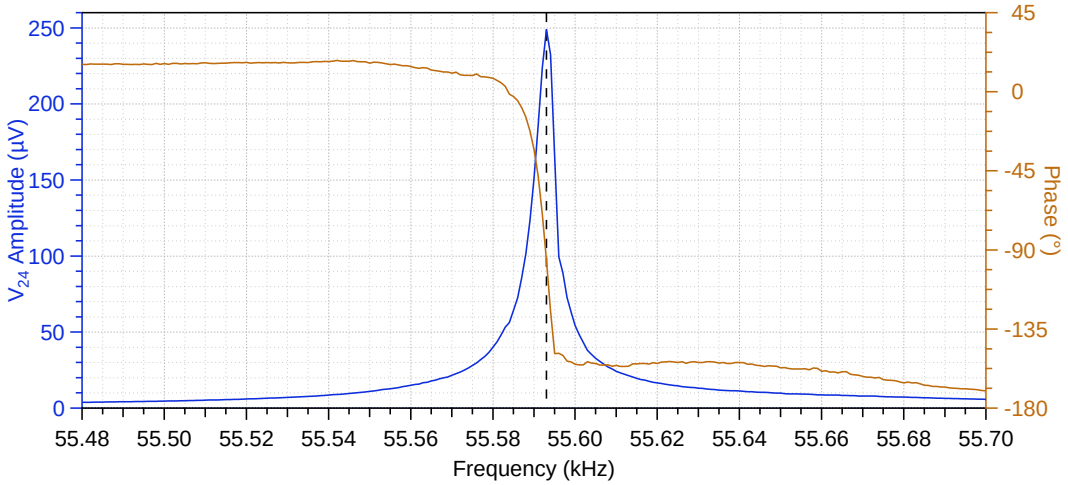

Figure 5.9: The strain gauge voltage (blue) and phase (orange) from V_{24} frequency responses as V_{13} is driven with a 0.05 V DC signal. These measurements determined that this probe (AFM132) has a resonant frequency of f_r=55.593 kHz when mounted in the cryo-AFM scan head.

5.3 Nanowire Substrate Landmarks

A cryogenic scanning experiment performed with superconducting nanowires requires the precise positioning of a scanner over the sample. This poses significant challenges since both the nanowire and the AFM tip positions have to be measured with a method that is accurate, cryogenically compatible, and benign to the nanowire sample. One potential scheme would be to pattern the substrate surface with landmarks that could be imaged with the cryo-AFM. Then, the scanner can be moved relative to these landmarks and accurately positioned above the nanowire. An ideal choice of landmark is a pattern that uniquely maps the substrate surface

so that an absolute measurement of the position of the tip relative to the nanowire is obtained when the pattern is scanned with the cryo-AFM. Therefore, a mapping scheme in which the surface of the silicon substrate is patterned in a unique way was implemented by ion milling specialized patterns onto the substrate surface. This was done before the nanowire was created because the nanowires are both physically and electrostatically fragile.

5.3.1 One- and Two-Dimensional de Bruijn Sequences

A pattern created from a *de Bruijn sequence* can be used to uniquely define the surface of a substrate that possesses a nanowire sample. A one-dimensional de Bruijn sequence is a mathematical sequence of order n that is composed of a predetermined alphabet with p entities, yielding a sequence of length p^n in which any subset of n neighbors in the sequence is unique.[192,193] For example, if a de Bruijn alphabet of [0, 1] ($p = 2$) is chosen, then Table 5.2 gives a possible de Bruijn sequence for various useful orders that were generated using a de Bruijn sequence generator tool.[194] The $n = 5$ sequence, for instance, contains $2^5 = 32$ entries; in this sequence, all sub-sequences of length $n = 5$ are unique. These sequences can then be converted into black and white patterns which we will show can be used to locate a nanowire at cryogenic temperatures. For example, Figures 5.10a and 5.10b depict the x and y patterns that are generated from the 8^{th} order de Bruijn sequence in Table 5.2, where black represents a zero and white represents a one. Patterns of this kind can later be used as masks for optical lithography which were transferred into the surface of the silicon substrates. A complete, two-dimensional de Bruijn pattern is schematically shown in Figure 5.10c by overlaying the x and y patterns. For all patterns presented here, black will indicated areas of the substrate that will be protected by unexposed photoresist while white will indicate areas that will be exposed and transferred into the substrate surface.

The choice of the order of the de Bruijn sequence to map the substrate surface depends on several properties of the cryo-AFM scanner. When the cryo-AFM is cooled to cryogenic temperatures, thermal contractions between the sample stage and the cryo-AFM alters the tip position

Table 5.2: Various de Bruijn Sequences

Order	Sequence with the binary alphabet [0,1]
5	0 0 0 0 0 1 0 0 0 1 1 0 0 1 0 1 0 0 1 1 1 0 1 0 1 1 0 1 1 1 1 1
6	0 0 0 0 0 0 1 0 0 0 0 1 1 0 0 0 1 0 1 0 0 0 1 1 1 0 0 1 0 0 1 0 1 1 0 0 1 1 0 1 0 0 1 1 1 1 0 1 0 1 0 1 1 1 0 1 1 0 1 1 1 1 1 1
7	0 0 0 0 0 0 0 1 0 0 0 0 0 1 1 0 0 0 0 1 0 1 0 0 0 0 1 1 1 0 0 0 1 0 0 1 0 0 0 1 0 1 1 0 0 0 1 1 0 1 0 0 0 1 1 1 1 0 0 1 0 0 1 1 0 0 1 0 1 0 1 0 0 1 0 1 1 1 0 0 1 1 0 1 1 0 0 1 1 1 0 1 0 0 1 1 1 1 0 1 0 1 0 1 1 0 1 0 1 1 1 0 1 1 0 1 1 1 1 1 1 1
8	0 0 0 0 0 0 0 0 1 0 0 0 0 0 0 1 1 0 0 0 0 0 1 0 1 0 0 0 0 0 1 1 1 0 0 0 0 1 0 0 1 0 0 0 0 1 0 1 1 0 0 0 0 1 1 0 1 0 0 0 0 1 1 1 1 0 0 0 1 0 0 0 1 0 0 1 1 0 0 0 1 0 1 0 1 0 0 0 1 0 1 1 1 0 0 0 1 1 0 0 1 0 0 1 1 0 1 1 0 0 0 1 1 1 0 1 0 0 0 1 1 1 1 1 0 0 1 0 0 1 0 1 0 0 1 0 0 1 1 1 0 0 1 0 1 0 1 1 0 0 1 0 1 1 0 1 0 0 1 0 1 1 1 1 0 0 1 1 0 0 1 1 0 1 0 1 0 0 1 1 0 1 1 1 0 0 1 1 1 0 1 1 0 0 1 1 1 0 1 0 1 0 1 0 1 1 1 0 1 0 1 1 0 1 1 0 1 0 1 0 1 1 1 1 1 0 1 1 0 1 1 1 1 0 1 1 1 0 1 1 0 1 1 1 1 1 1 1 1

(a) x de Bruijn **(b)** y de Bruijn **(c)** Combined $x-y$ de Bruijn

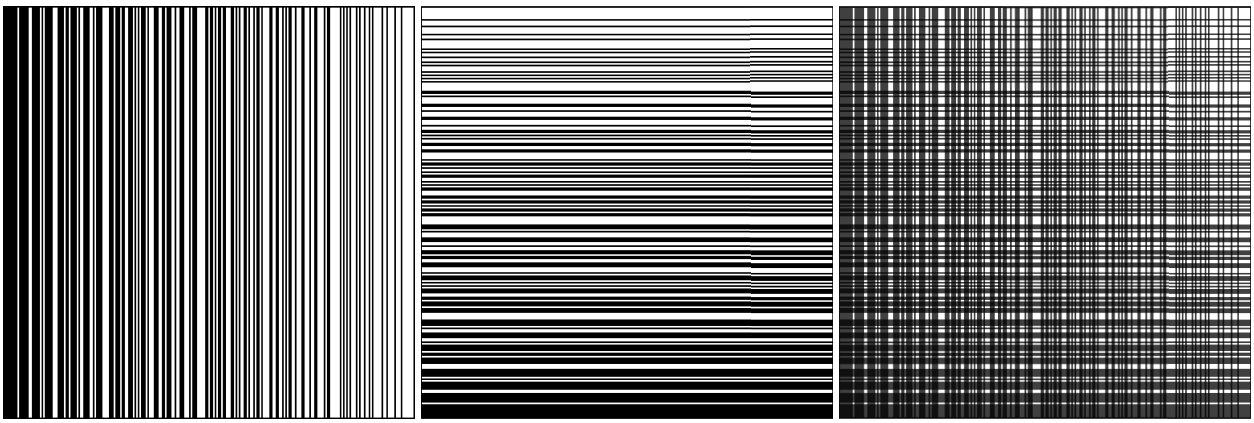

Figure 5.10: **(a)** x and **(b)** y de Bruijn patterns generated from the 8^{th} order de Bruijn sequence in Table 5.2. **(c)** Both patterns are superimposed on one another to from a region that is uniquely mapped in both the x and y directions.

relative to the substrate. Therefore, the de Bruijn pattern must cover a large enough area to ensure that the AFM tip remains above the pattern regardless of sizable thermal contractions, which are on order of 100 µm, that occur during a cool down. Another consideration is that the de Bruijn pattern must uniquely define the tip location on the substrate. This requires that the line width of each entry in the pattern is small enough to allow for a unique set of n entries to fit within a single scan range of the cryo-AFM when cold, but also large enough to be realisti-

cally fabricated with optical lithographic techniques. These conditions are represented by the following equations

$$l = 2^n \times \text{linewidth} \tag{5.1}$$

$$R = n \times \text{linewidth} \tag{5.2}$$

where l is the side-length of the patterned area, n is the de Bruijn order, and R is the cryogenic scan range of the cryo-AFM. Table 5.3 displays several of the size limitations that are imposed by Equations 5.1 and 5.2 for several de Bruijn patterns assuming an expected scan range of 16 µm with the previously discussed cryo-AFM at cryogenic temperatures. For our purposes, a de Bruijn order of $n = 8$ and a linewidth of 1.5 µm* are chosen since a pattern with these parameters will span a mapped area of 384 µm × 384 µm while displaying ~ 10 entries in a single scan range when cold. This smaller linewidth than what is represented in Table 5.3 will allow more lines to be visible within a single scan, making it easier to determine the location of tip within the de Bruijn pattern while also spanning a reasonable patterned area.

Table 5.3: Size limits for various de Bruijn patterns (16 µm scan range)

Order n	Maximum Linewidth (µm)	Mapped Area (µm × µm)
5	3.2	102
6	2.7	170
7	2.3	292
8	2.0	512
8*	1.5	384

*Parameters chosen to fabricate de Bruijn patterns.

An alternative substrate mapping that still uses the uniqueness of de Bruijn patterns can be employed by implementing a two-dimensional de Bruijn torus pattern.[193] The previously discussed de Bruijn sequences are simply one of the many unique solutions that form a one-

*The linewidth must be larger than the minimum resolution of the laser writer of ~ 0.5 µm

dimensional de Bruijn torus or sequence for a given order.[192] However, a two-dimensional de Bruijn torus of order m is a surface which contains all possible unique square arrays of size $m \times m$ consisting of the chosen alphabet.[193] For example, the $m = 4$ de Bruijn torus is displayed in Figure 5.11a for the familiar alphabet choice of $[1,0]$. Fabricating the large $m = 4$ torus on a substrate* would require either an extreme lithographic resolution or a very large substrate area. However, any subset of the $m = 4$ de Bruijn torus will also contain unique 4×4 matrices, so we elected to pattern our substrates with the 62×62 element subset highlighted with the orange square in Figure 5.11a and shown in Figure 5.11b which covered a $205\,\mu m \times 205\,\mu m$ area with $3.3\,\mu m$ diameter dots.

(a) Full de Bruijn Torus

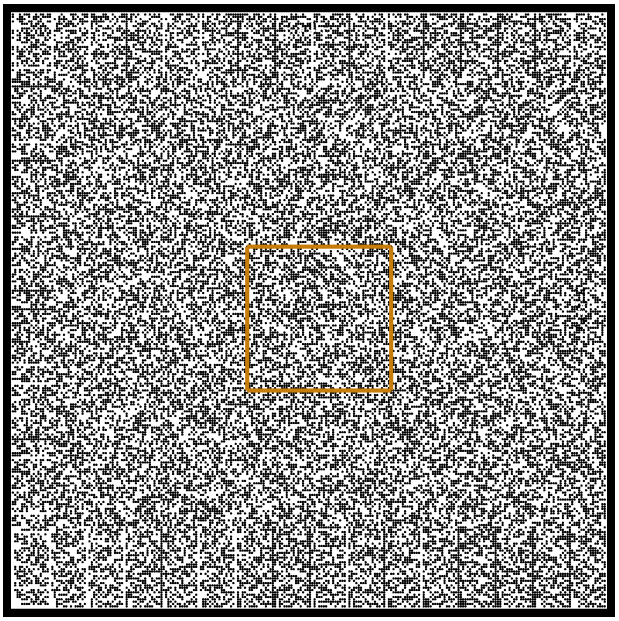

(b) de Bruijn Torus Subset

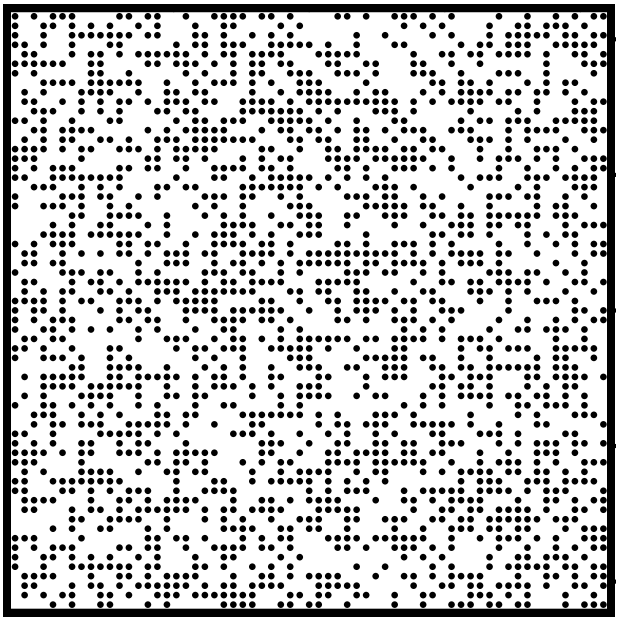

Figure 5.11: **(a)** The two-dimensional $m = 4$ de Bruijn torus that contains all possible and unique 4×4 binary arrays. The torus is formed by wrapping the top and bottom edges and then connecting the left and right edges. **(b)** The subset of the de Bruijn torus that was used to pattern nanowire substrates. For reference, the nanowires are intended to be located just below the bottom of **(b)**.

* $m = 2$ or $m = 3$ are too small to properly map a large enough area

5.3.2 de Bruijn Fabrication

A method to locate the superconducting nanowire samples at cryogenic temperatures with a scanner must be engineered while also considering possible issues that may arise in the nanowire fabrication process. The de Bruijn patterns (either Figure 5.10c or 5.11b) were transferred into silicon substrates (each with a 200 nm oxide coating) by ion milling a resist mask before any nanowires were fabricated to avoid damaging the nanowires during the de Bruijn lithography and transfer processes. A de Bruijn pattern was placed on each substrate so that the bottom edge of the pattern, just above where the nanowire would eventually be formed, was 850 µm from the one of the substrate edges. This was done to ensure that the sample location is compatible with the physical limitations imposed by cryo-AFM, while also avoiding the resist edge bead that is formed when spinning resists on substrates. First, 5 mm × 8 mm silicon substrates were cleaned with a standard 3-solvent rinse followed by spinning and baking a ~ 1.3 µm thick layer of Shipley S1813 photoresist. The de Bruijn pattern (either Figure 5.10c or 5.11b) was exposed with a maskless laser lithography system that has a lower resolution limit of 0.5 µm and easily exposes the 1.5 µm lines or the 3.3 µm dots.* Finally, the de Bruijn pattern was developed with AZ 917 developer, which is a Tetramethylammonium hydroxide (TMAH) based developer, followed by an oxygen-ashing step to clear any remaining resist scum resulting from the closely space lines or dots. This oxygen-ashing step is crucial since any resist scum will serve as an etch mask resulting in a flawed pattern transfer.

The de Bruijn pattern was transferred from the photoresist into the silicon substrate via argon ion milling with a Kaufman and Robinson (K & R) AJA ion mill equipped with a KDC 40 ion source that was previously described in Chapter 3. The substrates were mounted to a cooled stage and milled at a beam voltage of 500 V, a beam current of 56 mA, and an accelerating voltage of 300 V for 5 minutes to etch the exposed substrate by ~ 50 nm since the etch rate of the silicon substrates in this system was found to be close to 10 nm/min. The milled resist was

*Since the linewidths of the 8^{th} order de Bruijn pattern were near the resolution limit of the laser writer, a slightly higher exposure dose of 200 mJ cm^{-2} was required to clear thinner lines.

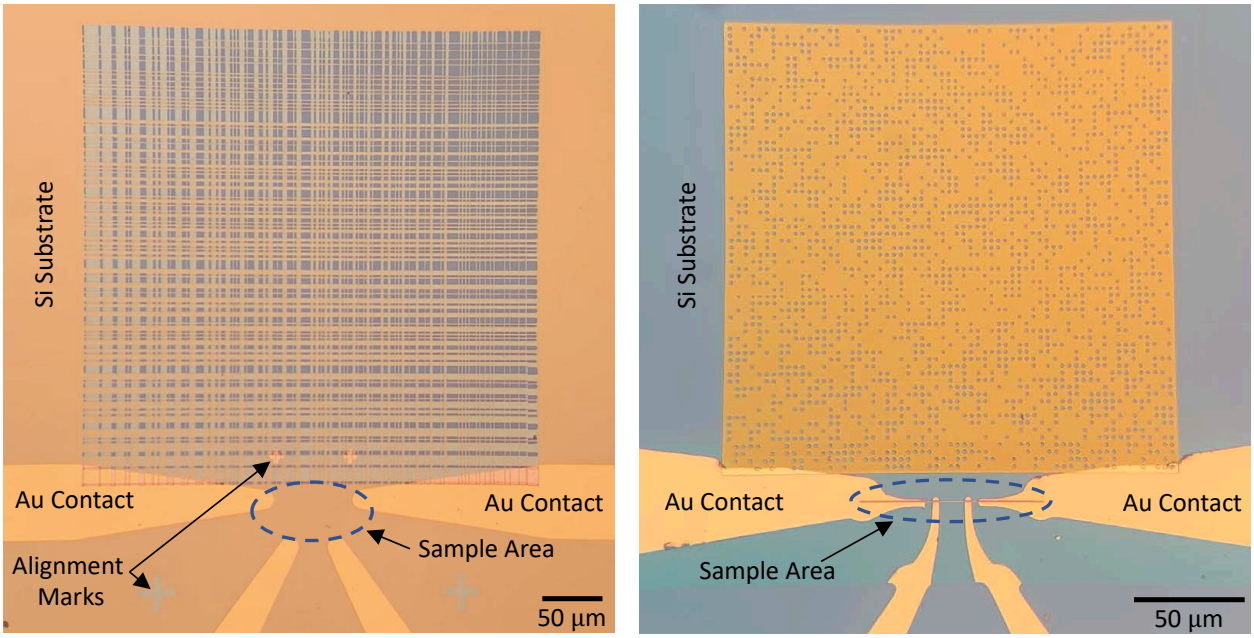

(a) **(b)**

Figure 5.12: **(a)** An optical image of the substrate mapping using two, orthogonal de Bruijn sequences with $n = 8$ and a linewidth of 1.5 µm and spans an area of 384 µm × 384 µm. **(b)** An optical image of the substrate mapping using a subset of the 4^{th} order de Bruijn torus spanning an area of 205 µm × 205 µm with dots that are 3.3 µm in diameter. The intended locations of the nanowires are denoted by the blue, dashed ovals and the substrates have pre-patterned gold contacts in a four-probe geometry.

removed by sonicating the samples in acetone for 10 minutes since photoresist that was milled with this ion mill became burned or baked (see Chapter 3) resulting in a decrease in solubility in acetone. However, this resist burning was not detrimental to milling a substrate by 50 nm since the patterns were unaffected for these short milling times and this issue only became problematic when attempting to mill for longer than 10 min.

Figures 5.12a and 5.12b show optical images of the resulting de Bruijn patterns etched into a silicon substrate by using the one-dimensional and torus sequences respectively. The de Bruijn mapping of Figure 5.12a is created by first patterning and milling the x-direction (Figure 5.10a) followed by patterning and milling the y-direction (Figure 5.10b). The y-direction pattern is aligned to the x-direction pattern during the exposure step with the alignment marks that were formed by milling the first pattern into the substrate, shown in Figure 5.12a. Milling two of these patterns results in the substrate mapping shown in Figure 5.12a with three milling depths of un-

milled silicon (where the substrate was protected by both patterns), of 50 nm (where the substrate was protected once by either pattern), and of 100 nm (were the substrate was unprotected by both patterns). If, however, the de Bruijn pattern that is generated from the two-dimensional de Bruijn torus is used, then only one milling step is required resulting in the substrate mapping shown in Figure 5.12b with only one etch depth of 50 nm.

5.4 Contact-Mode Cryogenic Atomic Force Microscopy to Map a Substrate

The mapping of phase slips along a superconducting nanowire with an AFM tip to locally perturb superconductivity first requires an experiment to locate the sample with the cryo-AFM. To accomplish this, the previously discussed de Bruijn patterns formed into the surface of silicon substrates were scanned with the self-sensing AFM probes that were mounted in the cryo-AFM. The resulting profilometry of the de Bruijn patterns then uniquely locates the tip position relative to the superconducting nanowire, which allows the sample stage to be moved relative to the tip (with the stick-slip Attocube movers) such that the tip is above the nanowire. This section will focus on the details of a generic cryogenic scanning experiment of a de Bruijn mapped substrate that was performed to locate the cryo-AFM tip position relative to a superconducting nanowire. The following experiment to locally perturb superconductivity within a nanowire sample will be discussed later in Chapter 6.

5.4.1 Scanning Preparations

A cryogenic scanning experiment first begins by mounting and verifying the nanowire sample and the self-sensing probe in the cryostat. First, a de Bruijn-mapped substrate was mounted onto the copper spacer block on the sample stage. Then, electrical measurement connections are made to the four probes of the superconducting nanowire sample with gold fingers which was followed by performing four-probe resistance measurements of the nanowire with an SR830 lock-in amplifier to ensure the connections are reliable. Next, the cryo-AFM scan

head was mounted below the sample as shown with the image in Figure 5.13. At this stage, resistive measurements of the four strain gauge resistors on the self-sensing AFM probe were performed (see Table 5.1) to ensure that the strain gauge is functioning properly. This check is vital since the delicate AFM tip may be destroyed if the strain gauge is not properly connected when the cryo-AFM approaches the sample as the tip could be "crashed" into the substrate surface. Measurements of the voltage offset from the bridge, resulting from the minute discrepancies between the bridge resistors, were also performed with an SR830 lock-in amplifier and a $\times 100$ bipolar preamplifier by driving V_{13} with an AC 0.05 V sine wave at 15 kHz and then measuring V_{24}. This offset voltage was corrected with a lock-in offset function to allow for accurate μV measurements of changes in V_{24}, which relates to the deflection of the AFM cantilever.

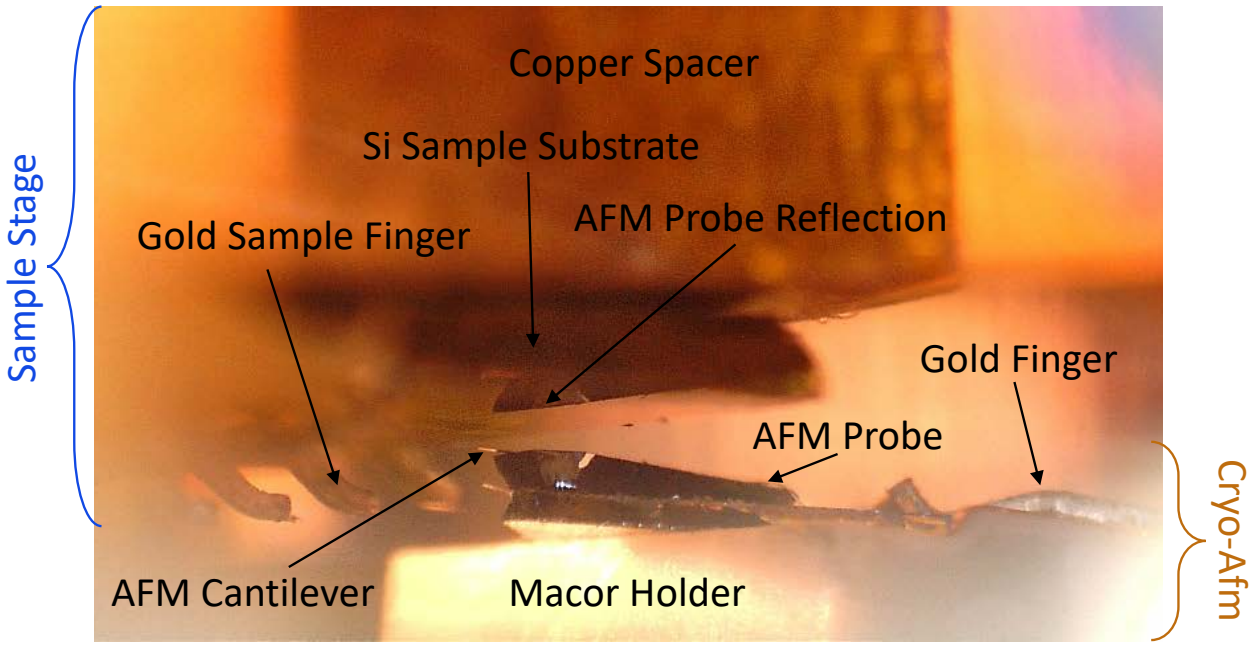

Figure 5.13: An optical image of the self-sensing AFM probe mounted in the cryo-AFM scanner below a sample (which is mounted on the sample stage) just before the tip is approached towards the sample surface.

The sample stage was then approached towards the cryo-AFM scan head after the strain gauge on the self-sensing AFM tip was verified. This was performed by controlling the z Attocube stick-slip positioner with a LabVIEW program to move the sample stage towards the

cryo-AFM scan head while simultaneously monitoring the offset-corrected signal from V_{24} as measured by an SR830 lock-in. Coarse approaching of the sample stage towards the AFM scan head is initially performed manually at room temperature with the cryostat open to air and while watching the tip-sample separation with a standard webcam. Once the sample has come to a safe distance from the AFM tip (typically within $\sim 300\,\mu m$ as shown in Figure 5.13), then the x and y Attocube positioners are adjusted to optimally place the tip over the center of the de Bruin pattern.

The AFM tip is then automatically approached toward the sample surface by using a combination of the z Attocube positioner on the sample stage and the z piezo on the cryo-AFM. First, a setback voltage V_{Setback} is chosen to determine the maximum allowed voltage change on V_{24} when the AFM tip contacts the substrate surface. Ideally, the approaching sequence is terminated for a minimal cantilever deflection, so V_{Setback} values of $0.7\,\mu V - 2.8\,\mu V$ at room temperature or $2.8\,\mu V - 8.0\,\mu V$ at cryogenic temperatures are chosen, corresponding to tip deflections of only $10\,nm - 40\,nm$. Then, in a process called *approaching*, an automated LabVIEW program safely brings the AFM tip to the substrate surface by first sweeping the full range of the z piezo on the scan head that the AFM tip is mounted to (see Figure 5.5) while monitoring the voltage from V_{24}. If there is no measured change in V_{24} during the sweep of the scan head z piezo, then the z Attocube that controls the z motion of the sample stage is stepped towards the AFM tip by $\sim 1/2$ the distance swept by the full range of the cryo-AFM z piezo. This process is repeated several times until the tip touches the substrate surface during one of the z piezo sweeps and a voltage change that exceeds the chosen V_{Setback} is measured on V_{24} by LabVIEW. The z position of the sample stage when the touch occurs is recorded by the previously discussed capacitive position sensor and then LabVIEW fully retracts the scan head z piezo. A correction Attocube step is performed based on where the touch occurred in the piezo sweep since it is not guaranteed that the touch occurred near the center of the range of motion of the scan head z piezo.

The scan plane must be matched to that of the substrate surface before scanning the de Bruijn mapping. This process, called *compensating*, is performed with an original Igor program that controls the x, y, and z piezos on the scan head through a data acquisition (DAQ) board. The AFM tip is first engaged on the substrate surface by manually controlling the z piezo in Igor to verify the piezo voltage where a touch occurs according to the chosen V_{Setback}. Then, the tip is sequentially engaged at various locations on the substrate (usually in a square pattern) and the z piezo voltage required to touch at each of these locations is recorded. A plane fit is next calculated from the touch voltages in the Igor program to determine the compensation that is required to electronically level the scan plane. This leveling is performed electronically rather than manually by sending some of the x and y piezo voltages to the z piezo as the x and y piezos are scanned, which causes the z piezo to adjust throughout the scan such that the scan plane is parallel to the sample surface. The amount of x–y voltage that is redirected to the z piezo is determined by the plane fit of the z piezo touch voltages during the compensation run. This compensation process is repeated after electronically leveling the cryo-AFM to ensure that the scan plane is now parallel to the sample surface.

The approaching and compensating processes are first performed at room temperature before a cooldown and the de Bruijn pattern is scanned at room temperature to determine the tip location. After recording the relative room-temperature x, y, and z locations between the tip and the de Bruijn pattern with the capacitive position sensor, the sample stage is retracted to a safe distance away from the scan head without changing the x or y sample stage locations to avoid crashing the tip into the substrate surface as the equipment undergoes thermal contractions during the cooldown. This room temperature observation of the tip location with respect to the de Bruijn pattern is vital in successfully finding a superconducting nanowire (or even the de Bruijn pattern) at cryogenic temperatures. In particular, it is extremely useful to know the z position of the sample stage when the tip touches the sample surface at room temperature when approaching at cryogenic temperatures since the vertical thermal contractions of the scanning equipment are reliably constant. Therefore, if the warm touch height is known, then

a relatively accurate guess of the z touch position at cryogenic temperatures may be made. Additionally, scanning the de Bruijn pattern at room temperature verifies that the tip is roughly centered within the pattern which indicates that the tip will remain over the de Bruijn pattern when the sample is cooled, even if the thermal contractions of the scanning equipment alters the x–y location of the tip.

5.4.2 Cryogenically Scanning the de Bruijn Pattern

Scanning a de Bruijn pattern on the sample surface at cryogenic temperatures requires that the effects of thermal contractions of the scanning equipment are considered. The cryo-AFM tip must be approached and compensated on the substrate surface once the cryostat has been cooled to $\sim 3\,\mathrm{K}$. As was previously noted, these processes are performed at room temperature while watching the sample and scan head with a webcam. However, there is no viable way to visually observe the approaching process while the cryostat is cold. As the scanner and cryo-AFM are cooled, thermal contractions alter the relative x, y, and z locations between the sample surface and the cryo-AFM tip. These contractions may cause x and y shifts occurring in random directions that are as large as $\sim 100\,\mu\mathrm{m}$; however, there is a high likelihood that the tip is somewhere above the de Bruijn pattern after a cooldown since the tip was roughly located in the center of the de Bruijn pattern at room temperature. Thermal contractions also cause a reliable change in the relative z position between the sample and the tip that reduces the sample-to-tip spacing by $\sim 80\,\mu\mathrm{m}$. Therefore, knowing the position sensor reading where the tip touched the substrate surface at room temperature is vital when approaching the sample stage towards the scan head at cryogenic temperatures.

The de Bruijn mapping is scanned with proportional-integral-differential (PID) contact mode once the cryo-AFM tip was approached and compensated at cryogenic temperatures. PID control is a common method of controlling a desired parameter, such as a temperature or a cantilever deflection, to a set point. For example, when scanning a de Bruijn pattern with $\sim 50\,\mathrm{nm}$ features, it is necessary to maintain a constant voltage on V_{24} (which corresponds to

the deflection of the AFM cantilever) with PID control of the z piezo voltage to perform profilometry measurements of the surface and to minimize wear of the AFM tip and cantilever. Scanning the AFM tip over these features causes the cantilever to deflect either towards or away from the substrate surface and therefore causes a change in the voltage on V_{24}. When such a voltage change is detected on V_{24}, the proportional term of the PID control applies a voltage to the z piezo that is proportional to the difference between the set point voltage and the measured voltage on V_{24}. However, only using the proportional term will always result in a finite difference between these voltages and so, purely proportional control can lead to ringing. Adding an integral term adjusts the correction voltage that is applied to the z piezo to minimize the accumulated error that is incurred between the V_{24} and the set point. We have found that balancing these two terms is sufficient to properly and smoothly control the cryo-AFM cantilever and that the remaining derivative term, which typically tunes the response time, is not required. In this way, the PID control continually adjusts the voltage on the z piezo to correct the voltage on V_{24} to match the desired set point voltage and the resulting z piezo voltage change (which is easily related to the piezo deflection) that was required to maintain a cantilever deflection of 50 nm is recorded as the profile of the substrate surface.

This PID scanning technique was performed on silicon substrates with de Bruijn mapping to locate the nanowire as shown in Figure 5.14a. First, a room temperature profilometry scan of the de Bruijn pattern was obtained via the PID contact mode implementation of the cryo-AFM and recorded as Scan 01, which is shown in Figure 5.14b. The location and scan range of the cryo-AFM tip for this room temperature scan is marked with a white dot and an orange box in Figure 5.14a respectively. Once the cryostat was cooled to 3 K, a cold scan was obtained without moving the x or y Attocubes and labelled Scan 02, which is shown in Figure 5.14c. The location and scan range of the cryo-AFM tip for this initial cold scan is marked with a white dot and a blue box in Figure 5.14a respectively. From these scans, the effects of the thermal contractions are noticed as a shift to the right in the tip location within the de Bruijn pattern. Then, the z piezo was retracted and the x and y Attocube positioners were adjusted to move the substrate

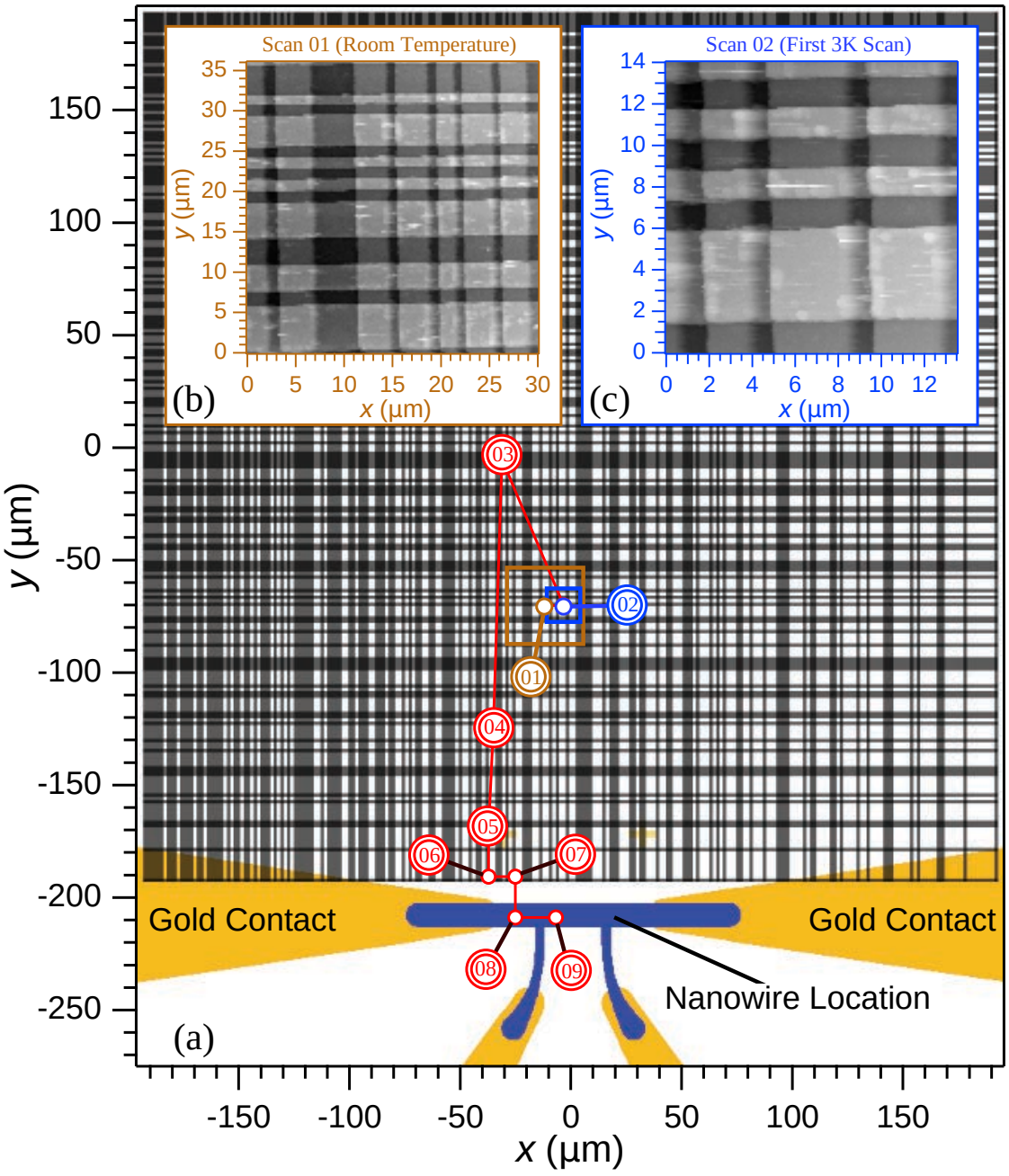

Figure 5.14: **(a)** A map of the scan locations at room and cryogenic temperatures performed to locate a superconducting nanowire. The centers of each scan (labelled by scan number) are denoted by the white circles. The red line connecting these dots shows the path that the scan head traced when finding the nanowire. **(b)** The initial profilometry data at room temperature obtained with a scan range of roughly ~ 30 µm × 30 µm is highlighted by the orange box in **(a)**. **(c)** The first cryogenic profilometry scan after cooling the cryostat to 3 K without moving the x or y Attocubes. The cold scan range of ~ 14 µm × 14 µm is highlighted by the blue box in **(a)**.

above the AFM tip to another location in the de Bruijn pattern where Scan 03 was obtained.* This process is repeated to move the scan head closer to the nanowire sample site and the tip location is recorded with Scans 04–08 until the nanowire was found in Scan 09 (which will be shown in Chapter 6).

With the previously described experiment, a superconducting nanowire may be located by implementing a self-sensing AFM-probe with a strain gauge cantilever in concert with coarse Attocube positioners and a de Bruijn mapping scheme. Once the nanowire sample is found with this cryogenic profilometry technique, the contactless scanning experiment to perturb superconductivity and map phase slip locations along the nanowire may be performed, which we will discuss in the following Chapter.

*We went the wrong way on this one!

Chapter 6

Mapping Phase Slips with Cryogenic Atomic Force Microscopy of Superconducting Nanowires

A cryogenic scanning experiment to map the locations of phase slips of the superconducting order parameter ψ in nanowires may elucidate the origin of the excess nanowire resistance that is observed below the critical temperature. Giordano attributed the excess resistance of indium nanowires that could not be explained by thermally activated phase slip (TAPS) to macroscopic quantum tunneling (MQT) events of the superconducting system. The existence of MQT that cause quantum tunneling phase slip (QTPS) events in superconducting nanowires as proposed by Giordano remains a subject of debate.[177–179, 181, 182, 184, 185, 187] While some theories and experiments[130, 131, 136, 145, 147, 154, 156, 159, 164, 181, 182] agree that MQT events causing QTPS in superconducting nanowires are responsible for the excess nanowire resistance, other theories and experiments[151, 164, 177–179, 185, 187] propose that defects or inhomogeneities in the nanowire cross section may elicit TAPS events at a different rate and therefore are the origin of the excess resistance. These theoretical discrepancies demand an experiment that can provide insight into the origins of the excess low-temperature nanowire resistance by determining if a correlation exists between the phase slip rate and nanowire inhomogeneities.

We therefore seek to cryogenically *map* the locations of phase slips along a superconducting nanowire with the scanning experiment proposed in Chapter 4. We postulate that the phase-slip rate may be experimentally influenced by *locally* perturbing superconductivity along the nanowire with either a dielectric or a magnetized tip that is scanned proximal to the nanowire with a cryogenic atomic force microscope (cryo-AFM). Recall that the resistance of a superconducting nanowire at a temperature T due to TAPS and the proposed MQT events is given by

$$R_{\text{Total}} = R_{\text{TAPS}} + R_{\text{MQT}} = \frac{\pi\hbar^2}{2e^2kT}\Omega e^{-\Delta F_0/kT} + A\frac{l}{\xi}\left[\frac{\Delta F_0}{\hbar\tau}\right]^{1/2} e^{-B\Delta F_0\tau/\hbar} \tag{6.1}$$

where ΔF_0 is the free energy barrier between the normal and superconducting states in the absence of an applied current. The TAPS and MQT models that were discussed in Chapter 4 and are represented with Equation 6.1 indicate that the wire resistance (and phase-slip rate) is exponentially dependent on the cross-sectional area A ($\Delta F_0 = uA\xi$) of the nanowire and indicates that phase slips occur at a higher rate at locations along the nanowire with smaller cross-sectional areas. Because of this, we expect the nanowire resistance to either exponentially increase or decrease when superconductivity is locally perturbed (or in other words, when the local condensation energy $u = (8\sqrt{2}/3)(H_c^2/8\pi)$ is perturbed) near a constriction along the wire. Therefore, if a cryo-AFM tip is scanned along a one-dimensional superconductor while simultaneously measuring the nanowire resistance, then we may experimentally determine if a correlation exists between the phase slip rate and any inhomogeneities in the nanowire.

The study of the apparent resistance caused by phase slips in the superconducting order parameter ψ requires samples that are one-dimensional so that fluctuations in ψ are only allowed along the lengths of these nanowires. Thus, it is vital to fabricate nanowires that are as narrow as possible and to use a material with a long coherence length, since superconductors are classified as one-dimensional nanowires by ensuring that the cross-sectional dimensions are small when compared to ξ. Therefore, materials with shorter coherence lengths (such as niobium with a coherence length of $\xi = 38\,\text{nm}$)[111,165] are not an attractive material choice as a result of the difficulty in fabricating a sample with the extremely small size-scales that are required in order to manifest phase slip events. In contrast, materials with longer coherence lengths (such as pure aluminum with a coherence length of $\xi = 1600\,\text{nm}$)[110] would be an ideal material choice since the size requirements of these nanowires are easier to fabricate and do not require the finest resolution techniques in order to realize a one-dimensional superconductor. However, the pure aluminum critical temperature of $T_c = 1.14\,\text{K}$[111] is lower than the base temperature of the available cryostat which is near 1.2 K,[109] so pure aluminum cannot be used as the sample material. We therefore chose to fabricate nanowires from sputter-deposited granular aluminum because this material has a modest coherence length of $\sim 150\,\text{nm}$ at $T = 0.9T_c$

(see Chapters 2 and 3), which suggests that a fabrication technique that is capable of producing nanometer-scale features is required to create nanowires using this material. Additionally, the material properties of granular aluminum films may be tuned during the sputter deposition by adjusting the amount of oxygen present during the sample growth, which enables the fabrication of nanowires samples with critical temperatures near $T_c = 1.7\,\mathrm{K}$ that are ideal for the cryostat.

The nanoscale of the desired one-dimensional granular aluminum samples requires a fabrication technique with a resolution limit that is capable of producing features that are smaller than the coherence length of granular aluminum of $\sim 150\,\mathrm{nm}$. Electron beam lithography (EBL), also termed scanning electron microscope (SEM) lithography, is one such fabrication technique that is widely implemented to create nanostructures.[126,147,156,164,169,171,172,174,195–198] Fabrication methods that utilize SEM lithography commonly employ poly(methyl methacrylate) (PMMA) as a lift-off resist. In this technique, PMMA resist is first spun onto a substrate and then exposed with an SEM followed by development and metallization. Then, the substrate is soaked in acetone, remover PG (RPG), or another solvent to dissolve the remaining PMMA resist and lift-off the sample. The details of this fabrication process can vary considerably due to the numerous options in resist molecular weights (if PMMA is used),[199] resist layering,[156,195,196] choice of developer,[200–203] developer temperatures,[202,204] sample deposition method (such as thermal evaporation or sputtering), lift-off solvents, and whether or not sonication is used to facilitate development[202] or nanowire lift-off.[205] EBL lift-off techniques may also be combined with etching practices to further reduce the sample size-scales.[164,171,197]

In addition to traditional lift-off techniques, SEM lithography may be exploited in combination with milling or etching methods to produce nanostructures. Rather than implementing PMMA as a positive-tone resist in which the exposed area is developed away, PMMA is instead employed as a negative-tone resist by exposing the PMMA layer with extremely large doses. These high doses cross-link the constituent PMMA polymers resulting in the insolubility of the cross-linked PMMA in acetone.[174] In this method, PMMA is first spun and baked onto a sili-

con substrate that has been metalized with the sample material. Then, the PMMA resist is exposed with the desired pattern with a large dose to cross-link the PMMA. Finally, the substrate is soaked in acetone, dissolving any unexposed resist. This leaves behind the cross-linked, patterned area which may now be used as either a wet- or dry-etch mask to define the superconducting nanowire geometry in the underlying sample layer.[174, 206, 207]

We attempted numerous combinations of EBL techniques to discover processes that repeatably produce granular aluminum nanowires which were scanned with a cryogenic atomic force microscope (cryo-AFM). First, we will discuss the wide range of lithographic processes that we explored in order to create trapezoidal or rectangular cross-sectional granular aluminum nanowires. Then, we will present the cryogenic scanning experiments that were performed to locally perturb superconductivity in these nanowires by using the home-built cryo-AFM (see Chapter 5) to scan a dielectric or a magnetized AFM tip near the wires in order to map phase slip events.

6.1 Electron Beam Lithography (EBL)

As we previously discussed, the size scale of the desired granular aluminum nanowires requires a lithographic technique with a smaller spatial resolution than what is provided by typical optical lithography systems. Electron beam lithography (EBL) uses a Scanning Electron Microscope (SEM) to expose a poly(methyl methacrylate) (PMMA) resist layer with a beam of electrons to produce resist features as small as $\sim 15\,\text{nm}$.[174, 198] However, the fabrication of nanowire samples in a four-probe geometry requires that the PMMA resist is used to either lift-off the sample or as an etch mask to transfer the exposed pattern from a PMMA layer into a sample layer, which typically results in slightly larger sample feature resolutions than what is achieved in PMMA resists. The generic principals and details of EBL that were used to ultimately realize nanowire samples will be discussed in this section.

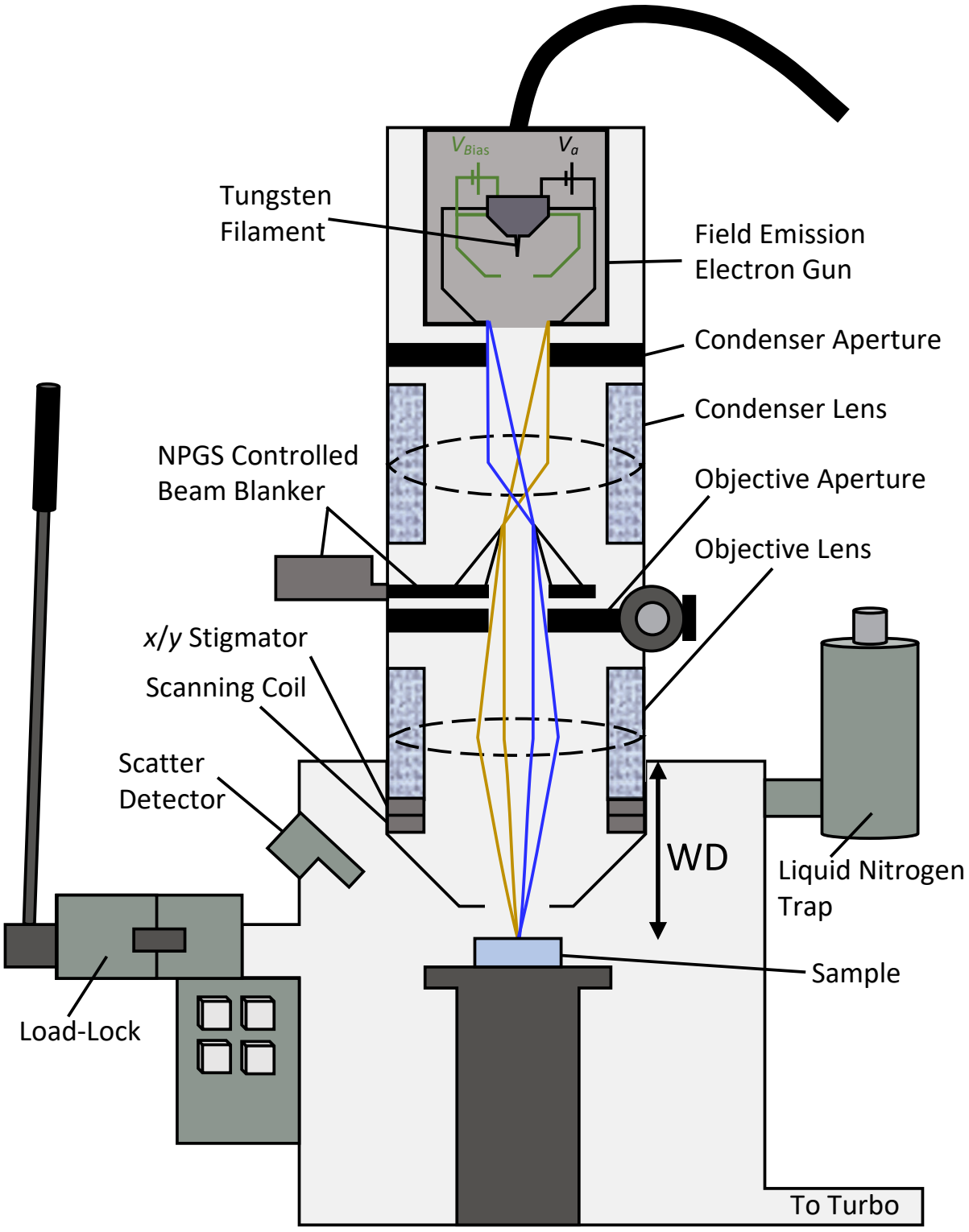

Figure 6.1: A schematic representation of a typical field emission SEM. This representation was modeled after the JEOL 6500F SEM that was used in this work. Select trajectories within the electron beam in the region of the SEM electron optics are denoted by the blue and orange paths.

6.1.1 The Scanning Electron Microscope (SEM)

Before exploring the numerous process details pertaining to SEM lithography, it is useful to discuss the electron optics and present the basic workings of a typical SEM, such as the JEOL 6500F that was used in this work. In a field emission SEM, which is schematically represented in Figure 6.1, a beam of electrons is generated with an electron gun at the top of the SEM column. The electron gun generates this electron beam by first thermionically emitting electrons from a tungsten filament. These electrons are then extracted from the region near the filament by a bias voltage V_{Bias} and are accelerated out of the gun with an accelerating voltage V_{a}. The trajectories of the electrons within the electron beam (represented by the blue and orange paths in Figure 6.1) are then controlled with a series of lenses and apertures as the electron beam moves through the SEM column. Here, "lens" refers to current-carrying coils (blue boxes and schematically represented with the dashed lenses) that influence the trajectories of electrons with a magnetic field and "aperture" refers to a plate with a small hole that blocks most of the electron beam, but allows portions of the beam to pass.

In order to perform high quality imaging and lithography, it is important to understand the function of the various electron optics within an SEM that are shown in Figure 6.1. The electron beam immediately encounters the condenser aperture after emerging from the field emission gun, which roughly collimates the beam. Then, the total beam current (that will eventually impinge on the surface of the sample) is controlled with the condenser lens by broadening the beam,[208] which creates diffuse trajectories that are blocked with the objective aperture.* In addition to blocking certain trajectories that are created with the condenser coils, the objective aperture also controls the size of the electron beam at the surface of the sample by adjusting the aperture size. Smaller apertures will result in smaller beam diameters which allows for higher resolution imaging or lithographic exposures to be performed. However, there is a trade-off since smaller apertures decrease the overall beam current, which either decreases the bright-

*Note that changing the objective aperture will also alter the beam current, however, this is not the primary role of the objective aperture and the beam current should be controlled by adjusting the current through the condenser coils.

ness for imaging applications or increases the required exposure time for lithographic applications. Finally, the electron beam is focused onto the sample surface with the objective lens.[208] When observing the surface of a sample, the electron beam is rastered with the the scanning coil and electrons that are scattered off the sample surface are detected and recorded with the scatter detector.

The first parameter that must be chosen for either application of the SEM is the accelerating voltage V_a. When exposing electron beam resists in lithographic applications, larger V_a are generally desired since high accelerating voltages yield collimated electron beams.[202] Rooks *et al.* have performed Monte Carlo simulations of the distributions of electrons in an electron beam for various accelerating voltages and found that the most collimated beams are obtained with $V_a = 100\,\text{kV}$ and that smaller accelerating voltages produce lower aspect ratio beams.[202] These low aspect ratio beams result in larger resist linewidths since the electron distribution is less localized when exposing the PMMA. Therefore, all of the lithographic work presented here was performed at 30 kV, which is the largest accelerating voltage that the JEOL 6500F SEM is capable of producing. When attempting imaging, however, accelerating voltages as low as 5 kV may be desired, especially for organic or fragile samples. Therefore, all imaging was performed at an accelerating voltage of 15 kV since the superconducting nanowires and test structures that we will discuss in this work are not fragile in this regard.

The electron beam requires an initial setup and optimization when using the SEM to perform imaging or lithographic exposures. First, an objective aperture size and a beam current that are appropriate for the intended application of the SEM must be determined and set. The JEOL 6500F SEM that was used is equipped with four objective apertures of sizes ranging from 30 µm – 1000 µm and are labelled such that the largest numbered aperture corresponds to the smallest diameter size. Therefore an objective aperture of 4 (corresponding to an aperture diameter of 30 µm) was used to expose fine features along with a beam current of $\sim 25\,\text{pA}$,[209] which was produced by choosing a probe current of "3" in the SEM control program. A slightly larger objective aperture of 3 (corresponding to an aperture diameter of 50 µm) was used to ex-

pose larger features or to image samples along with a beam current of 150 pA ~ 6500 pA, which was obtained by choosing a probe current of "6–13" in the control program.

Additionally, the JEOL 6500F SEM is equipped with a nanoscale pattern generation system (NPGS) controlled beam blanker (see Figure 6.1) that must be placed in the path of the electron beam if the SEM is intended to be used to perform lithographic exposures. The beam blanker is a conductive plate with a large opening that is placed above the objective lens. NPGS then rapidly controls the plate voltage to either block the beam from the sample by applying a large voltage (~ 200 V) to the plate in order to terminate the electron beam at the blanker or to allow the electron beam to pass through the blanker by grounding the plate voltage. By rapidly varying the beam blanker voltage in this way, the electron beam may be turned on or off and lithographic exposures may be performed on the sample. Therefore, it is vital that the alignment procedure (which will be discussed later) is performed with the grounded beam blanker inserted into the path of the electron beam before performing lithographic exposures since the presence of another conducting plane marginally alters the path of the electron beam. In other words, aligning the electron beam before inserting the beam blanker will result in a marginally misaligned electron beam, which is detrimental to the quality of ultra-fine lithographic features. Also, the beam blanker opening must be centered with respect to the objective aperture in order to achieve the best alignment when using the beam blanker.

The electron beam may now be aligned, focused, and characterized once the SEM has been configured with the desired objective aperture, beam current, and beam blanking settings. Beam alignment and focusing are performed by imaging a standard with 10 nm and 100 nm spherical gold nanoparticles, which is mounted onto the sample stage. First, the sample stage height is adjusted to focus the gold standard. However, a sample stage that is in the correct focal plane of the electron beam will not necessarily produce focused images or lithography since the beam shape also plays a major role in the quality of SEM microscopy. Several details of the electron optics can alter the beam shape such as the presence of the beam blanker, the exact profile of the various apertures, and the uniformity of the lens coils which may all led to an

astigmated or elliptically-shaped beam at the sample surface. Therefore, the shape of the electron beam is corrected to a circular shape by adjusting the x/y stigmators, which are located near the base of the SEM column as shown in Figure 6.1. The extreme advantage of performing the beam alignment using spherical gold nanoparticles becomes apparent since diagnosing an astigmated beam is generally difficult when imaging arbitrarily-shaped features. If the gold particles appear elliptical or not spherical in shape, then the electron beam is astigmated and further corrections with the x/y stigmators are required. Therefore, an iterative process is used to properly align the electron beam by first adjusting the sample height, then adjusting the x/y stigmators, and then repeating this process until the gold particles on the standard appear spherical and are in focus. Images of the gold nanoparticles before and after properly aligning and focusing the electron beam are shown in Figures 6.2a and 6.2b respectively. Note that the 10 nm gold particles can be resolved in the background of Figure 6.2b which indicates that the resolution of the SEM is at least as low as 10 nm with this particular alignment.

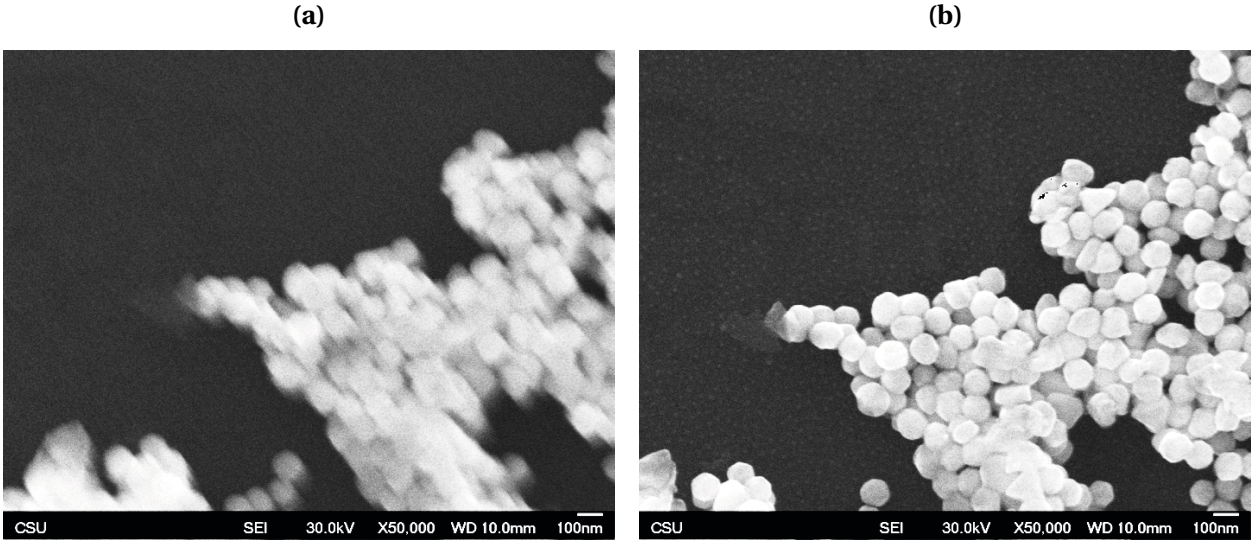

Figure 6.2: SEM images of the gold standard **(a)** before and **(b)** after the instrument was aligned. Note that both gold nanoparticle sizes of 100 nm and 10 nm are resolved in **(b)** with the smaller 10 nm particles in the background.

The beam current is then measured once the beam is properly aligned and focused by using a Faraday cup and picoammeter. A Faraday cup is a small, conductive cup with a hole in its center which is electrically connected to the picoammeter. If an aligned electron beam is focused through this hole, then all of the charge is collected in the conductive cup and an extremely accurate measurement of the total beam current may be performed. This measurement is critical when using the SEM for lithographic applications as it determines the amount of time that the beam blanker exposes the PMMA at each point in a lithographic pattern in order to achieve the desired exposure dose. As we previously noted, an aperture of 4 along with a spot size of 3 were used when exposing ultra-fine nanowire features such that the electron beam current at the sample surface was close to $\sim 25\,\text{pA}$, which proved to be essential in order to obtain the highest resolution exposures.[209]

6.1.2 EBL Process Details

In general, a Jeol 6500F SEM was used in this work to expose a layer of PMMA to create either a positive- or negative-tone pattern to lift-off or etch a nanowire sample in a four-probe geometry. Fabricating nanowire samples with SEM lithography is an involved process that requires numerous process steps and careful preparation. Additionally, several design and sample details must be carefully considered to successfully create nanowires with either implementation of PMMA resist. Although the generic EBL fabrication process is complex and requires careful consideration, SEM lithography can reliably and easily create samples with nano-scale features.

Pattern Design Details

Before exposing samples with an SEM, a lithographic pattern that dictates how the sample is exposed must be properly designed and configured. As we previously discussed, the nanoscale pattern generation system (NPGS) controls the voltage on the beam blanker to modulate the electron beam on the sample surface. During an exposure, the electron beam is rastered with the scanning coil (see Figure 6.1) and NPGS modulates the blanker voltage to turn the beam on or off at each pixel according to a lithographic pattern and various design parameters. The pixel

size that NPGS uses to expose the sample pattern is determined by the field of view (FOV) and a 16-bit digital to analogue converter that allows communications between the beam blanker on the SEM and the NPGS software on an external computer. For example, if a nanowire pattern is exposed using a FOV of 100 µm × 100 µm, then the pixel size that is distinguishable by NPGS is $100\,\mu m/2^{16} = 1.5\,nm$. However, additional considerations are required in order to exploit this minimum pixel size for a given pattern in the NPGS software.

In addition to the sample geometry, an electron beam pattern requires information about the exposure which must be properly configured within an NPGS pattern in order to perform high-resolution lithography.[209] In particular, the "center-to-center distance", the "line spacing", and the magnification must be determined and set in the NPGS design pattern before exposing a sample. Both the "center-to-center distance" and "line-spacing" parameters dictate the lateral and vertical spacings between each pixel in the pattern and should be set to the smallest possible size (as was previously determined by the FOV and the 16-bit digital to analogue converter). NPGS does not automatically populate these values with the minimum pixel size, so manually verifying that these parameters are properly set is vital to avoid exposing, for instance, a 100 nm feature with 100 nm spacing parameters.

The importance of the "center-to-center" and "line" spacings indicates that the magnification of the SEM during the exposure is also crucial because the FOV determines the pixel size. Larger numeric magnifications will result in smaller pixel sizes with which NPGS exposes the sample surface. However, the FOV is reduced for larger magnifications which drastically increases the difficulty of aligning the exposure pattern to pre-defined features. Additionally, some SEM models have "coarse magnification jumps" and writing ultrafine features at magnifications that are near these jumps can result in lower quality features.[209] For example, the Jeol 6500F series SEM has magnification jumps at 70×, 700×, 7000×, and 70000×. Therefore, a magnification of 1000× was chosen since this magnification is not close to any magnification jumps and also results in a usable FOV of 108.8 µm × 108.8 µm. This FOV is large enough to fa-

cilitate pattern alignment and large feature exposures while also yielding a minimum pixel size of 1.66 nm, which is small enough to properly expose ~ 100 nm nanowires.

Process Details

Sample preparation may begin after designing and optimizing the sample pattern in NPGS. Silicon substrates with an insulating oxide or nitride coating are first prepared with a standard 3-solvent rinse and then a layer of either 495K or 950K weight PMMA dissolved in anisole (A3) is spun and baked onto the clean substrate for 90 seconds with a 180 °C hotplate. Recall that thicker resist layers generally promote sample lift-off or better protect an underlying sample layer when an etching technqiue is used to transfer a lithographic pattern. Since PMMA resists are typically much thinner than the Shipley S1800 series photoresists that were used and discussed in previous Chapters, a slower spin speed of 2000 rpm was used to obtain PMMA thicknesses of ~ 120 nm for 495K PMMA and ~ 200 nm for 950K PMMA.[106] Therefore, it is important to program a ramp-up spin step from 500 rpm to 2000 rpm to create a more uniform resist coating. The PMMA-coated silicon substrates were next mounted to a conducting SEM pellet with copper tape to minimize resist charging during exposure with the electron beam, which is vital since resist charging may result in under-exposing the PMMA.

Next, the samples are loaded into a JEOL 6500F SEM to expose the PMMA resist. If nanoscale features are desired, then the SEM is initially configured with the beam blanker inserted into the SEM column, an accelerating voltage of 30 kV, an objective aperture of 4 with a 30 µm diameter, and a probe current of 3 (which adjusts the strength of the condenser lens) to obtain a beam current of ~ 25 pA at the sample surface. Then, the electron beam is aligned, focused, and characterized using a gold standard and a faraday cup as was previously discussed before performing any exposures. Once the electron beam is aligned, the SEM is moved above a sample and the sample stage is adjusted to focus the electron beam on the sample surface since the sample and gold standard are not the same thickness.* This focusing is performed on x-shaped

*The beam alignment does not need to be repeated.

scratches in the PMMA that were intentionally placed in the corners of the substrate and away from the sample area with a razor blade when the samples were mounted onto the conductive SEM pellets. Scratching the PMMA surface in this way ensures that the substrate surface will have defects (that are far away from the nanowire write area) that may be used to focus the electron beam because focusing on extremely clean and uniform spin-coated PMMA is nearly impossible.

The sample pattern is then exposed once the sample surface is focused and the sample area is located.* From numerous exposure tests, we found that positive-tone PMMA patterns are typically exposed with doses that range from $300\,\mu C\,cm^{-2} - 1200\,\mu C\,cm^{-2}$ depending on the feature width (larger features require smaller doses) and that negative-tone PMMA patterns are typically cross-linked with doses that range from $10000\,\mu C\,cm^{-2} - 80000\,\mu C\,cm^{-2}$. After exposure, the samples are developed and the remaining PMMA is implemented in lift-off or etching techniques to create a sample. There are numerous details that pertain to developing exposed PMMA resists, which we will explore in the next section.

6.2 Creating Nanowires with EBL

The previously described EBL process was used to create granular aluminum nanowires in a four-probe geometry with two distinct techniques, which are summarized in the following way. In the first method, PMMA is employed as a positive-tone resist to lift-off granular aluminum nanowires. First, silicon substrates with de Bruijn mapping (see Chapter 5) are spun and baked with a layer of PMMA resist as was previously described. Then, the resist is exposed with an SEM and subsequently developed with one of the several choices of PMMA developers. The developed resist is next metalized with a layer of granular aluminum and then lift-off is performed in an acetone bath. In the second method, PMMA is employed as a negative-tone resist as an etch mask to define the nanowire geometry in a layer of granular aluminum. Silicon substrates with de Bruijn mapping are initially metalized with a layer of granular aluminum to cover the

*If pre-existing features are on the substrate surface, then alignment is performed in NPGS.

entire substrate. Then, a layer of PMMA resist is spun and baked with the usual spin-coating parameters. Next, these samples are exposed with extremely large doses using the SEM and are then developed in an acetone bath to dissolve the unexposed resist. The samples are then either ion-milled or wet-etched to transfer the nanowire geometry from the PMMA etch mask into the granular aluminum film. Various process parameters were tested for both the positive- and negative-tone applications of PMMA with exposure tests before any four-probe wires were fabricated. Granular aluminum nanowires were then fabricated in a four-probe geometry once a set of optimal process parameters were empirically determined from these exposure tests.

6.2.1 Using PMMA as a Positive-Tone Resist

One commonly exploited nanoscale fabrication technique that is capable of producing the desired nanowire samples is to use poly(methyl methacrylate) (PMMA) as a lift-off resist. This is accomplished by implementing PMMA as a positive-tone resist such that the areas of the PMMA that are exposed with an electron beam are developed away. However, the extreme versatility of this technique indicates that the quality of nanoscale samples may vary considerably as a result of the numerous process options. Therefore, we explored the effects of resist layering,[156,195,196,198] developer,[200–203] developer temperature,[202,204] and metallization technique (sputtering and thermal evaporation) by exposing and processing a pinwheel of nanowires to determine the most robust nanowire lift-off recipe. This geometry is a particularly useful test structure to use when optimizing an EBL lift-off recipe since each nanowire in the pinwheel is written at a different angle which may therefore be used to diagnose any failures that are caused by an astigmated electron beam.

In order to create a nanowire fabrication recipe, several layering structures of 950K and 495K PMMA resists were tested. Layering a higher resolution resist (such as 950K PMMA) on top of a lower resolution resist (such as 495K PMMA) may be used to create undercut geometries* as a result of the larger features that form in the underlying resist layer when the resist stack

*For a schematic picture of an undercut, see Chapter 2.

is exposed.[198] Additionally, we hypothesize that multiple layers of the same molecular weight PMMA may be used to artificially increase the single layer resist thickness, which may improve lift-off quality by mitigating the detrimental effects from the resist sidewall coating when the resist is metallized. We explored these possibilities in this work by testing the exposure and lift-off parameters of monolayers of 495K and 950K weight PMMA in addition to bilayers of 950K PMMA spun on top of 495K PMMA (which we will denote with 950K/495K), 950K/950K, and 495K/495K. Nanowire patterns in a pinwheel geometry were exposed in these resist layer structures using the previously described EBL process with the JEOL 6500F SEM followed by development with a 3 : 1 mixture of isopropyl alcohol : methyl isobutyl ketone (IPA : MIBK),[200,202] called developer **A**. These tests determined that each resist layering (including the PMMA monolayers) yielded successful exposures in the PMMA layers with no signs of beam astigmatism. However, lift-off attempts with a ~ 50 nm layer of sputter-deposited granular aluminum failed with each of these resist stacks.

We hypothesize that developing the exposed PMMA with developer **A** could cause problematic geometries that could result in failed lift-offs. In order to understand the post-development feature geometry in the PMMA, a nominally 100 nm nanowire that was exposed in a bilayer of 950K/495K PMMA was imaged with the SEM and is shown in Figure 6.3. This image was obtained after coating the exposed and developed PMMA stack with 30 nm of granular aluminum, but before attempting lift-off. The granular aluminum layer was deposited to facilitate imaging with the SEM since conductive layers are easier to image than insulating layers. It became clear from Figure 6.3 that the nanowire that was exposed in the PMMA stack is much narrower than the nominal exposure width, which was most likely the reason behind the failed lift-off attempts in similar test samples. This narrower nanowire geometry in the resist may plausibly be a result of the PMMA resist stack swelling during development in **A**.[203]

The temperature dependence of developer **A** on the resist contrast as well as the addition of other developer components were explored in an attempt to resolve the resist swelling issue. Hu *et al.* have found that the contrast and sensitivity of PMMA resists increases when developed in

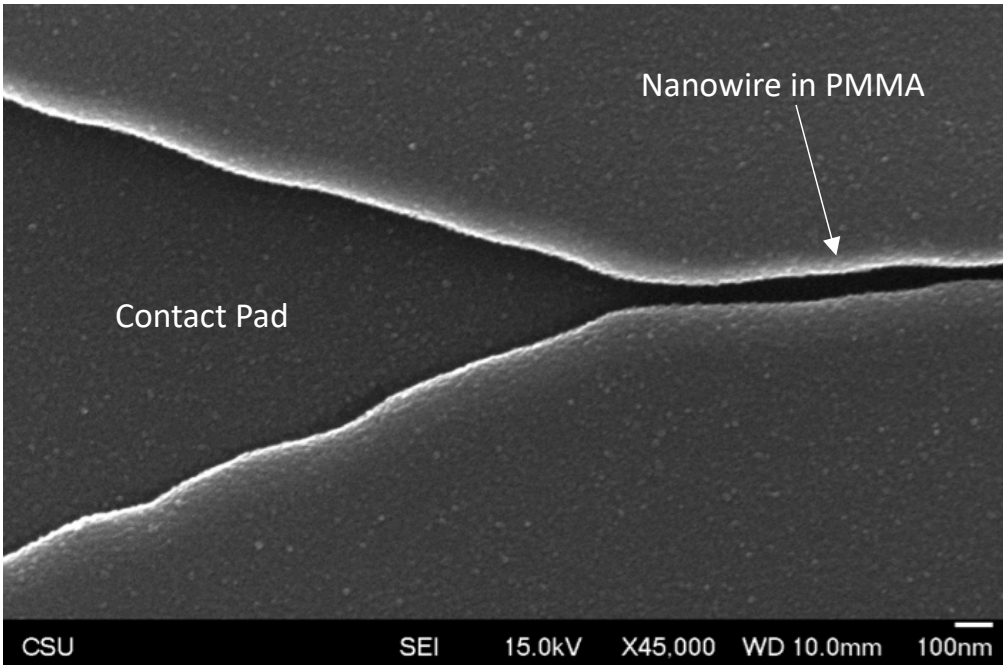

Figure 6.3: An SEM image of a nanowire near a contact pad in a bilayer of 950K/495K PMMA resist that was nominally exposed to be 100 nm in width with a dose of 600 $\mu C\,cm^{-2}$. This image was obtained at a magnification of 45000× and at an accelerating voltage of 15 kV. The PMMA was developed in a room temperature mixture of 3 : 1 IPA : MIBK (developer **A**) and then coated with 30 nm of granular aluminum to promote imaging with the SEM.

cold **A**. So, additional exposure tests of a pinwheel of nanowires were developed in this way, but resulted in failed lift-off attempts. Another potential method to increase the resist resolution is to add trace amounts (~ 1.5 %) of Methyl Ethyl Ketone (MEK) to developer **A**,[200] however, this resulted in the same lift-off issues. Therefore, we explored using an alternative PMMA developer to determine if lift-off nanowire features were possible with this recipe.

A mixture of 3 : 1 isopropyl alcohol : water (IPA : H_2O), called developer **B**, is another common PMMA developer that was implemented to mitigate the previously discussed problems that may be associated with developer **A**. Although developer **B** is less commonly used, Mohisin *et al.* found that this developer is capable of producing higher resolution features than developer **A** when using an accelerating voltage of 20 kV to expose the resist,[201] which is similar to the accelerating voltage that was used in this work. Additionally, Rooks *et al.* have observed an increase in the resist resolution when developing features with chilled developer **B**, although an accelerating voltage of 100 kV was used to expose these features.[202] Therefore, we tested the

(a) Room Temperature **(b)** 5 °C

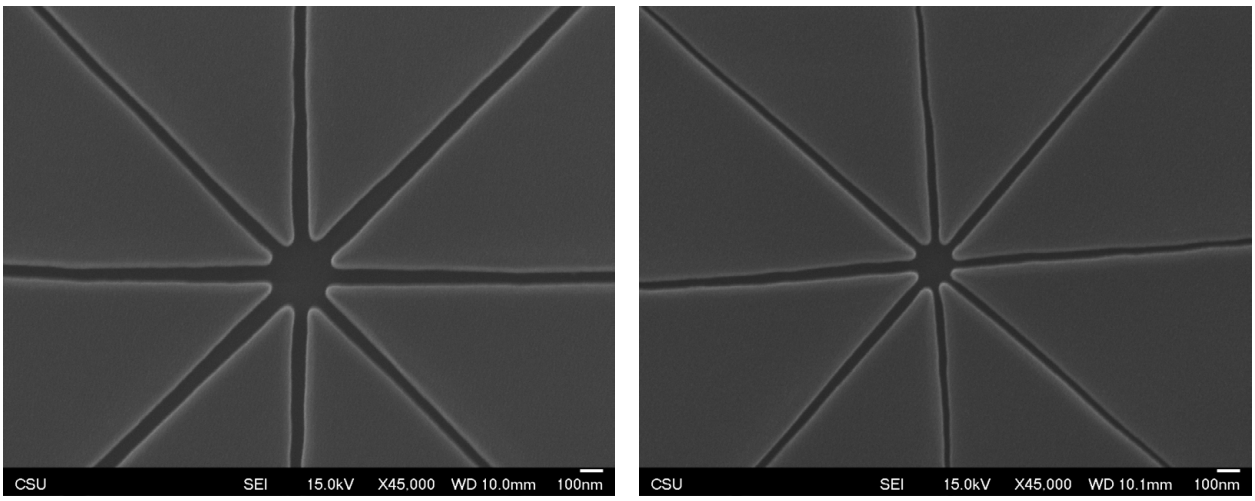

Figure 6.4: SEM images of nominally 30 nm wide nanowires in a pinwheel geometry that were exposed in a monolayer of 950K PMMA and were developed in **(a)** room temperature and **(b)** 5 °C 3 : 1 IPA : H_2O (developer **B**). The features in **(a)** were exposed with a dose of 707 μC cm^{-2} and the features in **(b)** were exposed with a dose of 969 μC cm^{-2}. These images were obtained with an accelerating voltage of 15 kV and a magnification of 45000×. Both substrates were coated with 10 nm of granular Al to promote imaging with the SEM.

efficacy and temperature dependence of developer **B** by exposing a pinwheel of 30 nm wide nanowires in a monolayer of 950K PMMA resist on two substrates. Each substrate was then developed in either room temperature or 5 °C developer **B** which resulted in the nanowire PMMA trenches that are shown in Figures 6.4a and 6.4b respectively. These tests revealed that a larger exposure dose of 969 μC cm^{-2} was required when the exposures were developed with chilled developer **B** when compared to the exposure dose of 707 μC cm^{-2} that was required when using room temperature developer **B**. Additionally, the exposures depicted in Figure 6.4 indicate that development with **B** results in much narrower nanowires in the PMMA when compared to nanowire features that were developed with **A** and that chilled developer **B** yields a slightly higher resolution. Therefore, we decided to use room temperature developer **B** to develop positive-tone PMMA resist for lift-off techniques since this developer creates promising PMMA trenches that seem likely to produce lift-off nanowires.

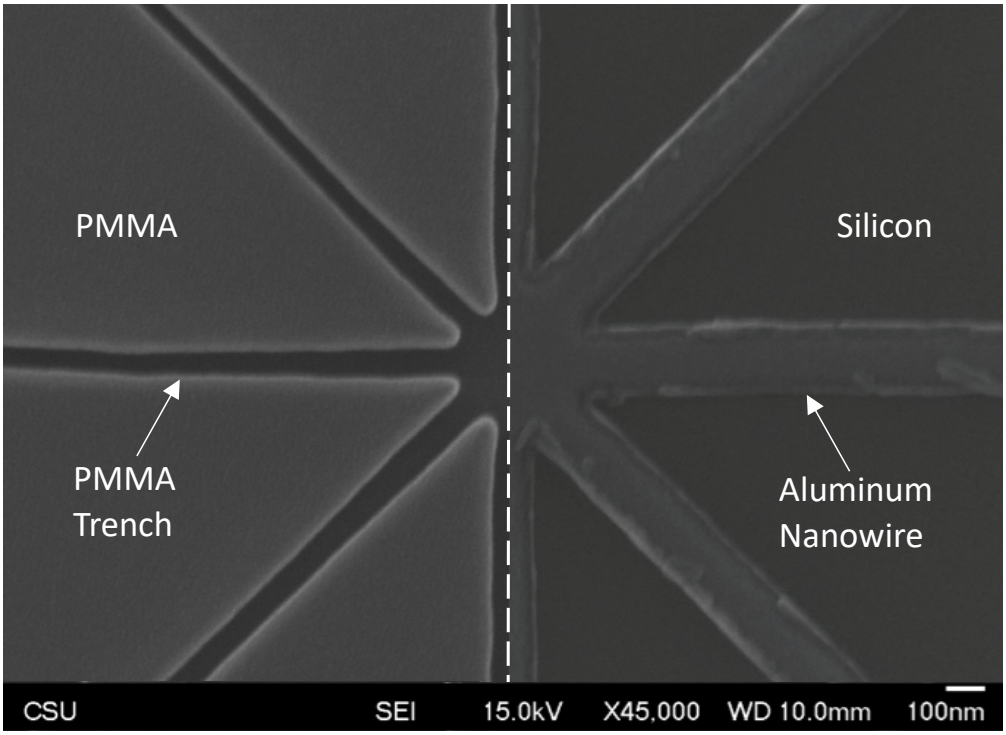

Figure 6.5: Left: An SEM image obtained with an accelerating voltage of 15 kV and a magnification of 45000× of nominally 30 nm wide nanowire trenches exposed in a layer of 950K PMMA. The PMMA was developed in a room temperature mixture of 3 : 1 IPA : H_2O (developer **B**) and then coated with a 10 nm Al layer to facilitate imaging (previously shown in Figure 6.4a). **Right:** An SEM image at the same accelerating voltage and magnification of a granular aluminum nanowire pinwheel that was sputtered to a thickness of 80 nm and lifted-off of a substrate that was processed identically to the one shown in the left image.

Test samples that were exposed with a pinwheel of nanowires and developed with room temperature developer **B** were then metallized with a layer of granular aluminum to determine if these nanowire trenches resulted in successful lift-off nanowires. First, a sample with 30 nm wide nanowire PMMA resist trenches was metalized via sputter deposition with 80 nm of granular aluminum and lifted-off in a room-temperature acetone bath. The right half of Figure 6.5 depicts an SEM image of this granular aluminum pinwheel of nanowires that was lifted-off from a sample with a pinwheel of nanowire trenches in a layer of 950K PMMA that was exposed and developed in the same manner as the resist that was also imaged with the SEM and shown with the left half of the image. Unfortunately, comparison of these images reveals that the lift-off granular aluminum wire widths are much wider than the trenches that were exposed in the

PMMA. This is an unexpected result since the only explanation for obtaining 150 nm wide lift-off nanowires from ~ 70 nm wide trenches is that the PMMA sidewalls were coated and the granular aluminum film was severed at a width of ~ 150 nm. As was discussed in Chapter 2, any sidewall coating of a lift-off resist is detrimental to the quality of the lift-off since the sample area becomes connected to the deposited metallic sheet, which may cause the nanowire features to lift-off with the rest of the metallic sheet. However, the SEM image of the lifted-off granular aluminum nanowires in Figure 6.5 shows rough nanowire edges with "flaps" of granular aluminum which indicates that the nanowires tore from the sputtered sheet during lift-off. Therefore, this lift-off technique with sputter-deposited granular aluminum will not produce nanowires that are narrower than ~ 150 nm and the nanowires that are produced do not have uniform edges.

One explanation for the lack of lift-off success that we experienced with sputtered granular aluminum nanowires using PMMA as a lift-off mask is potentially caused by the deposition method. When metallization is performed via magnetron sputtering, material is ejected from a ring on the target rather than from a point source. This non-point-source property of sputtering methods creates large angles of incidence of ballistic material in addition to the presence of diffusive sputtered material[108] that can easily coat the sidewalls of the PMMA. Because of this, metallization via thermal evaporation can mitigate issues related to the sidewall coating since the evaporation source is much more point-like as the metal is evaporated from a small boat that is heated with large currents. We therefore tried to thermally evaporate granular aluminum nanowires instead of sputtering; however, the system that we used is not capable of cooling the substrate in situ. As a result, the energy deposited into the PMMA by the hot evaporated aluminum hard-baked the PMMA layer which made lift-off even more difficult and unreliable. All attempts to reduce the sample heating including thermally anchoring the substrates, increasing the source-sample distance, and creating a thermal shield to occlude the sample from the hot evaporation components yielded the same difficulties and seemed to result in the same resist heating. Since lift-off is difficult when implementing sputtering or thermal evaporation, we decided to explore an alternative SEM lithographic technique to fabricate the desired nanowires.

6.2.2 Using PMMA as a Negative-Tone Resist

Extremely small nanodevices can also be fabricated by using PMMA as an etch mask. This technique implements PMMA as a negative-tone resist by exposing the resist with exceptionally high doses ($> 10\,000\,\mu C\,cm^{-2}$) to cross-link the PMMA polymers.[174,206,207] The sample is then "developed" in acetone which dissolves the *unexposed* resist, leaving behind the exposed and insoluble cross-linked PMMA. The remaining cross-linked resist is then used as a dry- or wet-etch mask to define the desired nanowires of superconducting material in an underlying layer. This technique was ultimately employed to reliably produce 30 nm – 200 nm nanowire structures and resulted in 150 nm wide four-probe nanowire samples.

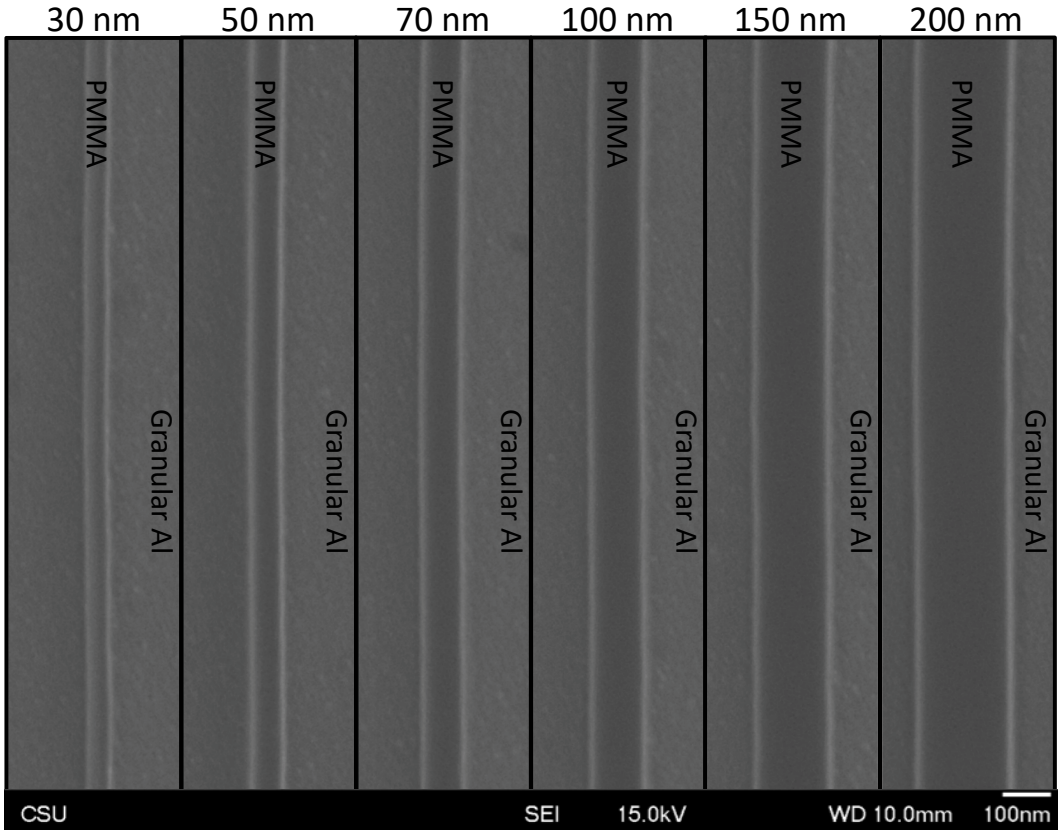

Figure 6.6: SEM images of 950K PMMA nanowires written at 30 nm, 50 nm, 70 nm, 100 nm, 150 nm, and 200 nm in width. These PMMA nanowires were written on a silicon substrate with a 70 nm layer of granular aluminum with a dose of $45\,000\,\mu C\,cm^{-2}$.

The optimal exposure parameters to create cross-linked nanowires of PMMA were determined from various exposure tests. These tests were performed on substrates that were sputter-coated with a $\sim 70\,\text{nm}$ layer of granular aluminum followed by spin-coating a layer of either 495K or 950K PMMA with the previously described spinning parameters. The samples were then mounted and electrically grounded to SEM sample pellets with copper tape to mitigate sample charging when exposing the PMMA with an electron beam as was previously described.* Then, several test nanowire structures ranging in width from $30\,\text{nm} - 200\,\text{nm}$ were exposed with large exposure doses with the SEM. The sample was then "developed" in acetone to dissolve the unexposed resist and leave behind the insoluble and cross-linked PMMA wires, shown with the SEM images in Figure 6.6, with dimensions that closely matched the pattern widths for exposure doses $> 30\,000\,\mu\text{C}\,\text{cm}^{-2}$. This is a robust method of producing cross-linked PMMA nanowires that cover a layer of sample material since this technique is not sensitive to the exact exposure dose (as long as the dose is large enough) or to the development time.

Transferring the PMMA Nanowires into Granular Aluminum

Now that PMMA nanowires have been fabricated, these features must be used as an etch mask in order to create superconducting nanowire samples in the underlying granular aluminum layer. We first explored the use of a wet-etch to transfer the nanowires from the PMMA into the granular aluminum sheet by etching an exposure test sample with Transene moly etchant, which is a phosphoric-acetic-nitric acid solution. The test sample was etched for $\sim 2\,\text{min}$ until the unprotected granular aluminum sheet was completely etched away, which creates granular aluminum nanowires with trapezoidal cross-sections as a result of the isotropic etching geometry. For example, as a granular aluminum sheet of thickness $\sim 50\,\text{nm}$ is wet-etched, the acid solution also laterally etches the granular aluminum nanowires beneath the PMMA nanowire by $\sim 50\,\text{nm}$ on each side, which forms sloped edges in the protected granular aluminum. Therefore, an accurate etch time combined with appropriately wide PMMA

*It is much easier to ensure that the sample is properly grounded with this technique (as opposed to the lift-off method) since there is a conductive sample layer beneath the PMMA layer.

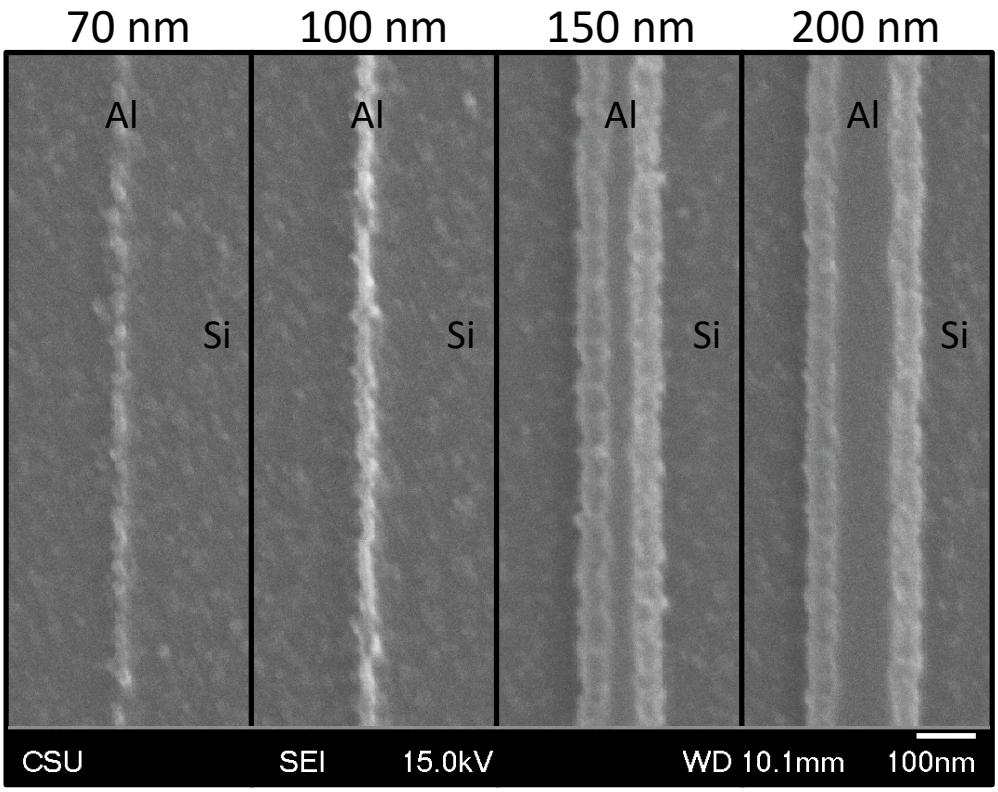

Figure 6.7: SEM images of granular aluminum nanowires created from wet-etching 495K PMMA nanowires with Trasene moly etchant. The PMMA nanowires were written at widths of 70 nm, 100 nm, 150 nm, and 200 nm with a dose of 80 000 $\mu C\,cm^{-2}$. As a reuslt of the isotropic nature of wet-etching, nanowires from PMMA wires of width < 100 nm were not reliably continuous. Granular aluminum nanowires that were masked by PMMA wires that were wider than 100 nm, however, were trapezoidal in cross section.

nanowire etch masks are crucial to successfully fabricate nanowire samples with this method because over-etching the sample may result in completely laterally etching through the granular aluminum nanowires. Therefore, wider PMMA nanowires of width 150 nm ~ 200 nm were required to properly produce ~ 100 nm wide granular aluminum nanowires. Figure 6.7 depicts several granular aluminum nanowires that were fabricated by wet-etching a granular aluminum sheet that was masked by 70 nm−200 nm wide cross-linked PMMA nanowires that were exposed in 495K PMMA resist with a dose of 80 000 $\mu C\,cm^{-2}$. While four-probe nanowire samples were eventually realized with this method, adhesion between the cross-linked PMMA and the granular aluminum layer became unreliable when wet-etching larger cross-linked patterns, which resulted in unreliable four-probe samples.

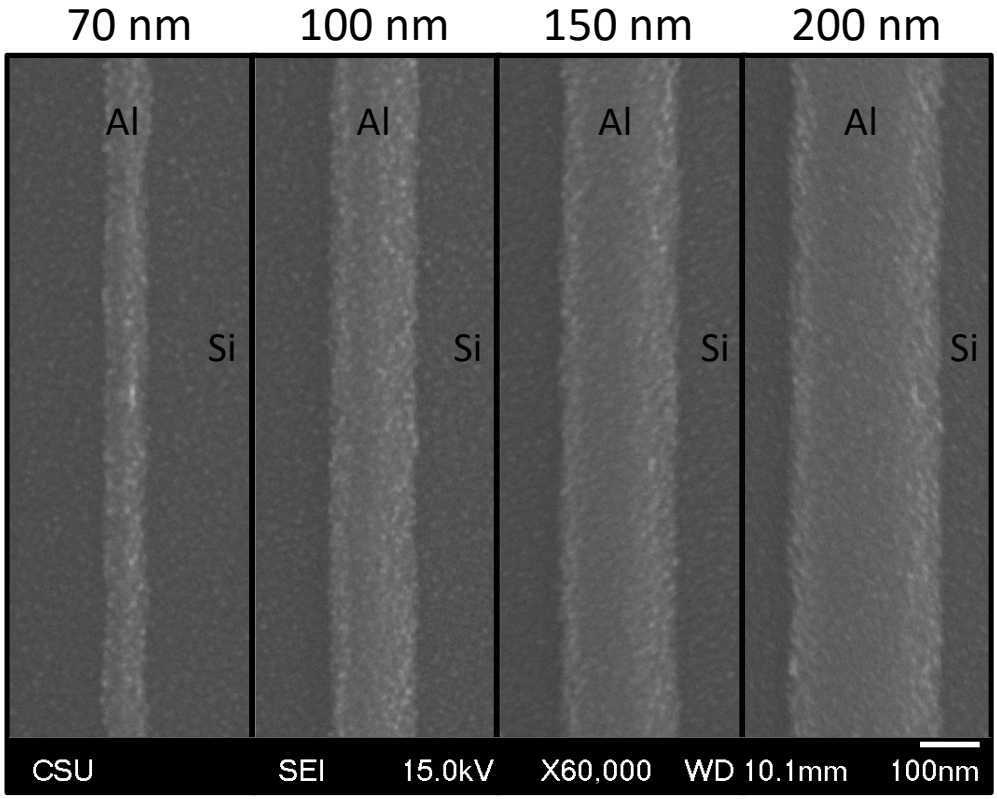

Figure 6.8: SEM images of granular aluminum nanowires that were created by milling 950K PMMA nanowires with the sputter system. The PMMA nanowires were written at widths of 70 nm, 100 nm, 150 nm, and 200 nm with a dose of 56 667 $\mu C\,cm^{-2}$.

Dry-etching or ion milling is an alternative method of transferring the nanowire geometry into an underlying sample layer. In this technique, the cross-linked PMMA nanowires are used as a milling mask to protect areas of the granular aluminum layer during ion bombardment. Unlike wet-etching, ion milling is not an isotropic process, and so nanowires that are transferred into a granular aluminum layer with this method have rectangular cross-sectional shapes and are closer in width to the PMMA nanowire etch masks. This method has been used by Cai *et al.* to produce thin gold wires by forming similar nanowires in a PMMA layer, adjusting the PMMA wire width with an oxygen ash, and then milling the sample.[174] In our work, PMMA nanowire structures that are written on a granular aluminum sheet were milled with either a Kaufman & Robinson (K & R) KDC 40 ion mill or with the sputter system, which were both described in Chapter 3. However, the etch rate of the PMMA was problematically fast in the K & R ion mill, which left the granular aluminum layer unprotected. So, nanowire samples were milled in the

sputter system since this milling method yielded a much more reasonable PMMA etch rate and consistently created narrow and smooth granular aluminum nanowires.*

Figure 6.8 shows SEM images of several granular aluminum nanowires that were fabricated by milling 950K PMMA nanowires that were 70 nm – 200 nm in width with the sputter system. In order to achieve these nanowires, however, the milling time had to be extremely accurate. Over-milling the substrate such that the PMMA wires were completely removed resulted in thinning the previously protected granular aluminum, which compromised the electric viability of the samples. We discovered that the voltage between the sputter anode and cathode (see Chapter 2) would increase when the sheet aluminum layer that was not covered by PMMA was completely milled through to compensate for the lack of conductive material on the copper sputter target. We were therefore able to use this rough metric to consistently and reliably stop the milling process at the correct time to produce clean nanowires in granular aluminum.

6.2.3 Creating Four-Probe Nanowires

Superconducting nanowires in a four-probe geometry were fabricated using both wet- and dry-etching techniques. These four-probe nanowire samples were exposed in either a monolayer of 495K or 950K PMMA using the previously discussed EBL processes and recipes on a silicon substrate with de Bruijn mapping that is coated with a layer of granular aluminum. The four-probe nanowire pattern required two separate exposures; one exposure patterned the fine nanowire features with a dose of 60 000 $\mu C\,cm^{-2}$ and a lower-resolution exposure patterned the four measurement contacts with a lower exposure dose of 30 000 $\mu C\,cm^{-2}$.† The nanowire patterns were exposed using the previously discussed EBL parameters for fine features and the larger contact features were exposed using the previously discussed EBL parameters for larger features. The large-feature process parameters were necessary to obtain a large beam current in order to reduce the low-resolution contact feature exposure time from several hours to only a

*As was described in Chapter 3, the success of the milling step with the sputter system required that the samples were properly grounded.

†In general, larger features required a smaller exposure dose to properly cross-link the PMMA.

few minutes. Since the beam parameters were changed between exposing the nanowire and contacts, the electron beam was realigned with the large-feature parameters and the beam current was remeasured after exposing the fine-feature nanowires. Additionally, each of these exposures required an alignment step in NPGS to either align the nanowire pattern to the de Bruijn mapping or to align the contacts to the nanowire. After both sets of exposures were completed, the sample was developed in acetone to dissolve the unexposed resist and leave behind a PMMA nanowire with four-probe contacts. At this stage, the PMMA nanowire mask may be used to transfer the four-probe nanowire geometry into the granular aluminum layer via a wet- or dry-etch as was previously discussed.

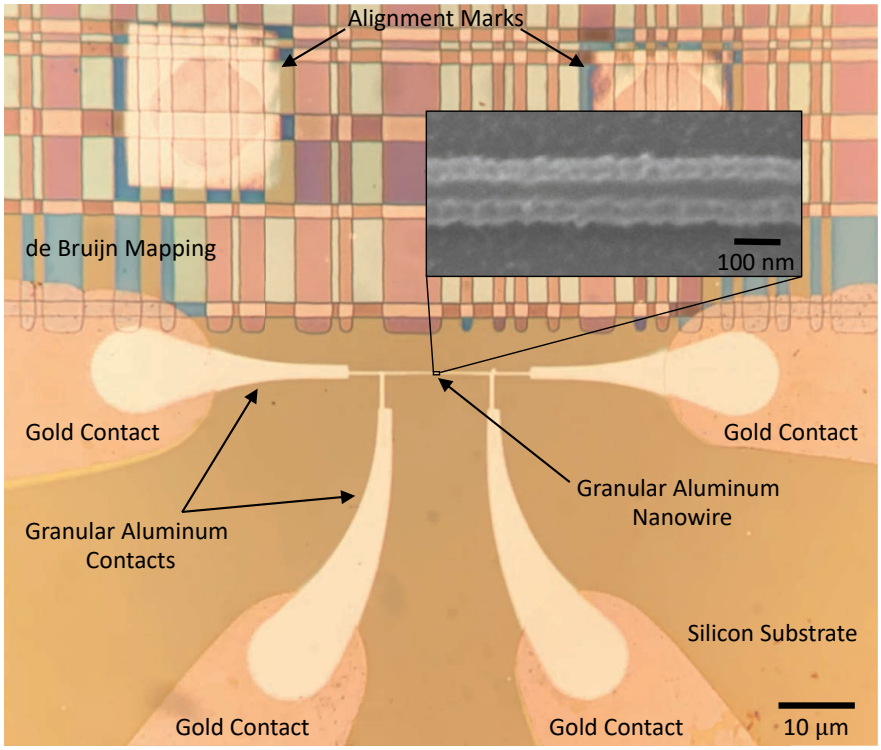

Figure 6.9: An optical image of a granular aluminum nanowire (NAl062619e) that was fabricated on top of pre-patterned gold contacts on a substrate with two orthogonal, one-dimensional de Bruijn maps (see Chapter 5). This nanowire was created using 950K PMMA as a wet-etch mask with Transene moly etchant and was grown to a thickness of 70 nm, written to be 150 nm wide, and is trapezoidal in cross-section (shown with the inset SEM image of a similar nanowire) as a result of the wet-etch. The alignment marks that were used to align the nanowire and granular aluminum contact patterns at the SEM are noted within the de Bruijn mapping.

Figure 6.9 depicts one of the four-probe granular aluminum nanowires that was fabricated using PMMA as a wet-etch mask. This particular nanowire (called NAl062619e) was formed from a 70 nm thick granular aluminum layer that was sputtered on top of pre-patterned gold contacts, which were 60 nm thick. This gold contact thickness was chosen so that the gold pads were thinner than the granular aluminum to ensure that the nanowire sample made reliable electrical connections to the gold while also ensuring that the gold is thick enough to have robust electrical connections to the cryogenic measurement equipment. Once the nanowire was wet-etched, the gold contacts become bridged by the four-probe granular aluminum contacts and nanowire sample. Wet-etching granular aluminum nanowires in this way produced some viable nanowires; however, the adhesion between the granular aluminum layer and the cross-linked PMMA during the wet-etch step was unreliable in general. Additionally, successful four-probe nanowires exhibited large two-probe contact resistances between the gold and aluminum layers which introduced excess noise in the resistance measurements of the sample. This two-probe noise is detrimental to the cryogenic scanning experiment that we seek to perform as the small changes in the wire resistance that are caused by phase slip events may be obscured.

Granular aluminum nanowires with continuous granular aluminum contacts were fabricated with a dry-etching technique in order to avoid the previously discussed downsides to using pre-patterned gold contacts. This sample geometry requires granular aluminum contacts that are much thicker than the final nanowire sample so that robust electrical connections may be made to the measurement equipment in the cryostat. One way to accomplish this would be to grow multiple layers of the sample material such that the contact area is thicker than the sample area. However, this cannot be accomplished since granular aluminum forms an insulating oxide layer when the material is exposed to air, which is necessary in forming a sample with this multiple layering method. Therefore, a process that begins with a bi-thickness layer of granular aluminum, which is depicted in Figure 6.10, is required to realize a granular aluminum nanowire sample with continuous granular aluminum contacts. First, silicon substrates with de

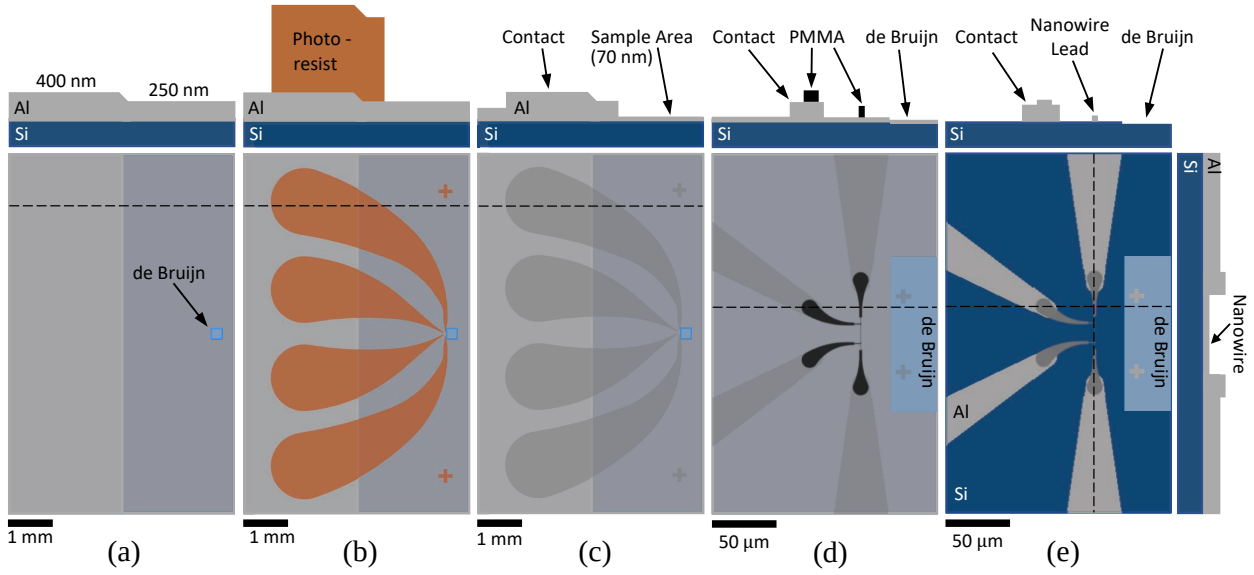

Figure 6.10: A schematic of the process used to fabricate granular aluminum nanowires via ion milling with sputter system. For clarity, the upper figures show the height profiles taken along the dashed lines. **(a)** A bi-thickness layer of granular aluminum (gray) is deposited on a silicon substrate (blue). **(b)** Optical lithography is performed to expose the four-probe contact pattern in a layer of S1813 resist (orange) to protect the underlying granular aluminum. **(c)** The sample is partially wet-etched in Transene moly etchant until the granular aluminum on the de Bruijn side is ~ 70 nm thick and then the photoresist is removed. **(d)** 950K PMMA is spun, baked, exposed, and developed as a negative-tone resist to form a cross-linked PMMA nanowire (black). **(e)** The sample is ion milled in the sputter system to transfer the nanowire pattern into the thinned granular aluminum layer. The side profile shows the granular aluminum height along the vertical dashed line. This process results in a ~ 70 nm thick granular aluminum nanowire that is continuous with granular aluminum contacts, which are as thick as ~ 400 nm to ensure that robust electrical connections are achieved.

Bruijn mapping were grown with a continuous and uniform layer of granular aluminum with two different thickness on each end of the substrate. This was accomplished by blocking half of the substrate that contains the de Bruijn pattern (where the nanowire sample will be formed) with a shutter for a portion of the deposition. After the other half of the substrate is coated with ~ 150 nm of granular aluminum, the shutter is moved (without stopping the sputter growth) and an additional ~ 250 nm of granular aluminum is deposited. This growth results in a silicon substrate with granular aluminum that is 150 nm + 250 nm = 400 nm thick on one side and is only 250 nm thick on the sample side with the de Bruijn mapping as shown in Figure 6.10a. This bi-thickness growth is performed to ensure that the granular aluminum measurement contacts are thick enough on the ~ 400 nm side to be used with spring pin contacts while also ensuring

that the 250 nm granular aluminum layer covering the sample site is thin enough to eventually form a nanowire sample with a desired nanowire thickness while preserving the continuity of the granular aluminum across the substrate surface.

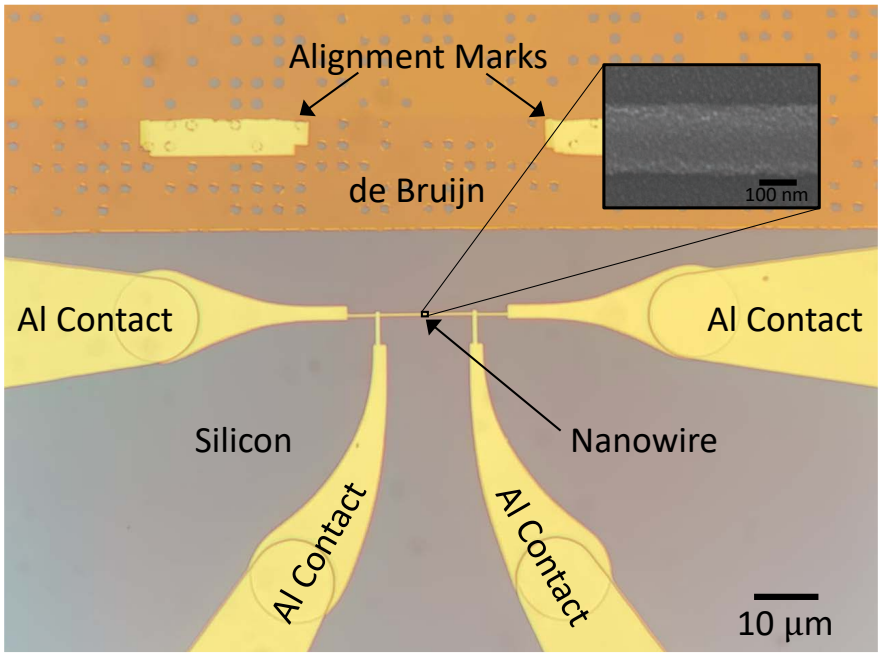

Figure 6.11: An optical image of a granular aluminum nanowire (NAl010220b) with continuous granular aluminum contacts that was fabricated using the process depicted in Figure 6.10. This particular wire is 40 nm thick and was written to be 150 nm wide (shown with the inset SEM image of a similar nanowire). The remnants of the alignment marks that were used to align the various optical and SEM lithographic patterns are noted within the de Bruijn mapping, but were nearly etched away as they were formed in the granular aluminum layer.

The optical and SEM lithographic steps are performed to define the contacts and nanowire once the silicon substrate is coated with a bi-thickness layer of granular aluminum. First, a four-probe lead geometry is exposed in S1813 photoresist such that unexposed photoresist protects the large-feature four-probe leads as shown in Figure 6.10b. Note that the nanowire area between the four contacts and near the de Bruijn pattern is unprotected at this stage. Next, the sample is partially wet-etched in Transene moly etchant until the aluminum at the nanowire site is close to 70 nm thick and the resist is removed resulting in the substrate shown in Figure 6.10c with multiple thicknesses of granular aluminum. Then, a four-probe nanowire pat-

tern is exposed and developed in a layer of 950K PMMA to cross-link the exposed area as shown in Figure 6.10d. The sample is then milled in the sputter system to transfer the nanowire pattern into the granular aluminum, which is then followed by another wet-etch to finish defining the sample. This process results in a four-probe granular aluminum nanowire with continuous granular aluminum contacts that is schematically shown in Figure 6.10e and resulted in the four-probe sample (called NAl010220b) that is shown with an optical image in Figure 6.11.

The nanowire depicted in Figure 6.11 (NAl010220b) is ideal for a scanning experiment with a cryogenic atomic force microscope (cryo-AFM). This four-probe granular aluminum nanowire was fabricated from the same granular aluminum layer as the granular aluminum contacts, which eliminates the 2-probe contact resistances and therefore reduces the resulting measurement noise (as we noted earlier). Additionally, this nanowire can be found with a cryo-AFM at cryogenic temperatures since the nanowire is positioned near a two-dimensional de Bruijn pattern (see Chapter 5). Ultimately, there are numerous combinations of lithographic and etching techniques that will reliably produce nanowire samples. While lift-off processes have produced nanowires, the wet- and dry-etching techniques proved to be more reliable methods to create granular aluminum nanowires in a four-probe geometry, which were eventually scanned at cryogenic temperatures.

6.3 Cryogenically Scanning Superconducting Nanowires

An experiment to map phase slips requires both a cryo-AFM and a superconducting nanowire sample, which have been realized in this work. In Chapter 5, we discussed the home-built cryo-AFM that was constructed to scan either a dielectric or magnetic AFM tip near a superconducting nanowire in order to locally influence superconductivity and therefore the phase slip rate. Then, previous portions of this Chapter presented robust electron beam lithographic techniques and recipes that produced granular aluminum nanowires. Now, we will discuss the scanning experiments of these granular aluminum nanowires using the cryo-AFM with both a dielectric and a magnetic tip.

6.3.1 Sample details

The relationship between the phase slip rate and possible inhomogeneities in superconducting nanowires were explored with two granular aluminum nanowire samples that were created in a four-probe geometry. Both of these nanowires were fabricated using the previously described SEM lithographic technique that employs PMMA as a negative-tone resist for use as an etch mask. The first nanowire (NAl062619e previously depicted in Figure 6.9) was fabricated with a wet-etch on top of gold measurement contacts while the second nanowire (NAl010220b previously depicted in Figure 6.11) was fabricated with ion milling in the sputter system and has continuous contacts made of granular aluminum (see Figure 6.10). The granular aluminum films that were etched to ultimately become nanowires were deposited via Magnetron sputtering aluminum at a rate of ~ 10 Å/s in an argon pressure of 6500 µTorr and with a partial oxygen pressure of ~ 50 µTorr, which were both controlled by Alicat mass flow controllers. These sample layers were either grown to a thickness of ~ 70 nm in the case of the wet-etched nanowire or to a bi-level thickness of 400 nm/250 nm (see Figure 6.10) in the case of the milled nanowire resulting in a final sample thickness of 40 nm after the entire milling process was completed. The PMMA nanowires on both samples were exposed to be 150 nm wide and 15 µm long between the two voltage leads. This PMMA geometry resulted in a nanowire with a trapezoidal cross-section that is 150 nm wide in the case of the wet-etched nanowire (NAl062619e) or resulted in a nanowire with a rectangular cross-section that is also 150 nm wide in the case of the milled nanowire (NAl010220b).

Table 6.1: Properties of Granular Aluminum Nanowires (NAl062619e & NAl010220b)

Nanowire	Cross-Section	T_c	R_{RT}	R_{4K}	ρ_{RT}	ρ_{4K}	RRR
		K	(Ω)		($\mu\Omega\cdot$cm)		ρ_{RT}/ρ_{4K}
NAl062619e	Trapezoidal	1.972	380	339	17.73	15.82	1.12
NAl010220b	Rectangular	1.831	133	112	5.32	4.48	1.19

The superconducting properties of each nanowire were characterized with room temperature and cryogenic resistive measurements, which are shown in Table 6.1, before scanning either granular aluminum nanowire sample. Special considerations are required when performing measurements of nanowires as these delicate samples are easily destroyed by static discharges. So, great care was taken to ground all electrical connections, work areas, and even the scientist when mounting these nanowire samples in the cryostat. The nanowire samples were mounted onto a grounded copper sample stage with Apiezon N thermal grease to thermally anchor the samples to the scanner, which is anchored to a liquid helium pot. Electrical connections were made to the nanowire via gold contact fingers that were harvested from a micro-USB connector as was described in Chapter 5. Once the samples were safely mounted, the cryo-AFM tip was positioned above the de Bruijn pattern where room temperature profilometry of the de Bruijn mapping was performed to determine the room temperature location of the AFM tip. Then, each nanowire was characterized by performing normal state resistance

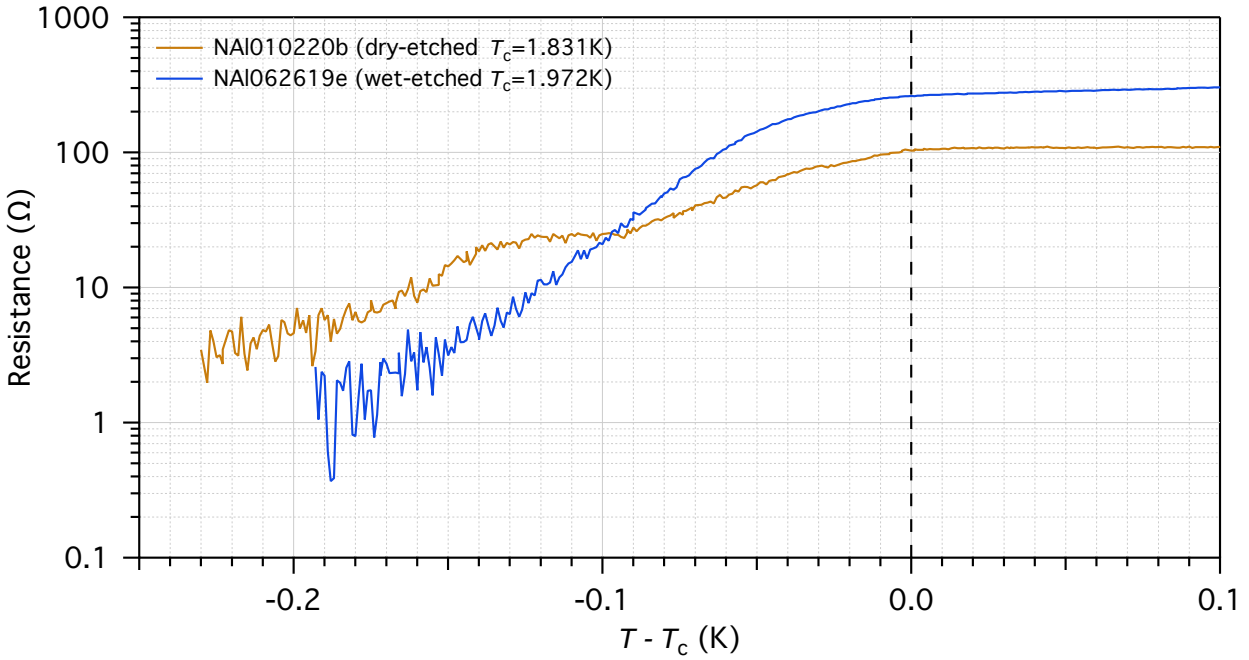

Figure 6.12: Critical transitions of the two granular aluminum nanowires that were fabricated using PMMA as either a dry- (orange) or as a wet- (blue) etch mask. The critical transitions are plotted on a resistance log scale against $\Delta T = T - T_c$ and the critical temperatures of each nanowire were determined to be $T_c = 1.831\,\mathrm{K}$ and $T_c = 1.972\,\mathrm{K}$ for the dry- and wet-etched nanowires respectively.

measurements at room and cryogenic temperatures, which were used along with either the trapezoidal or rectangular nanowire cross-section to infer the resistivity of each sample. Next, critical transition measurements of both nanowires, shown in Figure 6.12, were performed by applying a 10 nA current that was modulated by an SR830 lock-in amplifier and then measuring the resulting voltage with the same lock-in and a $\times 10$ FET preamplifier. The temperature of the samples was monitored with a Cernox thermometer and controlled with a manganin wire resistive heater during these measurements. Note that these samples each exhibit broad transition widths, indicating that phase slip events are likely occurring within these nanowires.

6.3.2 Scanning a Nanowire with a Dielectric Tip

In the first scanning experiment, the wet-etched nanowire (NAl062619e) was scanned with the cryo-AFM using a dielectric tip in an attempt to locally perturb the superconductivity along the nanowire. Recall that scanning a superconducting nanowire with a dielectric tip alters the capacitance per unit length of the nanowire and therefore alters the local electrostatic energy density outside the nanowire[177, 181, 183–185] which may either suppress or enhance the local superconductivity of the nanowire. So, the wet-etched nanowire (NAl062619e) was scanned with an unaltered self-sensing silicon AFM tip to obtain both cryogenic profilometry and simultaneous resistance measurements of the nanowire. These measurements could then be used to determine the phase slip rate as the tip is scanned along the nanowire.

The wet-etched nanowire sample was first characterized and located with the cryo-AFM in order to prepare for an experiment to map the phase slip rate along the nanowire. After characterizing the superconducting properties of the nanowire (see Table 6.1), the sample stage was approached towards the cryo-AFM scan head. This was followed by engaging the AFM tip on the substrate surface and then electronically leveling the scan plan of the cryo-AFM as was described in Chapter 5. Then, several contact-mode profilometry scans with proportional-integral-differential (PID) control were performed on the unique de Bruijn mapping of the nanowire substrate in order to find the nanowire with the cryo-AFM (see Chapter 5). Once

the nanowire was located, cryogenic profilometry of the nanowire using the full x–y scan range of ~ 16 µm of the cold cryo-AFM was obtained to center the AFM tip above the nanowire. Since a scan range of 16 µm is too large to properly image a ~ 150 nm nanowire, the y-piezo scanning voltage was limited to enhance the y spatial resolution, resulting in the cryogenic profilometry of the nanowire that is shown in Figure 6.13a.

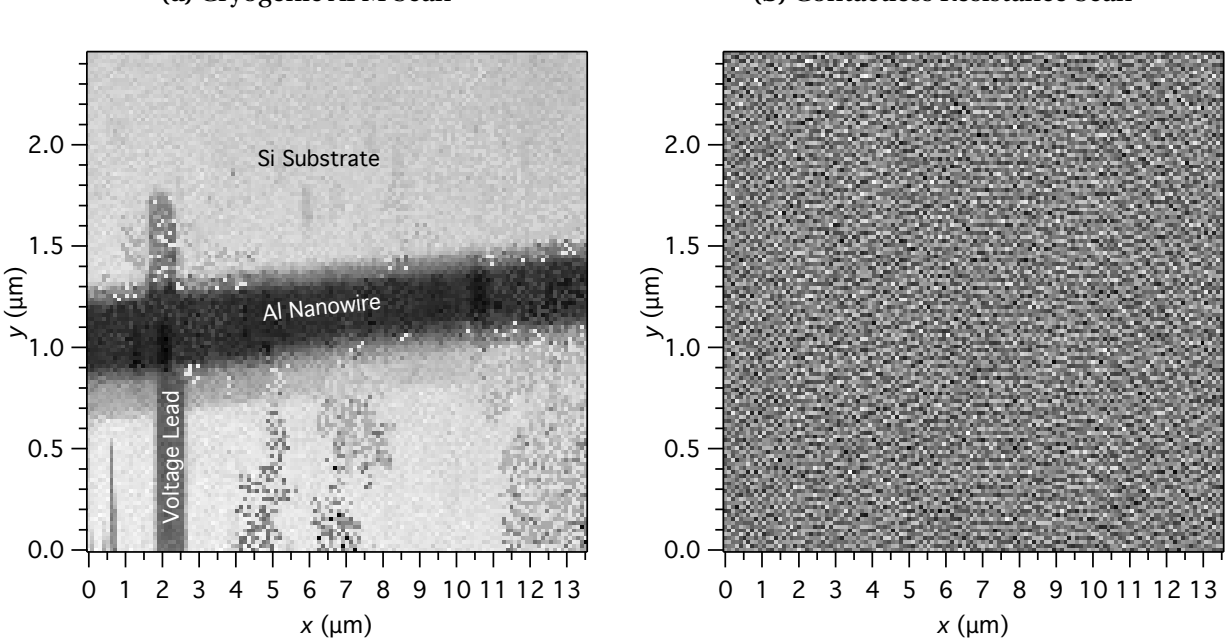

Figure 6.13: **(a)** Cryogenic AFM profilometry and **(b)** the resistance recorded at each location of the cryo-AFM tip during a contactless scan of the wet-etched granular aluminum nanowire (NAl062619e) at $T = 0.95T_c = 1.87\,\mathrm{K}$.

After locating the nanowire with the self-sensing AFM probe and optimizing the scan range, the contactless cryogenic scanning experiment to perturb superconductivity and map phase slips may be performed. The z piezo on the cryo-AFM is retracted until the dielectric silicon AFM tip is just barely above the sample surface. Then, the nominal nanowire resistance was recorded to be ~ 21.4 Ω at a temperature of $T = 0.95T_c = 1.87\,\mathrm{K}$ by applying an AC current of 10 nA to the nanowire and then measuring the voltage response with an SR830 lock-in amplifier as was previously described. While maintaining this constant temperature, the cryo-AFM

scanned the tip above the nanowire with the limited y scan range and with the full x scan range while recording the nanowire resistance at each tip position, shown in Figure 6.13b.

The resistance measurements of the nanowire when scanned with a dielectric tip in Figure 6.13b indicates that the presence of the dielectric tip did not influence the nanowire resistance, which was repeatedly observed with additional scans that were performed at various temperatures up to $T = 0.99T_c$. One explanation is that this 150 nm wide granular aluminum nanowire has cross-sectional dimensions that are too large to cause one-dimensional superconductivity to manifest. Another possible explanation is that the AFM tip, although a dielectric, cannot influence the local energy density on a scale that would cause a measurable change in the resistance. Therefore, we attempted to repeat this experiment with a different nanowire and also with a magnetized tip to more directly influence superconductivity.

6.3.3 Scanning a Nanowire with a Magnetic Tip

In the next scanning experiment that we attempted to perform, the dry-etched nanowire (NAl010220b) was intended to be scanned with a magnetically coated AFM tip. While no formal theory exists for the effects of a locally applied magnetic field on the superconductivity of a nanowire, it is reasonable to assume that a magnetic field will suppress superconductivity. Therefore, an AFM tip on a self-sensing probe was coated with a 40 nm layer of $Co_{25}Fe_{75}$ which was then magnetized with a small D44-N52 Ni magnet (see Chapter 5). Then, this magnetized AFM tip was mounted into the cryo-AFM in the cryostat along with the dry-etched granular aluminum nanowire sample by taking the previously discussed grounding precautions. Additional precautions were required for this experiment, however, since we found that the x attocube positioner (see Chapter 5) became unreliable after a cool down but still functioned properly at room temperatures. So, the tip was positioned at room temperature with Scans $01-03$ of the two-dimensional de Bruijn torus, shown in Figure 6.14, to position the tip such that only y attocube movements would be required after cooling the sample to cryogenic temperatures to avoid using the x attocube.

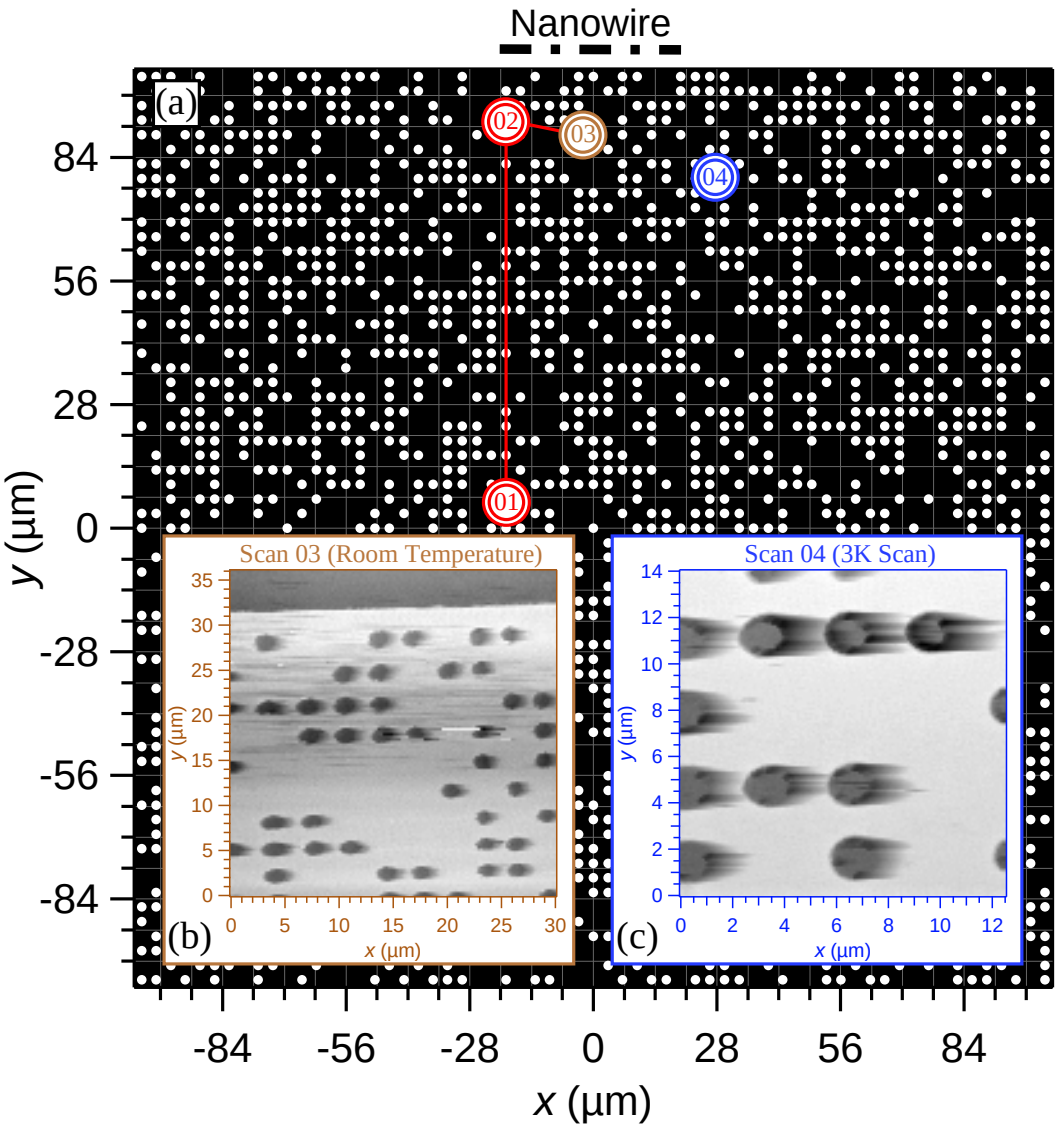

Figure 6.14: (a) A map of the scan locations at room and cryogenic temperatures to locate the superconducting nanowire with a magnetically coated AFM tip. Scans 01 – 03 were performed at room temperature and Scan 04 was performed at 1.6 K. **(b)** The profilometry data obtained (Scan 03) to locate the AFM probe at room temperature before the cool down. **(c)** The profilometry obtained (Scan 04) after cooling down and shows that there was a significant amount of thermal contraction that moved the tip such that the tip was not centered over the nanowire.

After strategically positioning the cryo-AFM at room temperature, the sample was cooled to cryogenic temperatures in order to perform the phase-slip mapping experiment with the magnetized tip. Similar preparations of characterizing the sample (see Table 6.1), approaching the sample towards the cryo-AFM, and then engaging and leveling the tip were performed with milled nanowire. The two-dimensional de Bruijn torus was then scanned to determine the cold

tip location, shown in Figure 6.14b with Scan 04, which indicated that the tip location problematically shifted during the cool down such that an adjustment with the x attocube positioner was required to find the nanowire as the tip was no longer vertically aligned with the sample. At this point, the experiment could not be completed as we discovered that the x-attocube sample stage positioner malfunctioned as we foresaw. Therefore, we warmed the cryostat to room temperature to correct the tip placement, which resulted in destroying the nanowire sample.

These scanning experiments typically resulted in the loss of the nanowire sample since the numerous granular aluminum nanowires that we attempted to test were destroyed when they were subjected to large temperature changes, which made cooling even one down successfully very rare. We believe that either electrostatic discharges during the cool down from the measurement instrumentation or stress and strain differences between the nanowire and the silicon substrate are causing this problematic nanowire destruction. The obstacles of a malfunctioning sample stage positioner at cryogenic temperatures combined with the high likelihood of losing a nanowire sample either when cooling down or warming up the cryostat makes further scanning experiments of nanowires of this kind impractical for the time being.

6.4 Project Outlook

The inconclusive results of these experiments warrants additional scanning experiments of superconducting nanowires. First, the scanning experiment with a magnetic tip can be reattempted with a repaired attocube positioner to determine if a locally applied field suppresses superconductivity enough to cause a measurable change in the wire resistance. Then, the previously discussed nanowire fabrication processes could be improved to create smaller nanowire samples or even to create a nanowire sample with artificial notch constrictions in the wire width where phase slip events are likely to occur.

The experiments that we previously presented were also hindered by the inability to reliably cool down granular aluminum nanowires to cryogenic temperatures without destroying the sample. We found that the nanowire samples were repeatedly destroyed when exposed to

large changes in temperature which may plausibly cause the wires to delaminate from the silicon substrate as a result of stresses and strains that are introduced into the granular aluminum film during the sample sputter deposition. Therefore, additional experiments could be performed (with a repaired cryo-AFM) using other superconducting materials such as indium or tin as these materials have reasonable critical temperatures of $\sim 3.4\,\mathrm{K}$ and $\sim 3.8\,\mathrm{K}$ respectively[115] that are compatible with the cryostat. Another attractive material that was previously unusable with this project is pure aluminum since this material has an atypically long coherence length of 1600 nm.[110] We did not explore nanowires that were fabricated with this material since the critical temperature of pure aluminum of $1.14\,\mathrm{K}$[111] is too low for the cryostat. However, there is a possibility of outfitting the cryostat with a He^3 refrigerator, which will lower the base temperature of the cryostat from $\sim 1.2\,\mathrm{K}$ to $\sim 500\,\mathrm{mK}$ making pure aluminum a viable material.

Closing Remarks

In conclusion, this work studies superconductivity in low-dimensional granular aluminum materials. We first focused on studying vortex dynamics in granular aluminum films with Chapters 2 and 3 to address the way in which these films could be implemented as vortex ratchets since these rectifiers may be used as fluxonic devices. In Chapter 2 we presented a novel method of fabricating both asymmetrically and symmetrically thickness-modulated films of granular aluminum to rectify vortex motion. While this experiment revealed that a sample with a symmetric thickness modulation exhibited reversible critical currents, the asymmetrically modulated sample did indeed rectify vortex motion by at most a factor of ~ 1.1 at an applied field of 4.7 G and at $0.85T_c$. However, this rectification was much less than the factor of ~ 2 that we expected from considering the slopes in each direction in the sawtooth-like thickness modulation. Therefore, we moved to address another related question in the field regarding the influence of the sample edge geometry on vortex nucleation and motion within superconducting films with the experiments that were presented in Chapter 3. Using either a dynamic optical lithographic method or a laser writer instrument, we performed multilevel lithography to fabricate superconducting films each with multiple tapered edges to probe the relationship between the slope of a tapered edge and the suppression of the geometric edge barrier to vortex nucleation. With these experiments, we found that lower critical currents were required to nucleate vortices over shallower tapers while shorter tapers with steeper slopes made it more difficult for vortices to enter, which indicates that shallower tapered edges do in fact result in reduced edge barriers. We observed that the critical currents that are required to nucleate vortices into a superconductor may be reduced by as much as a factor of ~ 2.4 with the longest and shallowest taper ($l = 4.0\,\mu$m) at an applied field of 11.5 G and at a temperature of $0.75T_c$ when compared to the critical currents required to nucleate vortices over a squared edge geometry. These findings showcase the importance of the sample edges on the vortex dynamics within a superconductor. In combination with the surface modulation studies that were presented in Chapter 2, we

propose that vortex motion may be drastically influenced by creating a thickness-modulated sample with tapered edges to realize a high quality ratchet.

In the last two Chapters, we attempted to address a long-outstanding question in the field regarding the nature of superconductivity in one-dimensional superconductors. In particular, there are disagreements regarding the origin of the low-temperature phase slips of the superconducting order parameter that cause an apparent resistance in nanowire samples which cannot be explained with early models that describe thermally activated phase slip (TAPS) events. One explanation posits that the superconductor is experiencing macroscopic quantum tunneling (MQT) events at these low temperatures that result in quantum tunneling phase slip (QTPS) events in order to explain this excess resistance while another theory claims that nanowire defects cause TAPS to occur at a different rate. A rigorous understanding of these processes has been hindered by challenges that are associated with fabricating uniform nanowires that are also sufficiently small enough to exhibit phase slip events. In this work, we proposed a cryogenic scanning experiment that employs a cryogenic atomic force microscope (cryo-AFM) that scans an AFM tip above a nanowire to influence the local superconductivity which will enable us to determine if a correlation exists between the local phase slip rate and nanowire inhomogeneities. In order to perform this experiment, the construction of a cryo-AFM along with methods of locating the nanowire at cryogenic temperatures were presented in Chapter 5. Chapter 6 then outlined a robust electron beam lithographic (EBL) method that employs poly(methyl methacrylate) (PMMA) as a negative-tone resist to produce superconducting granular aluminum nanowires. The scanning experiments that were performed on these nanowires were inconclusive as several unfortunate obstacles made further experiments impractical. However, these inconclusive results warrant additional scanning experiments that address these obstacles by repairing the scanning equipment and by fabricating nanowires with a different material.

Bibliography

[1] H. K. Onnes, *Commun. Phys. Lab.* **12**, 120 (1911).

[2] J. London, *Superfluids Vol. 1* (New York, 1950).

[3] W. Meissner, R. Ochsenfeld, Ein neuer Effekt bei Eintritt der Supraleitfähigkeit, *Naturwissenschaften* **21**, 787 (1933).

[4] M. Tinkham, *Introduction to superconductivity* (Courier Corporation, 2004).

[5] A. A. Abrikosov, Magnetic properties of superconducting alloy films, *J. Phys. Chem. Solids.* **2**, 199 (1957).

[6] J. R. Clem, Simple model for the vortex core in a type II superconductor, *J. Low Temp. Phys.* **18**, 427 (1975).

[7] G. Carneiro, E. Brandt, Vortex lines in films: Fields and interactions, *Phys. Rev. B* **61**, 6370 (2000).

[8] J. Pearl, Current distribution in superconducting films carrying quantized fluxoids, *Appl. Phys. Lett.* **5**, 65 (1964).

[9] A. Bezryadin, B. Pannetier, Role of edge superconducting states in trapping of multiquanta vortices by microholes. Application of the bitter decoration technique, *J. Low Temp. Phys.* **102**, 73 (1996).

[10] R. Cao, L. Horng, J. C. Wu, T. J. Yang, T. C. Wu, Pinning effects in Nb thin films with artificial pinning arrays, *J. Supercond. Nov. Magn.* **23**, 1051 (2010).

[11] J. Cuppens, G. W. Ataklti, W. Gillijns, J. Van De Vondel, V. V. Moshchalkov, A. V. Silhanek, Vortex dynamics in a superconducting film with a Kagome and a Honeycomb pinning landscape, *J. Supercond. Nov. Magn.* **24**, 7 (2011).

[12] J. C. Keay, P. R. Larson, K. L. Hobbs, M. B. Johnson, J. R. Kirtley, O. M. Auslaender, K. A. Moler, Sequential vortex hopping in an array of artificial pinning centers, *Phys. Rev. B* **80**, (2009).

[13] V. Metlushko, U. Welp, G. W. Crabtree, R. Osgood, S. D. Bader, L. E. DeLong, Z. Zhang, S. R. J. Brueck, B. Ilic, K. Chung, Interstitial flux phases in a superconducting niobium film with a square lattice of artificial pinning centers, *Phys. Rev. B* **60**, 12585 (1999).

[14] J. Van De Vondel, C. C. De Souza Silva, B. Y. Zhu, M. Morelle, V. V. Moshchalkov, Vortex-rectification effects in films with periodic asymmetric pinning, *Phys. Rev. Lett.* **94**, 2 (2005).

[15] Q. H. Chen, G. Teniers, B. B. Jin, V. V. Moshchalkov, Pinning properties and vortex dynamics in thin superconducting films with ferromagnetic and antiferromagnetic arrays of magnetic dots, *Phys. Rev. B* **73**, 14506 (2006).

[16] L. Dinis, E. M. González, J. V. Anguita, J. M. R. Parrondo, J. L. Vicent, Current reversal in collective ratchets induced by lattice instability, *Phys. Rev. B* **76**, 212507 (2007).

[17] W. Gillijns, A. V. Silhanek, V. V. Moshchalkov, C. J. Reichhardt, C. Reichhardt, Origin of reversed vortex ratchet motion, *Phys. Rev. Lett.* **99**, 247002 (2007).

[18] D. Perez De Lara, A. A. Alija, E. M. Gonzalez, J. I. Martin, M. Velez, J. M. Colino, J. V. Anguita, J. L. Vicent, Enhancement of synchronized vortex lattice motion in hybrid magnetic/amorphous superconducting nanostructures, *Appl. Phys. Lett.* **94**, 1 (2009).

[19] D. Perez De Lara, A. Alija, E. M. Gonzalez, M. Velez, J. I. Martin, J. L. Vicent, Vortex ratchet reversal at fractional matching fields in kagomélike array with symmetric pinning centers, *Phys. Rev. B* **82**, 1 (2010).

[20] T. Dröse, R. Besseling, P. H. Kes, C. M. Smith, T. Dröse, R. Besseling, C. M. Smith, P. H. Kes, C. M. Smith, T. Dröse, R. Besseling, C. M. Smith, Plastic depinning in artificial vortex channels: Competition between bulk and boundary nucleation, *Phys. Rev. B* **67**, 1 (2003).

[21] D. D. Morrison, R. M. Rose, Controlled pinning in superconducting foils by surface microgrooves, *Phys. Rev. Lett.* **25**, 356 (1970).

[22] K. Yu, T. W. Heitmann, C. Song, M. P. DeFeo, B. L. T. Plourde, M. B. S. Hesselberth, P. H. Kes, Asymmetric weak-pinning superconducting channels: Vortex ratchets, *Phys. Rev. B* **76** (2007).

[23] G. Carapella, G. Costabile, N. Martucciello, M. Cirillo, R. Latempa, A. Polcari, G. Filatrella, Experimental realization of a relativistic fluxon ratchet, *Phys. C Supercond.* **382**, 337 (2002).

[24] O. V. Dobrovolskiy, Abrikosov fluxonics in washboard nanolandscapes, *Phys. C Supercond.* **533**, 80 (2017).

[25] O. V. Dobrovolskiy, M. Huth, V. A. Shklovskij, Alternating current-driven microwave loss modulation in a fluxonic metamaterial, *Appl. Phys. Lett.* **107** (2015).

[26] M. B. Hastings, C. J. Reichhardt, C. Reichhardt, Ratchet Cellular Automata, *Phys. Rev. Lett.* **90**, 4 (2003).

[27] C. S. Lee, B. Jankó, I. Derényl, A. L. Barabási, Reducing vortex density in superconductors using the 'ratchet effect', *Nature* **400**, 337 (1999).

[28] M. V. Milošević, G. R. Berdiyorov, F. M. Peeters, Fluxonic cellular automata, *Appl. Phys. Lett.* **91**, 1 (2007).

[29] K. Miyahara, M. Mukaida, K. Hohkawa, Abrikosov vortex memory, *Appl. Phys. Lett.* **47**, 754 (1985).

[30] J. F. Wambaugh, C. Reichhardt, C. J. Olson, F. Marchesoni, F. Nori, Superconducting fluxon pumps and lenses, *Phys. Rev. Lett.* **83**, 5106 (1999).

[31] C. C. De Souza Silva, A. V. Silhanek, J. Van De Vondel, W. Gillijns, V. Metlushko, B. Ilic, V. V. Moshchalkov, Dipole-induced vortex ratchets in superconducting films with arrays of micromagnets, *Phys. Rev. Lett.* **98**, 1 (2007).

[32] B. L. Plourde, D. J. Van Harlingen, N. Saha, R. Besseling, M. B. Hesselberth, P. H. Kes, Vortex distributions near surface steps observed by scanning SQUID microscopy, *Phys. Rev. B* **66**, 545291 (2002).

[33] B. L. T. Plourde, Nanostructured Superconductors With Asymmetric Pinning Potentials: Vortex Ratchets, *IEEE Trans. Appl. Supercond.* **19**, 3698 (2009).

[34] Y. Togawa, K. Harada, T. Akashi, H. Kasai, T. Matsuda, A. Maeda, A. Tonomura, Rectified motion of vortices in a niobium superconductor observed by Lorentz microscopy, *Phys. C Supercond.* **426-431**, 141 (2005).

[35] Y. Togawa, K. Harada, T. Akashi, H. Kasai, T. Matsuda, F. Nori, A. Maeda, A. Tonomura, Direct observation of rectified motion of vortices in a niobium superconductor, *Phys. Rev. Lett.* **95**, 1 (2005).

[36] C. Reichhardt, C. J. Olson Reichhardt, Transport anisotropy as a probe of the interstitial vortex state in superconductors with artificial pinning arrays, *Phys. Rev. B* **79** (2009).

[37] R. Cao, T. C. Wu, P. C. Kang, J. C. Wu, T. J. Yang, L. Horng, Anisotropic pinning in Nb thin films with triangular pinning arrays, *Solid State Commun.* **143**, 171 (2007).

[38] G. Carneiro, Dynamical phase diagrams for moving vortices interacting with periodic pinning, *Phys. Rev. B* **66**, 54523 (2002).

[39] H. T. Lin, C. Ke, C. H. Cheng, Temporal chaotic behaviour of vortex motion in a type-II superconductors with periodically-distributed pinning centres, *Phys. C Supercond.* **470**, 1118 (2010).

[40] Q. Lu, C. J. Reichhardt, C. Reichhardt, Reversible vortex ratchet effects and ordering in superconductors with simple asymmetric potential arrays, *Phys. Rev. B* **75**, 54502 (2007).

[41] N. Mangan, C. Reichhardt, C. J. Reichhardt, Reversible to irreversible flow transition in periodically driven vortices, *Phys. Rev. Lett.* **100**, 1 (2008).

[42] F. Nori, C. Reichhardt, Dynamic phase diagram and orientational dependence for vortices in superconductors with periodic arrays of pinning sites, *Phys. C Supercond.* **332**, 40 (2000).

[43] C. J. Olson, C. Reichhardt, B. Jankó, F. Nori, Collective interaction-driven ratchet for transporting flux quanta, *Phys. Rev. Lett.* **87**, 177002 (2001).

[44] C. J. Reichhardt, C. Reichhardt, Commensurability, jamming, and dynamics for vortices in funnel geometries, *Phys. Rev. B* **81**, 224516 (2010).

[45] C. J. Reichhardt, C. Reichhardt, Rectification and flux reversals for vortices interacting with triangular traps, *Phys. C Supercond.* **432**, 125 (2005).

[46] C. J. Reichhardt, C. Reichhardt, Coherent and incoherent vortex flow states in crossed channels, *Europhys. Lett.* **88**, 47004 (2009).

[47] C. Reichhardt, C. J. Olson Reichhardt, Switching and jamming transistor effect for vortex matter in honeycomb pinning arrays with ac drives, *Phys. Rev. B* **81**, 24510 (2010).

[48] C. Reichhardt, C. J. Reichhardt, Spontaneous transverse response and amplified switching in superconductors with honeycomb pinning arrays, *Phys. Rev. Lett.* **100**, 1 (2008).

[49] C. Reichhardt, C. J. Reichhardt, Commensurability effects at nonmatching fields for vortices in diluted periodic pinning arrays, *Phys. Rev. B* **76**, 1 (2007).

[50] C. Reichhardt, C. J. Reichhardt, Moving vortex phases, dynamical symmetry breaking, and jamming for vortices in honeycomb pinning arrays, *Phys. Rev. B* **78**, 1 (2008).

[51] C. Reichhardt, N. Grønbech-Jensen, Critical currents and vortex states at fractional matching fields in superconductors with periodic pinning, *Phys. Rev. B* **63**, 54510 (2001).

[52] B. Y. Zhu, F. Marchesoni, F. Nori, Controlling the motion of magnetic flux quanta, *Phys. Rev. Lett.* **92**, 18 (2004).

[53] P. H. Kes, C. C. Tsuei, Two-dimensional collective flux pinning, defects, and structural relaxation in amorphous superconducting films, *Phys. Rev. B* **28**, 5126 (1983).

[54] M. Borromeo, F. Marchesoni, Noise-assisted transport on symmetric periodic substrates, *Chaos* **15**, 26110 (2005).

[55] P. Martinoli, J. L. Olsen, J. R. Clem, Superconducting vortices in periodic pinning structures, *J. Less-Common Met.* **62**, 315 (1978).

[56] V. A. Shklovskij, V. V. Sosedkin, O. V. Dobrovolskiy, Vortex ratchet reversal in an asymmetric washboard pinning potential subject to combined dc and ac stimuli, *J. Phys. Condens. Matter* **26** (2014).

[57] V. A. Shklovskij, V. V. Sosedkin, Guiding of vortices and ratchet effect in superconducting films with asymmetric pinning potential, *Phys. Rev. B* **80**, 1 (2009).

[58] V. A. Shklovskij, O. V. Dobrovolskiy, Frequency-dependent ratchet effect in superconducting films with a tilted washboard pinning potential, *Phys. Rev. B* **84**, 1 (2011).

[59] H. Castro, B. Dutoit, A. Jacquier, M. Baharami, L. Rinderer, Experimental study of the geometrical barrier in type-i superconducting strips, *Phys. Rev. B* **59**, 596 (1999).

[60] D. Cerbu, V. N. Gladilin, J. Cuppens, J. Fritzsche, J. Tempere, J. T. Devreese, V. V. Moshchalkov, A. V. Silhanek, J. Van De Vondel, Vortex ratchet induced by controlled edge roughness, *New J. Phys.* **15**, 63022 (2013).

[61] D. Majer, E. Zeldov, M. Konczykowski, Separation of the irreversibility and melting lines in Bi2Sr2CaCu2O8 crystals, *Phys. Rev. Lett.* **75**, 1166 (1995).

[62] P. Sabatino, G. Carapella, M. Gombos, Preferentially directed flux motion in a very thin superconducting strip with nanostructured profile, *J. Appl. Phys.* **112** (2012).

[63] C. A. Aguirre, Q. D. Martins, A. S. de Arruda, J. Barba-Ortega, Influence of an applied current on the vortex matter in a superconducting sample with structural defects, *Heliyon* **5**, e01570 (2019).

[64] D. Agassi, J. R. Cullen, Superconductor strip geometrical barrier in the presence of a normally incident weak field, *Phys. C Supercond.* **348**, 1257 (2000).

[65] A. Y. Aladyshkin, A. S. Mel'Nikov, I. A. Shereshevsky, I. D. Tokman, What is the best gate for vortex entry into type-II superconductor?, *Phys. C Supercond.* **361**, 67 (2001).

[66] L. V. Belevtsov, Vortex edge barriers and critical current density in granular superconductors, *Phys. Stat. Sol. B* **237**, 523 (2003).

[67] M. Benkraouda, J. R. Clem, Magnetic hysteresis from the geometrical barrier in type-II superconducting strips, *Phys. Rev. B* **53**, 5716 (1996).

[68] M. Benkraouda, J. R. Clem, Critical current from surface barriers in type-II superconducting strips, *Phys. Rev. B* **58**, 103 (1998).

[69] E. H. Brandt, Superconductors in realistic geometries: Geometric edge barrier versus pinning, *Phys. C Supercond.* **332**, 99 (2000).

[70] E. H. Brandt, Geometric edge barrier in the Shubnikov phase of type-II superconductors, *Low Temp. Phys.* **27**, 723 (2001).

[71] E. H. Brandt, G. P. Mikitik, E. Zeldov, Two regimes of vortex penetration into platelet-shaped type-II superconductors, *J. Exp. Theor. Phys.* **117**, 439 (2013).

[72] G. R. Berdiyorov, L. R. E. Cabral, F. M. Peeters, Surface barrier for flux entry and exit in mesoscopic superconducting systems, *J. Math. Phys.* **46**, 95105 (2005).

[73] A. Buzdin, M. Daumens, Electromagnetic pinning of vortices on different types of defects, *Phys. C Supercond.* **294**, 257 (1998).

[74] A. A. Elistratov, D. Y. Vodolazov, I. L. Maksimov, J. R. Clem, Field-dependent critical current in type-II superconducting strips: Combined effect of bulk pinning and geometrical edge barrier, *Phys. C Supercond.* **66**, 1 (2002).

[75] A. L. Fetter, P. C. Hohenberg, Hohenber, The mixed state of thin superconducting films in perpendicular fields, *Phys. Rev.* **159**, 330 (1967).

[76] N. Morozov, E. Zeldov, M. Konczykowski, R. A. Doyle, Geometrical and distributed surface barriers in Bi2Sr2CaCu2O8, *Phys. C Supercond.* **291**, 113 (1997).

[77] B. L. Plourde, D. J. Van Harlingen, D. Y. Vodolazov, R. Besseling, M. B. Hesselberth, P. H. Kes, Influence of edge barriers on vortex dynamics in thin weak-pinning superconducting strips, *Phys. Rev. B* **64**, 14503 (2001).

[78] M. J. Qin, H. K. Liu, S. X. Dou, AC susceptibility of type-II superconductor strips with geometric barrier, *Phys. C Supercond.* **377**, 416 (2002).

[79] D. Y. Vodolazov, Flux-flow instability in a strongly disordered superconducting strip with an edge barrier for vortex entry, *Supercond. Sci. Technol.* **32** (2019).

[80] D. Y. Vodolazov, Effect of surface defects on the first field for vortex entry in type-II superconductors, *Phys. Rev. B* **62**, 8691 (2000).

[81] D. Y. Vodolazov, I. L. Maksimov, E. H. Brandt, Vortex entry conditions in type-II superconductors. Effect of surface defects, *Phys. C Supercond.* **384**, 211 (2003).

[82] R. Willa, V. B. Geshkenbein, G. Blatter, Suppression of geometric barrier in type-II superconducting strips, *Phys. Rev. B* **89**, 1 (2014).

[83] Z. L. Xiao, E. Y. Andrei, Y. Paltiel, E. Zeldov, P. Shuk, M. Greenblatt, Edge and bulk transport in the mixed state of a type-II superconductor, *Phys. Rev. B* **65**, 94511 (2002).

[84] E. Zeldov, J. R. Clem, M. McElfresh, M. Darwin, Magnetization and transport currents in thin superconducting films, *Phys. Rev. B* **49**, 9802 (1994).

[85] E. Zeldov, A. I. Larkin, V. B. Geshkenbein, M. Konczykowski, D. Majer, B. Khaykovich, V. M. Vinokur, H. Shtrikman, Geometrical Barriers in High-Temperature Superconductors, *Phys. Rev. Lett.* **73**, 1428 (1994).

[86] C. P. Bean, J. D. Livingston, Surface barrier in type-II superconductors, *Phys. Rev. Lett.* **12**, 14 (1964).

[87] E. H. Brandt, Irreversible magnetization of pin-free type-II superconductors, *Phys. Rev. B* **60**, 11939 (1999).

[88] E. H. Brandt, Geometric barrier and current string in type-ii superconductors obtained from continuum electrodynamics, *Phys. Rev. B* **59**, 3369 (1999).

[89] A. V. Silhanek, N. Verellen, V. Metlushko, W. Gillijns, F. Gozzini, B. Ilic, V. V. Moshchalkov, Rectification effects in superconductors with magnetic pinning centers, *Phys. C Supercond.* **468**, 563 (2008).

[90] V. Rouco, A. Palau, C. Monton, N. Del-Valle, C. Navau, A. Sanchez, X. Obradors, T. Puig, Geometrically controlled ratchet effect with collective vortex motion, *New J. Phys.* **17** (2015).

[91] C. C. De Souza Silva, J. Van De Vondel, M. Morelle, V. V. Moshchalkov, Controlled multiple reversals of a ratchet effect, *Nature* **440**, 651 (2006).

[92] O. V. Dobrovolskiy, E. Begun, M. Huth, V. A. Shklovskij, Electrical transport and pinning properties of Nb thin films patterned with focused ion beam-milled washboard nanostructures, *New J. Phys.* **14** (2012).

[93] O. V. Dobrovolskiy, M. Huth, V. A. Shklovskij, Fluxonic properties of vortices in a washboard pinning potential fabricated by focused particle beam techniques, *Acta Phys. Pol. A* **121**, 82 (2012).

[94] I. Derényi, Application of the ratchet effect to improve material quality (reducing vortex density in superconductors and smoothing surfaces), *Appl. Phys. A* **75**, 217 (2002).

[95] G. Carneiro, Tunable ratchet effects for vortices pinned by periodic magnetic dipole arrays, *Phys. C Supercond.* **432**, 206 (2005).

[96] J. W. Ekin, Critical currents in granular superconductors, *Phys. Rev. B* **12**, 2676 (1975).

[97] J. D. Musgraves, B. T. Close, D. M. Tanenbaum, A maskless photolithographic prototyping system using a low-cost consumer projector and a microscope, *Am. J. Phys.* **73**, 980 (2005).

[98] J. C. Love, D. B. Wolfe, H. O. Jacobs, G. M. Whitesides, Microscope projection photolithography for rapid prototyping of masters with micron-scale features for use in soft lithography, *Langmuir* **17**, 6005 (2001).

[99] J. P. Spallas, R. D. Boyd, J. A. Britten, A. Fernandez, A. M. Hawryluk, M. D. Perry, D. R. Kania, Fabrication of sub-0.5 μm diameter cobalt dots on silicon substrates and photoresist pedestals on 50 cm×50 cm glass substrates using laser interference lithography, *J. Vac. Sci. Technol. B* **14**, 2005 (1996).

[100] E. S. Park, D. Jang, J. Lee, Y. J. Kim, J. Na, H. Ji, J. W. Choi, G.-T. Kim, Maskless optical microscope lithography system, *Rev. Sci. Instrum.* **80**, 126101 (2009).

[101] R. Gonski, J. Melngailis, Photolithography using an optical microscope, *J. Vac. Sci. Technol. B* **25**, 2451 (2007).

[102] H. Wu, T. W. Odom, G. M. Whitesides, Reduction Photolithography Using Microlens Arrays: Applications in Gray Scale Photolithography, *Anal. Chem.* **74**, 3267 (2002).

[103] N. Xiang, H. Yi, K. Chen, S. Wang, Z. Ni, Investigation of the maskless lithography technique for the rapid and cost-effective prototyping of microfluidic devices in laboratories, *J. Micromech. Microeng.* **23**, 25016 (2013).

[104] T. Naiser, T. Mai, W. Michel, A. Ott, Versatile maskless microscope projection photolithography system and its application in light-directed fabrication of DNA microarrays, *Rev. Sci. Instrum.* **77**, 63711 (2006).

[105] D. Sheet, Microposit S1800 series photoresists, *Shipley Company, Marlborough, MA* (1993).

[106] P. D. Sheet, MicroChem, *Newton, MA, USA* (2001).

[107] L. O. R. MicroChem, Lift-Off Resists, *Datasheet, Available from www. Microchem. com website* (2004).

[108] I. Knittel, M. Gothe, U. Hartmann, Quantitative analysis of sputter processes in a small magnetron system, *J. Vac. Sci. Technol., A* **23**, 1714 (2005).

[109] A. DeMann, S. Mueller, S. B. Field, 1K cryostat with sub-millikelvin stability based on a pulse-tube cryocooler, *Cryogenics.* **73**, 60 (2016).

[110] R. W. Cohen, B. Abeles, Superconductivity in Granular Aluminum Films, *Phys. Rev.* **168**, 444 (1968).

[111] C. Kittel, *Introduction to Solid State Physics* (John Wiley & Sons, 2005), 8th edn.

[112] Ralph B. Delano Jr., Edge Effects in Superconducting Films, *Solid. State. Electron.* **1**, 381 (1960).

[113] P. Chubov, V. Eremenko, Y. Pilipenko, Dependence of the Critical Temperature and Energy Gap on the Thickness of Superconducting Aluminum Films, *Sov. J. Exp. Theor. Phys.* **28**, 389 (1969).

[114] A. Larkin, Y. N. Ovchinnikov, Nonlinear conductivity of superconductors in the mixed state, *Sov. J. Exp. Theor. Phys.* **41**, 960 (1975).

[115] W. Klein, R. P. Huebener, S. Gauss, J. Parisi, Nonlinearity in the flux-flow behavior of thin-film superconductors, *J. Low Temp. Phys.* **61**, 413 (1985).

[116] J. W. Leem, J. S. Yu, Structural, optical, and electrical properties of AZO films by tilted angle sputtering method, *Thin Solid Films* **518**, 6285 (2010).

[117] F. G. Aliev, Generation of DC electric fields due to vortex rectification in superconducting films, *Phys. C Supercond.* **437-438**, 1 (2006).

[118] T. Schuster, M. V. Indenbom, H. Kuhn, E. Brandt, M. Konczykowski, Flux Penetration and Overcritical Currents in Flat Superconductors with Irradiation-Enhanced Edge Pinning: Theory and Experimen, *Phys. Rev. Lett.* **73** (1994).

[119] M. Konczykowski, L. I. Burlachkov, Y. Yeshurun, F. Holtzberg, Evidence for surface barriers and their effect on irreversibility and lower-critical-field measurements in Y-Ba-Cu-0 crystals, *Phys. Rev. B* **43** (1991).

[120] N. Chikumoto, M. Konczykowski, N. Motohira, K. Kishio, K. Kitazawa, The First Magnetic Penetration Field in BSCCO Single Crystals, Temperature Dependance and Electron Irradiation Effect, *Phys. C Supercond.* **189**, 1835 (1991).

[121] K. Christian, T. J. Rinke, *Photolithography: Basics of Microstructuring* (Siegl Druck & Medien GmbH & co. KG, 2017), first edn.

[122] E. J. Walker, Photoresist Standing-Wave Effects, *IEEE Trans. Electron Devices* **22**, 464 (1975).

[123] A. T. Hindmarch, D. E. Parkes, A. W. Rushforth, Fabrication of metallic magnetic nanostructures by argon ion milling using a reversed-polarity planar magnetron ion source, *Vacuum* **86**, 1600 (2012).

[124] A. A. Shanenko, M. D. Croitoru, M. Zgirski, F. M. Peeters, K. Arutyunov, Size-dependent enhancement of superconductivity in Al and Sn nanowires: Shape-resonance effect, *Phys. Rev. B* **74**, 3 (2006).

[125] M. E. Behrndt, R. H. Blumberg, G. R. Giedd, On the Influence of Aggregation on the Magnetic Phase Transition of Evaporated Superconducting Thin Films, *IBM J.* (1960).

[126] M. Park, M. Isaacson, J. Parpia, Resistance anomaly and excess voltage in inhomogeneous superconducting aluminum thin films, *Phys. Rev. B* **55**, 9067 (1997).

[127] C. Strunk, V. Bruyndoncx, C. Van Haesendonck, V. Moshchalkov, Y. Bruynseraede, C. Chien, B. Burk, V. Chandrasekhar, Resistance anomalies in superconducting mesoscopic Al structures, *Phys. Rev. B* **57**, 10854 (1998).

[128] C. Strunk, V. Bruyndoncx, C. Van Haesendonck, V. Moshchalkov, Y. Bruynseraede, B. Burk, C. Chien, V. Chandrasekhar, Nonmonotonic superconducting transitions in mesoscopic Al structures induced by radio-frequency radiation, *Phys. Rev. B* **53**, 11332 (1996).

[129] N. Giordano, Dissipation in a one-dimensional superconductor:\ Evidence for macroscopic quantum tunneling, *Phys. Rev. B* **41**, 6350 (1990).

[130] F. Altomare, A. M. Chang, M. R. Melloch, Y. Hong, C. W. Tu, Evidence for macroscopic quantum tunneling of phase slips in long one-dimensional superconducting Al wires, *Phys. Rev. Lett.* **97**, 5 (2006).

[131] T. Aref, A. Levchenko, V. Vakaryuk, A. Bezryadin, Quantitative analysis of quantum phase slips in superconducting Mo 76Ge 24 nanowires revealed by switching-current statistics, *Phys. Rev. B* **86**, 1 (2012).

[132] K. Y. Arutyunov, D. A. Presnov, S. V. Lotkhov, A. B. Pavolotski, L. Rinderer, Resistive-state anomaly in superconducting nanostructures, *Phys. Rev. B* **59**, 6487 (1999).

[133] H. Bartolf, A. Engel, A. Schilling, K. Il'In, M. Siegel, H. W. Hübers, A. Semenov, Current-assisted thermally activated flux liberation in ultrathin nanopatterned NbN superconducting meander structures, *Phys. Rev. B* **81**, 24502 (2010).

[134] M. Bell, N. Kaurova, A. Divochiy, G. Gol'tsman, J. Bird, A. Sergeev, A. Verevkin, On the nature of resistive transition in disordered superconducting nanowires, *IEEE Trans. Appl. Supercond.* **17**, 267 (2007).

[135] A. Bezryadin, Quantum suppression of superconductivity in nanowires, *J. Phys. Condens. Matter* **20** (2008).

[136] A. Bezryadin, Quantum suppression of superconductivity in nanowires, *J. Phys. Condens. Matter* **20**, 971 (2000).

[137] A. T. Bollinger, A. Rogachev, A. Bezryadin, Dichotomy in short superconducting nanowires: Thermal phase slippage vs. Coulomb blockade, *Europhys. Lett.* **76**, 505 (2006).

[138] A. T. Bollinger, A. Rogachev, M. Remeika, A. Bezryadin, Effect of morphology on the superconductor-insulator transition in one-dimensional nanowires, *Phys. Rev. B* **69** (2004).

[139] S. L. Chu, A. T. Bollinger, A. Bezryadin, Phase slips in superconducting films with constrictions, *Phys. Rev. B* **70**, 1 (2004).

[140] N. Giordano, Superconductivity and dissipation in small-diameter Pb-In wires, *Phys. Rev. B* **43**, 160 (1991).

[141] N. Giordano, Evidence for Macroscopic Quantum Tunneling in One-Dimensional Superconductors, *Phys. Rev. Lett.* **61**, 2137 (1988).

[142] N. Giordano, Superconducting fluctuations in one dimension, *Phys. B Condens. Matter* **203**, 460 (1994).

[143] N. Giordano, E. R. Schuler, Macroscopic quantum tunneling and related effects in a one-dimensional superconductor, *Phys. Rev. Lett.* **63**, 2417 (1989).

[144] A. Johansson, G. Sambandamurthy, D. Shahar, N. Jacobson, R. Tenne, Nanowire acting as a superconducting quantum interference device, *Phys. Rev. Lett.* **95**, 116805 (2005).

[145] C. N. Lau, N. Markovic, M. Bockrath, A. Bezryadin, M. Tinkham, Quantum phase slips in superconducting nanowires, *Phys. Rev. Lett.* **87**, 217003 (2001).

[146] P. Li, P. M. Wu, Y. Bomze, I. V. Borzenets, G. Finkelstein, A. M. Chang, Switching currents limited by single phase slips in one-dimensional superconducting Al nanowires, *Phys. Rev. Lett.* **107**, 1 (2011).

[147] J. S. Lehtinen, T. Sajavaara, K. Y. Arutyunov, M. Y. Presnjakov, A. L. Vasiliev, Evidence of quantum phase slip effect in titanium nanowires, *Phys. Rev. B* **85**, 94508 (2012).

[148] D. Lucot, F. Pierre, D. Mailly, K. Yu-Zhang, S. Michotte, F. De Menten De Horne, L. Piraux, Multicontact measurements of a superconducting Sn nanowire, *Appl. Phys. Lett.* **91**, 42502 (2007).

[149] J. E. Lukens, R. J. Warburton, W. W. Webb, Onset of quantized thermal fluctuations in "one-dimensional" superconductors, *Phys. Rev. Lett.* **25**, 1180 (1970).

[150] R. S. Newbower, M. R. Beasley, M. Tinkham, Fluctuation Effects on the Superconducting Transition of Tin Whisker Crystals, *Phys. Rev. B* **5**, 864 (1972).

[151] A. Rogachev, A. Bezryadin, Superconducting properties of polycrystalline Nb nanowires templated by carbon nanotubes, *Appl. Phys. Lett.* **83**, 512 (2003).

[152] A. Rogachev, A. T. Bollinger, A. Bezryadin, Influence of high magnetic fields on the superconducting transition of one-dimensional Nb and MoGe nanowires, *Phys. Rev. Lett.* **94**, 17004 (2005).

[153] A. Rogachev, T. C. Wei, D. Pekker, A. T. Bollinger, P. M. Goldbart, A. Bezryadin, Magnetic-field enhancement of superconductivity in ultranarrow wires, *Phys. Rev. Lett.* **97**, 137001 (2006).

[154] M. Sahu, M.-H. H. Bae, A. Rogachev, D. Pekker, T.-C. C. Wei, N. Shah, P. M. Goldbart, A. Bezryadin, Individual topological tunnelling events of a quantum field probed through their macroscopic consequences, *Nat. Phys.* **5**, 503 (2009).

[155] F. Sharifi, A. V. Herzog, R. C. Dynes, Crossover from two to one dimension in in situ grown wires of Pb, *Phys. Rev. Lett.* **71**, 428 (1993).

[156] M. Singh, M. H. W. Chan, Observation of individual macroscopic quantum tunneling events in superconducting nanowires, *Phys. Rev. B* **88**, 1 (2013).

[157] M. Singh, J. Wang, M. Tian, Q. Zhang, A. Pereira, N. Kumar, T. E. Mallouk, M. H. W. Chan, Synthesis and superconductivity of electrochemically grown single-crystal aluminum nanowires, *Chem. Mater.* **21**, 5557 (2009).

[158] M. Tian, N. Kumar, J. Wang, S. Xu, M. H. W. Chan, Influence of a bulk superconducting environment on the superconductivity of one-dimensional zinc nanowires, *Phys. Rev. B* **74**, 1 (2006).

[159] M. Tian, N. Kumar, S. Xu, J. Wang, J. S. Kurtz, M. H. W. Chan, Suppression of superconductivity in zinc nanowires by bulk superconductors, *Phys. Rev. Lett.* **95**, 4 (2005).

[160] J. Wang, M. Singh, M. Tian, N. Kumar, B. Liu, C. Shi, J. K. Jain, N. Samarth, T. E. Mallouk, M. H. W. Chan, Interplay between superconductivity and ferromagnetism in crystalline nanowires, *Nat. Phys.* **6**, 389 (2010).

[161] M. Zgirski, K. Y. Arutyunov, Experimental limits of the observation of thermally activated phase-slip mechanism in superconducting nanowires, *Phys. Rev. B* **75**, 172509 (2007).

[162] M. Zgirski, K. Y. Arutyunov, Resistive state of quasi-one-dimensional superconductors: Fluctuations vs. sample inhomogeneity, *Phys. E* **40**, 160 (2007).

[163] M. Zgirski, K. P. Riikonen, V. Touboltsev, K. Y. Arutyunov, Quantum fluctuations in ultranarrow superconducting aluminum nanowires, *Phys. Rev. B* **77**, 54508 (2008).

[164] M. Zgirski, K. P. Riikonen, V. Touboltsev, K. Arutyunov, Size dependent breakdown of superconductivity in ultranarrow nanowires, *Nano Lett.* **5**, 1029 (2005).

[165] K. Y. Arutyunov, D. S. Golubev, A. D. Zaikin, Superconductivity in one dimension, *Phys. Rep.* **464**, 1 (2008).

[166] W. A. Little, Decay of persistent currents in small superconductors, *Phys. Rev.* **156**, 396 (1967).

[167] J. S. Langer, V. Ambegaokar, Intrinsic Resistive Transition in Narrow Superconducting Channels, *Phys. Rev.* **164**, 498 (1967).

[168] D. E. McCumber, B. I. Halperin, Time Scale of Intrinsic Resistive Fluctuations in Thin Superconducting Wires, *Phys. Rev. B* **1**, 1054 (1970).

[169] Y. Chen, S. D. Snyder, A. M. Goldman, Magnetic-Field-Induced Superconducting State in Zn Nanowires Driven in the Normal State by an Electric Current, *Phys. Rev. Lett.* **103**, 1 (2009).

[170] Y. Chen, Y. H. Lin, S. D. Snyder, A. M. Goldman, Stabilization of superconductivity by magnetic field in out-of-equilibrium nanowires, *Phys. Rev. B* **83**, 3 (2011).

[171] T. Morgan-Wall, H. J. Hughes, N. Hartman, T. M. McQueen, N. Marković, Fabrication of sub-15nm aluminum wires by controlled etching, *Appl. Phys. Lett.* **104**, 1 (2014).

[172] T. Morgan-Wall, B. Leith, N. Hartman, A. Rahman, N. Marković, Measurement of critical currents of superconducting aluminum nanowires in external magnetic fields: Evidence for a weber blockade, *Phys. Rev. Lett.* **114** (2015).

[173] A. Falk, M. Deshmukh, A. Prieto, J. Urban, A. Jonas, H. Park, Magnetic switching of phase-slip dissipation in NbSe2 nanoribbons, *Phys. Rev. B* **75**, 20501 (2007).

[174] H. Cai, K. Zhang, X. Yu, N. Pan, Y. Tian, Y. Luo, X. Wang, Highly efficient and controllable method to fabricate ultrafine metallic nanostructures, *AIP Adv.* **5**, 117216 (2015).

[175] N. Giordano, Experimental study of localization in thin wires, *Phys. Rev. B* **22**, 5635 (1980).

[176] D. E. Prober, M. D. Feuer, N. Giordano, Fabrication of 300-Å metal lines with substrate-step techniques, *Appl. Phys. Lett.* **37**, 94 (1980).

[177] G. V. Pai, E. Shimshoni, N. Andrei, Resistivity of inhomogeneous superconducting wires, *Phys. Rev. B* **77**, 104528 (2008).

[178] C. Qiu, T. Qian, W. Ren, Phase slips in superconducting wires with nonuniform cross section: A numerical evaluation using the string method, *Phys. Rev. B* **77**, 104516 (2008).

[179] V. R. Misko, V. M. Fomin, J. T. Devreese, Strong enhancement of superconductivity in a nanosized Pb bridge, *Phys. Rev. B* **64**, 145171 (2001).

[180] T. Qian, W. Ren, P. Sheng, Current dissipation in thin superconducting wires: A numerical evaluation using the string method, *Phys. Rev. B* **72**, 14512 (2005).

[181] D. S. Golubev, A. D. Zaikin, Quantum tunneling of the order parameter in superconducting nanowires, *Phys. Rev. B* **64**, 14504 (2001).

[182] S. Khlebnikov, L. P. Pryadko, Quantum phase slips in the presence of finite-range disorder, *Phys. Rev. Lett.* **95**, 1 (2005).

[183] M. Vanević, Y. V. Nazarov, Quantum phase slips in superconducting wires with weak inhomogeneities, *Phys. Rev. Lett.* **108**, 187002 (2012).

[184] A. D. Zaikin, D. S. Golubev, A. van Otterlo, G. T. Zimányi, Quantum Phase Slips and Transport in Ultrathin Superconducting Wires, *Phys. Rev. Lett.* **79**, 3316 (1997).

[185] J.-M. M. Duan, Quantum decay of one-dimensional supercurrent: Role of electromagnetic field, *Phys. Rev. Lett.* **74**, 5128 (1995).

[186] D. Pekker, N. Shah, M. Sahu, A. Bezryadin, P. M. Goldbart, Stochastic dynamics of phase-slip trains and superconductive-resistive switching in current-biased nanowires, *Phys. Rev. B* **80**, 1 (2009).

[187] J.-M. Duan, Comment on "Quantum Phase Slips and Transport in Ultrathin Superconducting Wires", *Phys. Rev. Lett.* **79**, 3316 (1997).

[188] A. S. AG, Inertial XYZ Positioner ANPxyz100 User Manual (2002).

[189] A. S. AG, Inertial Motor Driving Controller ANC150 User Manual (2002).

[190] S. B. Field, J. Barentine, Capacitive position sensor with simultaneous, linear X-Y readout, *Rev. Sci. Instrum.* **71**, 2603 (2000).

[191] J. Siegel, J. Witt, N. Venturi, S. Field, Compact large-range cryogenic scanner, *Rev. Sci. Instrum.* **66**, 2520 (1995).

[192] N. G. de Bruijn, W. van der Woude, A combinatorial problem pp. 758–764 (1946).

[193] G. Hurlbert, G. Isaak, On the de Bruijn Torus Problem, *J. Comb. Theory* pp. 1–13 (1993).

[194] H. Kjellerstrand, de Bruijn Sequence, http://www.hakank.org/comb/debruijn.cgi.

[195] Y. Chen, K. Peng, Z. Cui, A lift-off process for high resolution patterns using PMMA/LOR resist stack, *Microelectron. Eng.* **73-74**, 278 (2004).

[196] Y. Chen, Z. Lu, X. Wang, Z. Cui, G. Pan, Y. Zhou, M. Muñoz, C. Hao, L. Yonghua, N. Garcia, Fabrication of ferromagnetic nanoconstrictions by electron beam lithography using LOR/PMMA bilayer technique, *Microelectron. Eng.* **84**, 1499 (2007).

[197] M. Savolainen, V. Touboltsev, P. Koppinen, K. P. Riikonen, K. Arutyunov, Ion beam sputtering for progressive reduction of nanostructures dimensions, *Appl. Phys. A* **79**, 1769 (2004).

[198] M. Stepanova, S. Dew, *Nanofabrication: Techniques and principles* (Springer Science & Business Media, 2011).

[199] M. Khoury, D. K. Ferry, Effect of molecular weight on poly(methyl methacrylate) resolution, *J. Vac. Sci. Technol. B* **14**, 75 (1996).

[200] G. H. Bernstein, D. A. Hill, W.-p. Liu, New high-contrast developers for poly (methyl methacrylate) resist New high-contrast, *J. Appl. Phys.* **4066** (2004).

[201] M. A. Mohsin, J. M. Cowie, Enhanced sensitivity in the electron beam resist poly(methyl methacrylate) using improved solvent developer, *Polymer.* **29**, 2130 (1988).

[202] M. J. Rooks, E. Kratschmer, R. Viswanathan, J. Katine, R. E. Fontana, S. A. MacDonald, Low stress development of poly(methylmethacrylate) for high aspect ratio structures, *J. Vac. Sci. Technol. B* **20**, 2937 (2002).

[203] S. Yasin, D. G. Hasko, H. Ahmed, Comparison of MIBK/IPA and water/IPA as PMMA developers for electron beam nanolithography, *Microelectron. Eng.* **61-62**, 745 (2002).

[204] W. Hu, K. Sarveswaran, M. Lieberman, G. H. Bernstein, Sub-10 nm electron beam lithography using cold development of poly(methylmethacrylate), *J. Vac. Sci. Technol. B* **22**, 1711 (2004).

[205] A. Khiat, P. Ayliffe, T. Prodromakis, High Density Crossbar Arrays with Sub-15 nm Single Cells via Liftoff Process only, *Sci. Rep.* **6**, 1 (2016).

[206] I. Zailer, J. E. Frost, V. Chabasseur-Molyneux, C. J. Ford, M. Pepper, Crosslinked PMMA as a high-resolution negative resist for electron beam lithography and applications for physics of low-dimensional structures, *Semicond. Sci. Technol.* **11**, 1235 (1996).

[207] H. Duan, J. Zhao, Y. Zhang, E. Xie, L. Han, Preparing patterned carbonaceous nanostructures directly by overexposure of PMMA using electron-beam lithography, *Nanotechnology* **20** (2009).

[208] JEOL, Scanning Electron Microscope: Basic knowledge for using the SEM, *Jeol* pp. 1–32 (2006).

[209] J. Nabbity, NPGS User's Manual (2012).